

New Resistive Plate Chambers with high counting rate capability for the CMS experiment

Mikołaj Ćwiok

*Thesis submitted to the Warsaw University
in partial fulfillment of the requirements
for the Doctor of Philosophy degree in Physics,
performed under supervision of Professor Wojciech Dominik*



Warsaw University
Faculty of Physics

2002
(revised: 26 May 2003)

*This revised version of the thesis includes corrections of
few minor errors spotted by the reviewers*

Contents

List of Figures	iii
List of Tables	x
Introduction	1
1 The CMS experiment for the LHC	4
1.1 The LHC physics programme	4
1.2 The Compact Muon Solenoid detector	8
1.2.1 Overview of the detector performance	8
1.2.2 Trigger System	10
1.2.3 Muon System	12
1.2.4 Muon Trigger	15
2 Charge avalanche development in uniform electric field	21
2.1 Parallel Plate Chambers	21
2.2 Baseline RPC design	22
2.3 RPC state of the art	23
2.3.1 Primary ionization processes in the gas	23
2.3.2 Detection of neutral particles	26
2.3.3 Gas gain	28
2.3.4 Space charge effect and streamers	30
2.3.5 Signal development on external electrodes	31
2.3.6 Efficiency and timing	34
2.3.7 Uniformity of the electric field	35
2.3.8 RPC operation at high particle fluxes	38
2.3.9 Streamer mode of operation	38
2.3.10 Avalanche mode of operation	39
2.3.11 Existing models	40
2.4 Design adopted for CMS	41

3	Experimental methods, materials and model detectors	44
3.1	Novel techniques	44
3.1.1	New composite materials for electrodes	44
3.1.2	Inverted Double Gap RPC	59
3.1.3	Improved spacers	60
3.2	Model detectors	62
3.2.1	Low and high resistivity prototypes	62
3.2.2	Full scale ME 1/1 prototype	65
3.2.3	Medium-size IDG prototype	67
3.2.4	Medium-size single gap prototypes	69
3.2.5	PPAC with resistive bakelite electrode	71
3.3	Testing methods	72
3.3.1	Pulsed accelerator beams	73
3.3.2	Gamma Irradiation Facility	74
3.3.3	Laboratory tests with X-ray tube	80
3.4	Method of data analysis from test beams	81
4	Experimental results	84
4.1	Pulsed beam results	84
4.2	Continuous irradiation results	89
4.3	Results on ME 1/1 full scale prototype	94
4.4	Stability of operation at high rates	97
4.4.1	Short-term stability	98
4.4.2	Medium-term stability	105
4.5	Single gap solution	113
5	Equivalent circuit simulations	128
5.1	Proposed model	129
5.2	Results of calculation	131
	Summary	134
	Acknowledgments	137
A	Conductivity measurement technique	138
	Bibliography	144

List of Figures

1.1	Spatial view of the LHC tunnel divided into 8 octants.	8
1.2	Expanded view of the CMS detector.	9
1.3	Inclusive p - p (or p - \bar{p}) cross sections and corresponding interaction rates for design luminosity of $10^{34} \text{ cm}^{-2}\text{s}^{-1}$ for selected physics processes.	11
1.4	Location and naming conventions of four muon stations in one quadrant of the CMS detector.	13
1.5	Particle fluxes vs energy in the gas layers of: (A) drift tubes in the CMS barrel, (B) CSCs in the CMS endcaps.	14
1.6	Expected hit rates in muon chambers due to: muons, hadronic punchthrough/back-splashes and electrons from thermal neutrons.	16
1.7	The PACT idea: a set of predefined hit patterns in four muon stations is used to estimate p_t of muons originated from the interaction point.	17
2.1	A standard design of a single gap RPC with one-dimensional readout.	23
2.2	A standard design of a double gap RPC with one-dimensional readout.	23
2.3	HEED simulation of the specific primary ionization and the average number of electrons per cluster for muons in two gases ($T = 20^\circ\text{C}$, $p = 760 \text{ Torr}$).	25
2.4	HEED simulation of the probability distribution of the number of electrons in primary ionization clusters for minimum ionizing muons in two gases ($\beta\gamma = 3$, $T = 20^\circ\text{C}$, $p = 760 \text{ Torr}$).	25
2.5	Simulated photon sensitivity of a double gap RPC structure.	28
2.6	Simulated neutron sensitivity of a double gap RPC structure.	28
2.7	The idea of a charge formation in the RPC gap.	30
2.8	The effect of space charges of an avalanche of high amplification on the applied electric field.	30
2.9	Equivalent circuit for weighting field calculation (Ramo's theorem) for single gap RPC.	32
2.10	Carrier current of electrons of an avalanche in the uniform electric field.	32
2.11	Carrier current of positive ions of an avalanche in the uniform electric field.	33

2.12	Carrier currents of an avalanche due to: electrons, positive and negative ions for attachment $\eta > 0$	33
2.13	Cross section of the spacer region in a typical RPC detector.	36
2.14	Cross section of the frame region in a typical RPC detector.	36
2.15	Calculated absolute electric field in the middle plane of a single gap RPC.	37
2.16	Plane view of the ME 2/1 signal planes (A) and corresponding cross section showing sub-modules configuration and ducts for signal cables connecting strips with the front-end electronics (B).	42
2.17	The same as in Fig. 2.16 for ME 2/2 module.	42
3.1	Expanded view of tested laminates for RPC electrodes.	46
3.2	Voltage dependence of the resistivity of several fresh bakelite samples after 5 minutes of applying the test voltage.	46
3.3	Temperature dependence of the resistivity of IT-99 type bakelite.	49
3.4	Short-term resistivity dependence on humidity for IT-99 bakelite.	49
3.5	Recovery of the bakelite resistivity after conditioning at 60° C for 24 hours for two types of bakelite.	51
3.6	Resistivity of four bakelite samples of the same type stored at room conditions during period of 10/1998-09/2002.	52
3.7	Medium-term effect of humidity of the surrounding gas medium on the bakelite resistivity.	53
3.8	Medium-term effect of dry gas on the resistivity of bakelite having both surfaces treated with linseed oil mixture.	54
3.9	Comparison of sampling and constant polarizing voltage measurements for PL-#11 bakelite sample.	55
3.10	Medium-term resistivity dependence on time after applying of constant polarizing voltages of ± 500 V for IT-99 bakelite sample.	57
3.11	Accumulated charge vs time for a constant polarizing voltage test from Fig. 3.10.	57
3.12	Cross section of Inverted Double Gap RPC with standard graphite-coated sub-modules.	60
3.13	Cross section of Inverted Double Gap RPC with sub-modules made out of specially developed aluminium-cladded bakelite plates.	60
3.14	A novel technique of improved spacer gluing.	61
3.15	A method of gap interconnection through special spacers used in Inverted Double Gap RPCs.	61
3.16	Schematic view of RPC 1 and RPC 2 prototypes tested at H2/SPS beam at CERN.	64

3.17	An Inverted Double Gap ME 1/1 prototype: (A) expanded view along φ ; (B) cross section along detector's symmetry axis.	66
3.18	Front view of the RPC ME 1/1 full scale prototype.	67
3.19	An Inverted Double Gap medium-size prototype tested in the GIF at CERN: (A) view in direction of the beam showing strip segmentation, (B) schematic cross section.	68
3.20	Single gap medium-size prototypes tested in the GIF at CERN: (A) view in direction of the beam showing strip sections of 10 mm and 8 mm width of one module, (B) schematic cross section through the modules.	70
3.21	Schematic view of the PPAC with a bakelite electrode.	72
3.22	Schematic diagram of the RPC test set-up at H2/SPS beam at CERN.	73
3.23	Layout of the Gamma Irradiation Facility X5/SPS test beam zone at CERN.	74
3.24	Schematic layout of a test beam set-up in the GIF zone used between 1997 and 2002.	75
3.25	Experimental set-up for monitoring of the gas gain in the PPAC detector irradiated with X-rays.	80
3.26	Idea of efficiency- and background rate measurement from the GIF data.	83
3.27	Example of cluster-to-cluster delay distribution for a run with source fully opened for medium-size prototype tested in the GIF in 2001.	83
4.1	Detection efficiency averaged over 2.5 s beam extraction cycle for high resistivity RPC 1 module.	85
4.2	Detection efficiency averaged over 2.5 s beam extraction cycle for low resistivity RPC 2 module.	85
4.3	Detection efficiency of high resistivity prototype RPC 1 as a function of time during the extraction cycle of the beam for various fluxes.	86
4.4	Detection efficiency of low resistivity prototype RPC 2 as a function of time during the extraction cycle of the beam for various fluxes.	86
4.5	Signal arrival time measured for RPC 1 as a function of time during the extraction cycle of the beam for various fluxes.	87
4.6	Signal arrival time measured for RPC 2 as a function of time during the extraction cycle of the beam for various fluxes.	87
4.7	Signal arrival time and time resolution of the low resistivity RPC 2 as a function of the particle flux.	87
4.8	Distribution of the avalanche arrival time with respect to the trigger defined by the beam counters for radiation flux of 640 Hz/cm ²	87

4.9	Cluster size measured in RPC 1 at the particle flux of 640 Hz/cm^2 .	88
4.10	Cluster size measured in RPC 2 at the particle flux of 640 Hz/cm^2 .	88
4.11	Efficiency of RPC 2 for minimum ionizing particles measured in the GIF as a function of the high voltage.	90
4.12	Efficiency of RPC 2 as a function of the nominal attenuation factor of the ^{137}Cs source.	90
4.13	Measured background rate due to photons in one gap of RPC 2 as a function of the nominal attenuation factor.	91
4.14	Time resolution of RPC 2 as a function of the nominal attenuation factor of the ^{137}Cs source.	91
4.15	Signal arrival time of RPC 2 as a function of nominal attenuation factor of the ^{137}Cs source.	92
4.16	The average strip multiplicity as a function of the nominal attenuation factor of the ^{137}Cs source.	92
4.17	The current drawn by one of RPC 2 planes as a function of the nominal attenuation factor of the ^{137}Cs source.	93
4.18	The departure of one layer of RPC 2 chamber thickness from the nominal one calculated from efficiency.	93
4.19	The departure of one layer of RPC 2 chamber thickness from the nominal one calculated from timing.	93
4.20	Detection efficiency of ME 1/1 prototype as a function of the high voltage for different source intensities.	95
4.21	Detection efficiency of ME 1/1 prototype as a function of the nominal attenuation factor for several operating voltages.	95
4.22	The efficiency of ME 1/1 prototype as a function of the width of the acceptance time window for two source intensities.	96
4.23	The arrival time distribution of the first signal with the source intensity of about $1 \text{ kHz/cm}^2/\text{gap}$ at the applied voltage corresponding to the knee of the efficiency plateau.	96
4.24	The average signal arrival time as a function of the high voltage.	96
4.25	The signal arrival time spread of ME 1/1 prototype as a function of the high voltage for several source intensities.	96
4.26	Efficiency of RPC 2 as a function of the ambient air temperature.	99
4.27	The signal arrival time of RPC 2 as a function of the ambient air temperature.	99
4.28	The signal arrival spread of RPC 2 as a function of the ambient air temperature.	100

4.29	The average strip multiplicity of RPC 2 as a function of the ambient air temperature	100
4.30	Detection efficiency and avalanche cluster size as a function of the applied voltage in double gap mode.	101
4.31	Corrected cluster rate as a function of the applied voltage in double gap mode. . .	101
4.32	Cluster rate as a function of the applied voltage in double gap mode and in single gap mode for two gaps independently.	102
4.33	Cluster length in time as a function of nominal operating voltage for RPC operated in double- and in single gap mode working at full source intensity.	102
4.34	PCMONTE simulation of the effective Townsend coefficient α_{eff} for several TFE/Iso-butane/SF ₆ gas mixtures at normal conditions.	103
4.35	The charge current in single RPC gaps as a function of applied voltage.	103
4.36	Rate of single hits and rate of clusters for fully opened source.	104
4.37	Rate of single hits for constant applied voltage of 10.4 kV measured during the three runs: full intensity, no source, full intensity.	104
4.38	Induced charge distributions at nominal working voltage of 4900 V for two intensities of 8 keV X-rays.	106
4.39	Counting rate as a function of voltage applied to the bakelite electrode for low intensity beam of 8 keV photons.	106
4.40	Measurements of the gas amplification stability in the PPAC detector for several intensities of X-ray beam.	108
4.41	Dependence of the normalized gas gain on time for several counting rates.	110
4.42	Initial values of corrected pulse-heights from a PPAC detector for each data set as a function of the average rate of avalanches per unit area.	110
4.43	Efficiency of single gap RPC modules as a function of normalized H.V. for two gas mixtures and for two intensities of gamma rays.	114
4.44	Rate of clusters of single RPC modules as a function of normalized H.V. for two gas mixtures and for two intensities of gamma rays	114
4.45	Current density in single gap RPC modules as a function of normalized H.V. for two gas mixtures at fully intensity of gamma rays.	115
4.46	Correlation between efficiency and current density measured for not-oiled RPC at full intensity of gamma rays for two gas mixtures	115
4.47	Rate of clusters without irradiation source as a function of the normalized H.V. .	117
4.48	Correlation between hit arrival times in one of MWPCs and not-oiled RPC. . . .	118

4.49	Distribution of the arrival time difference calculated for each pair of hits in two RPCs.	118
4.50	Test pulse time distributions for one of front-end boards showing offsets between individual channels due to: front-end chip and LVDS-to-ECL converter.	119
4.51	Signal arrival time of single gap RPC modules as a function of normalized H.V. for 97% - TFE gas mixture and for two intensities of gamma rays.	119
4.52	Signal arrival time of single gap RPC modules as a function of normalized H.V. for 0.7% - SF_6 gas mixture and for two intensities of gamma rays.	120
4.53	Signal arrival time distribution from one of the readout strips of not-oiled RPC module filled with 0.7% - SF_6 gas mixture and operated at 9.8 kV and at full source intensity.	120
4.54	Signal arrival time distribution from one of the readout strips of oiled RPC module filled with 0.7% - SF_6 gas mixture and operated at 9.8 kV and at full source intensity.	121
4.55	Signal arrival time distribution from one of the readout strips of not-oiled RPC module filled with 0.7% - SF_6 gas mixture and operated at 10.2 kV and at full source intensity.	121
4.56	Signal arrival time distribution from one of the readout strips of oiled RPC module filled with 0.7% - SF_6 gas mixture and operated at 10.2 kV and at full source intensity.	122
4.57	Signal arrival time spread of single gap RPC modules, with respect to the trigger counters, as a function of normalized H.V. for 97% - TFE gas mixture and for full intensity of gamma rays.	122
4.58	Efficiency and cluster size in strips for not-oiled RPC module as a function of normalized high voltage for 97% - TFE gas mixture and for full intensity of gamma rays.	123
4.59	Efficiency and cluster size in strips for not-oiled RPC module as a function of normalized high voltage for 0.7% - SF_6 gas mixture and for full intensity of gamma rays.	123
4.60	Probability of inducing signals on two strip groups at a time. as a function of position of the muon track along strip.	124
4.61	Efficiency and cluster size in strips for not-oiled RPC module as a function of normalized high voltage for: 0.7% - SF_6 gas mixture, full intensity of gamma rays and two strip sections having: 8 mm and 10 mm strip width.	125

4.62	Efficiency and cluster size in strips as a function of electronic threshold for oiled RPC module for: nominal voltage of 9.8 kV, 0.7%-SF ₆ gas mixture and full intensity of gamma rays.	125
5.1	Proposed working model for SPICE simulation: (A) Division of the active area into coaxial rings, (B) Cross section of a single ring, (C) Equivalent electric circuit.	129
5.2	Dependence of the measured current density with- and without irradiation on the effective gas gap voltage used to extract parametrization of the gas gain.	130
5.3	Simulated potential difference in the gas gap after starting the irradiation for low resistivity RPC with a highly resistive graphite paint.	132
5.4	Simulated potential difference in the gas gap after starting the irradiation for high resistivity RPC with a standard graphite coating.	132
A.1	Coaxial circular electrodes for electric conductivity tests of flat composite materials.	138
A.2	Electric circuit for volume resistivity measurements.	138
A.3	Electric circuit for surface resistivity measurements.	139
A.4	Cross section of the aluminium container for conductivity tests.	139
A.5	Experimental set-up for conductivity measurements in dry- and wet gas environments.	139
A.6	Special probe for conductivity measurements of specimens with permanent electrodes.	139
A.7	Special probe for resistivity measurements using conductive rubber technique.	141
A.8	Comparison of conductive rubber technique and silver paint method for IT-2002 sample at test voltage of 500 V.	141

List of Tables

3.1	Description of bakelite types referred in the text.	47
3.2	Parametrization of the bakelite resistivity ϱ as a function of temperature T in degree centigrade.	50
3.3	Total integrated current per unit area in a single RPC gap after 10 LHC years at peak luminosity.	56
3.4	Roughness parameter R_a for several not-oiled bakelite samples.	59
3.5	Mechanical and electrical characteristics of RPC 1 and RPC 2 prototypes.	65
3.6	Parameters of the data acquisition system used in the GIF during 1997-2002.	78
3.7	Conductivity of the electrodes, gas mixtures and RPC positions during 1997-2002 test beams in the GIF.	79
4.1	Calculated correlation factors h , measured counting rates and initial ambient temperature and pressure for each data set from Fig. 4.40.	109
5.1	Calculated deviation from the nominal applied voltage of 10 kV at 1 kHz/cm ² /gap for several sets of SPICE model parameters.	132
A.1	Accuracy specifications of KEITHLEY 487 unit.	140
A.2	Types of electrodes used in conductivity tests.	142

Introduction

The last three decades showed that the Standard Model (SM) [1–3] of strong and electroweak interactions is in excellent agreement with experimental observations. However, the electroweak symmetry breaking mechanism, responsible for acquiring the mass by elementary particles, predicts existence of a massive scalar Higgs boson [4–8], which is the last undiscovered SM particle.

A search for the Higgs particle is one of the main motivations to construct a very powerful hadron accelerator ever build, called Large Hadron Collider (LHC) at CERN¹ in Geneva. It will collide bunches of protons at 14 TeV centre of mass energy every 25 ns and will exploit energy region up to TeV range on the parton level. The designed luminosity is $10^{34} \text{ cm}^{-2}\text{s}^{-1}$. Also heavy ion collisions are foreseen at unprecedented energies per nucleon-nucleon of $5.5 \div 7 \text{ TeV}$, though at lower luminosity of $10^{27} \div 10^{30} \text{ cm}^{-2}\text{s}^{-1}$. The products of interactions will be studied by five experiments:

- ATLAS (*A Toroidal LHC Apparatus*) and CMS (*Compact Muon Solenoid*) - two general purpose detectors,
- ALICE (*A Large Ion Collider Experiment*) - designed for heavy ion physics,
- LHC-b - dedicated to the b-quark physics,
- TOTEM - designed for total cross section measurements, and for studying diffractive processes.

The LHC is due to start its operation in 2007. All experiments have been designed to take data for at least 10 years under presence of severe radiation environment.

The work presented in this thesis has concerned one of sub-detectors of the Compact Muon Solenoid experiment, namely Muon Trigger system. The Author is a member of the Warsaw CMS collaboration group² involved in development of fast, dedicated electronics for muon detection system based on gaseous muon chambers, called Resistive Plate Chambers (RPCs) [9]. The Warsaw Group has been actively participating in basic research on RPC technique in the framework of the CMS Muon Trigger project since its very beginning. The Author joined this

¹ *Conseil Européen pour la Recherche Nucléaire* - a French name of the initial establishment body gives origin to the abbreviation “CERN”.

² The Group associates members from the Institute of Experimental Physics of the Warsaw University (IEP) and the Soltan’s Institute for Nuclear Studies (SINS).

activity in 1996 and, in particular, has been responsible for developing, assembling, optimizing and testing various RPC prototypes.

At the begin of CMS definition the Resistive Plate Chambers seemed to be simple in manufacturing detectors according to the state of the art of early 90's [10]. However, later detailed R&D studies revealed several drawbacks of the baseline RPC design adopted for the CMS experiment. Even though, the RPC production phase has been started already, there is still place for improvements. Therefore, this thesis addresses possible sources of remedy to some of the problems, as well.

The work presented in this thesis is organized in chapters. In the first Chapter an overview of the physics studies at LHC is given. The CMS detector, with emphasis on the Muon Trigger system, is also briefly described there. In Chapter 2 principles of operation of RPC detectors, one of important CMS Muon Trigger components, are given. A current state of the art on RPC technique is described with the stress put on RPC potential to withstand hostile radiation environment foreseen in the CMS forward region. The performances of several RPC prototypes, constructed and assembled in the Detector Laboratory of the Institute of Experimental Physics (IEP) of the Warsaw University, have been studied in the radiation environment similar to the one foreseen at the LHC. The Chapter 3 contains detailed description of tested detectors, experimental methods used and studies of new composite materials for planar electrodes. In particular, stability of the electrical characteristics of materials for RPC electrodes has been measured as a function of various factors, such as: temperature, humidity and integrated charge. The results of the beam tests, performed by the Warsaw CMS Group during years 1997-2002, are discussed in Chapter 4, which is the main part of the thesis. Performances of tested RPC detectors as a function of electrodes' conductivity and the rate of avalanches induced in the gas gap are presented. The following observables are addressed: efficiency, time resolution, strip multiplicity and intrinsic noise rate. Results on short- and medium-term stability are also given. In Chapter 5 a working numerical model is presented, which computes the effective amplification field inside the gas gap. Parametrization of the gas gain on the electric field, obtained from the test beam data, has been used as an input to the model. The simulation confirms a key role of the stability of electrodes' conductivity with time for efficient RPC operation in the CMS forward regions. The techniques of electric conductivity measurement adopted for: selection and monitoring of the long-term stability of the resistivity of composite organic materials used for RPC electrodes in tested prototypes are discussed in the Appendix.

Among the results, it has been demonstrated that RPC consisting of only one gas gap can efficiently detect muons in presence of the background rate of $\sim 1 \text{ kHz/cm}^2$, the upper limit set for RPCs working in the CMS endcap regions.

Chapter 1

The CMS experiment for the LHC

1.1 The LHC physics programme

At present the Large Hadron Collider (LHC) [11] is being built at the European Laboratory for Particle Physics (CERN) in Geneva to study parton interactions in p - p collisions at $\sqrt{s} = 14$ TeV. It will be situated in an existing underground LEP¹ tunnel of 27 km circumference.

As it was pointed out in the Introduction the main physics goal of the LHC is to confirm existence of the Standard Model Higgs particle. The latest searches performed at LEP experimentally excluded Higgs mass (m_H) region below 114 GeV/ c^2 at 95% CL [12, 13]. On the other hand, the upper limit on m_H is somewhat 1 TeV/ c^2 since perturbative theory breaks down for too heavy Higgses. Also the electroweak precision fits used to predict the most likely value of the Higgs mass favour region of $m_H < 196$ GeV/ c^2 at 95% CL [14].

Besides search for Higgs, a wide energy range at the parton level can be explored due to the fact that the energy available in the collision $\sqrt{\hat{s}} = \sqrt{x_1 x_2 s}$ will vary from event to event according to fractions (x_1 and x_2) of the total momentum carried by two interacting partons of nuclei. The LHC can be operated also in heavy ion collision mode delivering ion beams from oxygen to lead.

In general, the physics programme at the LHC can be summarized as follows:

► Electroweak symmetry breaking mechanism [15–18]

There are several possible scenarios of Spontaneous Symmetry Breaking which have to be verified experimentally.

In the minimal SM one Higgs boson H must exist, but its mass cannot be predicted by the model. This elusive particle can be detected only by its decays. Depending on its mass range the most promising decay channels are the following:

¹The *Large Electron Positron* collider was shut down in 2000 and the accelerator was finally dismantled from the tunnel in 2002.

- $m_H < 130 \text{ GeV}/c^2$: $H \longrightarrow \gamma\gamma$
 $H \longrightarrow b\bar{b}$
- $130 \text{ GeV}/c^2 < m_H < 2m_Z$: $H \longrightarrow Z^{(*)}Z^* \longrightarrow 2l^+2l^-$
 $H \longrightarrow W^{(*)}W^{(*)} \longrightarrow ll\nu\nu$
- $2m_Z < m_H < 800 \text{ GeV}/c^2$: $H \longrightarrow ZZ \longrightarrow 2l^+2l^-$
- $m_H > 600 \text{ GeV}/c^2$: $H \longrightarrow ZZ \longrightarrow ll\nu\nu$
 $H \longrightarrow ZZ \longrightarrow ll + 2 \text{ jets}$
 $H \longrightarrow WW \longrightarrow l\nu + 2 \text{ jets},$ where $l = e, \mu$.

The predicted natural width of the SM Higgs is less than $1 \text{ GeV}/c^2$ for $m_H < 200 \text{ GeV}/c^2$ [19]. Therefore in this mass region the detector precision will contribute significantly to the reconstructed Higgs mass distribution.

In the Minimal Supersymmetric Standard Model (MSSM) five Higgs particles exist: light neutral scalar h° , heavy neutral scalar H° , pseudoscalar A° and charged H^\pm . The following channels can be used for discovery of the MSSM Higgses:

- $h^\circ, H^\circ \longrightarrow \gamma\gamma$
- $h^\circ \longrightarrow ZZ^*, H^\circ \longrightarrow ZZ^{(*)}$
- $h^\circ, H^\circ, A^\circ \longrightarrow \tau\tau$
- $t \longrightarrow H^\pm b, H^\pm \longrightarrow \tau\bar{\nu}_\tau$
- $h^\circ, H^\circ, A^\circ \longrightarrow \mu\mu$.

► Supersymmetry [15–17, 20]

The LHC is well suited to study the Supersymmetry (SUSY), a possible extension of the SM theory. SUSY introduces new particles (*sparticles*): *squarks* (spin 0), *sleptons* (spin 0), *higgsinos* (spin $\frac{1}{2}$) and *gauginos* (spin $\frac{1}{2}$), which are superpartners of the particles known from the SM. It will be possible to extend searches of the particles predicted by SUSY up to masses of $2.5 \text{ TeV}/c^2$. From experimental point of view the discovery of sparticles (*gluinos* and *squarks*) will be possible only by analysis of event topology, since theory predicts that no sparticles mass peaks can be observed. Therefore experiments have to identify final sparticles decay states of the form: $\text{jets} + E_t^{\text{miss}}$ or $\text{jets} + \text{leptons} + E_t^{\text{miss}}$. In particular, muon recognition in multi-jet environment will be essential. The evidence for SUSY particles will not be possible without good understanding of the background processes from the Standard Model.

► B-physics [15–17, 21, 22]

The LHC machine will serve as a huge B-factory since cross section for $b\bar{b}$ pair production

is of the order of hundreds microbarns, well above cross sections achievable in any other existing or planned B-factories.² The following studies related to B-physics will be performed at the LHC: CP violation in the beauty quark sector, measurement of the quark-antiquark mixing in B_d and B_s mesons, rare B meson decays (e.g. $B \rightarrow \mu\mu$). These measurements will require selecting muons above low p_t threshold of $2 \div 4 \text{ GeV}/c$.

► Top physics [15, 16]

At the LHC it will be possible to measure t quark mass with precision of $1 \text{ GeV}/c^2$, and to study rare top quark decay channels. The detectors have to identify precisely energetic muons, electrons and b -jets, present in the final state of the top quark decay.

► Precise measurements of known processes [15, 16]

Even if Higgs or SUSY particles would not be discovered at the LHC there is still a great interest in precise measurements of the SM parameters, total inelastic and elastic cross sections. The QCD coupling constant can be measured with high accuracy. Also several electroweak parameters, such as W mass and electroweak mixing angle, can be precisely determined. Studies of double- and triple vector boson couplings are feasible (WW , WZ , ZZ , $W\gamma$, $Z\gamma$, $WW\gamma$, WWZ). Moreover, production of W , Z bosons of high p_t is a background to many processes under interest, therefore identification of W , Z is of primary importance for experiments at the LHC.

► Exotica [15–17]

One of possible extensions of the Standard Model introduces new gauge bosons, W' and Z' , with a mass of several TeV/c^2 . Their discovery is possible at LHC up to about $5 \text{ TeV}/c^2$ in bosonic or fermionic decay channels: $Z' \rightarrow ZW$, $W' \rightarrow l\nu$, $Z' \rightarrow l^+l^-$. For example, a muonic decay modes of such heavy objects will require muon p_t measurement and sign of charge determination above $1 \text{ TeV}/c$.

At present three generations of quarks and leptons have been discovered. However, models containing fourth generation leptons and quarks with higher masses can be also considered. For instance, such fourth generation quark u_4 would predominantly decay to $W + b$ and only after certain integrated luminosity the signal can be visible over large $t\bar{t}$ and $W + jet$ background.

The other exotic topics which can be explored at the LHC include:

- *Monopoles* - particles with only one magnetic pole
- *Leptoquarks* - particles carrying both leptonic and barionic number

²HERA-B (HERA in DESY), Belle (KEKB in KEK), BaBar (PEPII in SLAC), CLEO-III (CESR in Cornell), CDF-II and D0-II (Tevatron in FNAL).

- *Technicolor* - a new strong interaction at high scale providing an alternative to Higgs mechanism of electroweak symmetry breaking by means of technipions
- *Extra Dimensions* - testing of the models assuming existence of additional spatial dimensions in order to solve the problem of hierarchy between the electroweak scale and the Planck scale (e.g. in the Randall-Sundrum model excitations of the graviton G having the lowest mass of the order of 1 TeV/c² can be observed via their decays into pair of fermions).

► Heavy ion physics [16, 23, 24]

At the LHC working in heavy ion collision mode search for the possible signatures of the Quark Gluon Plasma (QGP) will be performed. A dense hadronic matter above QGP threshold will be created at energies per nucleon-nucleon pair of $\sqrt{s_{NN}} = 5.5 \div 7$ TeV. Five kinds of nuclei can be collided: O, Ar, Kr, Sn, Pb at luminosities between $10^{27} \text{ cm}^{-2} \text{ s}^{-1}$ (for Pb) and $10^{30} \text{ cm}^{-2} \text{ s}^{-1}$ (for O, Ar) every 125 ns. The luminosity should be lower than in p - p mode because the particle multiplicity of one single event may reach 10^4 particles per unit of rapidity. One of important signatures of QGP is the modified production rate of $b\bar{b}$ resonances, which can be observed via their di-muon decays: $\Upsilon, \Upsilon', \Upsilon'' \rightarrow \mu^+ \mu^-$.

Collisions at the LHC will be studied by four experiments (see Fig. 1.1). The ATLAS (*A Large Toroidal LHC Apparatus*) [25] and the CMS (*Compact Muon Solenoid*) [16] are two general purpose detectors, while the ALICE (*A Large Ion Collider Experiment*) [24] and the LHCb [22] are dedicated for heavy ions physics and for B-physics, respectively. The fifth TOTEM detector [26], which components will be integrated with the LHC beam pipe in the vicinity of the CMS collision point, will serve for measurements of: the luminosity, total cross sections and diffractive processes.

Since theoretical models predict extremely small probabilities for interesting physics phenomena (e.g. Higgs particle(s) production), the LHC will provide very high interaction rates at some of the experimental beam-crossing points. The maximum proton beam energy of 7 TeV results from the maximal achievable dipole magnetic field of 8.3 Tesla. The designed luminosity for p - p collisions is $10^{34} \text{ cm}^{-2} \text{ s}^{-1}$, which corresponds to the integrated luminosity of about 100 fb^{-1} per year.³ Such high luminosity can be achieved due to: bunch collision frequency of 40 MHz, beam radius of $16 \mu\text{m}$ and 10.5×10^{10} particles per bunch. On average 17 inelastic p - p collisions will take place every 25 ns, what means almost 10^9 inelastic interactions per second. Statistically, in a single inelastic collision over 100 particles will be created, which will leave about 50 charged tracks in the detectors.

³Assuming that one equivalent LHC year lasts 10^7 s.

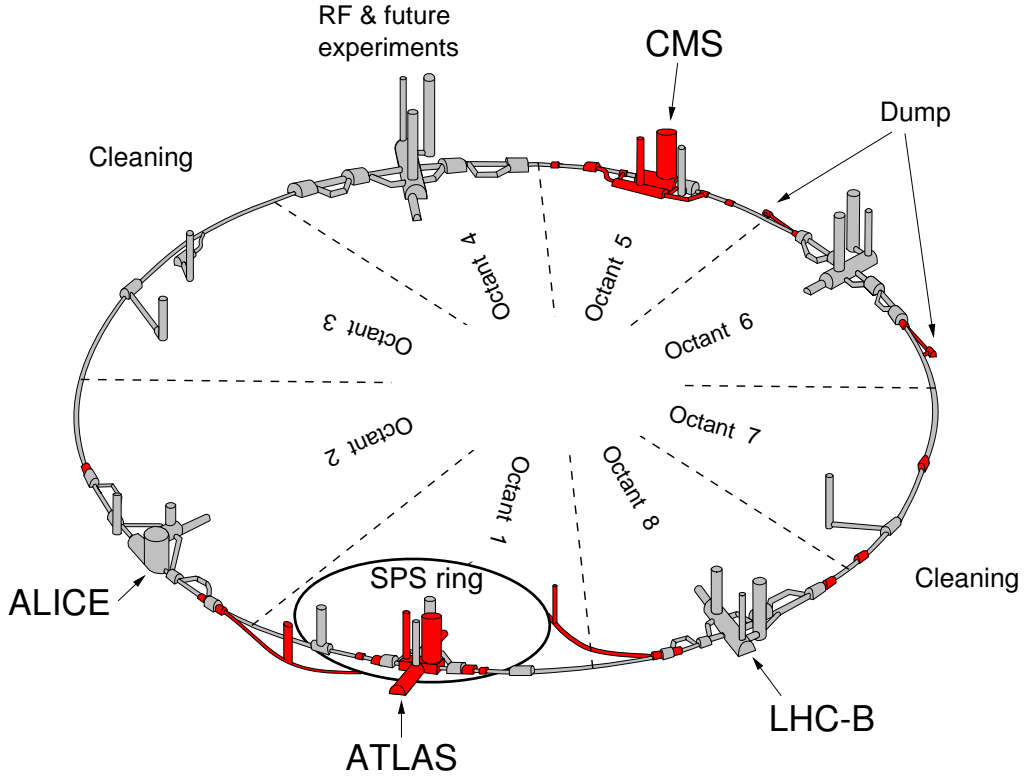


Figure 1.1: Spatial view of the LHC tunnel divided into 8 octants. The experiments will be located in caverns at four beam-crossing points.

In mid 2007 first collisions of proton bunches are foreseen. Initial luminosity will achieve $10^{33} \text{ cm}^{-2} \text{ s}^{-1}$ and only after first few years the maximum luminosity of $10^{34} \text{ cm}^{-2} \text{ s}^{-1}$ will be achieved. However, the low luminosity mode is attractive, in particular, for B-physics and top quark properties studies. Moreover, the integrated luminosity of 10 fb^{-1} , expected during first year of the LHC operation, should give evidence of the existence of SM or MSSM Higgs particles.

In the next Section the CMS detector will be briefly discussed.

1.2 The Compact Muon Solenoid detector

1.2.1 Overview of the detector performance

The general purpose Compact Muon Solenoid [16] experiment will precisely measure muons, electrons and photons over wide energy range. The detector has been designed to operate at the highest available luminosity. It consists of: the inner tracker, calorimeters and muon detection systems as it is shown in Fig. 1.2.

The major part of the detector is the magnet system. A solenoidal magnetic field shape is created by the superconducting coil having diameter of 6.2m and length of 13.5m. The

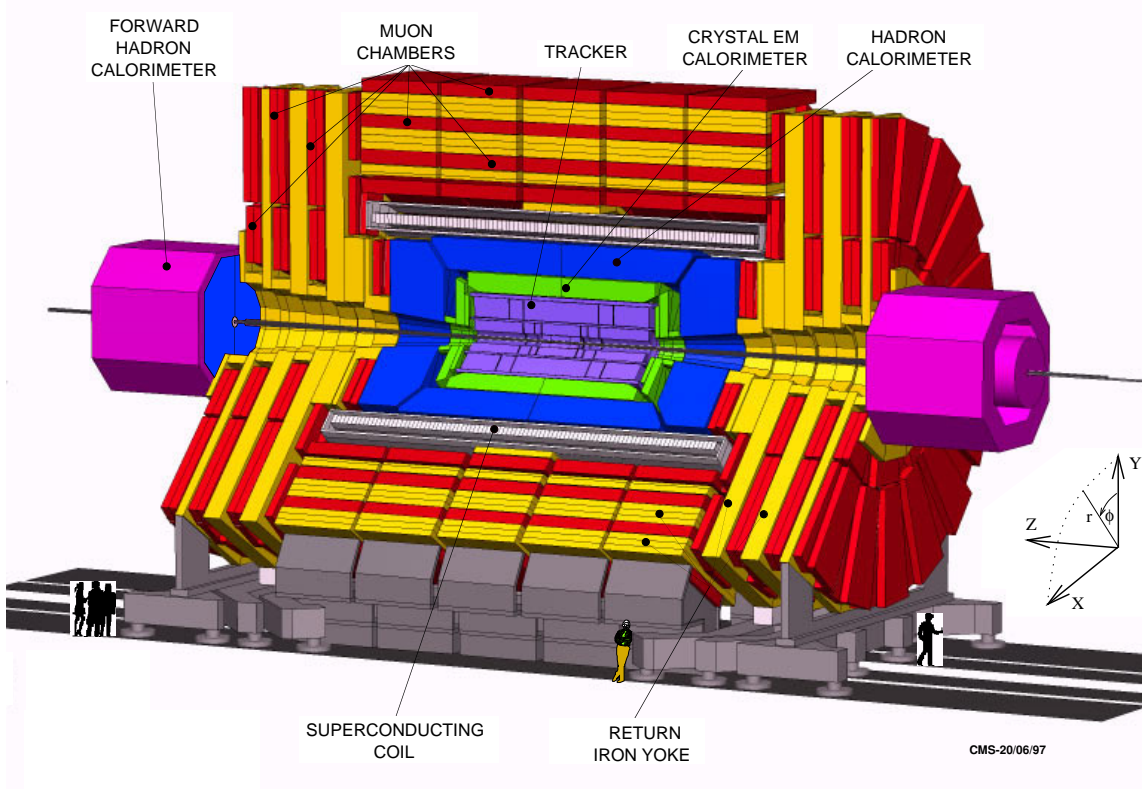


Figure 1.2: Expanded view of the CMS detector. The main parts of the detector are marked.

uniform 4 Tesla magnetic field created inside the coil provides necessary charged track bending in pseudorapidity⁴ region of $|\eta| < 2.4$. The large solenoid hosts the inner tracking system and two central calorimeters. The return iron yoke, situated outside the coil, closes the magnetic field lines and is interlaced with muon detectors.

The central inner tracker provides very accurate and efficient track measurements and excellent secondary vertex detection. It can efficiently reconstruct isolated high p_t tracks and tracks within jets up to $|\eta| < 2.4$. The impact parameter resolution of high p_t tracks is $20 \mu\text{m}$ and $65 \mu\text{m}$, respectively, in transverse- and in longitudinal plane with respect to the beam axis. In the central pseudorapidity region the momentum resolution $\Delta p/p$ is better than 5% for $p < 1 \text{ TeV}/c$ and it decreases with pseudorapidity to 20% at $|\eta| = 2.4$. The tracker is constituted of 3 layers of silicon pixel- and 10 layers of silicon strip detectors with very fine granularity. It has about 50×10^6 channels to be read out, the largest number from all CMS sub-detectors.

The homogeneous electromagnetic calorimeter (ECAL), made out of lead tungstate (PbWO_4) crystals, provides excellent electron/photon detection. Its predicted energy resolution is better

⁴Pseudorapidity (η) is defined as $\eta \equiv -\ln \tan \frac{\theta}{2}$, where θ denotes an angle measured from the beam axis in a coordinate system centered at the collision point.

than 1% for energy above 100 GeV and its angular resolution is $40 \text{ mrad}/\sqrt{E/\text{GeV}}$. The crystal matrix has lateral granularity of $\Delta\eta \times \Delta\varphi \approx 0.014 \times 0.014$. The ECAL extends up to $|\eta| = 3.0$ and covers about 26 radiation lengths X_0 and 1.1 nuclear interaction lengths λ . A compact ECAL design results from small Moliere radius ($R_M = 2 \text{ cm}$) and short radiation length ($X_0 = 9 \text{ mm}$) of PbWO_4 absorber.

The CMS hadron sampling calorimeter system (HCAL) consists of two components: the central hadron calorimeter (HB and HE in the barrel and in endcap regions, respectively) and the forward calorimeter (HF).

The central HCAL extends up to $|\eta| = 3.0$ and surrounds the ECAL. It is made out of non-ferromagnetic brass absorber interlaced with plastic scintillators. The HCAL has lateral granularity of $\Delta\eta \times \Delta\varphi \approx 0.087 \times 0.087$. The amount of absorber increases with pseudorapidity from 5λ at $\eta = 0$ to 10.5λ at $|\eta| = 3.0$. An efficient measurement of large hadronic showers in the barrel region is possible due to outer hadronic calorimeter (HOB), located just outside the coil, which consists of additional layers of scintillators. The expected energy resolution of the central HCAL is $65\%/\sqrt{E/\text{GeV}} \oplus 5\%$.

The HF calorimeter covers pseudorapidity range of $3.0 < |\eta| < 5.0$. The absorber material is copper, while the active medium consists of a matrix of radiation hard quartz fibers. The HF calorimeter has thickness of 10λ and expected energy resolution of $100\%/\sqrt{E/\text{GeV}} \oplus 5\%$.

The precise muon spectrometer, located in the return yoke, consists of three types of gaseous detectors: drift tubes (DT), cathode strip chambers (CSC) and resistive plate chambers (RPC). The muon tracks are bent in the magnetic field inside the return flux iron yoke of about 1.8 Tesla. The precise track measurement and muon triggering is performed by DTs in the barrel ($|\eta| < 1.3$) and by CSCs in the endcaps ($0.9 < |\eta| < 2.4$). The RPCs mainly serve for fast triggering purposes and will cover pseudorapidity range of $|\eta| < 2.1$. A more detailed specification of the CMS muon system will be given in Section 1.2.3.

1.2.2 Trigger System

Selection of interesting inelastic events from beam collisions is a very challenging task for experiments at the LHC since cross sections of physics phenomena to be studied cover several orders of magnitude. From Fig. 1.3 one can compare cross sections and event rates for design LHC luminosity for basic physics processes under interest. To obtain event⁵ recording rate of $\sim 100 \text{ Hz}$, achievable by modern mass storage devices, one requires multi-level trigger. The CMS collaboration has chosen two step trigger system.

⁵On average the amount of data from all 100×10^6 channels of the CMS detector is about 1 MB per single beam crossing.

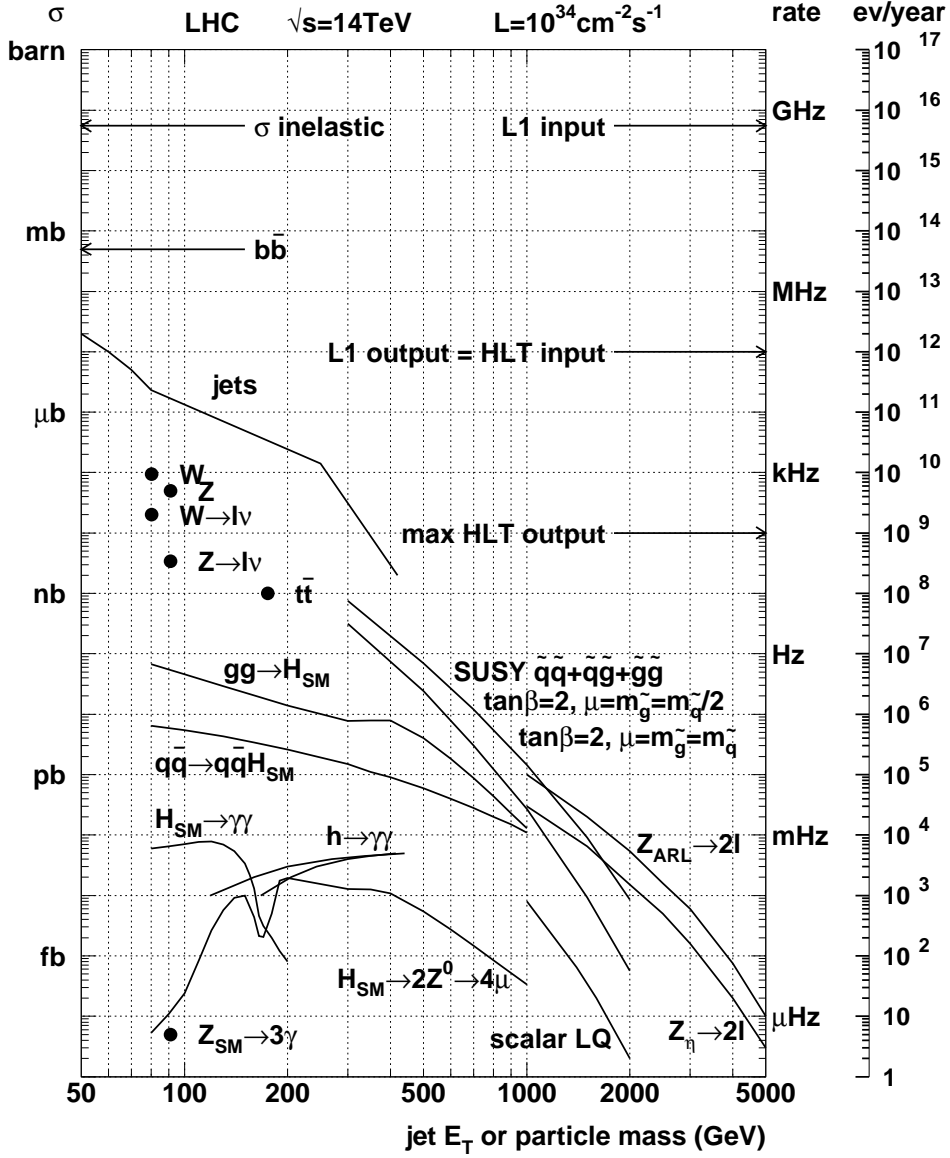


Figure 1.3: Inclusive $p-p$ (or $p-\bar{p}$) cross sections σ and corresponding interaction rates for design luminosity of $10^{34} \text{ cm}^{-2} \text{ s}^{-1}$ for selected physics processes [27].

The main task of the First Level Trigger (L1) is to reduce ~ 1 GHz rate from inelastic interactions to 100 kHz without dead time, which is acceptable by the High Level Trigger (HLT). The L1 trigger is based on custom electronics. It uses only coarsely segmented data from calorimeters and muon chambers. All high-resolution data is pipe-lined for $3.2 \mu\text{s}$ period (128 bunch crossings) during which decision must be made whether to retain an event for further consideration.

The HLT will bring down the event rate to a safe level of 100 Hz. This task will be performed by the on-line farm of 5000 commercial processors. Specialized software algorithms will use full event data in order to make a decision to record an event.

The L1 trigger is constituted of three subsystems: the Calorimeter Trigger, the Muon Trigger and the Global Trigger (GT). The Global Trigger relies on information provided by calorimeter- and muon trigger. It recognizes the following single objects: μ (any muon), μ_i (isolated muon, without nearby jet), e (isolated electron/photon), e_b (electron from b -quark decay), jet (local energy concentration in the calorimeter), τ (narrow τ -jet). For each single trigger object a coarse position (η, φ) and estimated E_t or p_t are delivered, as well as bunch crossing number the object is originating from. The Muon Trigger delivers list of 4 candidate muons of the highest p_t . The Calorimeter Trigger provides several lists of the 4 most energetic objects of the following types: isolated and not-isolated electron/photon in $|\eta| < 2.5$, central jets in $|\eta| < 3.0$, forward jets in $3.0 < |\eta| < 5.0$, τ -jets in $|\eta| < 3.5$. It also computes total E_t and E_t^{miss} in the whole system in $|\eta| < 5.0$. The main task of the Global Trigger is to apply selection criteria, which can be adopted according to needs, such as: different cuts on p_t , E_t or E_t^{miss} and multi-object triggers (2μ , $2jets$, $e\mu$, etc). In total 128 algorithms will be provided, each representing a complete physics trigger condition. A final logical OR is applied to these algorithms to generate a L1 accept signal.

1.2.3 Muon System

The main purposes of the CMS muon detection system are: muon identification, muon trigger, muon momentum measurements and muon sign of charge assignment.

The muon system is organized in four muon stations, which are referred further in this work as MB 1...MB 4 and ME 1...ME 4, respectively, in the barrel and in the endcaps. In addition, the endcap chambers are divided into three (in ME 1) or two parts (in ME 2...ME 4) denoted as ME n/m , where $n = 1 \dots 4$ corresponds to the station number and $m = 1, 2, (3)$ is the station sub-component number counting from the beam axis. Location of the muon stations in r - z plane⁶ of the CMS detector is schematically shown in Fig. 1.4.

The choice of the detector technology used in each region is governed by: detector occupancy due to particle production rates and the radiation environment, the system cost and the required precision. As will be shown later, the lower occupancies are in the barrel, which allows to use Drift Tubes of $150 \mu\text{m}$ position accuracy from single tube, but suffering from counting rate limitation. The Drift Tube is essentially a single wire chamber having a rectangular transverse profile of $4 \times 1.1 \text{ cm}^2$ area and length between 2 m and 4 m. Each of four DT stations consist of 12 layers of DTs divided into 3 super-layers. Two outer super-layers in each station serve for measurement

⁶Coordinate r denotes distance from the beam axis (z direction). The coordinate system is depicted in Fig. 1.2 and is centered at the collision point.

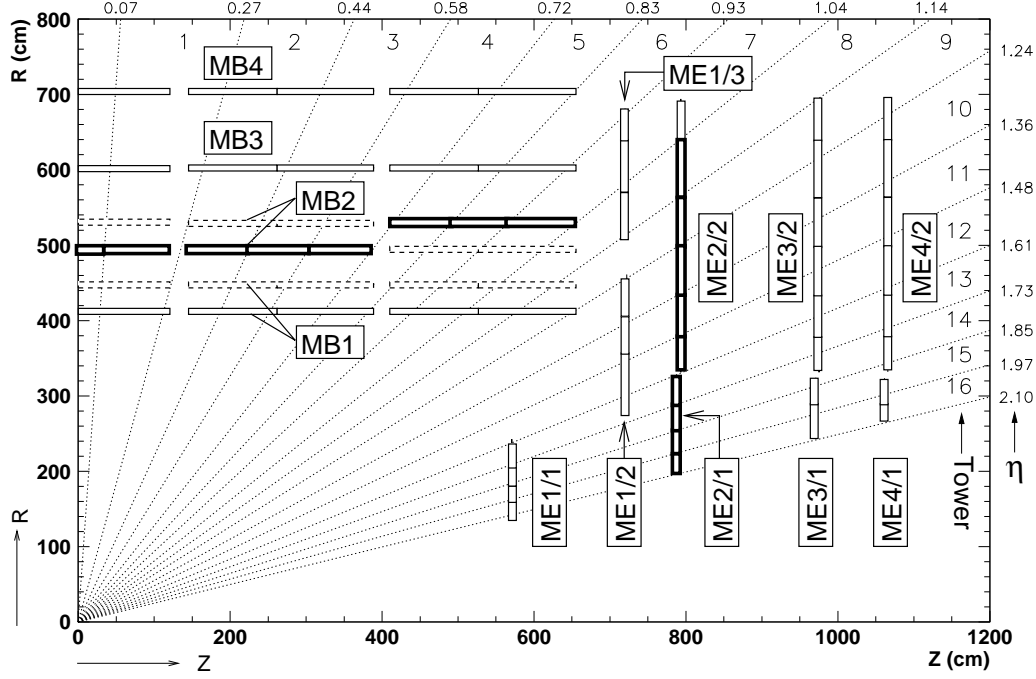


Figure 1.4: Location and naming conventions of four muon stations in one quadrant of the CMS detector. The RPC segmentation in z coordinate (for the barrel) and in r coordinate (in the endcap) is shown. Chambers thickness is not to scale. DT/CSC detectors are not shown for simplicity.

of the track bending in r - φ plane,⁷ while the middle one is used for z coordinate measurement.

The CSC technology has been chosen for the endcaps, where more severe radiation environment is expected, due to CSC capability to operate in charged particle rates up to 1.5 kHz/cm^2 and at 4 Tesla magnetic field. The Cathode Strip Chamber is a multi-wire proportional chamber having two planes of readout electrodes (strips and wires) allowing measurement of two coordinates at a time. Strips are shaped to maintain radial geometry and serve for φ coordinate measurement. Wires are used to determine r coordinate. The individual muon station consists of six active gas layers, each equipped with its own readout, and interlaced with honeycomb supports. The intrinsic spatial resolution of a CSC is about $50 \mu\text{m}$.

The redundancy of the muon triggering system is assured by use of Resistive Plate Chambers. The RPC is a parallel plate detector with two resistive electrodes equipped with the outer readout strip plane(s). Their possible advantages are: extremely fast response time ($\sim 10 \text{ ns}$), very good intrinsic time resolution ($\sim 1 \text{ ns}$) and relatively low costs of constructing large detection areas. Even single RPC layer allows one for instantaneous and unambiguous assignment of the signal induced by muon to a given bunch crossing (BX). The DTs and CSCs are slower detectors having maximal drift times of about 400 ns and 50 ns , respectively. They can also provide unambiguous BX identification, though, information from several detector layers must be combined by dedi-

⁷Variable φ is the angle measured on X - Y plane transverse to the beam as it is shown in Fig. 1.2.

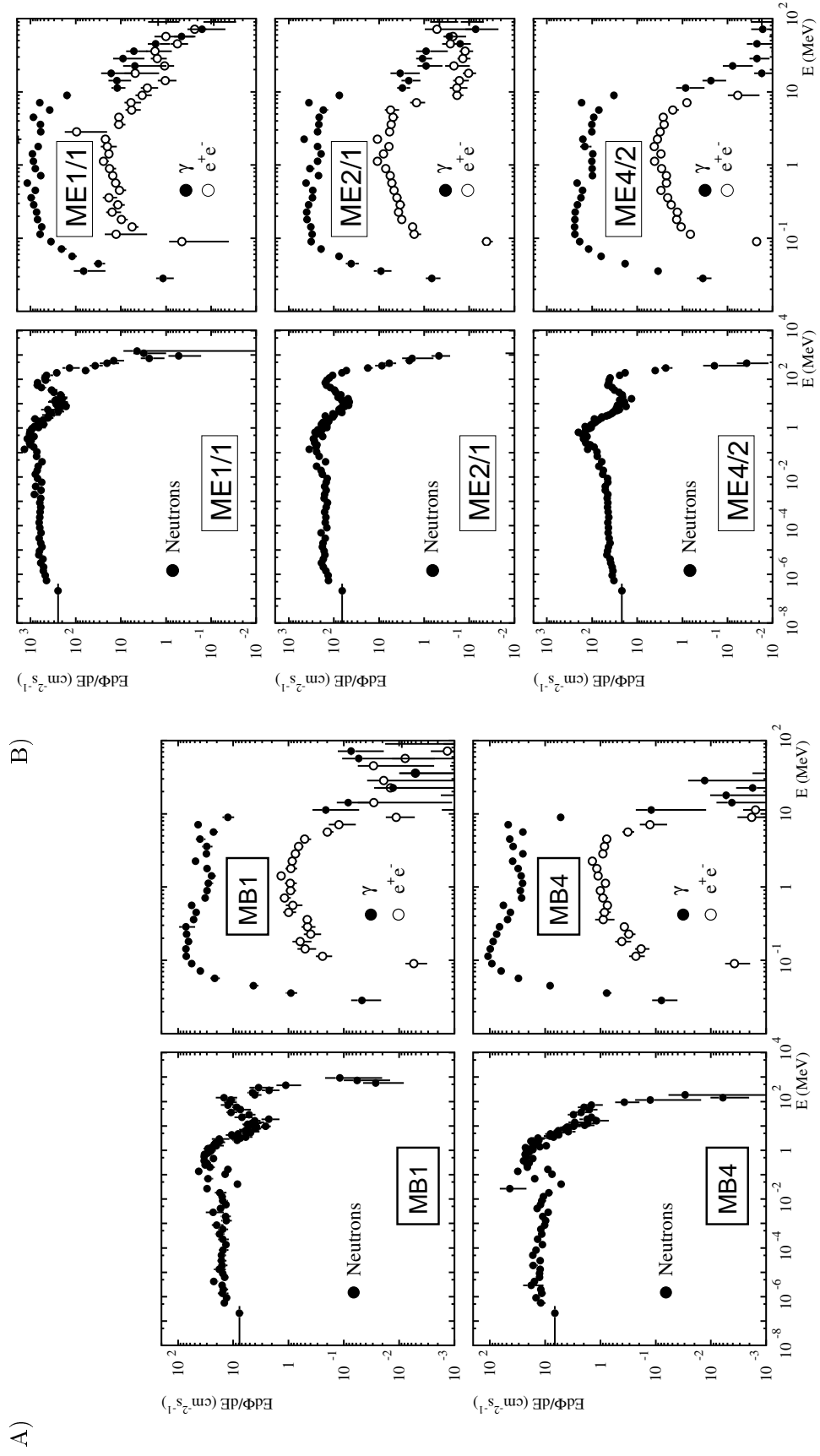


Figure 1.5: Particle fluxes vs energy in the gas layers of: (A) drift tubes in the CMS barrel, (B) CSCs in the CMS endcaps [28].

cated electronics to fulfill this task, which takes more than 25 ns. The RPC system can also serve for the track reconstruction as it is pointed out in Ref. [29].

The muon system should be able to withstand high radiation and interaction background expected at the LHC. The main sources of background signals generated in the muon system are:

- *neutral particles* - low energetic electrons from neutron captures by nuclei, inside- or in the vicinity of muon chambers, produced at the end of the reaction chain:
thermal neutron $\rightarrow \gamma \rightarrow e^+e^-$,
- *punch-through hadrons* - charged hadrons from hadronic cascades: backsplash from HF calorimeter, albedo, leaks from beam collimator shielding and central HE calorimeter,
- *decay muons* - muons originated from π/K decays inside the central cavity.

The high energy charged particles (muons and hadrons) are correlated in time with bunch crossings. Moreover, they will produce signals in the gas layers of the muon chambers with almost 100% probability and will penetrate all four stations. On the contrary, low energy electrons from neutral particles (n, γ) are uncorrelated and in most cases their energy is not enough to penetrate several muon stations at a time. In Figs. 1.5 A and 1.5 B simulated particle fluxes as a function of their energy are shown for the gas layers of the drift tubes and the cathode strip chambers, respectively. The amount of electrons appearing in the gas layers depends on sensitivities to neutrons and gammas of the materials constituting muon chamber walls and their surroundings. The comparison of expected signal rates (*hits*⁸) per unit area in the muon chambers originating from different sources is depicted in Fig. 1.6. The solid lines correspond to prompt and decay muons, empty circles - to hadronic punch-through and full circles - to electrons from neutrons and gammas. It can be seen that the hit rate is dominated by the background from neutral particles and increases with pseudorapidity. In the whole barrel region it does not exceed 10 Hz/cm². In the endcaps hit rates up to 100 Hz/cm² are foreseen. The only exception is ME 1/1 station, in which hit rate of some hundreds Hz/cm² is expected.

1.2.4 Muon Trigger

The Muon Trigger is an essential component of the L1 trigger. It consists of the following subsystems: the Drift Tube Trigger in the barrel, the Cathode Strip Chamber Trigger in endcaps, the Pattern Comparator Trigger (PACT) based on Resistive Plate Chambers in the barrel and endcaps and the Global Muon Trigger (GMT).

⁸A hit is essentially a logical *true* signal from an individual readout channel or from a group of channels having induced analog signal(s) above fixed threshold.

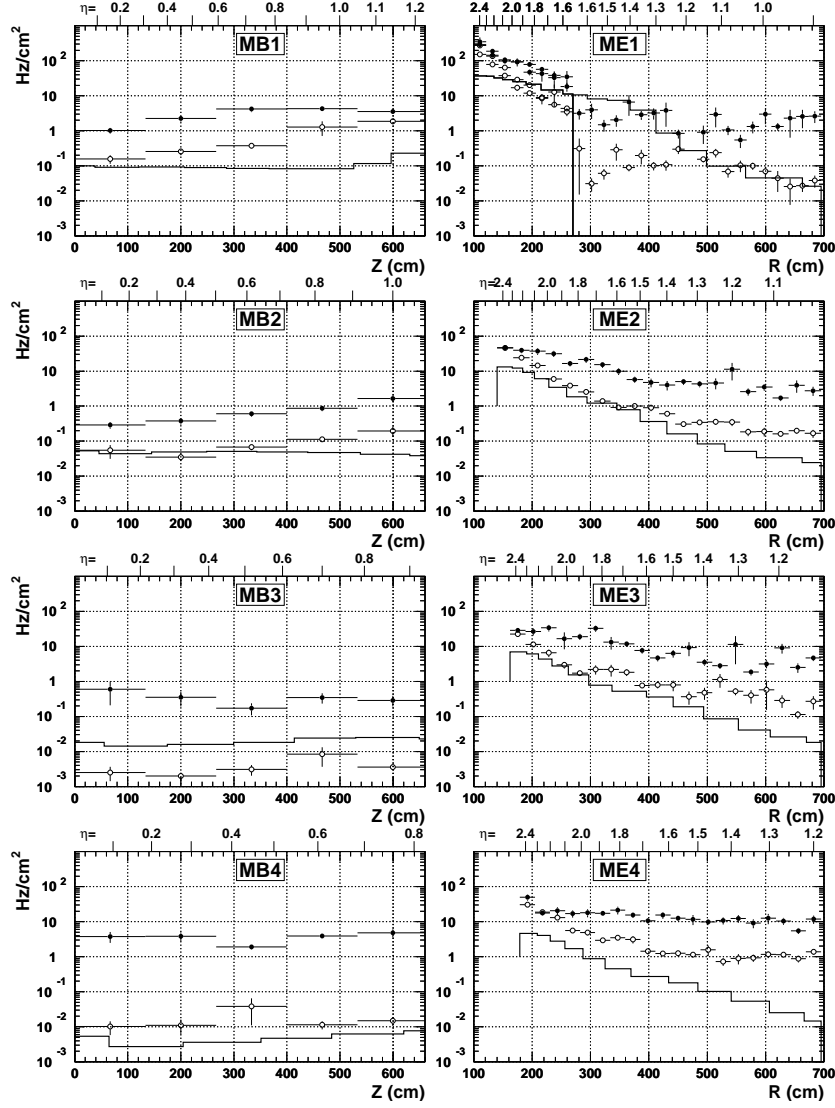


Figure 1.6: Expected hit rates in muon chambers due to: muons (solid line), hadronic punchthrough/backsplashes (open circles) and electrons from thermal neutrons (full circles) [27].

From each region (barrel, endcaps) two complementary and independent muon triggers are delivered. Such solution has numerous advantages because different types of detectors respond in different ways to various backgrounds. Namely, DT/CSC chambers have better rejection power for single background hits due to their multilayer structure as compared with RPC detectors. On the other hand, in DT/CSC detectors, due to their long electron drift times, single background hits from different bunch crossings or secondaries accompanying high energy muon tracks can mislead track finding algorithms causing some inefficiency. The GMT selects up to 4 candidate muon tracks of the highest p_t (*muon quadruplet*) on the basis of 4 similar quadruplets delivered by: DT Trigger (barrel quadruplet), CSC Trigger (endcap quadruplet) and PACT (barrel and endcap quadruplets).

Each of three subsystems has to resolve effectively muon tracks of p_t in the range of few GeV/c to 100 GeV/c. The DT and CSC triggers calculate η and φ coordinates of each track with precision of $\Delta\eta = 0.05$ and $\Delta\varphi = 2.5^\circ$, respectively. The RPC trigger, instead, works on a predefined grid of η, φ coordinates with resolution of $\Delta\eta \approx 0.1$ and $\Delta\varphi = 2.5^\circ$ (see Fig. 1.4).

PACT based on RPC detectors

The Pattern Comparator Trigger has to fulfill three basic functions simultaneously:

1. *Identifying candidate muon tracks.*

The segmentation of readout strips allows one to resolve crossing points of a bent muon track with RPC stations with spatial precision of ~ 1 cm in r - φ plane and in z - φ plane in the barrel- and endcap regions, respectively. A precise measurement of the muon track is performed by DT and CSC detectors.

2. *Assignment of a bunch crossing to the candidate tracks.*

The identified muon must be assigned to a given bunch crossing. An ambiguity may arise from DT and CSC information alone due to their: long drift times and long strips or wires. Due to fast RPC response (e.g. intrinsic time jitter below 15 ns and time resolution of ~ 1 ns) one can use trigger gates⁹ shorter than 20 ns.

3. *Estimation of the transverse momenta of candidate tracks.*

The magnetic field bends muon tracks in r - φ plane. In order to determine a transverse momentum p_t of the track, the RPC hit pattern from four RPC muon stations will be compared to a predefined set of patterns by a fast, dedicated electronics (see Fig. 1.7).

In total, the RPC based muon trigger system has sensitive area of 3400 m² and consists of about 2×10^5 readout channels. RPCs have strips parallel to the beam axis (z direction) in the barrel and radial ones in the endcaps to maintain projective geometry in φ direction with granularity of $\Delta\varphi = 5/16^\circ$. The segmentation in η direction is about $\Delta\eta \approx 0.1$. A schematic layout of RPC strip granularity in r - z plane of the CMS detector is shown in Fig. 1.4. The chosen strip granularity results from the required momentum resolution to resolve muons up to $p_t = 100$ GeV/c and from the maximal tolerable time spread below 5 ns due to:

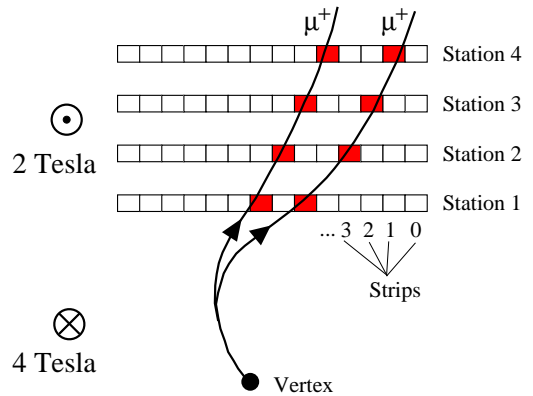


Figure 1.7: The PACT idea: a set of predefined hit patterns in four muon stations is used to estimate p_t of muons originated from the interaction point.

⁹Trigger gate is a time window of acceptance (width < 25 ns) used to detect signals from the same BX.

time of flight for different η values and the signal propagation time along strips (e.g. 6.5 ns for the longest strip of 1.3 m) [30–32]. The MB 2 and ME 2 stations, boldfaced in Fig. 1.4, are *reference planes* and serve for coarse assignment of η and φ to a candidate muon track. Depending on the region, strips of individual RPC modules are divided in η in 2, 3, 4 or 6 sections. In order to better resolve low energetic muons of $p_t < 6$ GeV/c the stations MB 1 and MB 2 are equipped with two double gap RPC layers each. Additional layers are marked with dashed lines in Fig. 1.4.

The PACT algorithm is organized in the following way [27]:

- The group of 8 consecutive strips in φ direction in each station form logical *segment* of $\Delta\varphi = 2.5^\circ$.
- Segments of the same η from 4 muon stations are combined in one *tower* of $\Delta\eta \times \Delta\varphi \approx 0.1 \times 2.5^\circ$. In the barrel the 4 muon stations, marked with solid lines in Fig. 1.4, are used for high p_t candidate muons. In addition, the PACT algorithm also checks the 4 innermost stations (i.e. all MB 1 and MB 2 layers) for low p_t candidate muons.
- Towers of the same η are grouped in one *ring* ($\varphi \in [0, 2\pi]$).
- The set of hits from each bunch crossing is compared to predefined patterns by custom made electronics. The search for candidate tracks is performed first in each tower, then in rings. Finally, two lists of ≤ 4 muon candidates are forwarded to the GMT: one from the barrel and one from two endcaps.

The baseline PACT algorithm (*4/4 algorithm*), requires coincidence of 4 out of 4 muon stations for *high quality* muon candidates. However, to improve the efficiency also *low quality* tracks having hits in only 3 out of 4 muon stations can be accepted (*3/4 algorithm*). The second algorithm is more vulnerable to generate false triggers due to uncorrelated background hits in RPC detectors. Therefore information about quality of candidate muon tracks is also forwarded to the GMT, along with estimated p_t, η and φ .

Requirements on RPC performance

The following requirements are imposed on RPC detectors for the CMS experiment [28, 33]:

- Detection efficiency $\geq 95\%$ at radiation rates up to 1 kHz/cm²
- The chambers should be operated in avalanche mode and must be filled with safe gases
- The width of the efficiency plateau ≥ 300 V with streamer¹⁰ probability $< 10\%$

¹⁰A streamer is a kind of spark discharge in the gas, which can induce signals up to few orders of magnitude higher than in avalanche mode. For this reason streamers must be avoided as they significantly deteriorate RPC spatial resolution.

- Time resolution better than 3 ns and 98% of signals must be contained within 20 ns time window to allow bunch crossing identification
- The average multiplicity of responding strips for single muon < 2
- Power consumption $< 2 \div 3 \text{ W/m}^2$
- The intrinsic RPC noise¹¹ should be $10 \div 20 \text{ Hz/cm}^2$ at most.

A single ionizing particle may cause several RPC strips to respond. Usually, in such case, a group of consecutive strips in φ direction has signals, which can be grouped into *clusters*. The larger cluster size is the worse estimation of transverse momentum will be. It is therefore crucial to keep the number of responding strips to real muons as low as possible and to reduce random background and noise hit rates.

As it was already pointed out in the previous Section, the total expected hit rates caused by the radiation can reach $\sim 10 \text{ Hz/cm}^2$ and $\sim 200 \text{ Hz/cm}^2$, respectively, in the barrel and in the endcaps. Nevertheless, a safety factor of about 3 is required to secure the operation of the muon trigger system in unknown radiation conditions. The most demanding part of the whole RPC system is the ME1/1 station, which is closest to beam line and extends up to $|\eta| = 2.1$. Because a coincidence of 4 (or 3) planes is required by the PACT algorithm, each RPC station must be very efficient, namely $> 98\%$ in the barrel at 100 Hz/cm^2 avalanche rate and $> 95\%$ in the endcaps at 1000 Hz/cm^2 . According to the baseline CMS design each muon station will be equipped with double gap RPC structure¹² in order to improve the efficiency at high rates [28]. Indeed, a sum of analog signals of two independent single gap detectors has better chance to induce a detectable signal. However, since sub-gaps have common readout, the hit rate due to uncorrelated background particles and RPC noise doubles. It should be mentioned, that the choice of a double gap technology has been driven by a sparse experimental data available when the CMS detector was in its early planning phase and when the rate capability was still a challenge to experimental groups working on RPCs [16]. The advantages of double- and single gap RPC techniques are discussed later in this thesis.

In addition to background rates from radiation, which are dominated by electrons from thermal neutrons, the uncorrelated intrinsic RPC noise signals contribute to the total hit rate. Each individual gas gap has certain probability to generate spontaneous discharges in the gas at extreme voltages. Local surface smoothness, quality of the assembling technology, gas mixture

¹¹The RPC noise signals are spontaneous electron avalanches caused by local imperfections of the inner electrode surfaces facing the gas, where the local electric field can exceed the nominal one resulting from the applied voltage.

¹²An individual double gap RPC layer consists of two independent chambers of 2 mm gas gap thickness with a common readout strip plane inserted between them. Detailed description of such structure is given in Section 2.2.

used and applied electric field strength are the main factors affecting the intrinsic RPC noise. Simulated data has shown that the baseline PACT algorithms (4/4 and 3/4) may generate too many false triggers if the intrinsic RPC noise will be significantly larger than $10 \div 20 \text{ Hz/cm}^2$ [33]. This serious problem concerns mainly the barrel RPC system for $|\eta| < 1.6$ where the rate due to thermal neutrons is $< 10 \text{ Hz/cm}^2$, as can be seen from Fig. 1.6. Minimization of the spontaneous noise rate is one of key issues to be solved in RPCs produced in large quantities. Nevertheless some precaution steps are also considered, namely modification of the PACT algorithm to take advantage of all 6 RPC layers available in the barrel in order to improve background rejection power [33].

The RPC characteristics should not deteriorate during 10 years of the LHC operation at the highest luminosity. The two most important parameters affecting long-term stability are maintaining constant gas gain and keeping intrinsic chamber noise at acceptable level.

In the next two Chapters principles of RPC operation and RPC techniques are discussed with emphasize on the ability to operate under high particle rates, which is essential for good performance of the Pattern Comparator Trigger. Further Chapter address experimental results obtained by the Author concerning: rate capability, intrinsic noise and operation stability issues. As will be shown later in this work, some problems may arise for the baseline RPC design and operation conditions described in *The Muon Project Technical Design Report* [28] during long-term operation at the highest particle fluxes. Possible sources of remedy are also discussed in this thesis.

Chapter 2

Charge avalanche development in uniform electric field

2.1 Parallel Plate Chambers

The Resistive Plate Chamber (RPC) detector, introduced by R. Santonico and R. Cardarelli in 1981 [9, 34], is the derivative of a wide range of gaseous detectors with parallel plate geometry. The ancestor of all Parallel Plate Chambers (PPCs) was the Plate Spark Counter by J.W. Keuffel [35, 36] developed in late 40's. It was made of two solid metallic electrodes forming uniform electric field of high intensity in the gas layer. The principle of operation of PPCs is based on detection of the current induced by moving electrons and ions liberated in the sensitive gas volume of the detector by the passage of an ionizing particle. Depending on gas amplification they could be operated either in *proportional (avalanche)* or in *spark mode*. Parallel geometry had certain advantages over wire counters with inhomogeneous $1/r$ electric field, namely, the response was faster since electrons started avalanches immediately and had less chance to be attached. Initially PPCs were used to study gas amplification processes. Later, Parallel Mesh Counters and Multi Step Avalanche Chambers were developed, in which two or more planar wire-mesh electrodes, partially transparent to drifting electrons, were used with a metallic anode plate [37]. In this class of detectors, called Parallel Plate Chambers (PPACs), the low field drift region was separated from the high field amplification region(s). The limitations in the operation of PPACs operated in proportional mode come from sparking and feedback processes in the gas. The ultra-violet photon emission by charge avalanches results in production of photoelectrons in the metallic electrodes and the gas itself. Also slow positive ions can extract electrons from the cathode far long after initial avalanche begins. The sparks (breakdowns) caused unacceptable dead times and could be harmful to readout electronics. These drawbacks could be partially overcome by using quenching gas mixtures absorbing secondary photons.

The rate capability in proportional mode, being the maximum counting rate at which no

decrease of the pulse-height is observed, was very good and reached 10^5 Hz/mm^2 at low gains [38]. At higher gains and at low counting rates the usual breakdown limit of 10^8 electrons per avalanche has been observed. However, above certain counting rate value the breakdown limit (or the highest gain achievable in proportional mode) started to be inversely proportional to the counting rate due to overlapping of avalanches in time and space.

The application of Parallel Plate Chambers was rather limited. Firstly, they were vulnerable to discharges damaging electrodes and introducing large dead times. Secondly, it was difficult to achieve good parallelism of the amplifying gap over areas larger than typical sizes of $10 \times 10 \text{ cm}^2$.

The Planar Spark Counters (PSC), introduced by Yu. Pestov, featured localized discharge due to one of the electrodes made out of semi-conductive glass. They improved substantially the rate capability of parallel plate detectors in spark mode [39]. Highly resistive electrodes suppressed the discharge at an early stage and affected the detector only locally. Such detectors were suitable as time measuring devices for Time-Of-Flight (TOF) experiments. Due to decrease of the gas gap the avalanche starting point was better defined and time resolution could be much improved for the cost of increasing gas density. Time resolution of 30 ps was reported for prototypes of $30 \times 30 \text{ cm}^2$ active area [40].

However it were Resistive Plate Chambers that combined good time and position resolution, large gain and ease of production in large areas. They were build of a weakly conductive composite material, known as bakelite, which made detector spark-protective. The sparks in RPCs were actually weak with respect to PPACs and called *streamers*, by a convention. The avalanche development was quenched on the resistive electrodes so that the discharge was localized to a few mm^2 area. The possible intrinsic time resolution was 1 ns (e.g. comparable to that of scintillators), which was adequate for triggering purposes. Low cost and rigidity of the bakelite allowed one to produce modules of few square meters sensitive area without a problem.

2.2 Baseline RPC design

A sketch of a single gap RPC structure is shown in Fig. 2.1. In order to preserve uniformity of the gap over large surface a grid of insulating cylinders (*spacers*) is glued. In a typical RPC detector two electrodes of $d_{bak}=2 \text{ mm}$ thickness are separated by the gas layer of $d=2 \text{ mm}$ width. Usually spacers have 10 mm diameter and are placed every 10 cm in a square grid. The whole structure is made gas-tight by means of an insulating frame glued on detector's edges. The frame also contains gas inlets and outlets. The outer faces of resistive electrodes are covered with thin conductive carbon layer (graphite paint) which distributes potential over the active area of the detector. In steady conditions the whole potential difference is applied to the gas gap only.

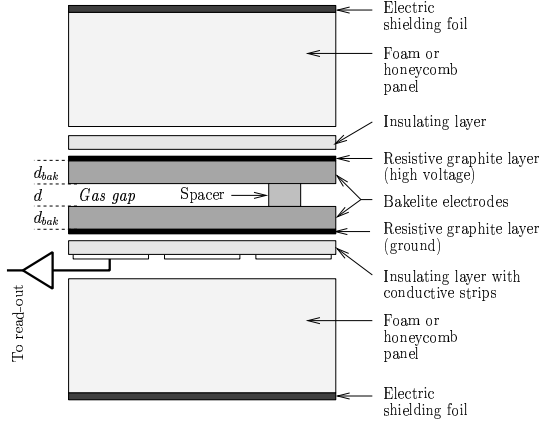


Figure 2.1: A standard design of a single gap RPC with one-dimensional readout.

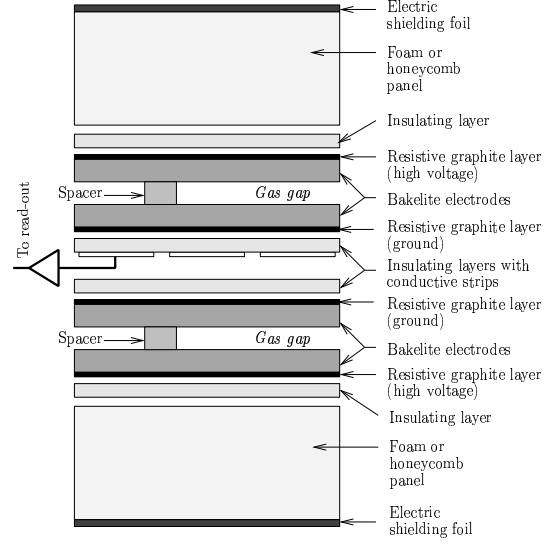


Figure 2.2: A standard design of a double gap RPC with one-dimensional readout. Signals from two sub-modules are summed on pick-up strips.

One of advantages of a RPC is separation of the field shaping electrodes (graphite) from the readout electrodes by a dielectric layer. The signal pick-up lines made of aluminium or copper glued onto insulator can be arbitrary shaped (e.g. to form strips or pads). Two dimensional readout is also possible if one attaches simultaneously two readout panels to the gas box from its high voltage- and ground side, which have strips ordered along perpendicular directions. The surface resistivity of the graphite layer is kept high on the surface facing the pick-up electrodes ($10^5 \div 10^6 \Omega/\square$) to make them transparent to signals developed inside gas layer. The graphite layer of the bakelite side without readout panels has surface resistivity of about $100 \Omega/\square$ in order to speed up recovery time of the electric field over area of a discharge. The gas box and strip panels are pressed between two rigid panels (e.g. foam, structured honeycomb) and the whole structure is electrically shielded.

A variant of RPC constituted of two independent chambers sharing common readout plane is depicted in Fig. 2.2. Such double gap RPC structure, discussed later in Section 2.4, is foreseen for the CMS muon system [28].

2.3 RPC state of the art

2.3.1 Primary ionization processes in the gas

The average kinetic energy loss per unit of path length of the incident charged particle is a summation of the energy lost to all electrons of atoms in the vicinity of this particle and is given

by a Bethe-Bloch formula [41, 42]

$$\frac{dE}{dx} = -K z^2 \frac{Z}{A} \frac{\rho}{\beta^2} \left[\frac{1}{2} \ln \frac{2m_e c^2 \beta^2 \gamma^2 T_{\max}}{I^2} - \beta^2 - \frac{C}{Z} - \frac{\delta}{2} \right] \quad (2.1)$$

where:

$$\begin{aligned} q = z q_e, m & - \text{charge and mass of the incident particle} \\ v = \beta c, \gamma = 1/\sqrt{1 - \beta^2} & - \text{velocity and Lorentz factor of the incident particle} \\ T_{\max} = \frac{2m_e c^2 \beta^2 \gamma^2}{1 + 2\gamma m_e/m + (m_e/m)^2} & - \text{maximum kinetic energy which can be transferred} \\ & \text{to a free electron in a single collision} \\ K = 4\pi N_A r_e^2 m_e c^2 & \approx 0.307 \text{ MeV g}^{-1} \text{ cm}^{-2} \\ m_e, r_e & - \text{electron mass and the classical electron radius} \\ Z, A & - \text{atomic number and atomic mass of the medium} \\ \rho & - \text{density of the medium} \\ I & - \text{mean excitation energy of the medium} \\ -\frac{C}{Z} & - \text{shell correction} \\ -\frac{\delta}{2} & - \text{density effect correction.} \end{aligned}$$

The RPCs should be fully efficient for muons emerging from the interaction region. For CMS the region of interest for muon momenta extends from 1 GeV/c up to 1 TeV/c. For such muons a relativistic rise of energy loss above the minimum of $\frac{dE}{dx}(\beta\gamma)$ distribution near $\beta\gamma \approx 3$ becomes significant. Dealing with a mixture of several compounds, as it is usually the case, one can use Bragg's additivity law to calculate average energy loss:

$$\left\langle \frac{dE}{dx} \right\rangle = \sum_j w_j \left. \frac{dE}{dx} \right|_j \quad (2.2)$$

where w_j denotes weight fraction of the j -th component.

Since ionization by collision is a statistical process it is subject to fluctuations. The number of primary ionization events per unit length n_p follows Poisson distribution

$$f_{SPI}(n_p, \langle n_p \rangle) = \frac{\langle n_p \rangle^{n_p} e^{-\langle n_p \rangle}}{n_p!} \quad (2.3)$$

with the average $\langle n_p \rangle [\text{mm}^{-1}]$ is called *specific primary ionization*. The $\langle n_p \rangle$ is roughly linearly dependent on the average atomic number of the gas [43]. The following formula can be used to calculate specific primary ionization of gas mixtures [44]:

$$\langle n_p \rangle = \sum_j \pi_j \langle n_p \rangle \Big|_j \Big/ \sum_k \pi_k \quad (2.4)$$

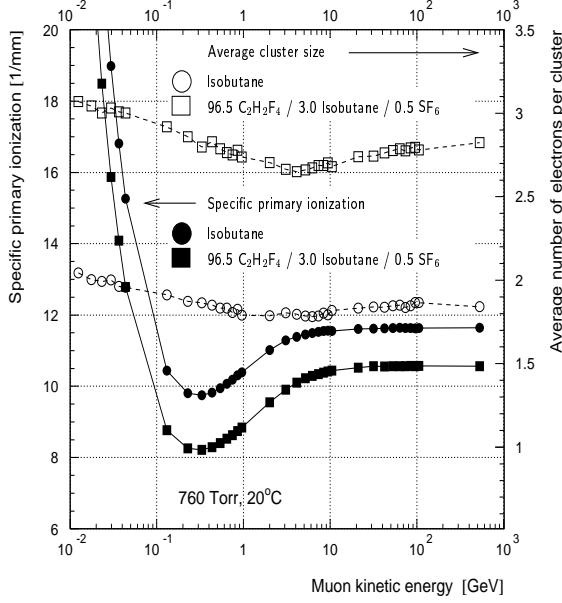


Figure 2.3: HEED simulation of the specific primary ionization and the average number of electrons per cluster for muons in two gases ($T = 20^\circ\text{C}$, $p = 760$ Torr).

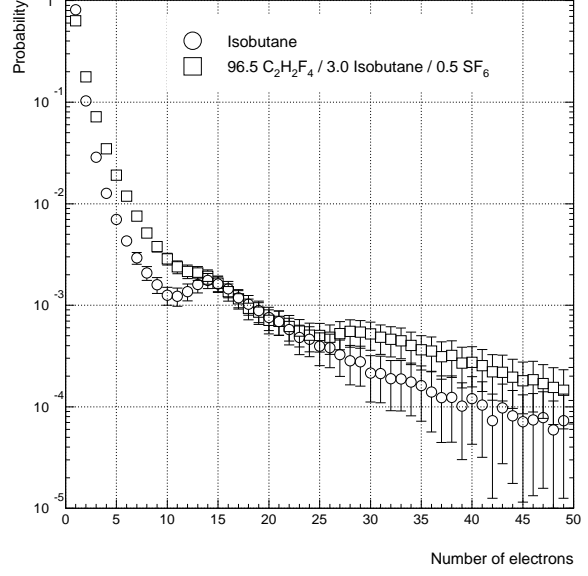


Figure 2.4: HEED simulation of the probability distribution of the number of electrons in primary ionization clusters for minimum ionizing muons in two gases ($\beta\gamma = 3$, $T = 20^\circ\text{C}$, $p = 760$ Torr).

where π_j is atomic or molecular number multiplied by partial pressure of the j -th component.

Simulated specific primary ionization and average number of electrons in a single cluster as a function of the muon kinetic energy are plotted in Fig. 2.3 for typical RPC gas mixture of Tetrafluoroethane/Isobutane/SF₆ (96.5/3.0/0.5).¹ The data was obtained by the Author using HEED program, a dedicated tool to compute energy losses of charged particles interacting with arbitrary chosen gas medium [45]. Results correspond to standard conditions of $T = 20^\circ\text{C}$ and $p = 760$ Torr (STP). Data points for Isobutane are given as a reference. Since the $\langle n_p \rangle$ parameter is proportional to gas density, it increases with pressure and decreases with temperature of the gas. Typical pressure variations between 1000 mbar and 1020 mbar and temperature variations between 15°C and 35°C result in change of $\langle n_p \rangle$ by 0.6% and 4% from its STP value, respectively.

The energy of primary electrons, which is approximately $\frac{1}{E^2}$ distributed, is dissipated into secondary ionization. The total number of electrons n_T is proportional to the energy loss of the incident charged particle in the gas volume considered [43]

$$n_T = \frac{\Delta E}{W} \quad (2.5)$$

where W is the effective average energy needed to produce one electron-ion pair. It is due to the fact that the range of secondary electrons is usually smaller than the distance between primary

¹Tetrafluoroethane = C₂H₂F₄ (Forane-134a) is also denoted as TFE further in the text.

collisions, the electrons form separated clusters over incident particle track. The step Δx between neighbour clusters obeys exponent distribution

$$f_{CLU}(\Delta x) = \langle n_P \rangle e^{-\langle n_P \rangle \Delta x}. \quad (2.6)$$

The distance x_j at which the j -th cluster is produced along the track follows the distribution:

$$A_j(x_j) = \frac{(x_j)^{j-1}}{(j-1)!} \langle n_P \rangle^j e^{-\langle n_P \rangle x_j}. \quad (2.7)$$

The probability $w(n)$ of producing cluster containing n electrons is called *electron cluster size distribution*. It has been determined experimentally for typical gases used in drift chambers and it has been found that for gas mixtures the following relation can be used to calculate electron cluster size distribution [46]:

$$w(n) = \sum_j \pi_j w(n) \Big|_j / \sum_k \pi_k \quad (2.8)$$

where π_j is the specific primary ionization cross section [47] multiplied by partial pressure of the j -th component.

Since no experimental data exists on the electron cluster size probability for gas mixtures, adopted recently for RPC detectors, which contain Tetrafluoroethane (TFE, $C_2H_2F_4$) and Sulfur hexafluoride (SF_6), one has to rely on Monte Carlo simulations only. The Author used HEED package [45] to compute $w(n)$ distribution for a typical RPC gas mixture of TFE/Isobutane/ SF_6 (96.5/3.0/0.5). The results are shown in Fig. 2.4. The simulated data for Isobutane is superimposed as a reference. It can be seen from Figs. 2.3 and 2.4 that for simulated TFE-based gas mixture a single cluster consists of about 3 electrons on average.

2.3.2 Detection of neutral particles

The gaseous detector is also sensitive to neutral particles, like photons and neutrons, providing that they interact with gas medium or detector's walls and produce secondary charged particles (e.g. in most cases they are electrons) in the sensitive gas volume. The processes responsible for interaction of photons and neutrons with materials constituting the detector, with emphasis on specific geometry of Resistive Plate Chambers, are briefly discussed below.

The photons can produce free electrons inside the gas medium by one of three absorption mechanisms, which cross sections depend on the photon energy E_γ , namely:

- *photoelectric conversion* - this process dominates at the lowest E_γ energies up to several keV,

- *Compton scattering* - is the most probable interaction for photons having energy between several keV and few hundred keV,
- *creation of electron-positron pairs* - is possible only for photons of $E_\gamma > 2 m_e$ and dominates at the highest photon energies.

On the contrary to the passage of charged particles these interactions are single localized events. Then, further ionizations by an electron liberated in the gas (or by electron-positron pair) take place.

Photons of well defined energy in the keV range emitted by radioactive isotopes or X-ray tubes are widely used for calibration of the response of proportional chambers. In these detectors the relation $n_T \propto E_\gamma$ is justified, where n_T denotes the total number of secondary electrons liberated in the gas due to ionization. The mechanism responsible for this proportionality is the following: a photon of energy E_γ is captured via photoelectric absorption by one of the atoms of the gas medium, which in turn emits photoelectron of energy $E_e = E_\gamma - E_j$, where E_j denotes the characteristic shell energy of that atom (e.g. K-edge). For each chemical element there is certain probability, depending on the atomic number (e.g. 85% for Argon [48]), that a second electron of energy slightly below E_j is produced in the radiation-less transition of the excited molecule to its ground state, called *Auger effect*. In this case the two electrons carry almost entire energy E_γ of the incident photon and, thus, will dissipate it by ionization to produce secondary electrons according to equation 2.5. For instance, in this work the mono-energetic X-rays have been used to test a Parallel Plate Avalanche Chamber with a bakelite anode. In RPCs, however, X-rays cannot be detected because of their low range in the bakelite plates (and other materials) surrounding the gas medium.

Photons of intermediate energies, e.g. emitted by radioactive isotopes like cesium ^{137}Cs ($E_\gamma = 662 \text{ keV}$) or cobalt ^{60}Co ($E_\gamma = 1.25 \text{ MeV}$), mainly interact by Compton scattering with detector's walls or gas medium. They traverse RPC detectors almost without interaction due to small photon absorption coefficient at energies between 10 keV and 100 MeV for Compton scattering (and for e^+e^- pair production as well) in comparison to that for photoelectric conversion at $E_\gamma < 10 \text{ keV}$.

As it was already pointed out in Section 1.2.3 neutron induced background will be the main contribution to the occupancy level in muon chambers of the CMS detector [28]. Slow thermal neutrons, produced in hadronic cascades originated in the CMS beam pipe or in the forward region, can be captured by nuclei of the material surrounding or constituting the muon detectors with subsequent photon emission. These photons mainly interacting by Compton-scattering can produce detectable electrons in gas layers of the muon chambers.

One can define *sensitivity to photons* of a given gaseous detector as the probability of having

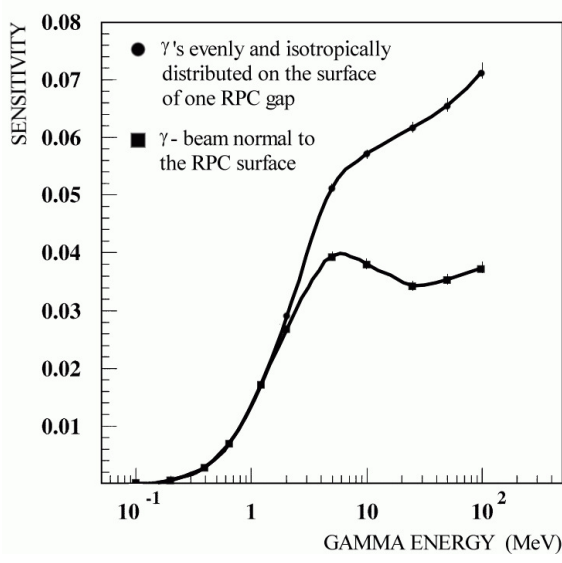


Figure 2.5: Simulated photon sensitivity of a double gap RPC structure [49].

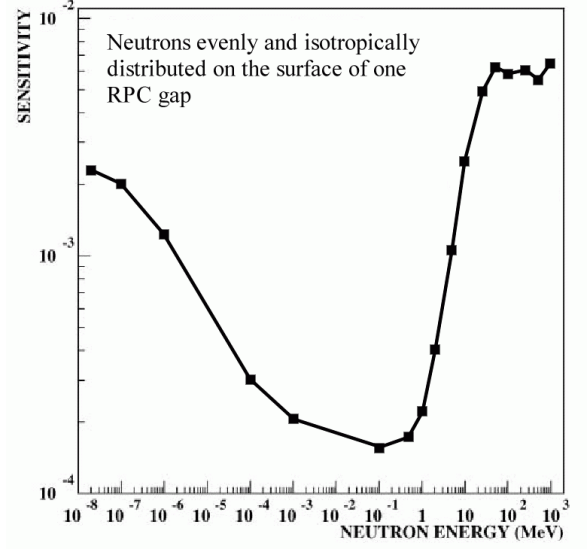


Figure 2.6: Simulated neutron sensitivity of a double gap RPC structure [50].

at least one free electron in the sensitive gas volume due to passage of the energetic photon. Similarly, detector's *sensitivity to neutron flux* can be introduced as the probability of neutron capture with emission of a photon leaving at least one electron in the gas layer. Obviously, these sensitivities depend on: neutral particle energy, materials constituting the detector and the number of active gas layers. For instance, in work by Altieri et al. [49] the sensitivity to photons below 100 MeV has been simulated for double gap RPCs of the CMS barrel region and the results are reproduced in Fig. 2.5. The authors predict an average sensitivity of about 2×10^{-2} in the case of photon energy spectra foreseen in low rapidity regions of the CMS detector, which are depicted in Fig. 1.5 A. The same group simulated sensitivity of double gap RPCs to neutrons below 1 GeV and its results are depicted in Fig. 2.6 [49]. For example, an average sensitivity to neutrons of energies corresponding to the barrel RPC muon station is about 10^{-3} .

2.3.3 Gas gain

In the presence of strong electric fields free electrons can gain sufficient energy between collisions to ionize molecules of the gas. The inverse mean free path for ionization is called first Townsend coefficient α [mm^{-1}] which represents number of positive ions produced per unit length of drift. If electronegative gases, like O_2 or SF_6 , are present in the gas mixture the electrons are attached to molecules and also negative ions will be produced. A second parameter called attachment coefficient η [mm^{-1}] represents the number of negative ions produced by one electron per unit length of drift. Therefore the number of electrons n_- created in step dx depends on the number

of positive ions n_+ and negative ions n_n as follows:

$$dn_- = dn_+ - dn_n = (\alpha - \eta) n_- dx \equiv \alpha_{\text{eff}} n_- dx. \quad (2.9)$$

It was found experimentally that for a given gas mixture the α/p and η/p coefficients depend only on E/p variable, called *reduced electric field* (p is the gas pressure) [51]. At low gas gains α is linearly dependent on the energy of drifting electrons and Korff's parametrization can be used:

$$\frac{\alpha}{p} = A e^{-Bp/E}. \quad (2.10)$$

During avalanche formation also photons are emitted by excited gas molecules. Such photons can ionize other gas molecules and start new charge avalanches even far away from the initial one. The emission of photons can spread out the electron multiplication region over the entire high-field zone. In order to keep avalanche growth localized, polyatomic *quenchers* are added as a remedy. Quenching molecules absorb photons in the ultraviolet range and, later, dissipate their excitation energy in radiation-less way.

Let us consider gas gap of the width d with several primary ionization clusters created at distances x_j from the cathode plane as it is schematically depicted in Fig. 2.7. At moderate gas gains, as long as space charge effects can be neglected, individual primary clusters develop avalanches which are independent from each other. In the uniform electric field (i.e. α_{eff} , η , drift velocity are constant) average charges due to j -th primary cluster having n_{oj} electrons as a function of the drift distance x counting from the cathode are given by formulas:

$$\langle Q_{j-}(x) \rangle = e_o n_{oj} \exp(\alpha_{\text{eff}}(x - x_j)), \quad \text{for electrons,} \quad (2.11)$$

$$\langle Q_{j+}(x) \rangle = e_o n_{oj} \frac{\alpha}{\alpha_{\text{eff}}} \left\{ \exp(\alpha_{\text{eff}}(x - x_j)) - 1 \right\}, \quad \text{for positive ions,} \quad (2.12)$$

$$\langle Q_{jn}(x) \rangle = e_o n_{oj} \frac{\eta}{\alpha_{\text{eff}}} \left\{ \exp(\alpha_{\text{eff}}(x - x_j)) - 1 \right\}, \quad \text{for negative ions,} \quad (2.13)$$

where $x \equiv x(t) = x_j + v_- t$ and v_- denote drift distance and electron drift velocity, respectively. For non-uniform electric fields a more general formula must be used:

$$n_-(l) = n_o \exp\left(\int_0^l \alpha_{\text{eff}}(x') dx'\right) \quad (2.14)$$

where l and x' denote total avalanche length and coordinate along electron drift line, respectively.

The process of avalanche multiplication is subjected to statistical fluctuations. If $\langle G(x) \rangle = \exp(\alpha_{\text{eff}} x)$ denotes mean electron number after covering distance x by the head of an avalanche, the probability of having gain G , in case of $\langle G(x) \rangle \gg 1$, is given by:

$$P(G, x) = \frac{1}{\langle G(x) \rangle} \exp\left(-\frac{G}{\langle G(x) \rangle}\right). \quad (2.15)$$

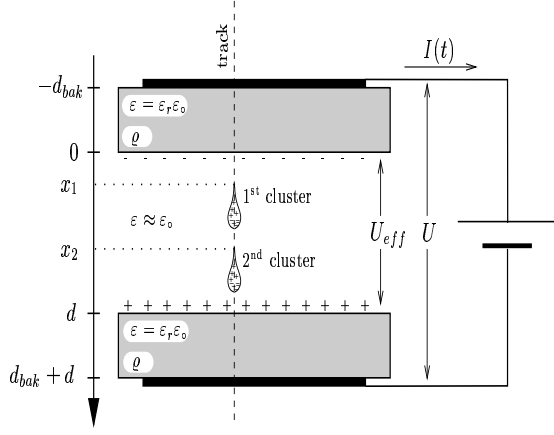


Figure 2.7: The idea of a charge formation in the RPC gap: primary clusters created at distances x_1 and x_2 from the cathode initiated two electron avalanches.

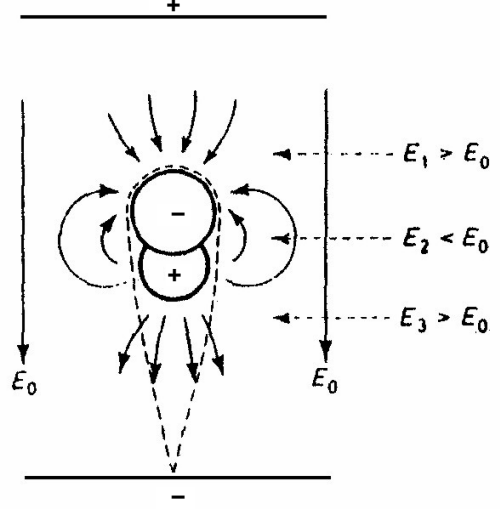


Figure 2.8: The effect of space charges of an avalanche of high amplification on the applied electric field $E_0 = U_0/d$ [51].

The above distribution is valid only for gas mixtures of negligible electro-negativity, such as Argon with hydrocarbons. For non-zero attachment a model by Legler [52] describes charge gain fluctuations more accurately:

$$P(G, x) = \begin{cases} k_o \frac{\langle G(x) \rangle - 1}{\langle G(x) \rangle - k_o} & \text{if } G = 0 \\ \langle G(x) \rangle \left(\frac{1 - k_o}{\langle G(x) \rangle - k_o} \right)^2 \left(\frac{\langle G(x) \rangle - 1}{\langle G(x) \rangle - k_o} \right)^{G-1} & \text{if } G > 0 \end{cases} \quad (2.16)$$

where $k_o = \frac{\eta}{\alpha}$. It can be seen from the above formula that there is always certain probability that the avalanche will not develop at all.

2.3.4 Space charge effect and streamers

The electric field generated by a cloud of electrons and ions during avalanche formation can distort electric field E_0 created by external voltage electrodes. This effect is schematically shown in Fig. 2.8. The field before and behind a head of the avalanche is enlarged by the space charges, while it is reduced between electron and ion cloud. A departure from a drop-like shape of the avalanche near its head at high gains has been observed in cloud chambers long ago [51]. Deviations from the nominal E_0 field by a few percent only have a remarkable effect on the gas gain, since the first Townsend coefficient depends roughly exponentially on the electric field.

At higher gain photons start to contribute the avalanche growth significantly by initiating

secondary avalanches. The field distortion by space charges and photon feedback force photoelectrons created outside the avalanche to move toward it which results in growth of the avalanche in all directions. Finally a streamer is formed, which is a thin plasma filament connecting two electrodes [53]. A threshold of about 10^8 electrons (Raether's limit) corresponds to the charge density at which space charge field becomes comparable to E_0 . This condition has been found to be universal for many gases at pressures ≥ 1 atm in parallel plate detectors [51]. The power dissipated in streamers inside RPCs depends on the gas mixture. It could vary from thousands of pC to 1 pC in some freon mixtures.

The region of electric fields for which space charge becomes sufficient to disturb external electric field, but before streamer discharge region, is called *saturated avalanche (proportional) mode*.

2.3.5 Signal development on external electrodes

For particle detectors made of perfectly conducting electrodes surrounded by insulating materials the current induced on a grounded electrode due to movement of a point charge Q in the electric field $\vec{E}(\vec{x})$ is given by Ramo's theorem [54, 55]:

$$I(t) = -Q(\vec{x}) \vec{E}_w(\vec{x}) \cdot \vec{v}_d \quad (2.17)$$

where: $\vec{x} = \vec{x}(t)$, $\vec{v}_d = \dot{\vec{x}}(t)$ – position and velocity of a point charge Q
 $\vec{E}_w(\vec{x})$ – weighting field obtained by removing charge Q ,
 putting the electrode of interest to unit voltage
 and grounding all other electrodes.

Let us consider an intrinsic cell of an array dS over the zone where the avalanche develops. Moreover, if external voltage supplying electrodes are made out of graphite we will consider it as a perfect conductor. In the case of uniform electric field approximation the equation 2.17 simplifies to:

$$I(t) = -Q(t) E_w v_d \quad (2.18)$$

where d , d_{bak} and ε_r denote, respectively, gas gap width, thickness- and relative dielectric permittivity of the bakelite, and

$$E_w = \frac{1}{d} \frac{\varepsilon_r}{2(d_{bak}/d) + \varepsilon_r} \equiv \frac{1}{d} k \quad (2.19)$$

is a weighting field from equivalent circuit shown in Fig. 2.9.

Because ions drift $100 \div 1000$ times slower than electrons and $v_+ \approx v_n$ one can assume with rather good approximation that ions start to move only after time T_- when all the electrons are

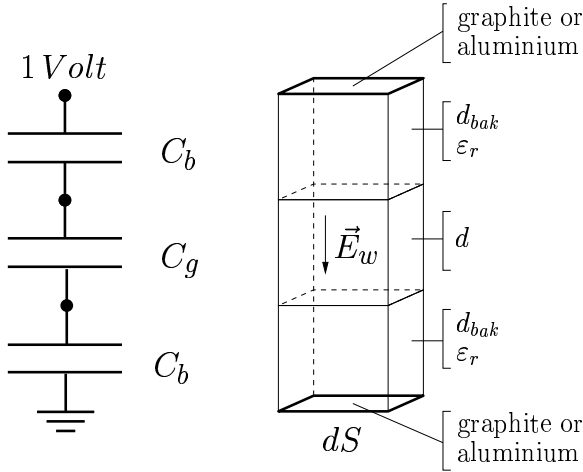


Figure 2.9: Equivalent circuit for weighting field calculation (Ramo's theorem) for single gap RPC assuming that resistive electrodes act as perfect insulators during avalanche formation.

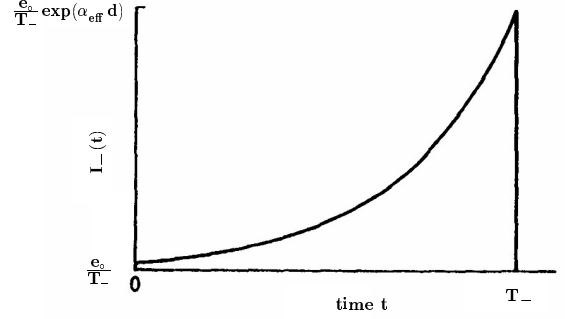


Figure 2.10: Carrier current of electrons of an avalanche in the uniform electric field ($n_o = 1$) [51].

collected in the anode [51]. In such case for a single cluster having n_o primary electrons created at a distance x_j from the cathode, the total current induced on external voltage electrodes is a sum of three contributions due to electrons, positive- and negative ions given, respectively, by the following formulas:

$$I_-(t) = k \frac{d - x_j}{d} \frac{e_o n_o}{T_-} \exp[\alpha_{\text{eff}} v_- t], \quad 0 \leq t \leq T_- \quad (2.20)$$

$$I_+(t) = k \frac{e_o n_o}{T_+} \frac{\alpha}{\alpha_{\text{eff}}} \left\{ \exp[\alpha_{\text{eff}}(d - x_j)] - \exp[\alpha_{\text{eff}} v_+ t] \right\}, \quad T_- \leq t \leq T_- + T_+ \quad (2.21)$$

$$I_n(t) = k \frac{d - x_j}{d} \frac{e_o n_o}{T_n} \frac{\eta}{\alpha_{\text{eff}}} \left\{ \exp[\alpha_{\text{eff}}(d - x_j - v_n t)] - 1 \right\}, \quad T_- \leq t \leq T_- + T_n \quad (2.22)$$

where $T_- = \frac{d - x_j}{v_-}$, $T_+ = \frac{d}{v_+}$ and $T_n = \frac{d - x_j}{v_n}$. The electron current carries $\frac{k}{\alpha_{\text{eff}} d}$ fraction of the total electron charge $\langle Q_{j-} \rangle$ released in the gap due to j -th ionization cluster. Typically: $d_{\text{bak}} = d = 2 \text{ mm}$, $\epsilon_r = 5 \div 10$ and $\alpha_{\text{eff}} = 5 \div 10 \text{ mm}^{-1}$, so that coefficient $k \simeq 0.7 \div 0.8$ and the ratio $1/(\alpha_{\text{eff}} d) \simeq 5 \div 10\%$.

A characteristic shape of the fast electron component is depicted in Fig. 2.10 for cluster started at the cathode by a single electron ($n_o = 1$, $x_j = 0$). The current due to positive ions is shown in Fig. 2.11. An expanded region around time instant T_- showing all three components can be seen in Fig. 2.12. It is the electron component $I_-(t)$ which allows one to achieve RPC time resolution of a nanosecond range due to its characteristic short rise time.

The formula 2.17 does not, however, accurately describe signals induced on electrodes embedded in materials with arbitrary electrical conductivity σ and permittivity ϵ . Situation is even

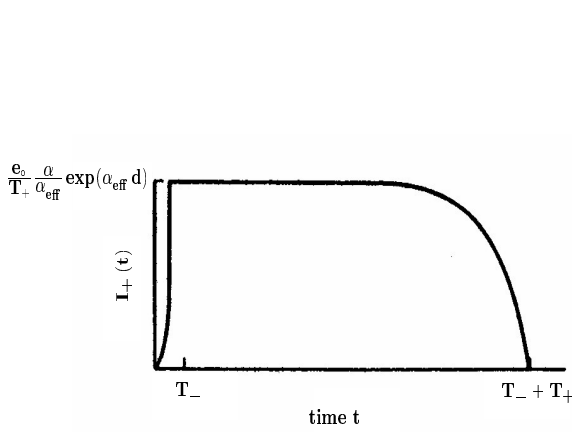


Figure 2.11: Carrier current of positive ions of an avalanche in the uniform electric field ($n_o = 1$) [51].

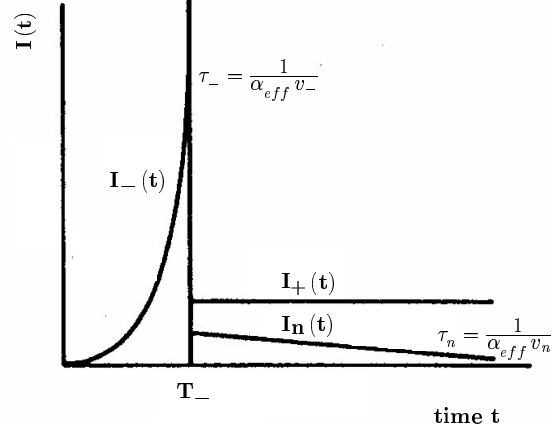


Figure 2.12: Carrier currents of an avalanche due to: electrons, positive and negative ions for attachment $\eta > 0$. In the above figure $\eta/\alpha = 0.5$ and $v_n \approx v_+$ [51].

more complex as ε and σ are frequency dependent [56].

Several theoretical attempts have been carried out so far to describe signals in detectors with weakly conductive media [57–59]. It was only recently that formulas applicable to Resistive Plate Chambers have been derived by Riegler et al. [60, 61]. It has been shown analytically that in RPCs having low resistivity plates (i.e. 2mm-thick bakelite plates of $\varrho = 10^{10} \Omega\text{cm}$ separating 2mm-wide gas gap) the induced currents on the outer field shaping electrodes (e.g. thin carbon layer, metallic foil) are not distorted due to conductivity of the plates. But in a standard RPC design, where signals are read out from metallic strips insulated from resistive carbon layer, the pulses induced on external pick-up strips are slightly distorted, however, for a typical graphite resistivity of $10^5 \Omega/\square$. In consequence a non-zero cross talk between neighbouring strips occurs. The results obtained by Riegler et al. are in agreement with earlier experimental measurements by Battistoni et al. [62] addressing signal transparency of high resistivity cathode in wire chambers with external strip readout. The authors of Ref. [62] demonstrated that the full signal transparency plateau starts for graphite resistivity of about $10^5 \div 10^6 \Omega/\square$. They also proposed an electric working model which very well reproduced the experimental data.

A capacitive coupling between neighbouring strips and the shielding ground plane is another source of cross-talks. In the CMS detector strip widths will range from 0.8 cm to 3.8 cm, depending on the region. Strip lengths will be 85 cm and 130 cm in the barrel and will range from 20 cm to 84 cm in the endcaps. The signal propagation time along strip $\tau_p \approx 1 \text{ ns} \div 6 \text{ ns}$ is comparable with the rise time of the fast electron component $\tau_- \sim 1 \text{ ns}$, therefore, all signal lines should be treated as long transmission lines. The time spread of signals from RPC detectors employed in the CMS is given not only by intrinsic RPC time resolution but also depends on: time of flight

variation of incoming particles, propagation delay along strip and additional time spread due to front-end electronics used.

2.3.6 Efficiency and timing

In RPC detectors for trigger purposes only fast electron component $I_-(t)$ is useful due to its characteristic fast rise time. This current carries fast charge q_e which is a sum of fast charges delivered by all clusters in the gas gap:

$$q_e = k \sum_j Q_{j-} = k \sum_j n_{oj} e_o G_j \quad (2.23)$$

where G_j denotes charge gain of the j -th cluster, which is subjected to statistical fluctuations as it was already discussed in Section 2.3.3.

Due to statistical fluctuations of the distance x_j at which j -th cluster is created given by equation 2.7, the average charges carried by electrons, positive- and negative ions due to j -th cluster can be, respectively, evaluated as:

$$\langle Q_{j-} \rangle = e_o n_o \left(\frac{\langle n_p \rangle}{\langle n_p \rangle + \alpha_{\text{eff}}} \right)^j \exp(\alpha_{\text{eff}} d) \quad (2.24)$$

$$\langle Q_{j+} \rangle \simeq \frac{\alpha}{\alpha_{\text{eff}}} \langle Q_{j-} \rangle \quad (2.25)$$

$$\langle Q_{jn} \rangle \simeq \frac{\eta}{\alpha_{\text{eff}}} \langle Q_{j-} \rangle. \quad (2.26)$$

It can be seen that the higher α_{eff} is the smaller contribution due to secondary clusters becomes. Usually in 2 mm gap RPCs operated at atmospheric pressure only first two clusters contribute to the visible signal. Average charges carried by electronic- and by total current due to all clusters in the gas gap, respectively, are equal to:

$$\langle Q_- \rangle = e_o n_o \exp(\alpha_{\text{eff}} d) \frac{\langle n_p \rangle}{\alpha_{\text{eff}}} \quad (2.27)$$

$$\langle Q_{\text{tot}} \rangle = \frac{\alpha}{\alpha_{\text{eff}}} \langle Q_- \rangle = e_o n_o \frac{\langle n_p \rangle \alpha}{\alpha_{\text{eff}}^2} \exp(\alpha_{\text{eff}} d). \quad (2.28)$$

The ratio of detectable fast component $\langle q_e \rangle = k \langle Q_- \rangle$ to the total avalanche charge $\langle Q_{\text{tot}} \rangle$ is therefore given by $\frac{k}{\alpha d}$. It is a diminishing function of the electric field as long as space charge effects can be neglected [63]. Since the gas gain grows with the electric field a detection efficiency plateau is observed above certain working voltage applied to the chamber when the average induced charge reaches threshold set on fast front-end charge amplifiers.

Supposing that only one cluster constitutes the signal and the gain fluctuations are given by the equation 2.15 one can estimate intrinsic time resolution of a single gap RPC as:

$$\sigma_t = \sqrt{\langle t^2 \rangle - \langle t \rangle^2} = \frac{\pi}{\sqrt{6}} \frac{1}{\alpha_{\text{eff}} v_d} \quad (2.29)$$

where $t(G) = \frac{1}{\alpha_{\text{eff}} v_d} \ln \frac{G_{\text{thr}}}{G}$ is a threshold crossing time corresponding to avalanche gain G and threshold G_{thr} [64]. Since in typical gases used in RPCs, both, v_d and α_{eff} increase with the electric field one expects improvement of the time resolution with the operating voltage.

2.3.7 Uniformity of the electric field

The response uniformity of individual detectors is a crucial issue for operating the large detection systems, such as RPC-based muon trigger for the CMS experiment. The electric field uniformity inside amplification region of any parallel plate detector has significant impact on the detector performance since the charge gain steepens with the electric field. Two main factors influencing field uniformity can be distinguished, namely: mechanical parallelism of the gas gap and geometry of the external field shaping electrodes.

A mechanical tolerance of commercially available bakelite plates of typical thickness of $d_{\text{bak}} = 2\text{ mm}$ is about $20\text{ }\mu\text{m}$. The accuracy of machining spacers and frames is about $20\text{ }\mu\text{m}$, as well. The glue used for assembling RPC gas boxes can cause additional uncertainty of the gap width and field distortions near spacers and frames due to glue film thickness and glue leaks, respectively. Although, a $20\text{ }\mu\text{m}$ deviation corresponds to the electric field non-uniformity of about 1% only in case of 2 mm-wide gas layer, the charge gain variations as large as $10\% \div 20\%$ are expected purely due to difference of the avalanche length for typical working conditions corresponding to effective Townsend coefficients in the range of $5\text{ mm}^{-1} \div 10\text{ mm}^{-1}$.

Micro-scale deviations from the average surface profile, described by a characteristic length called *roughness parameter*, are in the range of $0.1\text{ }\mu\text{m} \div 1\text{ }\mu\text{m}$ for typical materials used for RPC electrodes. It has been learned since early developments on RPC technique that the smoothness of inner surfaces facing the gas is an important parameter affecting intrinsic RPC noise rate² and the dark current.³ For many years the only practical solution to reduce the intrinsic noise was to clad internal surfaces of RPC gas boxes with a thin layer of organic linseed oil. This procedure smooths electrode surfaces due to masking imperfections of the original bakelite surface [9]. In mid 90's, however, significant progress was made with introduction of new bakelite laminates clad with melaminic resin during the production process and characterized by roughness comparable to that of polymerized linseed oil [66].

The RPC detectors should be constructed in such a way that dead areas do not exceed few percent of the active area. Deviations from uniformity of the electric field inside a gas

²Spurious and spontaneous discharges in the gas triggered by microscopic sharp edges on the electrode surfaces facing the gas.

³Current drawn by the chamber from the high voltage power supply in absence of ionizing particles traversing the detector.

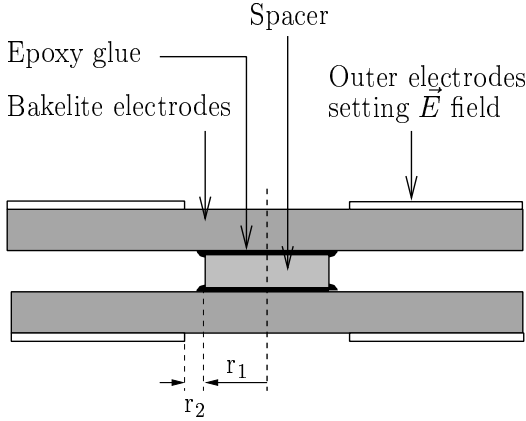


Figure 2.13: Cross section of the spacer region in a typical RPC detector.

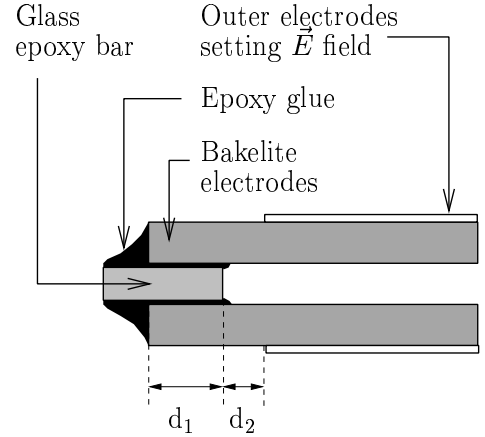


Figure 2.14: Cross section of the frame region in a typical RPC detector.

layer may occur close to spacers' and frame's walls depending on the geometry of external field shaping electrodes (e.g. resistive graphite coating) and electrical properties of RPC constituents. Moreover, in reality some overpressure is always applied to a RPC gas box, what results in widening of the gas gap over zones far from spacers and frame. Thus, field strength close to the spacers and frame becomes higher than in the rest of detector's active volume, and so does the noise rate.⁴ Eventual glue leaks or linseed oil remnants around spacers and near the frame may introduce increase of the noise rate, as well.

In Figs. 2.13 and 2.14 typical designs for spacer and frame are shown, respectively. The gaps between field shaping electrodes and walls surrounding the gas volume (denoted as r_2 and d_2 on the figures) have significant impact on the field uniformity and the dark current. Therefore, a proper setting of the geometry of external field shaping electrodes can reduce the electric field in the gas in the vicinity of spacers and frames, what reduces the noise rate.

For instance, in work by Ammosov et al. [65] several graphite painting scenarios have been investigated for an ideal single gap RPC (i.e. completely flat electrodes, no glue leaks, no linseed oil treatment) with highly resistive bakelite electrodes using a dedicated numerical model which accounts for all surface and volume currents. The results of those simulations concerning electric field strength variations in the middle plane of RPC gap as a function of the distance from RPC edge are reproduced in Fig. 2.15. It can be seen that the smallest deviations from the nominal applied electric field, and thus the smallest dead zones, occur if field shaping electrodes cover

⁴This is one of the reasons for which gas boxes of RPC detectors are mechanically squeezed between two flat and rigid panels (e.g. structured honeycombs, plastic foams) to preserve flatness of the gas gap over large detection area.

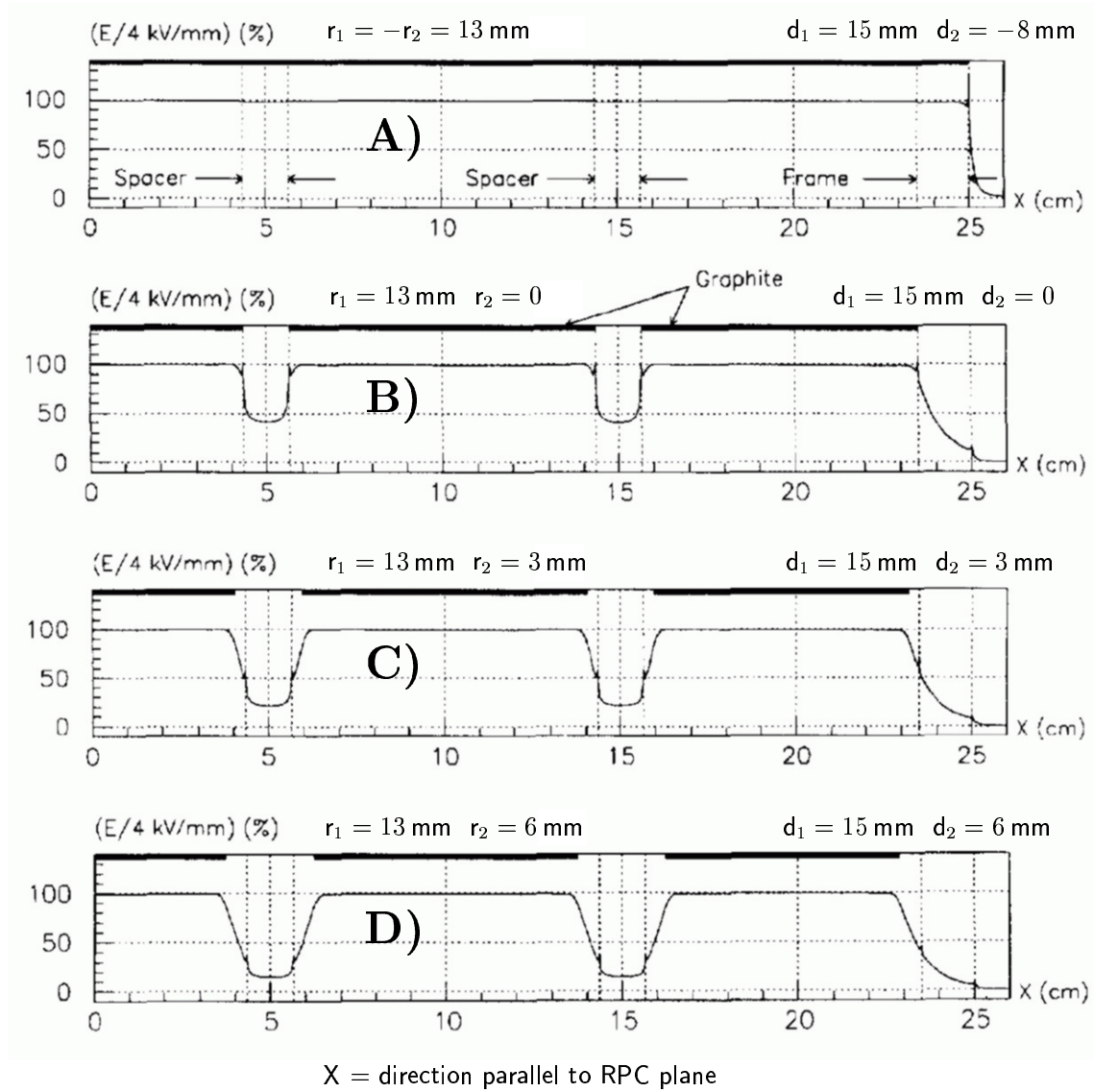


Figure 2.15: Calculated absolute electric field (in percent of the nominal one) in the middle plane of a single gap RPC. Results for 4 graphite painting scenarios are depicted. Dimensions r_1 , r_2 and d_1 , d_2 are introduced in Figs. 2.13 and 2.14, respectively [65].

entire area over spacers ($r_2 = -r_1$) and partially cover the frame ($d_2 < 0$). However, from the operational point of view of large detection systems, such solution generates unacceptable dark current. For example, electrode configurations shown in Figs. 2.15 B and D generate smaller dark currents by factors of 2 and 6, respectively, than scenario depicted in Fig. 2.15 A. Thus, depending on RPC application, a compromise should be achieved between acceptable dark current, noise level and tolerable dead zones of the detector.

2.3.8 RPC operation at high particle fluxes

In Resistive Plate Chambers the maximal achievable gain is inversely proportional to the counting rate due to limitation of the current that may flow through the electrodes because of their specific resistance ϱ and relative dielectric permittivity ε_r . Therefore, the rate capability is governed by: the characteristic charging time $\tau \sim \varrho \varepsilon_0 \varepsilon_r$ of the electrodes, the average total avalanche charge $\langle Q_{\text{tot}} \rangle$ and the rate of avalanches R_{aval} per unit area. As a result of the dynamic voltage drop across resistive plates the electric field in the irradiated part of a sensitive detector volume is reduced. The effective voltage U_{eff} applied to the gas is given by (see Fig. 2.7):

$$U_{\text{eff}} = U - 2 \cdot \varrho \cdot d_{\text{bak}} \cdot \frac{dI}{dS} = U - 2 \cdot \varrho \cdot d_{\text{bak}} \cdot R_{\text{aval}} \cdot \langle Q_{\text{tot}} \rangle. \quad (2.30)$$

A long-term passage of the current may influence resistivity of the plates due to dissipated power or accumulated charge.

2.3.9 Streamer mode of operation

For a long time RPCs were operated in a high amplification regime (gains $\sim 10^8$ electrons) in which the induced signals were so large (few hundred pC) that no front-end amplifiers were needed. Although it was very convenient feature for constructors of large detection systems the application of such detectors was limited to low rates experiments only (i.e. 100 Hz/cm² at most) [67].

As it was already stated in the previous Section, if the whole area- or some part of a RPC detector is irradiated the local density of a current flowing through the resistive electrodes is proportional to the rate of electron avalanches induced by ionizing particles appearing in the gas medium. In fact, the effective electric field inside the affected region is lower than the nominal one (without irradiation) due to potential drop across electrodes which is proportional to the resistivity of the plates. Measurements of the efficiency dependence on the particle flux have been done by many experimental groups by means of: pulsed accelerator beams of different spot sizes and limited duty cycles, and continuous exposure of the whole detector area to photons from radioactive sources or from a nuclear reactor. Tests with concentrated pulsed beams of $3 \times 3 \text{ cm}^2$ spot area and 300 ms spill⁵ duration showed that for standard RPCs, having plates of $10^{11} \Omega\text{cm}$ volume resistivity, the efficiency decreased with time elapsed from the spill start [68]. Later results on RPCs with different electrodes' resistivity ($4 \times 10^{11} \Omega\text{cm} \div 4 \times 10^{10} \Omega\text{cm}$) tested using $10 \times 10 \text{ cm}^2$ pulsed beams of 2.6 s spill duration demonstrated similar effects [67, 69, 70].

⁵During spill time particles are extracted from the accelerator and delivered to individual experimental areas.

Furthermore, low resistivity chambers started to lose efficiency at about 100 Hz/cm^2 , while high resistivity ones already at few tenths of Hz/cm^2 . The difference in rate capability for concentrated and diffuse pulsed accelerator beams was also demonstrated by Williams et al. for small RPC prototypes of different plate conductivities and materials [71, 72]. However, it has been found that for constant flux of ionizing particles the rate capability was significantly smaller in comparison to pulsed beam tests [73].

Because of very good timing and expected low production costs of large detection areas the Resistive Plate Chambers were proposed for muon trigger systems in general-purpose LHC experiments in early 90's [10]. However the rate capability had to be much improved as severe radiation background conditions are foreseen at LHC.

2.3.10 Avalanche mode of operation

Two sources of remedy for the rate limitation were investigated: increasing the electrical conductivity of the plates and reducing the gas amplification. The drawbacks of the first method were higher dark current and dissipated power, as well as increased intrinsic noise [69]. The second method decreased power dissipated by the chamber, but required fast, high gain amplifiers which transferred charge amplification from the gas to the front-end electronics [74]. It was reported in Refs. [75–77] that operation at gains $10^5 \div 10^6$, a factor 100 smaller than in streamer mode, resulted in improvement of the rate capability by a factor of 20 for pulsed beam tests of different sizes [75–77]. The authors found that up to 1 kHz/cm^2 average delay due to rate (*time walk*), time resolution and efficiency were not deteriorated significantly. Again, for continuous irradiation of the entire single gap RPC with photons emitted by ^{137}Cs and ^{60}Co radioactive sources, which induced similar avalanche rates per unit area as in the case of pulsed beam tests, the efficiency drop below 85% was reported [78].

Recently RPCs operated in avalanche mode have been chosen by three out of four LHC experiments [28, 79, 80], where RPC detectors will be employed. They must exhibit full efficiency at rates of about 1 kHz/cm^2 and weak dependence of their timing and spatial resolution on the counting rate variations. Another problem with operation of RPCs in proportional mode is the width of the voltage range corresponding to a streamer-free efficiency plateau. A coexistence of avalanche and streamer signals is harmful in terms of: strip multiplicity, time resolution and dead time.

Several experimental groups intensified their R&D in view of adopting RPC technique for LHC needs by means of:

1. Search for more dense and more quenching gas mixtures which are non-flammable and

environment-safe,⁶ containing: HFC gases (e.g. Tetrafluoroethane $C_2H_2F_4$, Pentafluoroethane C_2HF_5), Isobutane ($i-C_4H_{10}$), Sulfur hexafluoride (SF_6) and Argon [81–83].

2. Developing alternative RPC geometrical structures and new construction materials: double gap [28], wide gap [84, 85] and multi-gap [86–88].

The Warsaw CMS Group has also actively participated in those efforts starting from 1993. For instance, a significance of the avalanche mode for achieving full efficiency at pulsed accelerator beams of 2.5 s duration at counting rates up to 500 Hz/cm² has been shown for a double gap RPC made out of standard commercial bakelite plates [89].

In work by Di Ciaccio [81] peaked distributions of induced pulse-height spectra were reported for a single gap RPC filled with binary gas mixtures of $C_2H_2F_4/i-C_4H_{10}$. The operation in a saturated avalanche regime, where space charges limit growth of an avalanche, widened streamer-less efficiency plateau to 600 V ÷ 800 V and increased the rate capability beyond 100 Hz/cm² for continuous irradiation.

An important progress concerning suppression of avalanche-to-streamer transition has been achieved due to adding small amounts of strongly electronegative SF_6 gas to the working gas mixture. It was demonstrated by Camarri et al. [83] that SF_6 fraction as small as 0.5% can provide streamer-free efficiency plateau over 1 kV range in a single gap RPC of 2 mm gas gap.

2.3.11 Existing models

Several attempts to understand and describe RPC behaviour in a saturated avalanche mode were performed in recent years. The goal was not only to reproduce the experimental data, but also to give some predictions on the choice of adequate gas mixture or detector design. Here three available models are briefly described:

1. *Simple Monte Carlo saturation model* [83, 90].

An exponential growth of avalanches induced by primary ionization clusters is stopped if they reach fixed saturation charge Q_{sat} and, then, all electrons from stopped avalanches are only allowed to drift toward the anode. The model has the following input parameters: Q_{sat} (characteristic saturation charge), $\alpha(E)$ (Townsend coeff.), $\eta(E)$ (attachment coeff.), $v_d(E)$ (electron drift velocity), $\langle n_p \rangle$ (specific primary ionization) and n_o (mean number of electrons in single ionization cluster). For a given gas mixture the value of Q_{sat} is varied to best fit experimentally measured pulse-height distributions.

⁶Gas mixtures for LHC detectors have to comply CERN's safety regulations and the Montreal convention. In particular, many freon gases, like CF_4 and CF_3Br , widely used so far by the RPC community, have been banned.

2. *Detailed Monte Carlo simulation involving dynamic calculation of the space charge field* [91].

The gas gap is divided into disks in which electron charges are distributed following Gaussian distribution (width depends on transverse diffusion and drift length). The electric field on symmetry axis of the avalanche is calculated dynamically in each time step. Simulated gas properties are used as an input to the model, namely: $\alpha(E)$ (Townsend coeff.), $\eta(E)$ (attachment coeff.), $v_d(E)$ (electron drift velocity), $D_T(E)$ (transverse diffusion coeff.), $D_L(E)$ (longitudinal diffusion coeff.), $\langle n_p \rangle$ (specific primary ionization) and $w(n)$ (electron cluster size distribution). The signals induced on external pick-up electrodes are calculated using special integral representation of the solution for the static electric field of a point charge in three layer geometry with different permittivities and conductivities [60]. The model reproduces peak-shaped distribution of charges induced on external strips. However, in order to match efficiency and streamer probability from the experimental data the authors of the model have to multiply attachment- and diffusion coefficients by some factors close to unity. This correction could be related either to imperfect calculation of the gas transport parameters and/or to a larger spread of the electron cloud in the head of a real avalanche due to space charge than that simply caused by a diffusion assumed in the model.

3. *Logistic Saturated Avalanche Model* [63].

The authors of this model use the following equation to describe electron avalanche multiplication inside the gas gap:

$$\frac{dn_-}{dx} = \alpha_{\text{eff}} n_- - \beta(n_-)^2.$$

A second term added to the right hand side of the equation 2.9 represents suppression of the electron multiplication process in the head of an avalanche due to presence of space charges. The model has three free parameters which must be derived from experimentally measured charge gain dependence on the applied electric field. This statistical model correctly describes dependencies of the average total- and induced charges as a function of the electric field, however, it cannot be used for simulation of pulse-heights from single events.

2.4 Design adopted for CMS

The CMS collaboration has chosen as a baseline the standard double gap RPC design [28], which cross-section is schematically shown in Fig. 2.2. In such structure the induced signal is a sum of two signals from two identical sub-modules facing each other having common readout plane

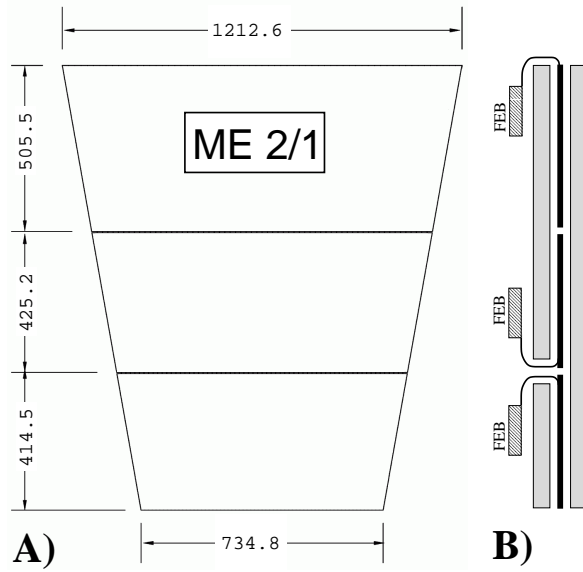


Figure 2.16: Plane view of the ME 2/1 signal planes (A) and corresponding cross section showing sub-modules configuration and ducts for signal cables connecting strips with the front-end electronics (B).

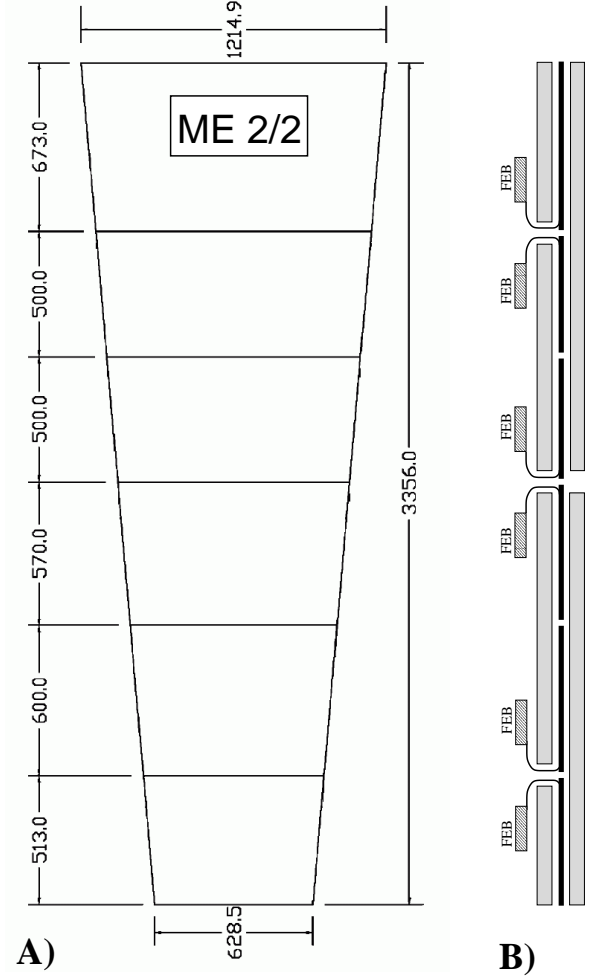


Figure 2.17: The same as in Fig. 2.16 for ME 2/2 module.

inserted between them [92]. The efficiency ε_{eff} of a double gap structure can be expressed in terms of efficiencies of its sub-gaps ε_1 and ε_2 as:

$$\varepsilon_{\text{eff}} = 1 - (1 - \varepsilon_1)(1 - \varepsilon_2). \quad (2.31)$$

Two gaps may exhibit full efficiency even if individual sub-gaps suffer from efficiency losses due to rate. At given working voltage the time resolution of a double gap chamber is slightly better than for each sub-unit due to larger average pulse-heights.

By the time RPCs were proposed for installation in the CMS experiment studies on these detectors working in avalanche mode at high particle fluxes were still under way. Although the Warsaw CMS Group is responsible for RPC-based muon trigger electronics, it is also doing research on gaseous detectors in the framework of the CMS muon system. The Author, being a

member of this Group, actively participated in adopting RPC technique in view of its implementation in large rapidity regions of the CMS detector. In consequence several improvements have been proposed and experimentally verified.

For instance, a standard double gap solution causes difficulties in extraction of the signals from strips in CMS endcaps because RPC stations in those regions have between 2 and 6 η -sections. On the contrary, in the CMS barrel strips of individual double gap modules are not segmented in η direction at all, thus, providing free access to strips on their both ends. Two examples of strip segmentation in η direction of endcap RPC chambers are shown in Figs. 2.16 A and 2.17 A for ME 2/1 and ME 2/2 module, respectively. Because readout strips are situated between two sub-modules there would be no virtual space left for strip termination and signal cables in case of two identical sub-modules. Therefore, according to the baseline CMS design, large single gap modules are divided into smaller ones for the cost of relaying on information from single gaps in the vicinity of the borders between some η -sections. The segmentation of trapezoidal sub-gaps and paths for signal cables are depicted for ME 2/1 and ME 2/2 modules in Figs. 2.16 B and 2.17 B, respectively. It can be seen that in endcap regions each double gap muon station having more than 2 η -sections consists from 3 to 6 single gap units of different sizes, instead of two identical ones. The Warsaw CMS Group proposed an alternative solution, namely, the Inverted Double Gap structure discussed later in this thesis, allowing one to overcome drawbacks of the baseline double gap design concerning signal extraction.

The CMS collaboration still has not decided whether to use linseed oil coating of the inner bakelite surfaces for improvement of the electrodes' smoothness. Such procedure was mainly used in experiments working in streamer mode. If improperly done during mass production of the detectors, it could deteriorate RPC system performance significantly, as it was in the case of the BABAR experiment [93]. There is also a concern that, due to its organic nature, the oil can deteriorate under high radiation environment, spoiling the performance of the RPC system in a long term. The necessity of linseed oil coating is also addressed in this thesis.

Recently another difficulties during mass production of RPCs have been revealed, namely, insufficient mechanical strength of spacers glued to the bakelite [94]. An improved technique of spacer gluing developed by the Warsaw CMS group lacks such drawbacks and allows larger accidental gas overpressure than standard spacer gluing.

With development of novel composite materials for RPC electrodes having low specific resistance, one can ask whether double gap structure is really needed for efficient detection of minimum ionizing particles at counting rates of the order of $1 \text{ kHz/cm}^2/\text{gap}$ foreseen in RPC muon stations in the CMS endcaps. A possibility of utilizing single gap chambers in CMS large rapidity regions is also studied in this thesis.

Chapter 3

Experimental methods, materials and model detectors

In this Chapter various experimental techniques and concepts on Resistive Plate Chambers with high counting rate capability are presented. The following subjects are addressed in forthcoming Sections: special composite materials for RPC electrodes, novel techniques of RPC assembling, construction of double- and single gap RPC prototypes and a dedicated PPAC model detector, experimental set-ups and methods of data analysis.

3.1 Novel techniques

3.1.1 New composite materials for electrodes

Characteristics of materials used for electrodes of Resistive Plate Chambers are very important for long-term experiments in which stable and efficient operation is required over many years. It has been demonstrated in several works [89, 95, 96] that maximal detectable flux of RPC-like detectors depends on the electrode volume resistivity. Several materials have been proposed for RPC electrodes, such as: bakelite [9], glass [97] or plastic [98]. In this work, however, only bakelite-like materials will be addressed since the CMS collaboration has decided to implement this RPC technique [28].

A bakelite laminate is a composite organic material which consists of several layers of cellulose sheets impregnated with phenolic resin (Phenolic Formaldehyde polymer) and cured at high temperature and pressure to form flat, few-millimeter thick plates. For outer bakelite surfaces (*skins*) a melaminic resin is often used to improve hardness and to achieve shiny-looking surfaces. These relatively cheap composite materials are widely used in the industry as electric insulators or as decorative panels.

The aim of the measurements presented in this Section was to select an adequate material for RPC electrodes among commercially available and specially developed bakelite samples. Partial

results have been published in Refs. [99, 100] and presented during one RPC workshop [101].

Measurement techniques

Surface- and volume resistivity were determined experimentally by the Author using techniques described in the Appendix A. Dimensions of examined samples and test electrodes were standardized. A dominant source of errors was due to uncertainty of the electrodes' geometry, namely: $3 \div 4\%$ for volume- and 16% for surface resistivity measurements. A special probe for long-term resistivity measurements was developed. It provided necessary electric shielding and allowed one to monitor temperature and humidity of an arbitrary chosen gas environment inside the probe.

Since the laboratory where all the samples had been stored between 1997 and 2002 was not air-conditioned, the ambient conditions exhibited seasonal changes. In particular a significant decrease of the humidity was observed during winter periods when the central heating system was turned on. Annual temperature variations ranged from 15°C to 30°C and the mean room temperature was 25°C .

It is well known fact that surface resistivity strongly depends on surface contamination and outside humidity [102, 103]. Special measures, like proper cleaning and assuring stability of temperature and humidity, must be undertaken to get reproducible results. Although surface resistivity was also measured by the Author, the results should be treated as an estimation of the order of magnitude only and are not addressed in this thesis.

The quality of bakelite surfaces is an important parameter affecting RPC performance, namely, the rate of spontaneous discharges triggered by local surface imperfections where the electric field can exceed the nominal applied one. An increase of this noise rate also manifests in a larger dark current drawn by the chamber. To quantify average smoothness of different bakelites for RPC electrodes a roughness parameter R_a [μm], commonly adopted in general engineering practice, was used. It is defined as the vertical deviation of the surface from its average profile. Measurements were performed at CERN using Rodenstock RM 600 laser profilometer¹ for several bakelite samples. An instrument uses non-contact technique based on dynamic focusing of an infrared laser beam of $2\mu\text{m}$ spot size on a tested horizontal specimen with $0.005\mu\text{m}$ vertical resolution. Each individual measurement corresponded to a scanned area of $6 \times 6\text{mm}^2$. Such measurements of a micro-scale smoothness help to select the adequate bakelite material. However, a visual inspection of the inner bakelite surfaces before assembling of a RPC gas box is also very important, since even single scratch (i.e. macro-scale effect) may lead to increase of chamber's intrinsic noise and dark current. Thus careful handling during bakelite production, transportation and machining is essential.

¹Courtesy of I.Crotty (CERN) and CERN Metrology Service. These contributions are here acknowledged.

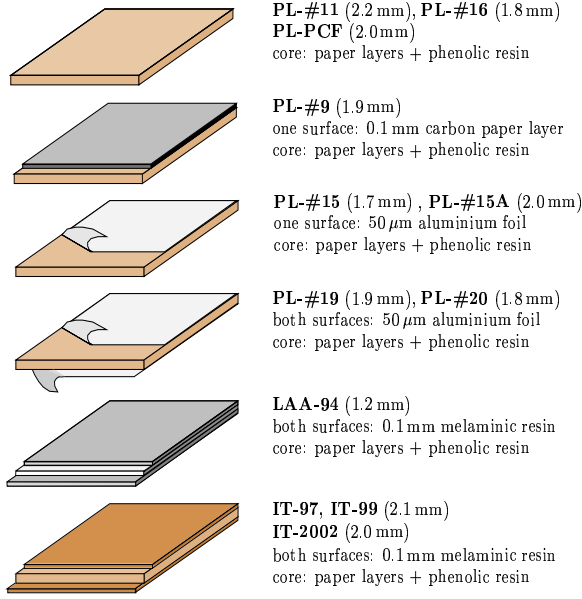


Figure 3.1: Expanded view of tested laminates for RPC electrodes.

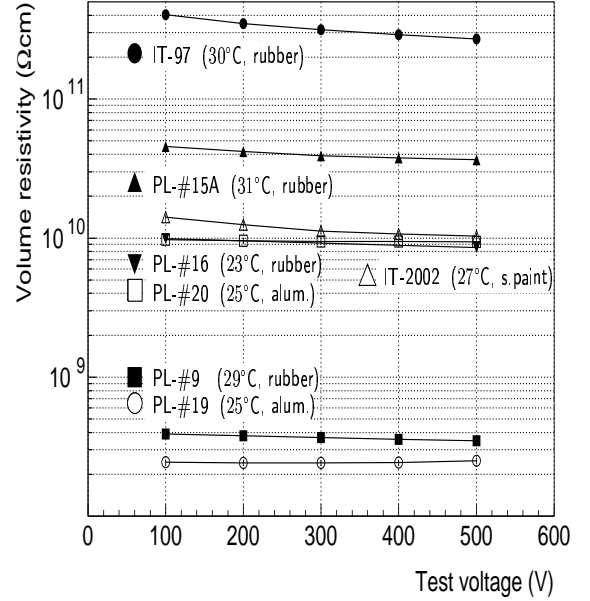


Figure 3.2: Voltage dependence of the resistivity of several fresh bakelite samples after 5 minutes of applying the test voltage. Results are not corrected for ambient air temperature (shown in parentheses).

Materials tested

Several bakelite laminates, both, commercially available and specially developed, were examined in view of selecting suitable material for electrodes of RPCs working at high rates. Tested materials originated from three European manufacturers: Pan-Pla Laminates (Pavia, Italy), Izo-Erg (Gliwice, Poland) and Argolite (Willisau, Switzerland). A short characteristic of each type of bakelite is given in Tab. 3.1. In Fig. 3.1 an expanded view of bakelite layers is schematically shown. The thickness of tested bakelite plates ranged from 1.2 mm to 2.2 mm and their volume resistivity covered almost four orders of magnitude between $10^8 \Omega\text{cm}$ and $10^{12} \Omega\text{cm}$.

Results on conductivity

The conductivity mechanism of insulating materials is in most cases the ionic one. With introduction of detectors operating at high luminosities, which use insulators, the impact of ionic conductivity on ageing effects becomes more relevant. The problem concerns not only bakelite and glass RPCs, but also micro-strip and CsI-based detectors. The chemistry of such ionic currents and the resistivity changes with accumulated charge are not well understood at present. For

Table 3.1: Description of bakelite types referred in the text.

Structure		Factory ^{*)}	Name	Thick- ness [mm]	Description and/or usage
Core	Skin				
phenolic		PL	PL-PCF	2.0	standard commercially available highly resistive bakelite used for frames and spacers in some tested RPC prototypes
			PL-#11	2.2	
			PL-#16	1.8	
phenolic	0.1 mm carbon paper layer of $25 \text{ k}\Omega/\square$ surface resistivity (one side)	PL	PL-#9	1.9	resistive skin eliminates graphite coating process of outer RPC bakelite surfaces; inverted double gap low resistivity model RPC detector tested in 1997
phenolic	$50 \mu\text{m}$ aluminium foil (one side)	PL	PL-#15	1.7	inverted double gap low resistivity full scale ME 1/1 prototype
			PL-#15A	2.0	
phenolic	$50 \mu\text{m}$ aluminium foil (two sides)	PL	PL-#19	1.9	specially developed sample for monitoring of long-term conductivity changes used for RPC electrodes after removing of the aluminium foil from one bakelite side; inverted double gap low resistivity model RPC detector tested during 1999-2001
			PL-#20	1.8	
phenolic	melaminic (two sides)	IT	IT-97	2.1	high resistivity inverted double gap model RPC detector tested in 1997 two single gap low resistivity model RPC detectors tested in 2002
			IT-99	2.1	
			IT-2002	2.0	
phenolic	melaminic (two sides)	CH	LAA-94	1.2	high resistivity thin bakelite plates used by CERN's Lepton Asymmetry Analyzer Group for construction of multi-gap RPCs

^{*)} PL = Izo-Erg S.A., Gliwice, Poland

IT = Pan-Pla Laminates, Gruppo Frati, Pavia, Italy

CH = Argolite AG Kunststoffplattenwerk, Willisau, Switzerland.

example, it is known that in standard float glass the conductivity is due to movement of the alkaline ions, like sodium. After long-term operation in electric field the sodium ions migrate toward the cathode which results in a depleted layer near the anode surface. As the result a permanent growth of the resistivity is observed. On the contrary, the bakelite and the linseed oil consist of much more complicated compounds and many kind of ions may contribute to the observed current. An electrolytic model for bakelite plates in RPC has been proposed by Va'vra [104] in which ionic current involves charge exchange mechanism among different ions in the bakelite and in the gas medium. The charge carriers (H^+ and negative ions) came from dissolved molecules of phenol impurities. In a fresh, uncured linseed oil the conductivity is due to fatty acid organic molecules ($R-COOH$). In both cases hydrogen and oxygen molecules are delivered near the cathode and the anode, respectively. The water trapped in electrodes or in oil plays an important role in the charge exchange cycle, thus, modulates the conductance significantly. A rapid increase of the resistivity may occur after accumulating certain amount of charge when ions responsible for conductivity are used up and simply plate the anode. Increasing of the bakelite resistance by orders of magnitude may drive RPC into a Malter effect [105], when cathode becomes a good insulator and the rate of ion buildup due to electron avalanches is higher than its removal from the insulating layer.

The stability of the charge gain and of the electrodes' electric conductivity is critical for efficient operation of triggering RPCs at high fluxes in the CMS experiment. Knowing the electric characteristics of the bakelite in its "fresh" state (e.g. stored on a shelf after production) does not guarantee however long-term stability. Several factors influencing the bakelite resistivity, both, prior to assembling of RPCs and during their operation, should be considered:

- absorbed radiation dose,
- long-term passage of the avalanche current through the bakelite plates,
- variation of humidity of the surrounding environment (working gas mixture, outside air),
- variable contamination of water inside the electrodes,
- temperature of the electrodes,
- ageing due to slow processes changing chemical composition of the bakelite (e.g. further polymerization),
- treatment of the bakelite sides facing the gas with a thin layer of polymers to improve smoothness of the surface.

The radiation damage to the bakelite has been extensively tested by others and no significant changes were observed up to 20kGy of absorbed dose [106]. Comparing to the maximal doses of 100 Gy and 1 Gy foreseen, respectively, for endcaps- and for the barrel regions of the CMS

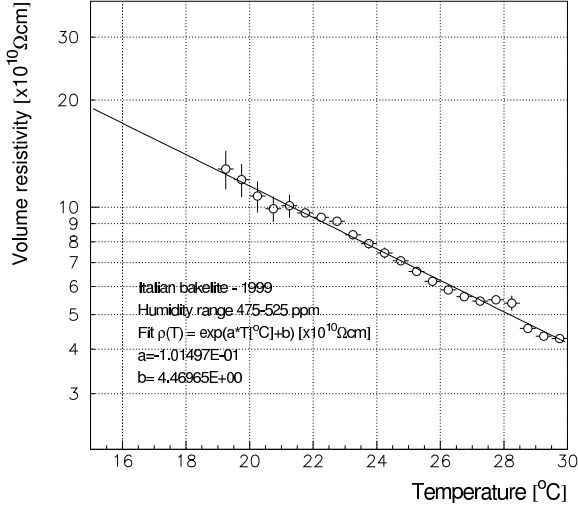


Figure 3.3: Temperature dependence of the resistivity of IT-99 type bakelite. A fitted exponent was superimposed.

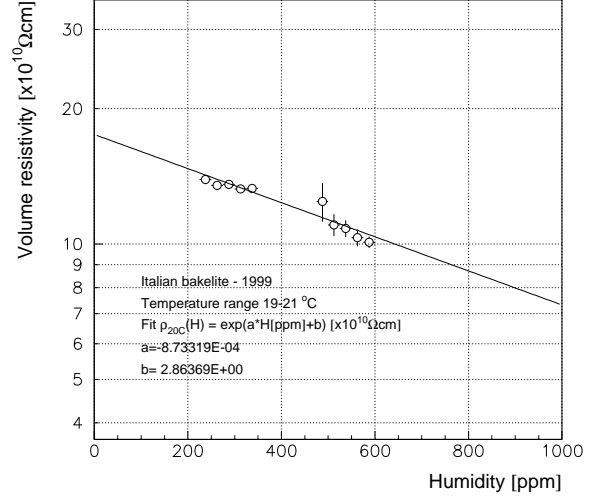


Figure 3.4: Short-term resistivity dependence on humidity for IT-99 bakelite. Data points were scaled to 20° C using parameterization $\rho(20^\circ\text{C}) = \rho(T) \times \exp\{0.101 (T - 20^\circ\text{C})\}$ from Fig. 3.3. A fitted exponent was superimposed.

detector [28], one can safely assume no conductivity changes due to irradiation during 10 years of LHC operation.

The dependence of the volume resistivity on the applied test voltage deviates slightly from Ohmic behaviour. When strength of the electric field increases more carriers became available, thus an increase of the conductivity is observed. In Fig. 3.2 resistivity of seven bakelite types as a function of test voltage is shown. Measurements were performed for “fresh” samples, i.e. shortly after their delivery. Average ambient temperatures and measurement techniques used are also superimposed.

It is pointed out in Ref. [102] that weakly conductive laminates exhibit strong dependence of their resistivity ρ on temperature T following formula $\rho(T) \propto e^{a/T}$, where $a > 0$. For temperature range of interest ($15 \div 35^\circ\text{C}$) an exponential approximation is justified and is often used in the literature [56, 107]. As a typical example in Fig. 3.3 the electric conductivity dependence on temperature is shown for bakelite IT-99. The measured temperature dependence exhibit exponential behavior (solid line). The data has been collected for 17 days of sampling-type measurements.² For temperature dependence measurements only runs with given humidity equal to 500 ± 25 ppm were taken into account since bakelite conductivity also depends on humidity

²Resistivity measured during $\frac{1}{2}$ h period of applying a constant polarizing voltage of 500 V. Runs were repeated every hour.

Table 3.2: Parametrization of the bakelite resistivity ϱ as a function of temperature T in degree centigrade.

Fitted function $\varrho(T) = \varrho_{20} \times e^{-a(T-20^\circ\text{C})}$				
Bakelite type	ϱ_{20} [Ωcm]	a [$^\circ\text{C}^{-1}$]	Humidity range [ppm]	Test duration
IT-99	1.149×10^{11}	0.101	475 – 525	17 days
IT-2002	4.480×10^{10}	$9.91 \cdot 10^{-2}$	800 – 1200	24 h
PL-#19	8.128×10^9	0.114	1000 – 1600	24 h
PL-#20	1.449×10^{10}	0.104	600 – 800	24 h

of the surrounding gas medium as will be demonstrated later in this Section. To disentangle influence of temperature from other effects it is convenient to normalize resistivity values to a fixed temperature T_0 . Wherever possible the resistivity has been normalized to $T_0 = 20^\circ\text{C}$ using function $\varrho(T_0) = \varrho(T) \times e^{a(T-T_0)}$, where positive constant a was determined for each bakelite type. In Tab. 3.2 results of such fits are listed. For the last three materials, however, a faster method was used by means of initial pre-heating of the whole aluminium container to 30°C and allowing it to cool down slowly to a room temperature during 24 hours (the stability of the humidity for those measurements can be read from Tab. 3.2).

The electric conductivity depends strongly on the water content inside bakelite plates [108]. The process of water vapour exchange with ambient air starts even before bakelite is made in the factory, since water can be confined in semi-products used for the production. After manufacturing resistivity depends on storage conditions and it is difficult to compare samples which history is unknown.

For instance in Fig. 3.4 a correlation between conductivity and humidity of ambient air is shown for IT-99 bakelite. The data was collected during 17 days of sampling-type measurements, previously described in this Section, and it was corrected for temperature effects. Exponential dependence of the resistivity on humidity of the surrounding gas can be seen from the data shown in the figure (solid line). However, data points do not correspond to fully saturated values at given humidity due to limited duration of the test. As will be shown below a time constant needed to saturate the resistivity level varies from tens of days to several months.

To study effect of water content on bakelite resistivity water residuals were removed from samples by conditioning them at 60°C during 48 hours in an oven and cooling them down to room temperature before starting measurements.³ The results of the conditioning for two samples of bakelite are plotted in Fig. 3.5. The volume resistivity increased, in comparison to fresh samples,

³Conductive rubber technique has been chosen for safety due to potential damage of the silver paint at high temperatures.

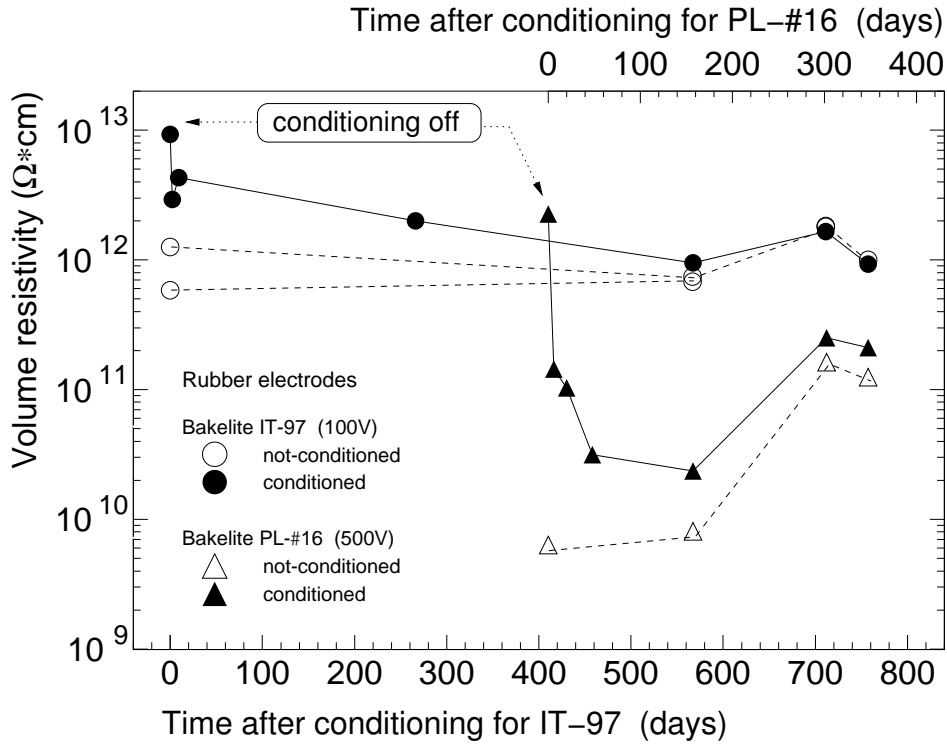


Figure 3.5: Recovery of the bakelite resistivity after conditioning at 60° C for 24 hours for two types of bakelite (full circles and triangles). Open markers correspond to reference not-conditioned samples.

during heating by up to few orders of magnitude. The relative change is less pronounced for the high resistivity sample IT-97. The slow process of absorption of water vapour from the air leads to an increase of the conductivity with time. Eventually conditioned and fresh samples reached the same resistivity level which also depends on temperature and humidity in the laboratory. From this data one can conclude that conductivity changes attributed to water residuals inside the bakelite are reversible.

Another interesting issue concerns variation of the bakelite resistivity due to long-term storage and possible natural ageing. It has been studied for specially developed low resistivity phenolic bakelite PL-#19 having both skins made of 50 μm thick aluminium foils integrated during production process. Since an effective area allowing exchange of water vapour for $10 \times 10 \text{ cm}^2$ specimens is limited to the edges only, the samples can stay longer in their fresh state. In Fig. 3.6 an evolution of the electric conductivity for PL-#19 bakelite during nearly 4 years is plotted, starting from initial level of $5 \times 10^8 \Omega\text{cm}$. All three measurement techniques were used for comparison. The results shown correspond to sampling measurements of 5 min duration time. All samples originate from the same physical bakelite sheet and were stored in the same place in the laboratory. Each of four tested specimens had voltage electrode made of aluminium foil which

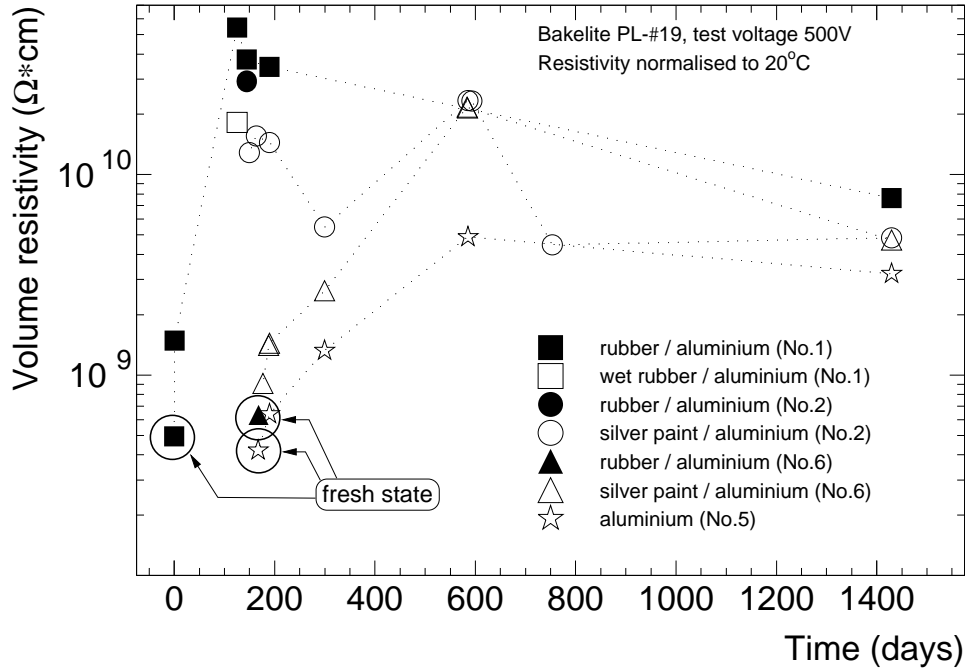


Figure 3.6: Resistivity of four bakelite samples of the same type stored at room conditions during period of 10/1998-09/2002. Detailed explanation is given in the text.

assured best electrical contact with the bakelite. For *silver painted* samples only readout and guard electrodes were painted. For the sample *No. 5* a ring of 25 mm inner diameter and 2.5 mm width was etched from readout side (i.e. 91% of the surface was still covered by the aluminium foil). The beginning of the time scale on the figure corresponds to removal of the aluminium foil from one side of samples *No. 1* and *No. 2*. About 5 months later protective foils have been removed from the sample *No. 6* and, then, the resistivity very close to the initial value for sample *No. 1* was observed. It can be also seen that at this level of conductivity the rubber (*No. 6*, circled filled triangle) and the aluminium electrode technique (*No. 5*, circled open star) yield comparable results. The initial rise of resistivity observed for all samples was presumably due to drying in the air containing less percent of water vapour than the bakelite. Also seasonal humidity variations in the laboratory resulted in conductivity changes by a factor up to 6 (*No. 2*, open circles). After 4 years one can clearly observe a saturation of the electric conductivity. The resistivity of sample *No. 5* (open stars) reached level of $3 \times 10^9 \Omega\text{cm}$ — almost one order of magnitude higher than its initial value. At the same time results for samples having silver painted electrodes were about two times higher. Moreover, they were compatible to a value obtained with rubber electrode

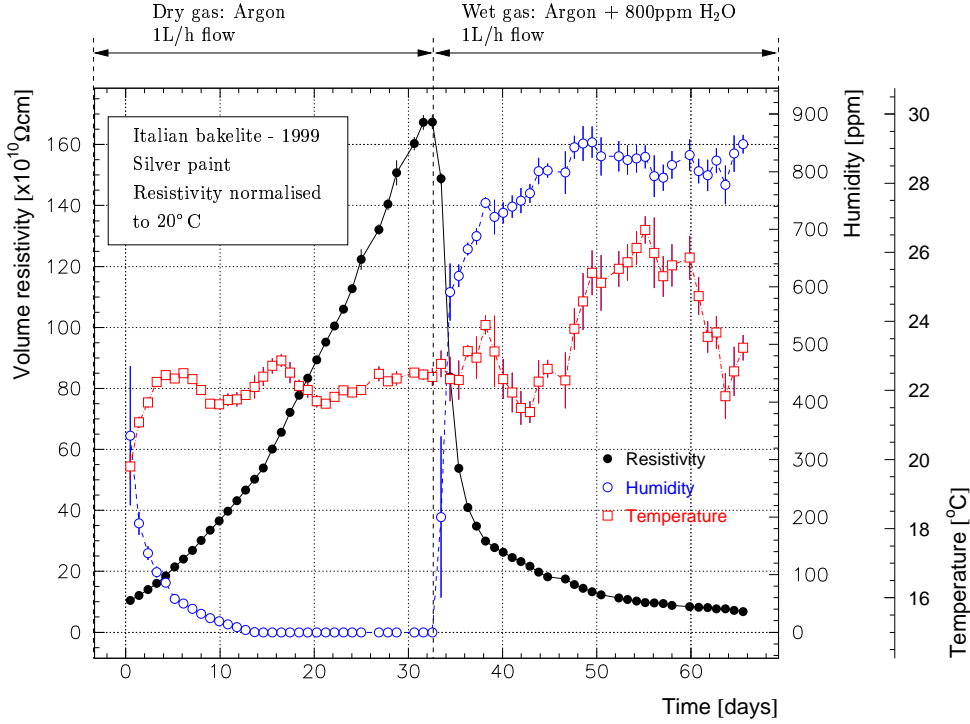


Figure 3.7: Medium-term effect of humidity of the surrounding gas medium on the bakelite resistivity. Data points (full circles) were normalized to 20° C .

techniques after applying corrections discussed in the Appendix A. From observed seasonal variations of the resistivity for sample *No.2* (open circles) shown in Fig. 3.6, it is possible to infer that conductive silver paint is preamble to water vapour, which allows one to use this technique for long-term studies of resistivity changes in controlled gas medium surrounding specimen under test.

Another issue to be studied is the possibility of bakelite conductivity changes due to drying during constant exposure to a dry gas environment (e.g. electrodes of RPC detectors in the CMS experiment intended to operate for at least 10 years). To study this effect solely (i.e. minimizing the contribution due to the effect of accumulated charge) a dry Argon gas⁴ was flowing at rate of 1 dm³/h through the aluminium container with IT-99 bakelite sample inside. Silver painted electrodes were used to allow exchange of water vapour via both sides of tested laminate. From the results of sampling measurements⁵ plotted in Fig. 3.7 it can be seen that after 32 days the resistivity rose by a factor of 17 from its initial value of $1 \times 10^{11} \Omega\text{cm}$ without signs of showing a saturation. During that time the integrated current of about 0.012 C/cm²

⁴Argon bottle of 5.0 (99.999%) purity was used.

⁵Described previously in this Section for temperature calibration curves.

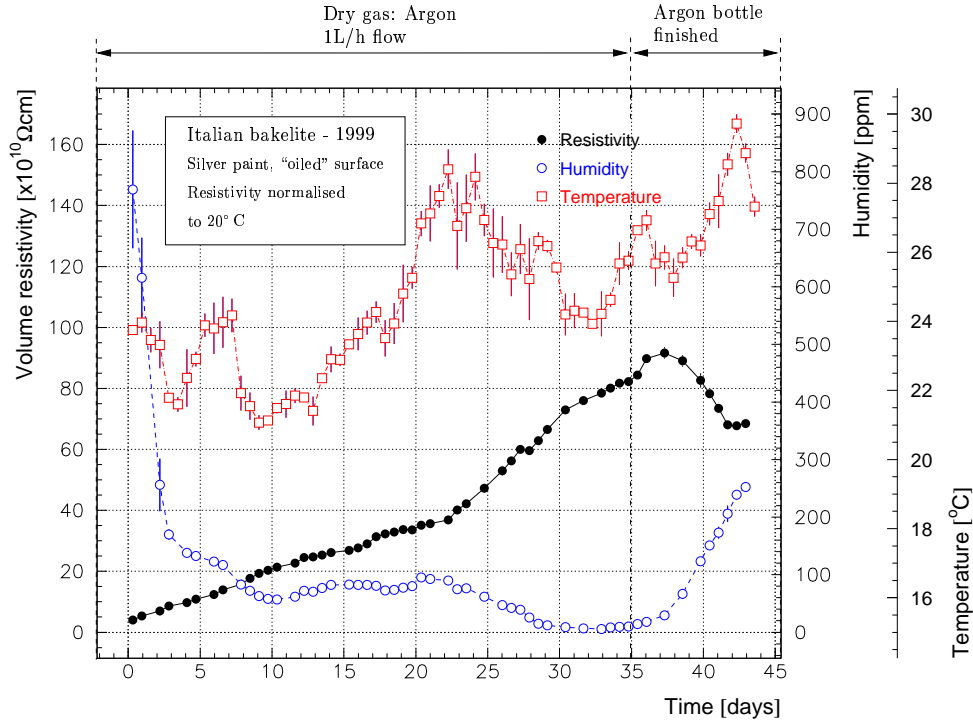


Figure 3.8: Medium-term effect of dry gas on the resistivity of bakelite having both surfaces treated with linseed oil mixture. Data points (full circles) were normalized to 20° C .

has been measured. In the second part of the test 800 ppm of water was added to Argon gas. As a result the conductivity was restored to its initial value of $1 \times 10^{11} \Omega\text{cm}$ after 20 days and the process of water absorption still continued. It is evident from the data that for constant humidity of the surrounding gas medium the bakelite materials need tens of days to achieve stable resistivity value, thus, short-term measurements (i.e. lasting few hours or few days only) can be somewhat misleading. For instance, in work by Ahn et al. [109] extensive tests of the resistivity dependence on temperature and humidity are presented, however, most probably the results do not correspond to the fully saturated levels of the bakelite conductivity due to limited duration of individual sampling measurements corresponding to fixed temperature and humidity of the surrounding air.

The effect of linseed oil coating, a commonly used procedure for reduction of spurious discharges due to surface roughness, on the speed of bakelite drying was also investigated. The same sample of IT-99 bakelite was treated with linseed oil mixture⁶ and allowed to dry in air for several days. Afterward, a test with dry Argon gas was performed. As can be seen from Fig. 3.8 the resistivity increased 18 times from $5 \times 10^{10} \Omega\text{cm}$ after 37 days, almost at the same rate as

⁶Linseed oil mixture proportions by volume: 47.5% Heptane + 47.5% Linseed oil varnish + 5% Siccative.

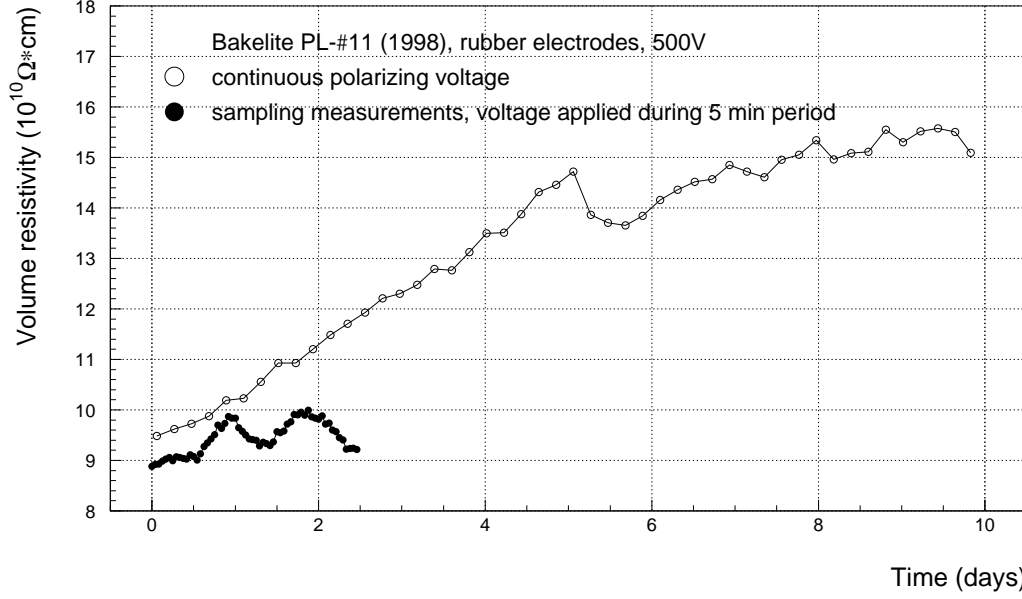


Figure 3.9: Comparison of sampling (full circles) and constant polarizing voltage (open circles) measurements for PL-#11 bakelite sample.

without linseed oil coating. At the end of the test, after stopping the Argon, humid air started to penetrate the gas system which resulted in slow increase of the bakelite conductivity.

The effect of long-term passage of the current through the bakelite electrodes must be also studied for RPCs working at high counting rates. Knowing total avalanche charge $\langle q \rangle$ delivered in RPC gas gap and expected rate of avalanches one can deduce current density which passes through resistive plates. This current causes a voltage drop across resistive plates and reduces the effective electric field applied to the gas. In the worse case of ME1/1 muon station the avalanche rates up to $1 \text{ kHz/cm}^2/\text{gap}$ are foreseen including safety factors [28, 33]. For typical electronics thresholds and Tetrafluoroethane-based gas mixtures a typical high voltage working point corresponds to $\langle q \rangle \sim 30 \text{ pC}$ [110–112]. For practical reasons (e.g. efficiency loss, worsening of time resolution) an effective gap voltage should not differ from the nominal one by more than 100 V, which sets upper limit on the bakelite resistivity of $8 \times 10^9 \Omega \text{cm}$. In Tab. 3.3 the integrated current is shown for the barrel- and the endcap CMS regions and for two scenarios: with- and without safety factor of 4 applied to simulated neutron fluxes. The influence of the current passing through RPC electrodes on the volume resistivity of RPCs working at large rapidity regions of the CMS experiment is not well understood, yet. Ageing studies performed so far by CMS, ATLAS, and LHCb experimental groups working on RPC techniques for the LHC reached at most: 0.05 C/cm^2 , 0.3 pC/cm^2 and 0.4 pC/cm^2 , respectively [110, 111, 113]. It was also demonstrated by others that typical bakelite materials exhibit gradual increase of the

Table 3.3: Total integrated current per unit area in a single RPC gap after 10 LHC years at peak luminosity ($\Delta t = 7 \cdot 10^7$ s, $\langle q \rangle = 30$ pC, intrinsic RPC noise: $10 \text{ Hz/cm}^2/\text{gap}$).

Safety factor for neutron flux	Barrel		Endcaps	
	Charge [C/cm ²]	Rate [Hz/cm ² /gap]	Charge [C/cm ²]	Rate [Hz/cm ² /gap]
none	0.03	15	0.4	210
$\times 4$	0.06	30	1.7	810

volume resistivity at constant test voltage applied [77, 108, 109]. For example, in work by Crotty et al. [77] it is suggested that the electric field causes outgassing of water from tested laminate which leads to decrease of its conductivity.

The effect of applying continuous polarizing voltage over long period of time was tested for PL-#11 and IT-99 bakelite samples. In Fig. 3.9 the conductivity dependence on time for the same sample of PL-#11 laminate is depicted for sampling (full circles) and continuous (open circles) measurements. During sampling measurements, in which test voltage of 500 V was applied during 5 minutes every hour, only periodic conductivity changes can be observed due to daily variations of temperature and humidity in the laboratory. For continuous polarizing voltage, the resistivity grows 1.6 times over first 10 days of measurements. By that time integrated current of about 0.016 C/cm^2 was collected (or 0.05 C/cm^2 if one applies a correction factor of 3 due to use of conductive rubber technique discussed in the Appendix A). The second sample tested was the IT-99 laminate having silver painted electrodes, which assured good electrical contact of electrodes with bakelite and, simultaneously, allowed exchange of water vapours between the sample and the ambient air. For this specimen a constant polarizing voltage of 500 V has been applied for several months. During tests the upper lid of the resistivity probe hosting the sample was opened to enable contact with the ambient air. The results normalized to 20°C are shown in Fig. 3.10. It can be seen that the resistivity increases four times from the initial value of $3 \times 10^{10} \Omega\text{cm}$ over first 35 days of the test. From Fig. 3.11 one can observe that after this period of time the integrated current of 0.14 C/cm^2 was measured. In the second period of 110 days the polarizing voltage was reversed. This resulted in the immediate drop of the resistivity by 30% followed by a local minimum at about $9 \times 10^{10} \Omega\text{cm}$, though, the conductivity has not been restored to its initial value and continued to decrease. The resistivity reached $2.5 \times 10^{11} \Omega\text{cm}$ at the end of measurement and corresponding integrated current of -0.11 C/cm^2 was measured during applying negative polarizing voltage. Equivalently, the absolute charge per unit area of 0.39 C/cm^2 was moved through the bakelite plate from the beginning of the test. One can conclude on the results presented in Fig. 3.10 that the observed change of the conductivity due to

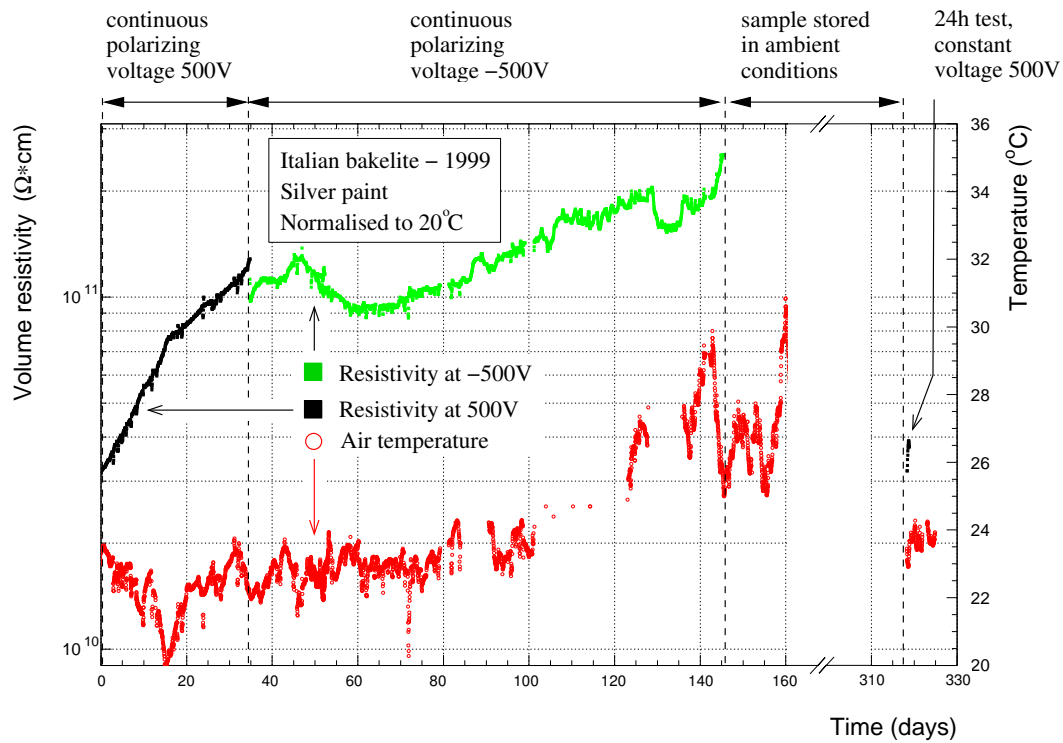


Figure 3.10: Medium-term resistivity dependence on time after applying of constant polarizing voltages of ± 500 V for IT-99 bakelite sample. Results were normalized to 20°C .

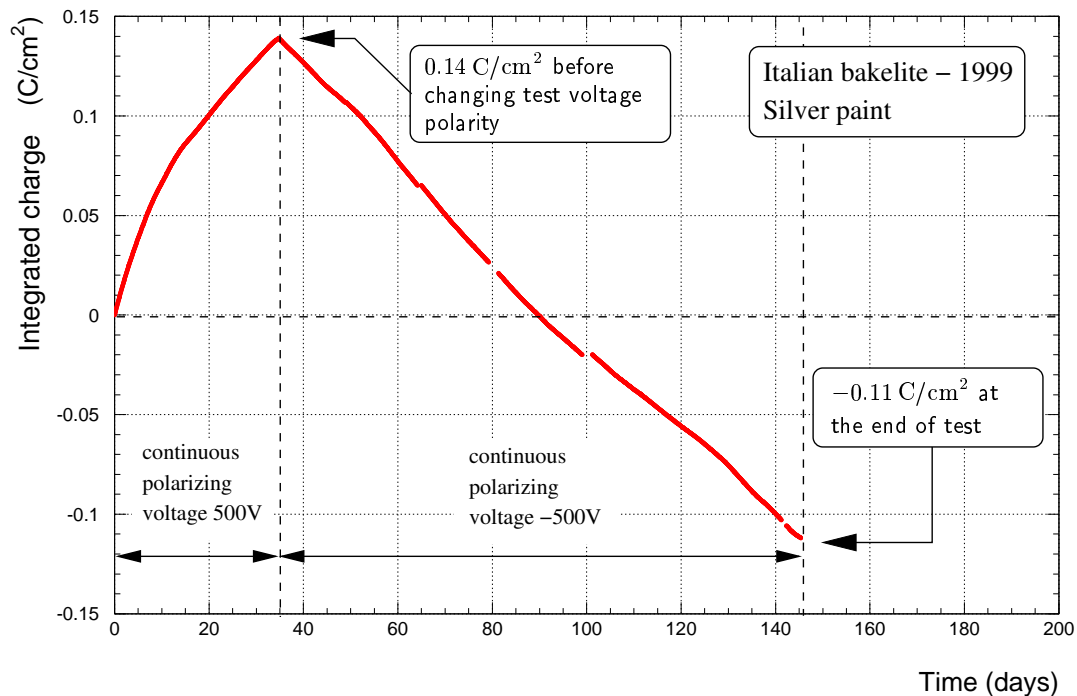


Figure 3.11: Accumulated charge vs time for a constant polarizing voltage test from Fig. 3.10.

continuous polarizing voltage was not permanent since the resistivity was restored after storage of the plate on the shelf for 6 months in ambient conditions. This effect may lead to the restoration of the initial resistivity level of electrodes constituting RPC detectors working at high counting rates, when the voltage is off during periodical few-month shut-downs of the LHC machine.

In Ref. [104] an increase of the resistivity by a factor of 5 is reported for the bakelite used in RPCs for the BABAR experiment after $\sim 0.7 \text{ C/cm}^2$ and $\sim 0.15 \text{ C/cm}^2$ integrated current in air and in dry boil-off Nitrogen, respectively. However, the results on conductivity for CMS-like bakelite⁷ IT-99 presented in this Section showed even much faster ageing, both, in dry Argon- and in open air environment. Therefore, on the basis of the results on sampling measurements with dry- and wet gases and with continuous polarizing voltage it can be stated that addition of small amount of water vapour to the working gas mixture is essential in order to assure long-term stability of the RPC operation at high rates. Therefore, at least in large rapidity regions of the CMS detector, such enriching of the working gas mixture should be seriously considered by the CMS collaboration.

Surface smoothness

Several bakelite samples have been sent to CERN for surface quality tests with a precise laser profilometer. For each specimen an area of about $6 \times 6 \text{ mm}^2$ was examined. The results are listed in Tab. 3.4. It can be seen that melamine-phenolic-melamine samples IT-97 and LAA-94 gave the best results on R_a parameter, though standard commercially available PL-PCF phenolic laminate was only slightly worse. For recently developed IT-99 and IT-2002 laminates values close to $0.15 \mu\text{m}$ are expected since they were produced by the same company, but using improved technology of manufacturing special laminates for HEP experiments [94]. It can be seen from the table that special phenolic laminates with aluminium foil integrated during the production process on their both sides (like PL-#19 and PL-#20) have few times higher roughness than melaminic samples if one removes the foils. Therefore such bakelites, well suitable for conductivity measurements, seem not to be adequate for construction of low noise RPCs. As will be shown in Chapter 4 the RPC detector made out of IT-2002 melamine-phenolic-melamine bakelite exhibits very low intrinsic noise and dark current even if internal detector surfaces are not treated with the linseed oil. These observations raise hope that specially developed composite material, similar to IT-2002 laminate, but having additional integrated layer of aluminium foil on one side can be a good novel material for RPC electrodes.

There are recent experimental indications that in RPCs operated at high rates and filled with Tetrafluoroethane-based gas mixtures some fraction of highly corrosive fluorine acid (HF)

⁷Produced by the same factory as the bakelite plates for the BABAR experiment.

Table 3.4: Roughness parameter R_a for several not-oiled bakelite samples ($6 \times 6 \text{ mm}^2$ scan area, $0.005 \mu\text{m}$ resolution).

Bakelite type	$R_a [\mu\text{m}]$	
	Side 1	Side 2
LAA-94	0.14	0.13
IT-97	0.17	0.12
PL-PCF	0.18	0.13
PL-#15A	1.40	0.62 *
PL-#19	0.52 *	0.49 *

* after removal of the aluminium foil.

is produced [114]. It is believed that HF acid formed from water vapours and $\text{C}_2\text{H}_2\text{F}_4$ freon was responsible for permanent etching of glass in a large RPC system of the BELLE detector at KEK, Japan [115]. However, long-term influence of traces of HF acid on degradation of the bakelite surface or the linseed oil coating has not been studied, yet. For this reason studies are concentrated on finding the best method of purifying the gas in a closed circulation loop of the RPC gas distribution system in the CMS detector.

3.1.2 Inverted Double Gap RPC

An Inverted Double Gap (IDG) RPC is essentially a stack of two identical single gap RPCs each equipped with its own strip readout plane. Two variants of IDG structures developed by the Warsaw CMS Group are depicted in Figs. 3.12 and 3.13 in case of standard graphite-coated sub-modules and the ones made out of specially developed aluminium-cladded bakelite,⁸ respectively.

The readout planes are placed on external faces of a double gap RPC structure. A thin metallic plate on ground potential, sandwiched between two independent RPC planes, serves for electric screening of the sub-units; the plane is separated electrically from the electrodes. The two RPCs are pressed together (put in tight contact) in the single mechanical structure. The module is assembled between two flat and rigid structured plates which assure good mechanical contact of all elements and the flatness of the structure. An analog sum of signals induced by avalanches from two gaps, picked-up on the readout electrodes, forms the final signal.

In an IDG structure, on the contrary to a classic double gap RPC adopted for CMS endcaps, almost arbitrary strip-to-ground coupling can be chosen and proper strip termination can be assured independently on strip plane granularity. An IDG, when combined with a novel spacer technique presented in the next Section, allows one to avoid dead- or low efficiency zones between

⁸These special bakelite laminates are discussed in Section 3.1.1. A conductive silver paint can be used instead of the aluminium foil. More details about RPCs constructed using this technique is given in the next Section.

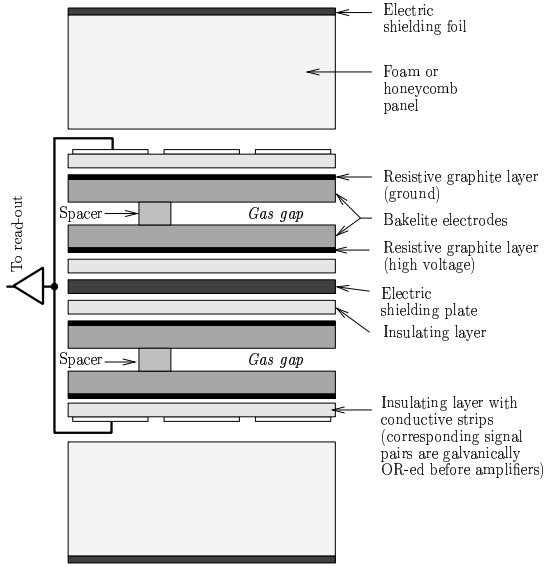


Figure 3.12: Cross section of Inverted Double Gap RPC with standard graphite-coated sub-modules.

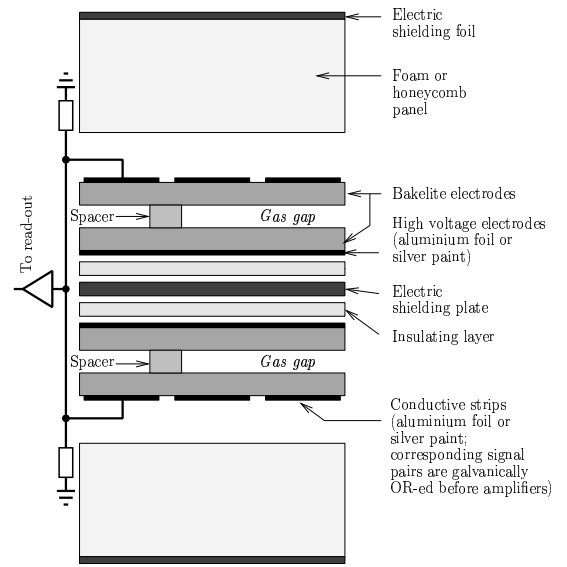


Figure 3.13: Cross section of Inverted Double Gap RPC with sub-modules made out of specially developed aluminium-cladded bakelite plates.

some η -sectors in endcap RPC modules (see discussion in Section 2.4).

3.1.3 Improved spacers

The traditional way of attachment the grid of spacers to the bakelite surface (see Fig. 2.13) might not provide sufficient mechanical strength of the structure in case of accidental overpressure applied to the RPC gas box. The thickness of the glue film can vary from one spacer to another, thus, introducing non-uniformity of the gas gap width. Moreover, glue leaks around spacers are not so rare, which increase areas of the reduced detection efficiency. There are also experimental indications that the gluing technique used so far is sensitive to chemical impurities of the bakelite surfaces, which caused, for example, detachment of spacers in recently assembled RPCs for the LHC experiments and the BABAR detector [94].

A novel spacer gluing technique developed by the Warsaw CMS Group allows one to overcome these limitations. Its idea is schematically depicted in Fig. 3.14. The new gap assembling procedure is explained below. Firstly the ring-shaped spacers and insulating plastic screws of 3 cm length having cone-shaped heads are prepared and carefully cleaned. Then a set of holes corresponding to the desired grid of spacers is drilled in both bakelite plates simultaneously. The outer parts of the holes are made wider to form cones of 45° angle. The holes of the bottom

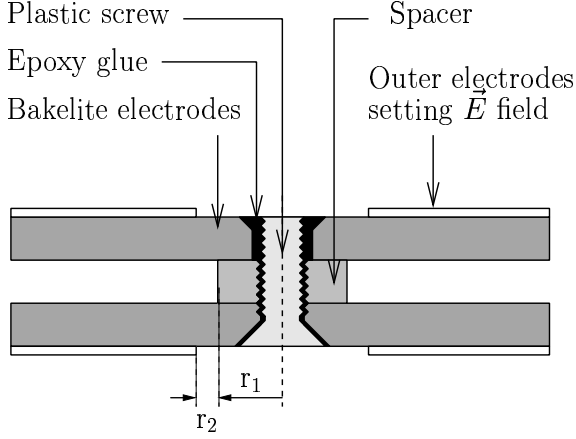


Figure 3.14: A novel technique of improved spacer gluing.

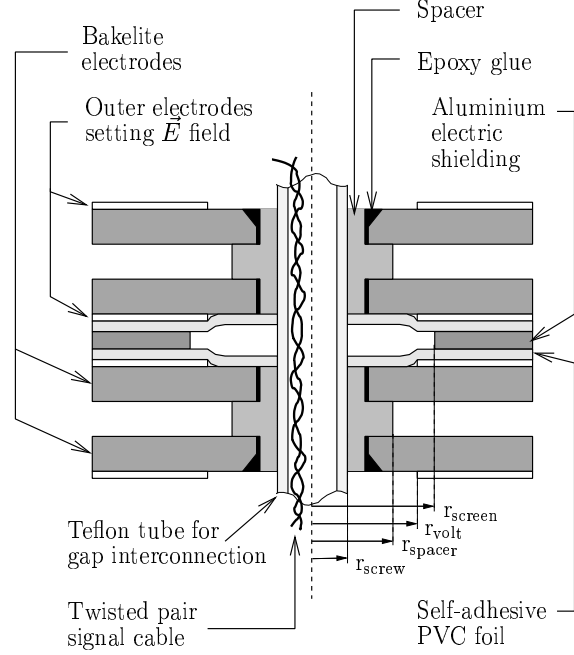


Figure 3.15: A method of gap interconnection through special spacers used in Inverted Double Gap RPCs.

sheet are thread. In the next step all plastic screws are firmly twisted to the bottom plate and only thin layer of epoxy glue is used to maintain gas tightness. Also frames are glued on the bakelite edges at this stage of assembly. After 24 hours all spacers are screw without any glue and upper bakelite plate is glued to the frame. A set of holes prevent accidental movement of the upper plate, thus, possibility of glue leak into the sensitive gas volume is minimized. At the same time specially designed screw nuts are used to firmly junction bottom- and upper plates together over each of the spacers. These nuts are designed in such a way to allow filling with the epoxy glue an empty space between plastic screw and the bakelite to provide gas tightness and good mechanical strength of the junction. After next 24 hours the protruding parts of the plastic screws are removed.

A special version of spacers was also proposed for Inverted Double Gap RPCs in the areas where interconnection of the signal strips of two sub-gaps is required (e.g. double gap CMS endcap modules having more than two strip sections in η). In Fig. 3.15 a schematic drawing of such spacers is depicted. They are essentially rings having outer- and inner diameters equal to 18 mm and 12 mm, respectively. The two sub-gaps are aligned by means of insulating Teflon tubes of 6 mm inner diameter. At the final stage of constructing double gap module the thin

twisted pair signal cables are inserted into the tubes for interconnecting of the corresponding pick-up strips. Such “big” spacers were used in two IDG prototypes described in Sections 3.2.2 and 3.2.3. This technique can substantially reduce zones of limited detection efficiency between some η -sections in RPCs for the CMS endcap regions, where only one gas layer is active (see Figs. 2.16 and 2.17). For typical endcap chambers covering $\Delta\varphi = 10^\circ$ a set of 3 “big” spacers would solve the gap interconnection problem in case of IDG structure. Moreover, additional mechanical stiffness can be achieved in the middle part of the detector if Teflon tubes are thread at both ends allowing to use nuts to screw two sub-gaps and structured readout panels together.

The techniques described above reinforce junction of spacers to the electrode surface that may be problematic when the standard fixation procedure is used, especially if the inner surface of the plates is covered with melamine. This simple technological operation allows one to control the surrounding of the spacers and it increases the safety level for breaking caused by accidental pressurization of the gap.

3.2 Model detectors

Selected bakelite laminates and novel RPC assembling techniques discussed in Section 3.1 were used to build several small- and medium-size prototypes in view of testing their characteristics in radiation environment expected at the LHC. Four double gap and two single gap RPCs, as well as a special version of PPAC detector, were developed and assembled in the Detector Laboratory of IEP, Warsaw University. The construction details of these model detectors are given below.

3.2.1 Low and high resistivity prototypes

When the operation of large area RPC at high rate environment is required, the material on the electrodes should be selected in such a way that the avalanche current in the gap causes negligible voltage drop on the electrodes. Significance of the field variations in the gap is related to the steepness of the gas gain versus field dependence at the working voltage. The maximal current that may flow across the gas gap is set by the resistance of electrodes, thus, setting the limit of the product of the avalanche charge and the avalanche rate. With increasing radiation rate, the charge gain (avalanche charge) shall automatically decrease resulting in loss of the detection efficiency. The loss of efficiency is enhanced due to an exponential-like pulse-height distribution. On the basis of a simple RC circuit considerations one can estimate that the proper resistivity should be in the range of $10^9 \Omega\text{cm}$ for stable operation at rates exceeding 1 kHz/cm^2 (providing that the average total avalanche charge is $\sim 30 \text{ pC}$). An obvious way to improve the rate capability of a RPC is, therefore, to use a material with lower resistivity for the electrodes.

However, if the conductivity of the electrodes becomes too high the operation of the detector should possibly suffer from the limitations related to the PPAC configuration.

The question can be raised whether a detector with parallel electrodes of moderate volume resistivity will have the features of a Resistive Plate Chamber — independence of operation of neighbouring areas. For this reason two double gap RPC modules were built in a similar way, but using electrode material with nominal volume resistivity different by about three orders of magnitude. Both detectors were assembled in the Inverted Double Gap RPC structure which has been already introduced in Section 3.1.2. The high- and low resistivity chambers are denoted further in this work as RPC 1 and RPC 2, respectively. The detectors are schematically depicted in Fig. 3.16.

Sensitive areas of RPC 1 and RPC 2 have dimensions, respectively, $50\text{ cm} \times 50\text{ cm}$ and $24\text{ cm} \times 24\text{ cm}$. The readout electrodes were made of 1.5 mm thick G-10 plates with copper foils on two sides. The strip pattern was etched on the plane facing the gas gap. The other plane was connected to the ground thus assuring shielding of the module. The strips were 10 mm wide with 2 mm spacing. The double gap RPCs were assembled in such a way to have strips in both planes in the same direction. Pairs of corresponding strips of the double gap module were connected together at one end, thus forming a common readout structure. Other ends of strips were individually terminated on $1\text{ k}\Omega$.

Each single gap RPC was build with two parallel plates of bakelite separated by 2.2 mm and 2.0 mm in RPC 1 and RPC 2 prototypes, respectively. A fixed distance over the whole surface between two plates — the width of the sensitive gas volume, was assured by the frame inserted along the edges and by spacers forming a matrix of 100 mm pitch. An improved technique of spacer gluing, described in Section 3.1.3, was implemented. Spacers having 10 mm diameter and the external frame were made out of highly resistive bakelite with about $10^{12}\text{ }\Omega\text{cm}$ volume resistivity. Edges exposed to the gas and high electric field were carefully polished.

The RPC 1 was made out of 2 mm thick bakelite plates⁹ clad with thin melamine film having the volume resistivity of about $6 \times 10^{11}\text{ }\Omega\text{cm}$. The surfaces of the plates were smooth and shiny due to the cladding as well as because of using refined tools in the production procedure. It has been demonstrated by others that RPC made out of sufficiently good surface quality material does not need oiling for acceptable operation with low spurious noise [116]. Therefore, inner surfaces of this RPC were not treated with linseed oil. The resistivity of the surface was about $1.5 \times 10^{11}\text{ }\Omega/\square$.

For the construction of the RPC 2 a special bakelite with low specific resistance has been

⁹Courtesy of the INFN group from Bari. This bakelite is denoted as IT-97 in Section 3.1.1.

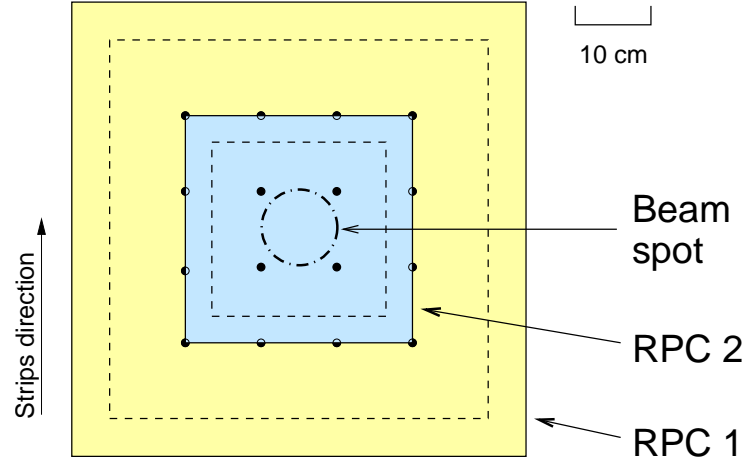


Figure 3.16: Schematic view of RPC 1 and RPC 2 prototypes tested at H2/SPS beam at CERN. Dashed squares represent active areas of the chambers. A grid of spacers is also superimposed.

developed¹⁰ according to the Warsaw CMS Group specification. The volume resistivity of 1.9 mm thick plates was $5 \times 10^8 \Omega\text{cm} \pm 40\%$. The developmental samples were used for electrodes. Because of rather poor quality of surfaces facing the gas volume, the modules of the RPC 2 were coated with linseed oil mixture after the chamber assembly. The benefit from the surface smoothing by linseed oil treatment for the RPC operation is documented in the literature [66]. The modules of the RPC 2, however, were not tested before the treatment. For the surface treatment a standard linseed oil mixture with additive of hardener was used.¹¹ The siccative, containing salts of manganese and lead, accelerates hardening of a thin film of liquid and assures uniform hardening in the volume in presence of air. The resistivity of the surface before treatment was about $2 \times 10^{10} \Omega/\square$.

The RPCs forming IDG structure were positioned in such a way as to have the spacers in the same location in the detection plane, though no special care was taken to achieve precise positioning.

The outer surfaces of RPC units that face the central shielding plate were coated with a graphite solution providing low surface resistivity of about $100 \Omega/\square$. The outer surfaces on the readout side had higher surface resistivity; in case of the RPC 1 module the surface resistivity due to graphite varnish coating was about $200 \text{ k}\Omega/\square$ and in case of the RPC 2 it was set to $25 \text{ k}\Omega/\square$ during the bakelite production by integration of a sheet of carbon paper (the conductivity of the surface might be too high for the efficient pick-up of signals, i.e. signal transparency of $\sim 50\%$ can be expected according to Ref. [62]). Conductive surfaces of each single gap RPC were

¹⁰Produced by IZO-ERG S.A., Gliwice, Poland. This bakelite is denoted as PL-#9 in Section 3.1.1.

¹¹Linseed oil mixture proportions by weight: 49% Linseed oil varnish + 49% Turpentine + 2% Siccative.

Table 3.5: Mechanical and electrical characteristics of RPC 1 and RPC 2 prototypes.

		RPC 1	RPC 2
Dimensions of the active area	[cm ²]	50 × 50	24 × 24
Gas gap width	[mm]	2.2	2.0
Thickness of the bakelite plates	[mm]	2.0	1.9
Volume resistivity of the electrodes	[Ωcm]	6 × 10 ¹¹	5 × 10 ⁸
Inner surface resistivity	[Ω/□]	1.5 × 10 ¹¹	2 × 10 ¹⁰ *)
Outer surface resistivity (readout side)	[kΩ/□]	~ 200	~ 25
Strip width (pitch)	[mm]	10 (12)	10 (12)
Strip length	[mm]	568	302
Linseed oil coating		no	yes

*) Measured before oil coating procedure.

protected with 200 μ m thick PVC foil. The detector may be powered by applying difference of electric potentials to the conductive surfaces. The surfaces facing strip planes were grounded and a negative high voltage was applied to the surfaces facing the central shielding plane. Due to the individual connections of the sub-units of double gap modules to the power supplies, the single gap operation of the detector could be studied. This feature is common for all double gap prototypes discussed in this Chapter.

Mechanical and electrical parameters of the modules are summarized in Tab. 3.5.

3.2.2 Full scale ME 1/1 prototype

The full scale prototype of the RPC module for the CMS detector was constructed in Warsaw, according to specifications given in *The Muon Project Technical Design Report* [28] concerning ME 1/1 muon trigger station. The module has a trapezoidal shape and a radial geometry of readout strips. The trapezoid has the following dimensions: height 96 cm, short base 29 cm and long base 47 cm. The active area covers 10° in φ and 1.65÷2.1 in η -units at the position foreseen for ME 1/1 muon station in the CMS detector. The detector is a stack of two single gap RPCs assembled in the Inverted Double Gap (IDG) structure, as it is shown in Figs. 3.17 A-B. The single gaps act as independent detectors and have their own readout strips on the anode side. The high voltage sides of the sub-units facing each other are separated by insulating 0.3 mm thick self-adhesive PVC foils and by thin aluminium plate on ground potential which serves as electrical screening. Each sub-module has 2 mm gas gap between 2 mm thick resistive electrodes. The bakelite plates used for electrodes were manufactured according to the Warsaw CMS Group specifications¹². Their resistivity was about $4 \times 10^{10} \Omega\text{cm} \pm 30\%$ when measured

¹²Produced by IZO-ERG S.A., Gliwice, Poland. This bakelite is denoted as PL-#15A in Section 3.1.1.

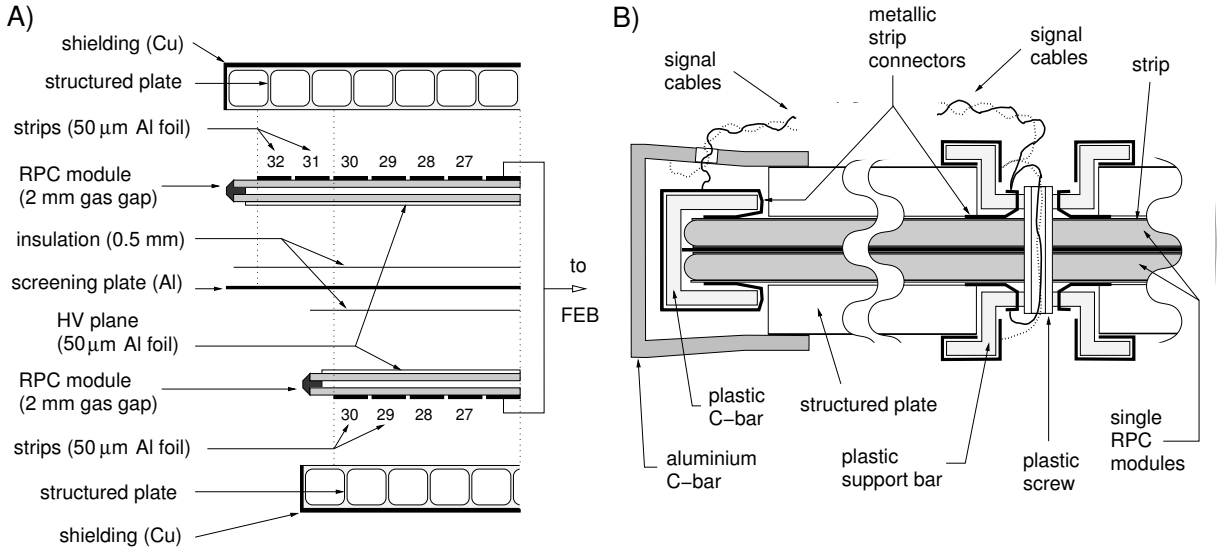


Figure 3.17: An Inverted Double Gap ME1/1 prototype: (A) expanded view along φ ; (B) cross section along detector's symmetry axis showing details of signal extraction from the edge- and the central part of the detector. Figures are not to scale.

at 22° C. An aluminium foil of 50 μm thickness was pressed onto one side of the bakelite plate during production process. The anode surface was then etched to form strips. The advantage of this solution, as compared to a standard graphite coated RPC, is easier distribution of the high voltage on the cathode surface at high avalanche rates.

The grid of spacers glued to both electrode surfaces and the frame placed along the edges assure stability of the distance between electrodes. As in the case of previously described prototypes a technique of reinforced spacer gluing was used. The frames and spacers are made out of highly resistive bakelite of about $10^{12} \Omega\text{cm}$.

Each of two sub-gaps has strips segmented into four η -sections. The strips in both chambers are parallel and aligned. One chamber has smaller active area and only 28 strips in φ direction in each η -section, instead of 32 strips in the second, wider unit. This allows an overlap of modules in φ in the ME1/1 station, what assures that at least one gap is active in the detection ring formed by the modules.¹³ The gap between adjacent strips in φ and η directions is 2 mm. The strip segmentation and pitch width are shown in Fig. 3.18.

In each module there are 16 spacers of 10 mm diameter and 3 special ones located in the middle of the chamber for gap interconnection. The later ones have 16 mm diameter and a central opening of 10 mm diameter, as it is shown in Fig. 3.15. The openings in both chambers are aligned to host the cylindrical plastic screws, which hold firmly two chambers together and

¹³Present RPC geometry differs from the one specified in Ref. [28]. In particular, the requirement of overlapped ME1/1 modules has been abandoned.

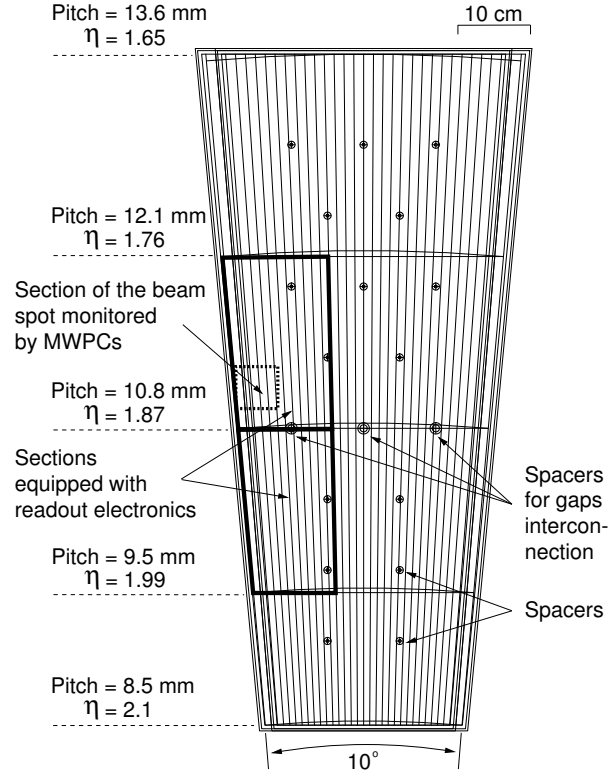


Figure 3.18: Front view of the RPC ME 1/1 full scale prototype. Active area covers 10° in φ and 1.65-2.1 in η .

provide the ducts for signal cables from the central part of a single gap RPC. The way of extracting signals from strips is sketched in Fig 3.17 B. Corresponding strips on the edges of the detector were OR-ed by metallic connectors pressed onto the strips. Similar connectors were used to pick up electrical signals in the central group of strips and the corresponding strips were OR-ed by thin insulated wires going through the openings in special spacers.

The IDG version of ME 1/1 muon station with gap interconnection has smaller area of reduced efficiency over the border between two central η -sections as compared to the design proposed in Ref. [28], which requires dividing of one RPC layer into two separate sub-units in order to extract signals from the central part of the detector.

3.2.3 Medium-size IDG prototype

Another medium-size model RPC was constructed in Warsaw for testing: stability of operation at high rates, new mechanical design and new materials for electrodes. The detector consists of two rectangular sub-modules of 2 mm width of the gas gap assembled in an Inverted Double Gap configuration, in which high voltage planes of the two modules are facing each other. The sensitive gas area of the detector is $81.2 \times 39.2 \text{ cm}^2$.

The electrodes are made of 2 mm thick bakelite plates having the volume resistivity of $1.2 \times$

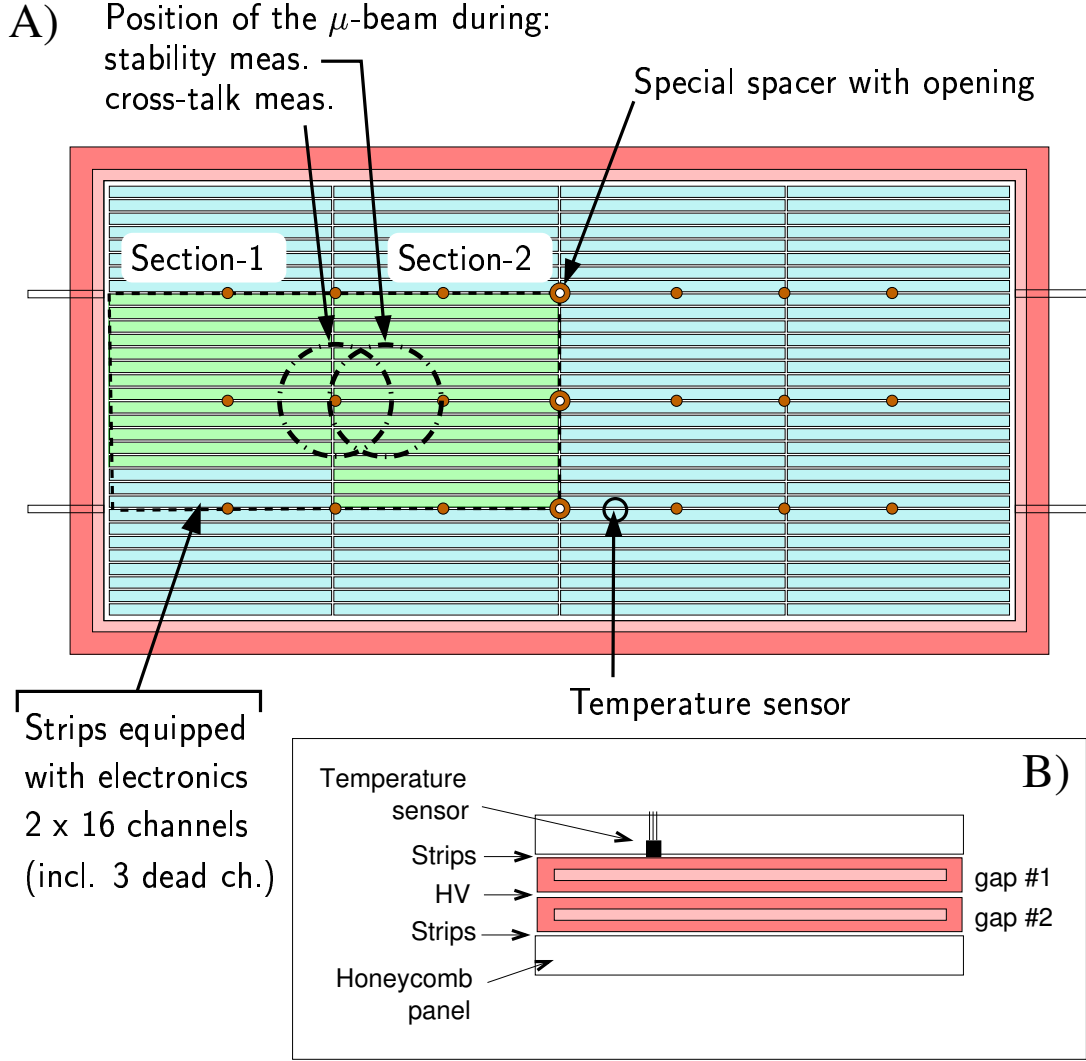


Figure 3.19: An Inverted Double Gap medium-size prototype tested in the GIF at CERN: (A) view in direction of the beam showing strip segmentation, (B) schematic cross section (not to scale).

$10^{10} \Omega\text{cm}$ when measured at 22°C . The high voltage plane and the strip readout plane were formed directly on the outer bakelite surfaces by $50 \mu\text{m}$ thick aluminium foil integrated during the production of the plates.¹⁴ An advantage of this technique over the standard graphite coating was already explained in Section 3.2.2. The anodes were etched to form $10 \times 200 \text{ mm}^2$ strips in four sections of 32 strips. A 2 mm gaps were left between sections and between adjacent strips of each section. The corresponding pairs of strips of single modules were wire-OR-ed and connected to individual readout channels, thus allowing the double gap mode operation. The details of the

¹⁴Produced by IZO-ERG S.A., Gliwice, Poland. The bakelite is denoted as PL-#20 in Section 3.1.1. This developmental laminate has both surfaces covered with metallic foil during the production process, to facilitate resistivity measurements and to protect phenolic core from accidental scratches. A metallic foil has been removed from sides facing the gas before assembling the gaps.

strip segmentation can be seen in Fig. 3.19. As in the case of ME 1/1 prototype, a technique of reinforced spacer gluing was used and the three central spacers had special openings for gap interconnection (see Section 3.1.3).

Two single gap modules were pressed by 10 mm thick rigid honeycomb plates which provided electric shielding and extraction of the signals by means of small metallic springs gently pressed to the surface of the strips. Each channel is grounded via 1 k Ω resistor. The cathode planes were insulated by 0.3 mm thick self-adhesive PVC foils from a thin aluminium plate kept at ground potential which was inserted between two sub-modules.

Initially the chamber was tested in the GIF without oil-coating. For beam tests in 2001 the inner surfaces of two sub-gaps were treated with linseed oil mixture¹⁵ in order to improve their smoothness and to reduce the noise rate. Also one of the gaps was equipped with an electronic temperature sensor of LM 35 type in contact with the bakelite electrode.

3.2.4 Medium-size single gap prototypes

Two identical single gap medium-size rectangular prototypes of $82.6 \times 39.8 \text{ cm}^2$ sensitive gas volume were built in Warsaw in 2002. The main motivation for their construction was demonstration that a single gap RPC has rate capability adequate for CMS needs when operated in saturated avalanche mode. Moreover, such technique can save labour and material costs, and part of the saved costs could be spent on improving quality of the bakelite plates and of the gap assembling technology.

A developmental sample of low resistivity and low roughness bakelite was employed for the electrodes.¹⁶ The resistivity of 2 mm thick plates was $1.0 \times 10^{10} \Omega\text{cm}$ when measured at 27°C. The outer surfaces of the bakelite were cladded with a thin layer of melamine film to achieve lustrous surface. A special care was taken to avoid accidental scratches during all stages of gap assembling. The frames were made out of 2.1 mm thick and 3.5 cm wide glass epoxy bars. To prevent glue leaks to the gas area the rows, 0.1 mm deep and 5 mm wide, were milled on both sides of the bars 5 mm away from the gas edge. All glued areas were dulled and cleaned first. The frame was equipped with 2 gas inlets and 2 gas outlets placed in the corners. Such localization eases removing of a liquid mixture during eventual oil-coating procedure. A grid of 21 polycarbonate spacers having 2 mm height and 10 mm diameter assured constant gas gap thickness. On the contrary to previously discussed prototypes, highly resistive materials for spacers and frames were used this time (i.e. polycarbonate and glass epoxy). The reinforced spacer gluing technique, already discussed in Section 3.1.3, was implemented as well. In the final

¹⁵Linseed oil mixture proportions by volume: 48% Linseed oil varnish + 48% Heptane + 4% Siccative.

¹⁶Produced by Pan-Pla Laminates, Frati Group, Pavia, Italy. The bakelite is denoted as IT-2002 in Section 3.1.1.

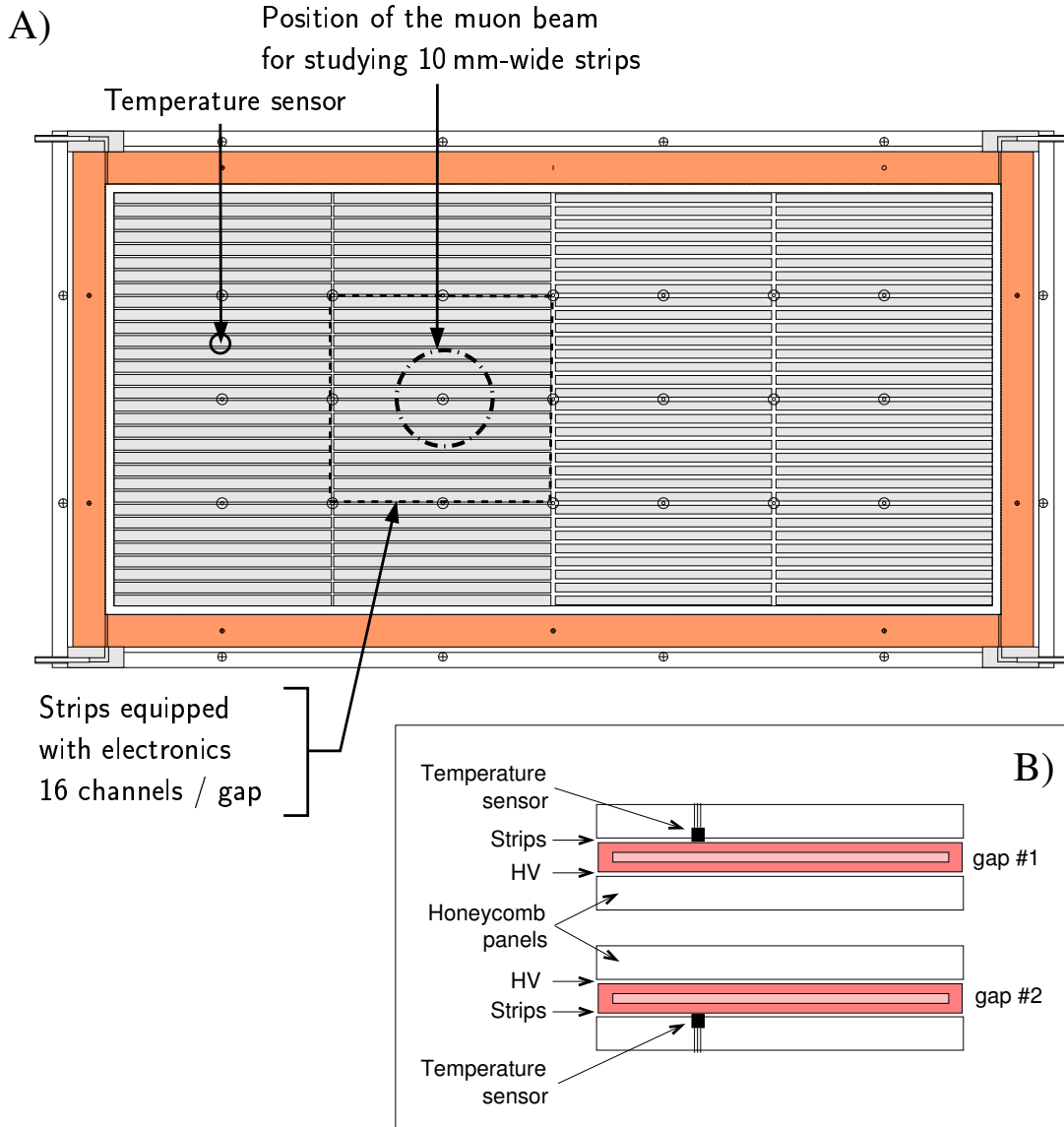


Figure 3.20: Single gap medium-size prototypes tested in the GIF at CERN: (A) view in direction of the beam showing strip sections of 10 mm and 8 mm width of one module, (B) schematic cross section through the modules (not to scale).

stage of closing the gas boxes in a dust-free environment the inner surfaces were cleaned with iso-propanol alcohol, distilled water and a stream of dry air.

On the contrary to previous two prototypes, described in Sections 3.2.2 and 3.1.2, the bakelite lacked factory pre-integrated metallic foils for field shaping electrodes. The external field shaping- and readout electrodes were painted on the bakelite surface with a special conductive silver paint. A sufficient electric contact between the bakelite and the paint has been proved in Section 3.1.1. The outer bakelite surfaces of assembled gaps were dulled and cleaned prior to painting the common cathode plane and the strips. A 0.2 mm thick self-adhesive PVC foil was then glued

onto cathode side to provide electric insulation. The strip segmentation is similar to that of rectangular IDG, namely, four sections of 32 strips each, as it is depicted in Fig. 3.20. Two sections were equipped with $10 \times 200 \text{ mm}^2$ strips and remaining two with $8 \times 200 \text{ mm}^2$ ones. All strips belonging to the same group have 12 mm pitch. The gap between sections is 4 mm, except 2 mm gap between sections having wide strips.

Each gap was firmly pressed between two rigid and flat foam panels of 12 mm thickness. The outer sides of the panels have copper layers for electric shielding of the structure. The panel from readout side is equipped with metallic springs which are in electrical contact with the painted strips for signal extraction. Load resistors of $1 \text{ k}\Omega$ are used to ground the strips. An electronic temperature sensor of LM 35 type has been embedded in the anode foam panel for monitoring of the bakelite temperature in each of two detectors.

Internal surfaces of one RPC module have been treated with the linseed oil mixture¹⁷ and, afterwards, have been dried with clean air for a few days. Therefore, one can study an influence of the oiling procedure on the performance of two RPCs built using same technology and materials.

3.2.5 PPAC with resistive bakelite electrode

In order to study an impact of the avalanche rate on the gas gain a dedicated Proportional Parallel Plate Chamber (PPAC) with the electron collecting electrode made out of resistive material has been constructed in the Detector Laboratory of IEP. The chamber has one resistive anode made out of $10 \text{ cm} \times 10 \text{ cm} \times 2 \text{ mm}$ bakelite plate. A scheme of the detector is shown in Fig. 3.21. The mechanical construction allows one to change the anode plate, thus measurements with different resistive materials are possible. For measurements reported in this thesis, the bakelite plate having volume resistivity of about $4 \times 10^{10} \Omega \text{ cm}$, when measured at 22°C , has been chosen.¹⁸ The same material has been used for construction of the ME 1/1 prototype described in Section 3.2.2. High voltage is applied to the bakelite surface by means of conductive electrode having 80 mm diameter, made of $50 \mu\text{m}$ aluminium foil which was integrated to the bakelite surface during the production process. The cathode plane, made of stainless steel mesh, is placed at 2 mm distance from the bakelite surface and is grounded via $10 \text{ k}\Omega$ resistor. This electrode is used for the pulse read out. Second mesh plane is positioned at 6 mm distance from the readout plane. This region serves as X-ray conversion volume and as drift gap for electrons from primary ionization. A thin mylar window, very well transparent to X-rays, closes the gas volume. The detecting structure allows to amplify the primary electron charges due to X-ray conversion in the drift region. The monitoring of the gas gain can be easily done due to characteristic peak-shaped

¹⁷Linseed oil mixture proportions by volume: 48% Linseed oil varnish + 48% Heptane + 4% Siccative.

¹⁸Produced by IZO-ERG S.A., Gliwice, Poland. This bakelite is denoted as PL-#15A in Section 3.1.1.

charge distribution obtained under irradiation with mono-energetic X-rays.

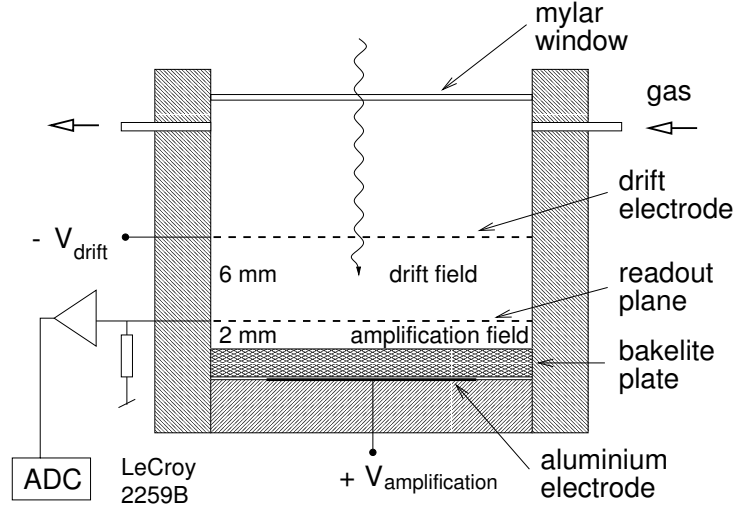


Figure 3.21: Schematic view of the PPAC with a bakelite electrode.

3.3 Testing methods

In order to test RPCs in the working regime similar to that expected at the LHC three approaches have been studied:

- Pulsed high-intensity hadron beams from the SPS accelerator at CERN. This method allows to create avalanche rates up to few kHz/cm² in a single RPC gap during relatively short period of time of particles extraction from the accelerator to the experimental area (about 2.5 seconds). The high rate can be created only locally inside a RPC gap due to limited size of the beam spot (few cm²).
- Pulsed low-intensity muon beam from the SPS accelerator combined with a strong ¹³⁷Cs radioactive source in the Gamma Irradiation Facility (GIF) at CERN. The source can create constant and almost uniform background rate of up to tens of kHz/cm² over the entire surface of medium-size chambers depending on the distance from the source and RPC sensitivity to photons. The muon beam serves for monitoring of the efficiency and time resolution.
- Tests of 10 × 10 cm² RPC-like detectors with an X-ray generator performed in the Detector Laboratory of IEP. This method allows long-term monitoring of the stability of the gas gain of avalanches induced by photons in a PPAC detector with one resistive electrode. The spot of specially focused X-ray beam covers area of about 1 cm².

3.3.1 Pulsed accelerator beams

The hodoscope formed by RPC 1 and RPC 2 was installed in the H2/SPS beam at CERN and tested during the period of September 1997. Experimental set-up is shown in Figs. 3.22 and 3.16. The set of scintillator counters defined the trigger selecting particles traversing $10 \times 10 \text{ cm}^2$ area in the plane of the hodoscope. Two $10 \times 10 \text{ cm}^2$ drift chambers, placed upstream and downstream allow particle tracking. The hadron beam has been defocused in order to illuminate a largest possible area of the hodoscope, though, the majority of particles from hadron beam crossed area of about $2 \times 2 \text{ cm}^2$, while the muon beam of low intensity illuminated the entire investigated area of $10 \times 10 \text{ cm}^2$. The high rate capability studies of the IDG RPCs were performed with the hadron beam. The SPS beam has 2.5 s duration of particles extraction cycle with a period of 14 s.

During the beam test 14 central strips of each IDG RPC module were equipped with front-end preamplifiers¹⁹ having 10 MHz bandwidth and charge sensitivity about 1.5 mV/fC. The outputs of the amplifiers were fed to discriminators via 10 m long coaxial cables. The amplified signals were discriminated at 30 mV. The width of discriminated pulses was set to 50 ns. Discriminated signals converted to differential ECL standard were connected to the multi-hit time-to-digital converter (TDC) module in CAMAC (LeCroy 2277 of 1 ns time resolution operated in a common start mode with $1 \mu\text{s}$ time range). Thus the arrival time of leading edges of avalanche pulses could be recorded during $1 \mu\text{s}$ after the trigger from the set of scintillator counters.

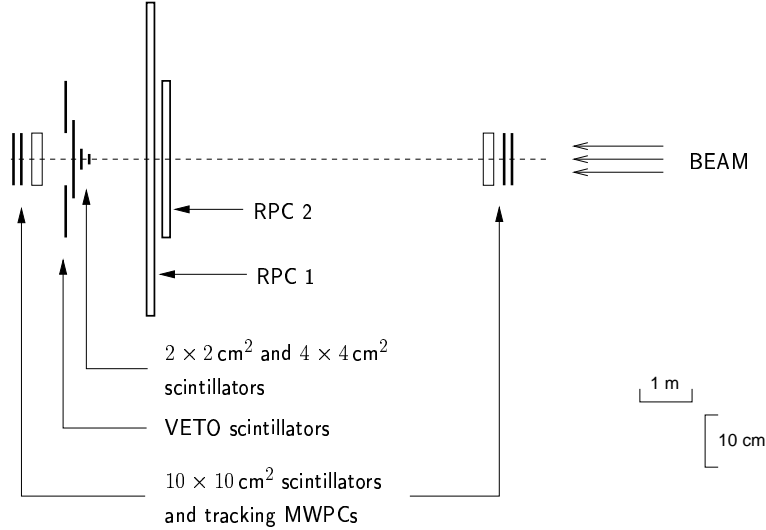


Figure 3.22: Schematic diagram of the RPC test set-up at H2/SPS beam at CERN.

¹⁹Courtesy of the INFN group from Bari. Detailed description of the amplifiers can be found in Ref. [116].

3.3.2 Gamma Irradiation Facility

The Gamma Irradiation Facility (GIF) at CERN, schematically shown in Fig. 3.23, offers the possibility to study a detector performance in a high background environment like the one expected at the LHC. The set-up with ^{137}Cs source emitting 662 keV gamma rays of 15 Ci activity²⁰ located at the X5/SPS beam line allowed one to measure efficiency and timing for minimum ionizing particles for the detector uniformly and continuously irradiated with controlled radiation rate. The lead container collimates photons inside a pyramid of $6 \times 6 \text{ m}^2$ base at 5 m distance from the source. Background rates may be varied by means of a set of remotely controlled lead filters placed in front of the source. The filters and the collimator are designed in such a way to achieve almost uniform photon intensity in horizontal- and in vertical directions for a given distance from the source plane. The energy spectrum of the photons illuminating tested detectors

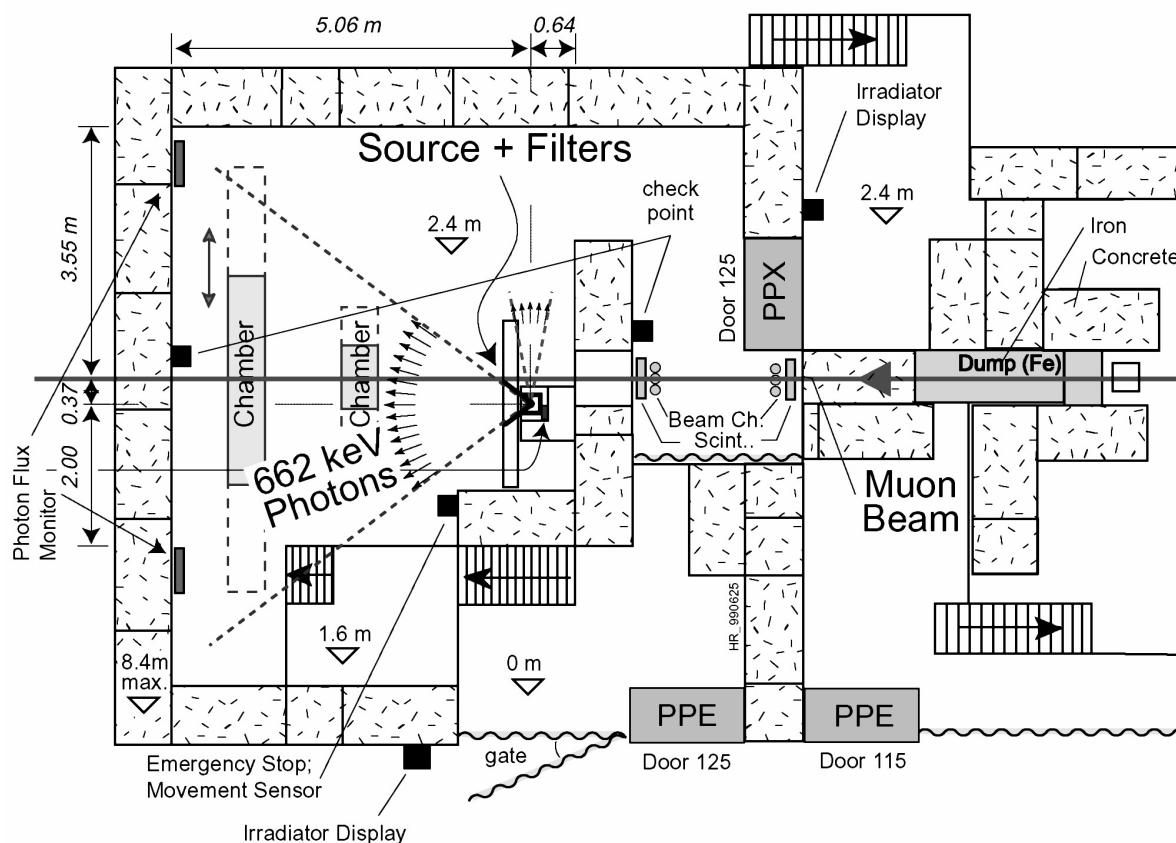


Figure 3.23: Layout of the Gamma Irradiation Facility X5/SPS test beam zone at CERN [117]. Photons from the radioactive source produce a sustained high rate of random hits in tested detectors. Concrete walls protect from radiation.

²⁰Source activity as of March 1997 [117].

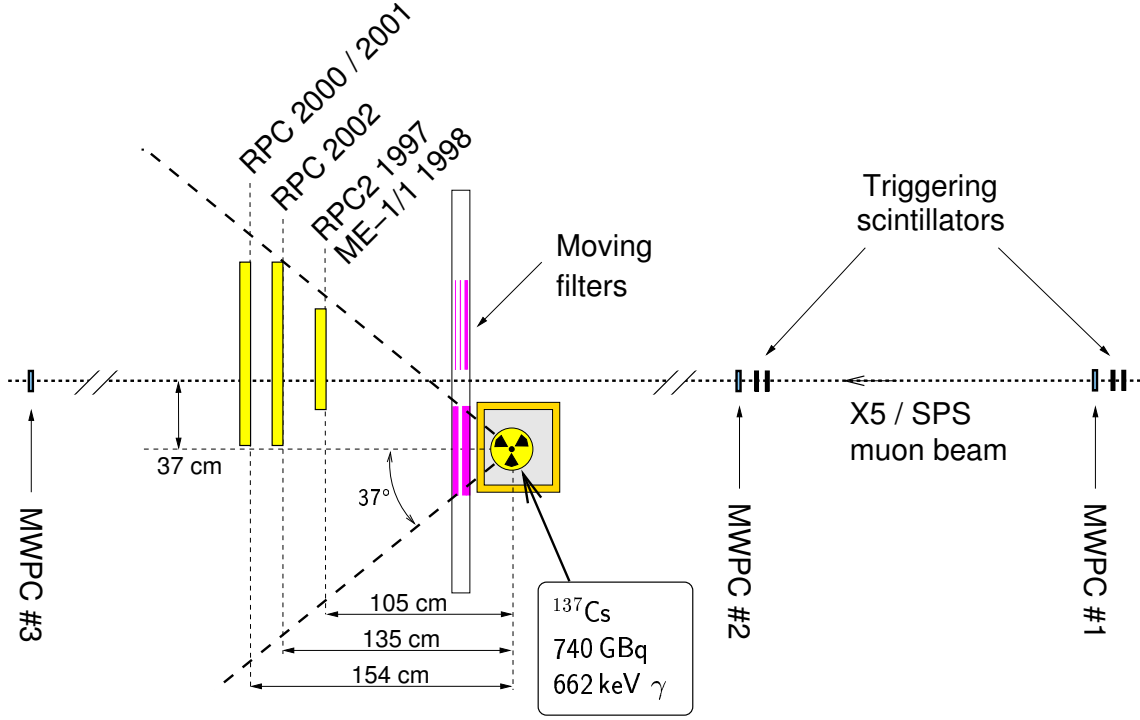


Figure 3.24: Schematic layout of a test beam set-up in the GIF zone used between 1997 and 2002. Positions of tested RPC prototypes are superimposed.

depends on the absorption factor set by lead filters configuration. Besides of the main peak at $E_\gamma = 662 \text{ keV}$ also photons of lower energies from Compton scattering and fluorescence of the lead contribute to the spectrum. For example, at 155 cm in front of the source set to its full intensity the photon flux amounts to $1.4 \times 10^6 \text{ cm}^{-2} \text{ s}^{-1}$ (from which 56% are direct photons of $E_\gamma = 662 \text{ keV}$ and 44% are scattered photons of $E_\gamma < 662 \text{ keV}$ coming from the concrete floor and walls) [117]. However, the attenuation factor (or the nominal source intensity) referred in this work concerns only 662 keV photons.

The axis of the muon beam is located: 37 cm and 65 cm from the source in horizontal- and in vertical directions, respectively, and 126 cm above the floor level. The beam consists of 120 GeV/c muons and has intensity up to 100 Hz/cm^2 . The size and the time structure of the muon beam are similar as in the case of H2/SPS measurements. A trigger for the data acquisition system (DAQ) is provided by a coincidence of two $6 \times 6 \text{ cm}^2$ scintillators. The SPS beam is monitored by three MWPCs of $10 \times 10 \text{ cm}^2$ sensitive area, though, only two of them placed upstream the beam have been used in the analysis. More detailed information about the GIF can be found in Ref. [117].

In the cases of double gap RPCs avalanches due to background radiation in individual gaps

are uncorrelated because electrons from Compton scattering are not energetic enough at this energy to penetrate materials separating two gaps²¹. Hence, a half of the rate measured by a double gap chamber is an approximate measure of minimum ionizing particles rate inducing the same current in the both gaps.

In total five RPC detectors developed and constructed by the CMS Warsaw Group have been tested in the GIF during period of 1997-2002: three IDG prototypes and two single gap ones. Since all chambers were operated in the avalanche mode, the charge-sensitive fast amplifiers²² were employed for the strip readout. The logical signals from front-end boards were read out with multi-hit TDCs of 0.5 ns and 1 ns resolution for LeCroy models 3377 and 2277, respectively. The TDCs operated in a common stop mode provide information about signal arrival time of the last 16 hits from each channel with respect to the trigger pulse from a coincidence of beam scintillators which was delayed with a programmable delay box by 1.5 μ s. In Tab. 3.6 main characteristics of the data acquisition system are summarized.

Details about gas mixtures used, position of the chambers and availability of the muon beam during individual test periods in the GIF are given in Tab. 3.7.

The distance of tested chambers from the source plane varied from one beam test to another between 105 cm and 155 cm. Positions of the detectors are schematically shown in Fig. 3.24. All distances were measured between the the foam or honeycomb panel closest to the source and the vertical source plane. The distance between middle planes of the individual gas layers was about 8 mm, except single gap prototypes tested in 2002 when it was 60 mm.

During 1997-2002 tests several Tetrafluoroethane-based gas mixtures have been studied. It was reported by Camarri et al. [83] that small addition of strongly electronegative SF₆ gas to the mixture of TFE/Isobutane improves RPC performances by widening the efficiency plateau due to streamer suppression. Therefore, since 1998 test beams a small percentage of SF₆ freon has been added to the base TFE/Isobutane gas mixture. All gases were provided by CERN; no special filters were installed to remove possible impurities in the gas mixture. The working mixture was supplied through copper pipes to the GIF zone, where it was distributed to the chambers via plastic Rilsan pipes. In the cases of double gap modules tested sub-gaps were connected in series to the gas line, while single gap ones had independent gas supply. The gas flew at speed of 1 \div 2 dm³/h, which was lower than typical flow rates foreseen in the CMS RPC system of about 4 \div 12 dm³/h [119].

The front-end electronics used in the tests differed from one test to another since it had been constantly developed. Because of the limited number of available front-end boards (FEBs) and

²¹For instance, the probability of penetrating 2 mm thick bakelite plate by electrons of 662 keV kinetic energy is only 0.6% according to GEANT simulations [118].

²²Courtesy of the INFN-Bari group.

the speed of the DAQ system only part of the strips have been read out.

During tests in 1997 the RPC 2 prototype was equipped with hybrid charge amplifiers of 1.5 mV/fC sensitivity — the same as during H2/SPS tests [116]. The standard leading edge discriminators were used with threshold set to 50 mV (33 fC) followed by NIM-ECL converters. Only 14 central strips out of 19 were connected to the amplifiers.

In the next years special front-end chips produced by INFN-Bari group were used [27, 28, 120]. Those chips contain integrated: charge sensitive amplifiers, shapers and discriminators providing LVDS output signals (a standard chosen for interconnecting RPC FEBs with the Pattern Comparator Trigger electronics in the CMS detector). During test beams LVDS signals had to be translated to ECL standard due to long distance between experimental area and the counting room where readout TDCs were situated.

For tests of the ME 1/1 prototype two central groups of 12 consecutive strips corresponding to the tested area of the detector were equipped with FEB electronics. A single readout board had two 6-channel front-end chips equipped with charge amplifiers of 1.6 mV/fC sensitivity.

In the case of rectangular IDG prototype two horizontal 16-strip sections were read out as it is shown in Fig. 3.19. Each FEB had two 8-channel front-end chips with charge amplifiers of 2 mV/fC sensitivity. The performance of a model IDG detector was tested in several positions of the beam spot on the RPC surface and for different electronics thresholds. Tests of single- and double gap operation were also performed.

For the latest single gap prototypes the same electronic boards have been used as in the case of 2000-2001 tests. For preliminary results reported in this thesis only one section of strips was equipped with the FEB in each tested gap as it is shown in Fig. 3.20. The geometric regions covered by strips equipped with readout electronics and illuminated with the muon beam were aligned.

There are experimental indications that the chamber performance at given applied voltage depends on ambient temperature and pressure. The dark current of RPC gaps, the atmospheric pressure, temperature and humidity of the air were monitored during the tests. From 2001, in addition to a set of sensors installed in the experimental area, a dedicated temperature sensors have been located in contact with external bakelite surface for detector temperature monitoring as it is shown in Figs. 3.19 and 3.20.

Table 3.6: Parameters of the data acquisition system used in the GIF during 1997-2002.

Detector	IDG RPC 2	IDG ME 1/1	Model rectangular IDG		2 model rectangular single gaps
Year	1997	1998	2000	2001	2002
Amplifiers	Single channel hybrids of 1.5 mV/fC sensitivity [116]	6-ch. integrated chip of 1.6 mV/fC sensitivity [28, 120]	8-ch. integrated chip of 2 mV/fC sensitivity [27]		
Signal digitization	Discriminators followed by NIM-to-ECL converters; output signals of fixed 50 ns length	Discriminator- and LVDS monostable circuits inside the chip followed by external LVDS-to-ECL converters; output signals of fixed 100 ns length			
Threshold(s)	50 mV (33 fC)	128 mV (80 fC)	150, 200 mV (75, 100 fC)	200 mV (100 fC)	200 mV (100 fC)
Readout TDC	LeCroy 2277		LeCroy 3377		
TDC resolution	1 ns		0.5 ns		
TDC range	64 μ s		32 μ s		

Table 3.7: Conductivity of the electrodes, gas mixtures and RPC positions during 1997-2002 test beams in the GIF.

Detector	IDG RPC 2	IDG ME 1/1	Model rectangular IDG		2 model rectangular single gaps
Year	1997	1998	2000	2001	2002
Bakelite volume resistivity [Ωcm] (Temperature, meas. technique)	5×10^8 (29°C, c. rubber)	4×10^{10} (22°C, c. rubber)	1.2×10^{10} (22°C, Al foil)		1.0×10^{10} (27°C, s. paint)
Distance from the source plane	105 cm	105 cm	154 cm	154 cm	135 cm
Gas mixture composition TFE/i-C ₄ H ₁₀ /SF ₆	<i>90% TFE-mixture</i> 90.0 / 10.0 / 0.0	<i>1.5% SF₆-mixture</i> 95.0 / 3.5 / 1.5	<i>1.5% SF₆-mixture</i> 95.0 / 3.5 / 1.5	Period 1 <i>97% TFE-mixture</i> 96.8 / 3.2 / 0.0	Period 1 <i>0.5% SF₆-mixture</i> 96.0 / 3.5 / 0.5
				Period 2 <i>0.5% SF₆-mixture</i> 96.3 / 3.2 / 0.5	Period 2 <i>0.2% SF₆-mixture</i> 96.3 / 3.5 / 0.2
					Period 3 <i>97% TFE-mixture</i> 96.5 / 3.5 / 0.0
					Period 4 <i>0.7% SF₆-mixture</i> 95.8 / 3.5 / 0.7
Availability of the muon beam	Yes	Yes	Yes	Period 1 only	Yes

3.3.3 Laboratory tests with X-ray tube

The experimental set-up shown in Fig. 3.25 has been used to study: stability of the gas gain, pulse-height spectra and capability of detecting high particle fluxes by a dedicated PPAC detector made out of three parallel electrodes: a bakelite electrode and two metallic mesh electrodes. The construction of this model detector is described in Section 3.2.5. The PPAC was operated in proportional mode under various intensities of X-rays over long period of time. The detector performance, when irradiated with an intense radiation flux, and possible effects of variation of the bakelite electrode conductivity on a medium-term stability of operation can be studied. The signal from the middle cathode mesh was read out via chain of amplifiers: a fast charge-sensitive amplifier followed by a linear amplifier of regulated gain. The peak-sensing LeCroy 2259B ADC of 1 mV resolution was used for the final pulse-height measurement. Thus one can investigate the standard RPC operation using pulse-height analysis.

The detector was operated in the gas flow mode. A single wire proportional counter, installed in the same gas line, served as stability monitor of the gas mixture, since the gas gain depends on ambient temperature and pressure and on the gas composition fluctuations. Pulse-height of low intensity 5.9 keV X-rays from ^{55}Fe source was used as a reference. Additional proportional wire counter, with thin beryllium window and with gas volume sealed, served to monitor the stability of the radiation flux from the X-ray tube with a copper target emitting 8 keV photons. The area of the beam spot in the PPAC drift plane was 0.88 cm^2 .

Intensity of the incident X-ray flux was controlled in two ways: by setting the current of an X-ray tube and by changing the amount of absorber²³ in a bottom collimator placed in front of the beryllium window of the X-ray tube shown in Fig. 3.25. The counting rate in the flux monitoring detector was kept constant at a safe level allowing full detection efficiency due to high attenuation of the incoming X-ray beam in the upper collimator shown in Fig. 3.25.

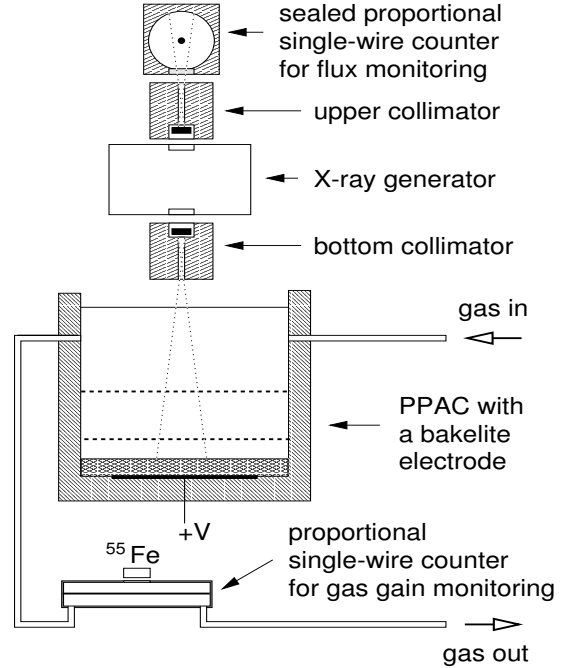


Figure 3.25: Experimental set-up for monitoring of the gas gain in the PPAC detector irradiated with X-rays.

²³For attenuation of an X-ray beam copper disks of 0.1 mm thickness and of 1 cm diameter were used. Single disk reduced counting rate in the PPAC detector by a factor of 3.

The measurements were performed with Argon-based gas mixtures. This choice was motivated by a characteristic peak-shaped pulse-height distribution when the detector is irradiated with mono-energetic X-rays which makes it easy to monitor the gas gain variations.

3.4 Method of data analysis from test beams

The method of data analysis from H2/SPS and X5/SPS test beams is a typical one used in testing of the ionizing particle detectors. Ionizing particles from the SPS accelerator triggered the DAQ system. The trigger pulse was provided by a set of fast detectors, namely, a scintillator counters hodoscope. This signal was used as a reference time instant for timing and efficiency measurements of tested chambers. The arrival times of leading edges of logical signals (*hits*) from RPC strips were recorded using time-to-digital converter with multi-hit capability. A schematic snapshot of a single event is depicted in Fig. 3.26 A in case of beam tests performed in the GIF. In the example shown, hit arrival times from a group of 16 consecutive strips are marked with small vertical bars.

Two operation modes of the DAQ system were used:

1. *Common start mode* during H2/SPS hadron test beam:

A history of RPC hits during $1\mu\text{s}$ after the trigger pulse was recorded.²⁴ Since no intense and continuous background was present an information about hits coming long before the beam was not necessary. Such measurements allowed efficiency, timing and positional resolution measurements only. The rate of incoming particles was obtained from scintillator counters of different sizes placed before tested detectors by means of CAMAC scalers which were reset before each spill.

2. *Common stop mode* during all tests in the GIF:

A history of RPC hits during tens of microseconds (i.e. $32\mu\text{s}$ or $64\mu\text{s}$ depending on TDC module type) before the trigger pulse delayed by about $1.5\mu\text{s}$.²⁵ Due to severe background hits from photon Compton scattering the hits coming before the beam carry important information about the rate of avalanches induced by photons.

Due to nature of multi-hit TDC modules used, only limited number of subsequent hits from individual readout channel (strip) could be stored. In the case of *common stop mode* up to 16 last signals before delayed trigger pulse (*COMMON STOP signal*) were recorded. On the contrary, in *common start mode* up to 16 first hits after the trigger pulse provided by scintillators hodoscope

²⁴A sufficient delay with respect to the trigger pulse from scintillators hodoscope was provided by means of a delay line formed from long signal cables between RPC electronics and the control room.

²⁵The trigger pulse from scintillators hodoscope was specially delayed with respect to signals from RPCs by a dedicated programmable delay box.

were stored for each channel. The time elapsed from the beginning of the particle extraction cycle from the SPS accelerator (*spill*) to the experimental area, where all tested detectors were situated, was also recorded for each event. The duration of the spill and the SPS beam cycle differed from one beam test to another, however, their typical values were 2.5 s and 14 s, respectively. For fixed operating conditions, such as: gas mixture, radiation environment, and RPC high voltage working point, about 2×10^4 events were collected. Such data set is considered as an individual *run*.

The method of efficiency calculation for each run is common for H2/SPS and GIF measurements, namely, only RPC signal arrival times falling into a fixed *beam time window* with respect to the trigger pulse were accepted for the analysis (see Fig. 3.26 A). For each run the position of the window was chosen in such a way to contain majority of signals from RPC strips caused by muons/hadrons which simultaneously triggered scintillators hodoscope. Several widths of the time window were studied, ranging from 10 ns to 100 ns. In order to classify an event as a good one a search for a hit inside the beam time window was performed. The earliest signal found within this window was taken as the one corresponding to the chamber's response (i.e. to the muon/hadron track). The RPC efficiency is then defined as the ratio of events having hits falling within the beam time window to the total number of triggers recorded. Therefore, the chamber's efficiency and timing properties studies come from beam tracks.

A single avalanche can induce signals above a fixed electronics threshold on more than one strip. The number of strips responded for a single minimum ionizing particle from hadron- or muon accelerator beam is called *strip cluster size* or *strip multiplicity*. It was calculated in two ways for analyses presented in this thesis, namely:

- The number of strips, geometrically covered by the beam and by the triggering counters, which have hits inside a fixed beam time window. In some analysis by others only adjacent strips having signals are taken into account, what shifts an average cluster size of a given run toward smaller values [121], though, in this work it was not required.
- The same algorithm as above, except that only hits after fixed time from the first one inside a fixed beam time window are accepted [116]. Usually 10 ns or 20 ns windows are used.

In order to estimate the real rate of avalanches induced by gamma rays for a given run during measurements in the GIF, the hits were grouped into *clusters*. The following cluster finding algorithm was used: a fixed time window (20 μ s-wide) with respect to the trigger pulse was opened, but before the beam time window dedicated to muon efficiency measurements. Then all hits were ordered according to their arrival time for each strip section separately. For each pair of neighbouring hits within single section the search for a time interval of at least 200 ns was performed, which separated the clusters. The idea of cluster finding is sketched in Fig. 3.26 B. The

first hit of a cluster defined the avalanche arrival time. Two methods of cluster rate calculation were used, referred as *direct counting method* and *slope method* in this thesis. The first method was a simple counting of the number of clusters in a fixed time window. The second one assumed that the delay between subsequent non-correlated clusters should follow exponential behavior. From the slope of such distribution the corrected cluster rate can be calculated which is close to the real rate of avalanches for the high voltages corresponding to the efficiency plateau. Because the cluster finding algorithm does not distinguish between clusters closer than 200 ns in time, the direct counting method may result in the rate underestimation by a factor up to 2 with respect to the corrected method at the highest rates. An example of the delay distribution between subsequent clusters is depicted in Fig. 3.27 for medium-size prototype tested in the GIF in 2001 filled with gas mixture denoted as $0.5\%-SF_6$ in Tab. 3.7. Empty histogram bins near zero result from required minimal time interval between individual clusters.

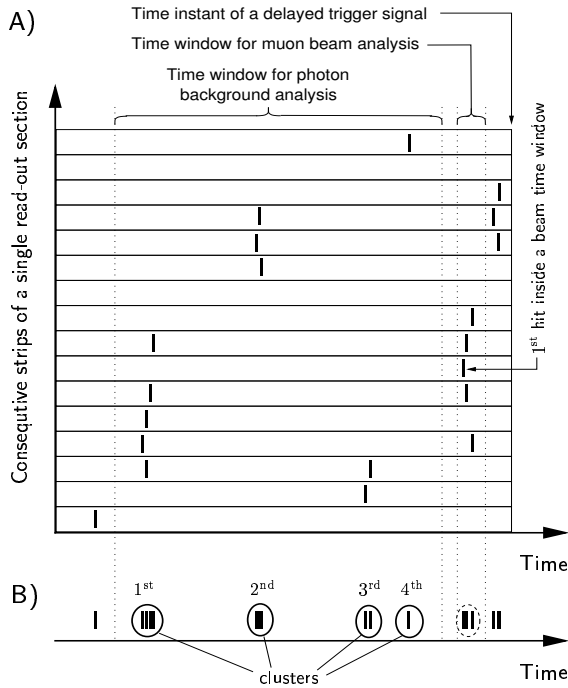


Figure 3.26: Idea of efficiency- and background rate measurement from the GIF data. This event, classified as good one, has muon strip multiplicity equal to 5 (A) and 4 clusters due to photons in the time window studied (B).

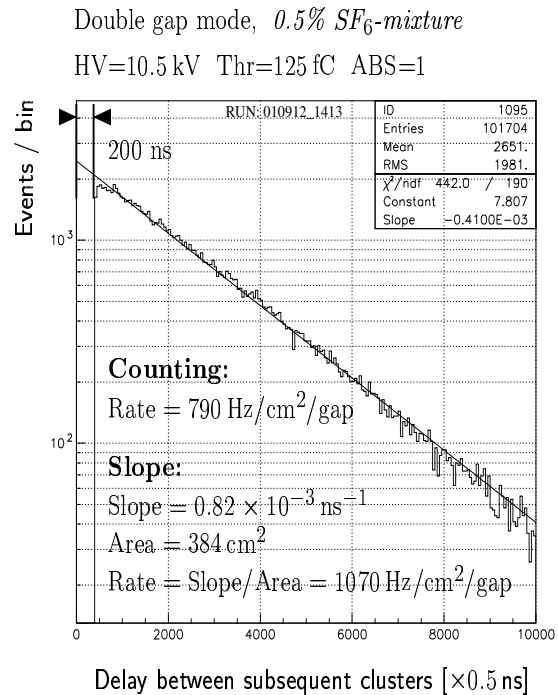


Figure 3.27: Example of cluster-to-cluster delay distribution for a run with source fully opened for medium-size prototype tested in the GIF in 2001. The cluster rates obtained with direct- and slope methods are shown.

Chapter 4

Experimental results

In this Chapter the results on accelerator beam tests and laboratory measurements of several RPC prototypes and model detectors, performed by the Warsaw CMS Group during period of 1997-2002, are discussed. The preliminary analyses of the data have been published in Refs. [122–128] and presented during several CMS collaboration meetings [101, 112, 129].

The main aim of the first test using pulsed hadron beams from CERN’s SPS accelerator was to demonstrate usefulness of a double gap RPC structure, made out of developmental low resistivity bakelite plates, at high particle rates affecting relatively small detector’s area. Then, in order to simulate hostile radiation environment foreseen at the LHC, one small-size and four medium-size RPC prototypes were tested in the Gamma Irradiation Facility at CERN under uniform and continuous flux of gamma rays inducing hit rates of the order of 1 kHz/cm^2 in a single RPC gas layer. The obtained results address various vital aspects of RPC operation at high counting rates, such as: efficiency, timing, strip multiplicity, intrinsic noise rate and stability of the detector performance with time. The role of gas mixture composition, with emphasis on small addition of electronegative SF_6 gas, was studied. Beam tests also served for experimental verification of several new concepts in RPC technique, for instance: Inverted Double Gap RPC, reinforced spacers, aluminium coated external surfaces of the bakelite electrodes.

Finally, possible ageing phenomena related to RPCs working at high particle rates were studied using dedicated Parallel Plate Avalanche Chamber with the bakelite anode and operated under intense photon flux from the X-ray generator.

4.1 Pulsed beam results

Tests in the SPS beam of RPC 1 and RPC 2 prototypes were performed with chambers filled with binary gas mixture of TFE/Isobutane (90/10) and operated in avalanche mode. The axis of the beam coincided with the center of the grid of spacers as it is schematically shown in Fig. 3.16.

Measurements using pulsed beams characterized by periodical extraction of 14 s and 2.5 s

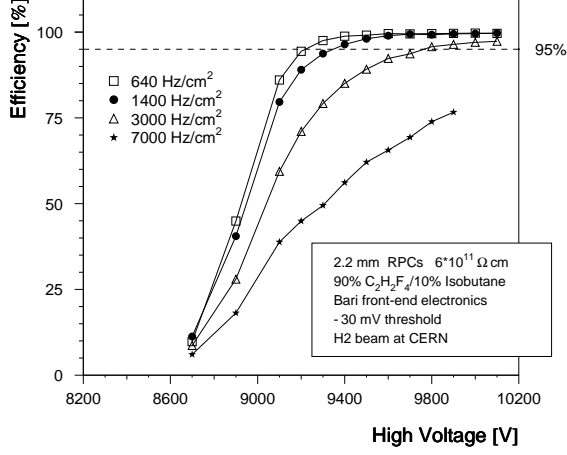


Figure 4.1: Detection efficiency averaged over 2.5 s beam extraction cycle for high resistivity RPC 1 module as a function of the supply voltage for several particle fluxes. The particle flux quoted is an average over the time of a spill. Signal discrimination threshold was 30 mV in all measurements.

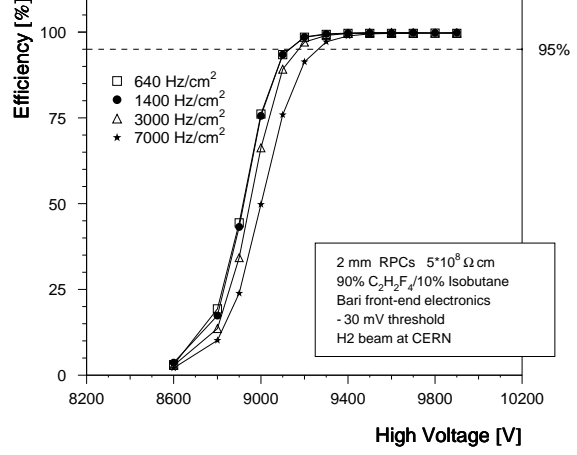


Figure 4.2: Detection efficiency averaged over 2.5 s beam extraction cycle for low resistivity RPC 2 module as a function of the supply voltage for several particle fluxes. The particle flux quoted is an average over the time of a spill. Signal discrimination threshold was 30 mV in all measurements.

spill, reveal an advantage of the low resistivity RPC. In Fig. 4.2 the detection efficiency of the RPC2 module is shown as a function of the applied voltage for different particle rates. The efficiency is averaged over 2.5 s of the spill duration. The RPC 2 exhibits full efficiency with common plateau width of 500 V up to the highest rate applied. An increase by 100 V in the operation voltage range observed at 7 kHz/cm² rate, remains small with respect to the plateau width. The shift may be partially due to the variation of the ambient temperature during one week period of tests. Rate independence of the slope of the efficiency curve hints that pulse-height distribution, not measured during the test, has peaked shape which is preserved in this range of rates.

The rate limitation clearly appears in Fig. 4.1 in case of the high resistivity RPC1 module. The avalanche current reduces dynamically the electric field in the gas gap due to high resistivity of the electrodes. Already at 3 kHz/cm² the 95 % level of efficiency is barely achieved at the highest voltages.

The results on the efficiency presented above are averaged over spill duration of 2.5 s. However, RPC efficiency and timing as a function of the irradiation time during the beam spill have been also studied. In measurements shown in Figs. 4.3 and 4.4 for RPC1 and RPC2 modules, respectively, the working high voltages have been chosen 300 V above the knee of the efficiency

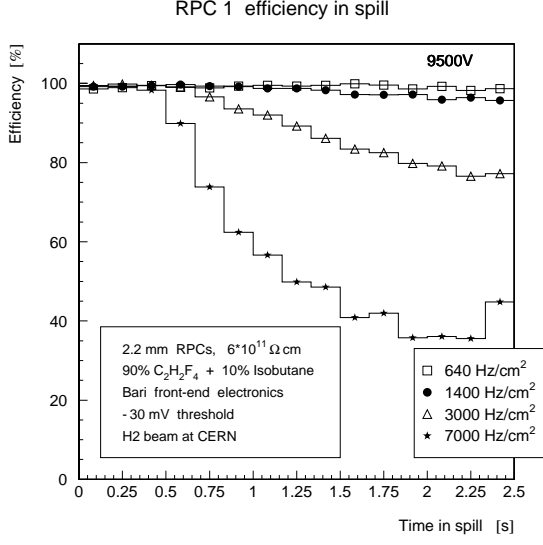


Figure 4.3: Detection efficiency of high resistivity prototype RPC 1 as a function of time during the extraction cycle of the beam for various fluxes.

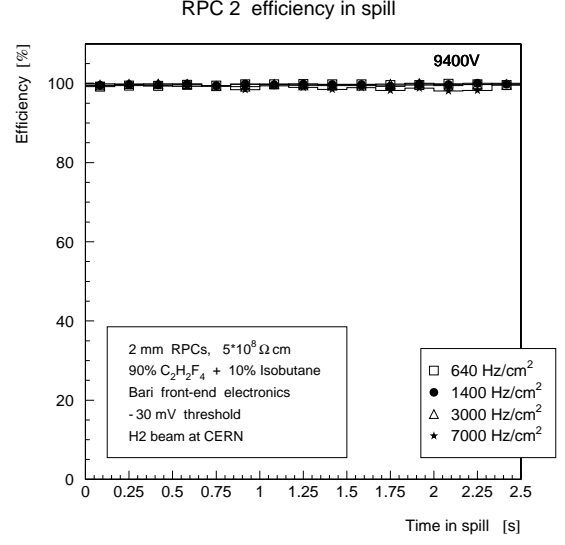


Figure 4.4: Detection efficiency of low resistivity prototype RPC 2 as a function of time during the extraction cycle of the beam for various fluxes.

plateau (i.e. 95 %) at 640 Hz/cm^2 . It can be seen that the detection efficiency of the RPC 1 prototype decreases dramatically with the irradiation time during the spill for the highest rates. In the case of the RPC 2 detector the full efficiency is maintained during the beam spill for all intensities studied. It is important to point out that during first 500 ms of spill the high resistivity RPC 1 operates with full efficiency, thus measurements with periodic irradiation of few hundred milliseconds duration may give misleading results on the efficiency (see for example Ref. [86]). It is clear that continuous irradiation periods much longer than seconds are necessary for correct evaluation of the RPC operation. One has to mention that the intensity of hadron beam was increasing during the extraction period and was reaching stability at the level by a factor up to 1.5 higher than the average after about 0.7 s.

The avalanche arrival time, measured with respect to the beam counters, as a function of the time in the spill is shown in Figs. 4.5 and 4.6 for high- and low resistivity RPCs, respectively. The delay of the avalanche increases with the rate, which can be explained by a dynamic drop of the amplification field in the gap. In the case of the RPC 2 the shift is of the order of 2 ns between 640 Hz/cm^2 and 7000 Hz/cm^2 . The shift is much more pronounced for the RPC 1; even at moderate rate of 640 Hz/cm^2 the RPC 1 begins to loose its time properties 1.5 s after the beginning of the irradiation. The time walk shows tendency to saturate when an equilibrium is reached; one can estimate that the maximum time walk related to variations of the radiation rate is about 2 ns and 9 ns for, respectively, low- and high resistivity RPCs operated at the

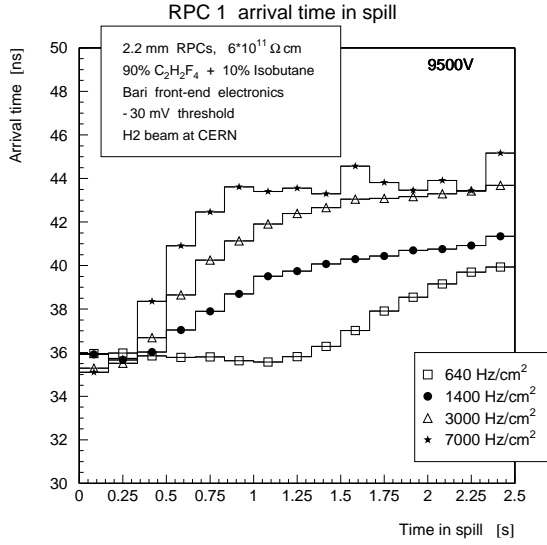


Figure 4.5: Signal arrival time measured for RPC 1, with respect to the trigger counters, as a function of time during the extraction cycle of the beam for various fluxes.

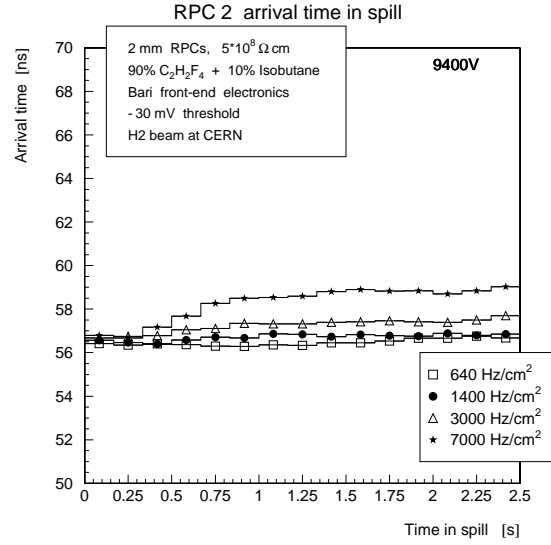


Figure 4.6: Signal arrival time measured for RPC 2, with respect to the trigger counters, as a function of time during the extraction cycle of the beam for various fluxes.

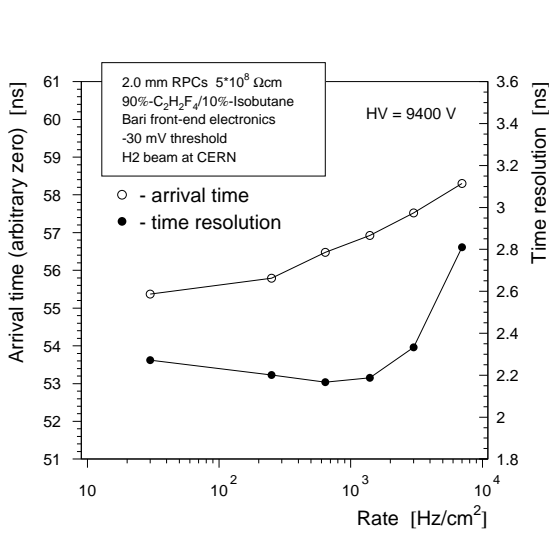


Figure 4.7: Signal arrival time and time resolution of the low resistivity RPC 2 as a function of the particle flux. The module operated at the high voltage 200 V above the knee of the efficiency plateau for medium fluxes.

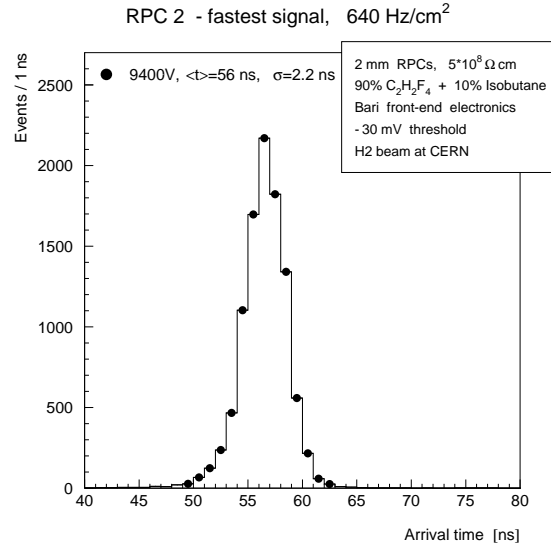


Figure 4.8: Distribution of the avalanche arrival time with respect to the trigger defined by the beam counters for radiation flux of 640 Hz/cm². The value of the voltage applied to the RPC 2 module was 200 V above the knee of the efficiency plateau.

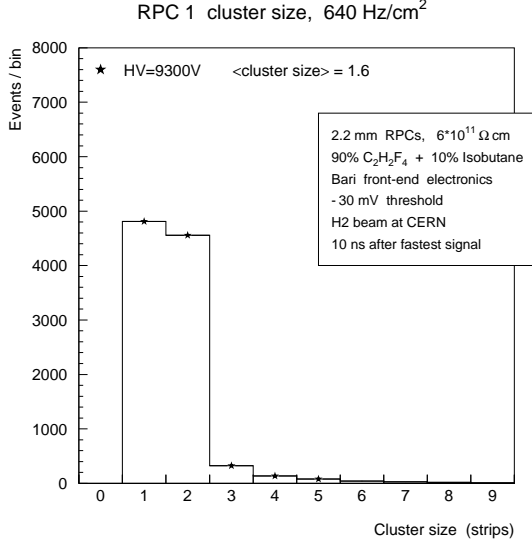


Figure 4.9: Cluster size measured in RPC 1 at the particle flux of 640 Hz/cm^2 . The cluster is defined by signals arriving within 10 ns after the fastest one.

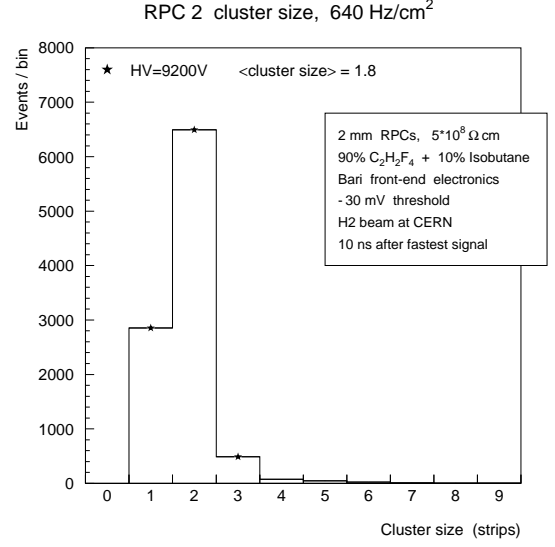


Figure 4.10: Cluster size measured in RPC 2 at the particle flux of 640 Hz/cm^2 . The cluster is defined by signals arriving within 10 ns after the fastest one.

given working point. During first few hundred milliseconds of the irradiation both detectors exhibit time walk smaller than 0.5 ns. The phenomenon of the rate dependence of the time walk, observed for the high resistivity RPC, is a severe limitation when the radiation intensity varies either with time or within area of the detector.

Timing characteristics of the RPC 2 show very small dependence on rate as can be seen from Fig. 4.7. Time resolution as a function of rate remains at the level of 2.2 ns up to rates as high as 3000 Hz/cm^2 ; the width of the time distribution increases by about 0.5 ns at 7000 Hz/cm^2 . However, these results are biased by the limited time resolution of the TDC module used (1 ns) and by unknown time spread introduced by the scintillators hodoscope used for triggering purpose. The full width at the base (i.e. at the level of 2%) of the time distribution is about 13 ns as can be seen from Fig. 4.8 for the rate of 640 Hz/cm^2 . An increase in the charge amplification results in fastest arrival time of the avalanches with more narrow time spread.

The cluster multiplicity has been measured taking into account strips fired within 10 ns after the fastest one. The results for RPC 1 and RPC 2 chambers are depicted in Figs. 4.9 and 4.10, respectively. The criterion on the time window for cluster reconstruction was introduced in Ref. [116]. The narrow width of the acceptance window used for strip multiplicity measurements is justified by observed delayed cross-talk in the readout electronics (i.e. artificial effect), which could lead to apparent enlargement of the cluster size. Measurements were performed for

both RPCs in the same point of the efficiency curves corresponding to the radiation intensity of 640 Hz/cm^2 . The cluster multiplicity measured for the low resistivity RPC 2 has narrow distribution with the mean of 1.8 strip; the high multiplicity tail (i.e. multiplicity larger than 4) is much less pronounced for the RPC 2 than it is in the case of the RPC 1. This demonstrates that the amplification process is well localized in the RPC made out of the material having volume resistivity of about $5 \times 10^8 \Omega\text{cm}$. The abundance of events with multiplicity 1, observed for the RPC 1 module, may be explained as resulting from the smaller avalanche charge for the RPC with high resistivity electrodes.

The results obtained for the low resistivity RPC 2 module confirm that a Resistive Plate Chamber detector has intrinsic capability of high rate operation. The volume resistivity of the electrodes should be selected to match the required performance. Electrical characteristics of the electrodes are crucial for stable operation of a RPC in the wide range of the radiation rates. Moreover, the fluctuations of the avalanche process, due to the dynamic behavior of the chamber, are less pronounced for the detector with low resistivity electrodes. The stable operation up to rates around 7000 Hz/cm^2 has been achieved with the efficiency plateau broader than 500 V using pulsed beams of minimum ionizing particles of 2.5 s spill duration. Due to low resistivity of the electrodes the RPC 2 module has excellent time characteristics: time resolution of 2.2 ns has been measured up to rates of 3000 Hz/cm^2 . The total width at the base of the arrival time distribution is about 13 ns. Double gap RPCs with electrodes of low resistivity can operate in the most demanding regions of the CMS detector, where the radiation background at the level exceeding 1 kHz/cm^2 may be expected. The results significantly contributed to the RPC muon system definition in *The Muon Project Technical Design Report* [28].

4.2 Continuous irradiation results

In order to demonstrate usefulness of low resistivity RPC prototype (denoted as RPC 2), well behaving for periodic beam fluxes of high intensity, also at continuous ionizing particle beam covering entire detector's surface, it was tested in the Gamma Irradiation Facility at CERN [117]. The experimental set-up, similar for all tests performed in the GIF, is described in Section 3.3.2. During the tests the same gas mixture as for pulsed beam tests was used (denoted as *90%-TFE* in Tab. 3.7). The data was taken using the same amplifiers as in the case of the pulsed hadron beam test, but at higher discrimination threshold of 50 mV (33 fC). The RPC 2 chamber was located at 105 cm distance from the radioactive ^{137}Cs source plane. Intensity of gamma rays was controlled by a set of moving lead absorbers located in front of the source.

For the efficiency measurement of minimum ionizing particles from SPS accelerator presented

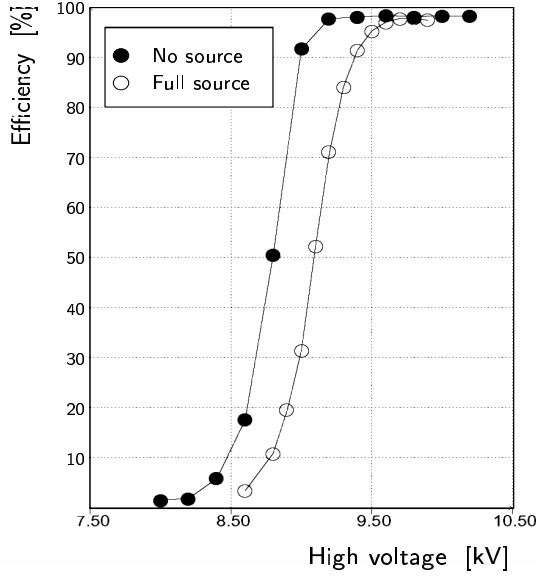


Figure 4.11: Efficiency of RPC 2 for minimum ionizing particles measured in the GIF as a function of the high voltage for the source fully opened (open circles) and fully closed (filled circles).

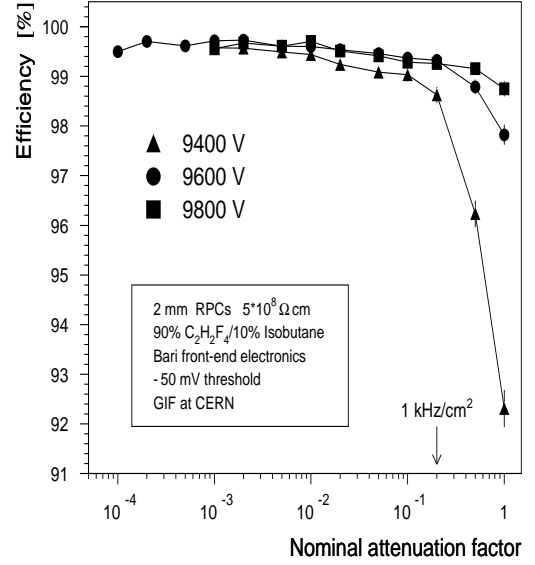


Figure 4.12: Efficiency of RPC 2 as a function of the nominal attenuation factor of the ^{137}Cs source. Attenuation value corresponding to the radiation intensity of 1 kHz/cm^2 in the single gas gap is indicated.

in this Section a 100 ns-wide time window of acceptance was used. The efficiency as a function of the high voltage is shown in Fig. 4.11 with the full source intensity (open circles) and without source (full circles). As one might expect the efficiency curve with source is displaced. The shift by about 300 V can be attributed to the voltage drop across the resistive electrodes due to the avalanche current at high counting rate.

The detection efficiency for minimum ionizing particles as a function of continuous background rate is shown in Fig. 4.12. The chamber has efficiency exceeding 98% up to $1\text{ kHz/cm}^2/\text{gap}$, the rate level expected in some regions of the CMS muon detector [28], with the plateau at least 400 V wide. The effect of the rate starts to be visible at the highest radiation rates as the narrowing of the plateau width. The exposure time at each voltage point was at least 15 minutes. Thus short-term stability of operation of the chamber can be demonstrated.

In Fig. 4.13 the rate of hits grouped into clusters per unit area is depicted, according to the algorithm given in Section 3.4, at the working voltage of 9.6 kV for which efficiency for muons is $\geq 98\%$. On the contrary to the minimum ionizing particles, which ionize the gas in both chamber planes at a time, the photons of few hundred keV can be seen by one plane only. The counting rate shown in the figure corresponds to a single RPC gap. The rate grows linearly with the source intensity, which should be expected from constancy of the chamber efficiency as a function of

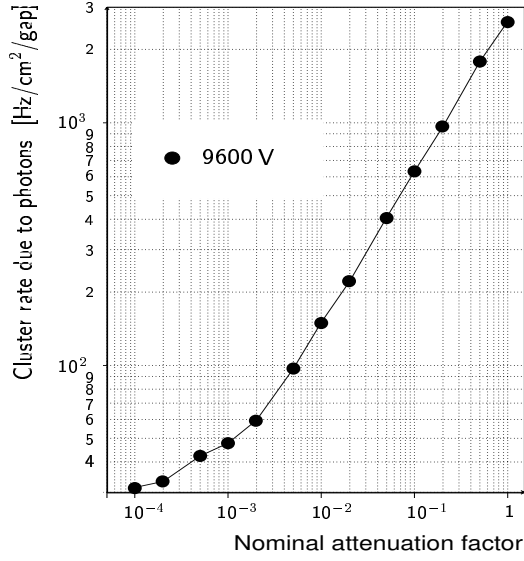


Figure 4.13: Measured background rate due to photons in one gap of RPC 2 as a function of the nominal attenuation factor.

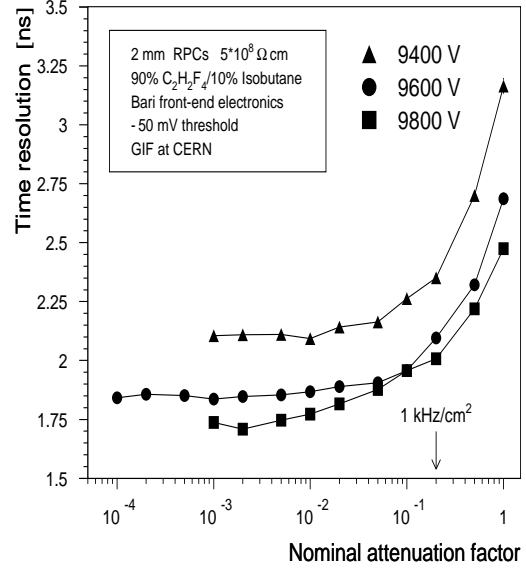


Figure 4.14: Time resolution of RPC 2 as a function of the nominal attenuation factor of the ^{137}Cs source.

the source intensity. Only at low photon fluxes the curve tends to saturate at $\sim 30 \text{ Hz/cm}^2/\text{gap}$ level, what indicates existence of non-negligible contribution due to the intrinsic noise rate of the detector.

The time resolution of the low resistivity RPC is only slightly rate dependent up to $1 \text{ kHz/cm}^2/\text{gap}$ as it can be seen from Fig. 4.14. The resolution improves with the applied voltage. Timing characteristics measured during medium term irradiation are very similar to the ones recorded in the previous tests using pulsed beam. It indicates that operation of the chamber with electrode resistivity of about $5 \times 10^8 \Omega\text{cm}$ stabilizes rapidly after beginning of irradiation. The measurement of the signal spread in time is performed relative to the trigger signal provided by the beam scintillator hodoscope. If this signal exhibits some jitter, this jitter will be added in quadrature to the measured time resolution. Since the measurements were performed together with measurements of INFN-Bari chamber [130], it is possible to use both chambers in order to estimate the scintillator signal spread. The estimated trigger spread in time is about 0.5 ns , therefore, it does spoil slightly the RPC 2 time resolution.

From Fig. 4.15 one can observe that the time walk of the signals from the RPC 2 operated at 9400 V , corresponding to the knee of the efficiency curve, is about 1.5 ns in $1 \text{ kHz/cm}^2/\text{gap}$ range of radiation rate. The delay of signals gradually increases with rate for a given voltage.

Another important feature to be studied is the strip multiplicity. The same criteria as in the H2/SPS data analysis were used, namely, the strip multiplicity is equal to the number of

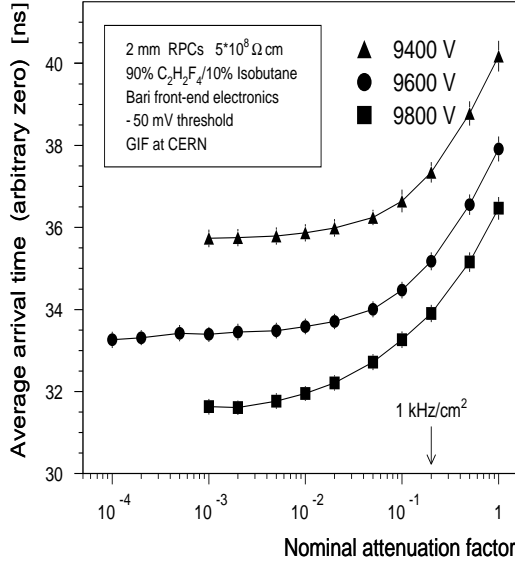


Figure 4.15: Signal arrival time of RPC2, with respect to the trigger counters, as a function of nominal attenuation factor of the ^{137}Cs source.

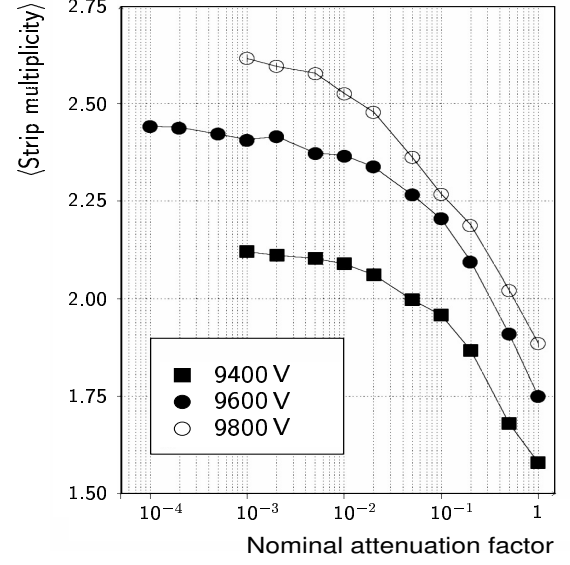


Figure 4.16: The average strip multiplicity as a function of the nominal attenuation factor of the ^{137}Cs source.

strips which responded in the time window of 10 ns after the earliest signal. The average strip multiplicity is depicted in Fig. 4.16 as a function of the nominal attenuation factor for three high voltage values. At a given applied voltage the strip multiplicity exhibits a steady decrease with the source intensity, which may be attributed to the decrease of the effective high voltage and stays below 2.5 strips, which corresponds to 3 cm size.

The current drawn by the chamber as a function of the nominal attenuation factor is depicted in Fig. 4.17. As one may expect at a given high voltage the current increases with the source intensity, and different current densities observed for three curves corresponding to the same rate result from increase of the gas gain with the applied electric field. For instance, the power dissipated in a single module at the rate of 1 kHz/cm² is about 4 W/m² and 7 W/m² at 9400 V and 9800 V, respectively.

The variation of the efficiency and average timing across the chamber has been used as a measure of the gas gap width uniformity. In this analysis the data where only one plane was powered has been used. The chamber was logically divided into narrow regions of 1 mm width and in each one the efficiency and the average signal arrival time were measured. Then, the dependencies of the efficiency and the arrival time on the applied voltage, measured over the chamber's area covered by scintillators hodoscope, were used in order to estimate the local value of the electric field. This value was then used to calculate the local departure from average gap

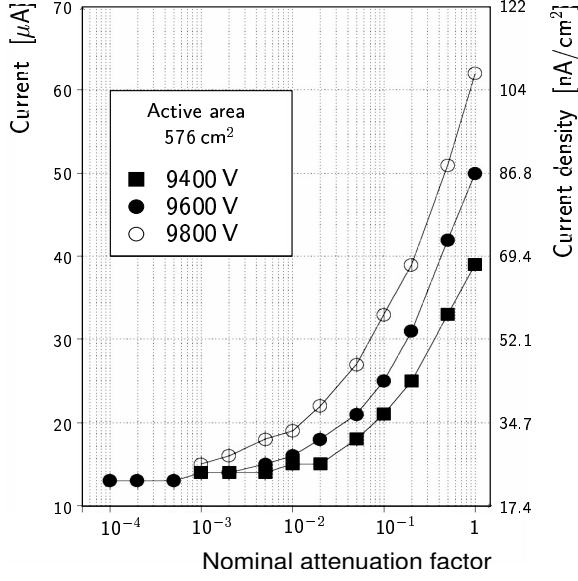


Figure 4.17: The current drawn by one of RPC 2 planes as a function of the nominal attenuation factor of the ^{137}Cs source.

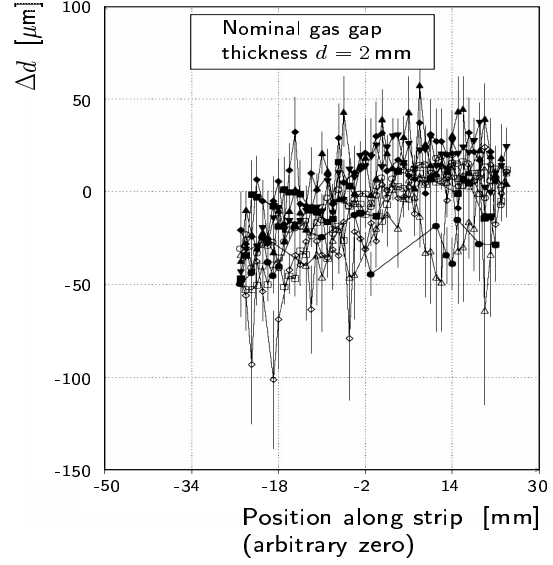


Figure 4.18: The departure of one layer of RPC 2 chamber thickness from the nominal one calculated from efficiency.

width providing that the dependence of the efficiency¹ and timing depend linearly on the electric field. The data from several runs at different high voltage values is plotted together in Figs. 4.18 and 4.19 where the distance was estimated from efficiency and from timing, respectively. The vertical axis shows local deviation from the nominal chamber thickness. Both figures reveal similar behavior and the distance variation below $50 \mu\text{m}$ over the area investigated. The variation of the pulse arrival time across the chamber's area, covered by triggering scintillators and tracking MW-PCs, does not exceed about 2 ns at the highest voltage used, while the efficiency dependence on the position can be observed only at low voltages, where the efficiency does not exceed about 95%. The second RPC plane showed much smaller variation concerning gas gap width, efficiency

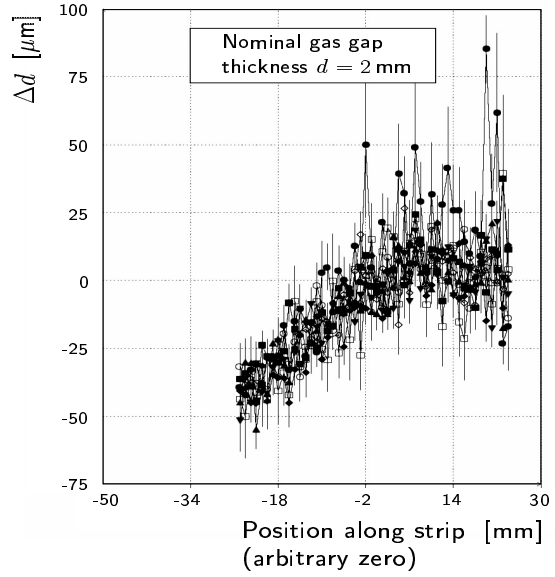


Figure 4.19: The departure of one layer of RPC 2 chamber thickness from the nominal one calculated from timing.

¹The voltage region where a single RPC gap has efficiency for muons $< 95\%$ was used in this analysis.

and timing over the area investigated.

It has been demonstrated that a RPC with low resistivity electrodes operates well under high radiation environment expected at the LHC. The dynamic drop of the electric field and the space charge in the gap do not cause degradation of the detector performance beyond the limits defined for the fast muon trigger in the CMS experiment. It is clear that the resistivity of the electrodes of a RPC has to be chosen carefully according to the conditions expected in the experiment. The RPC made out of bakelite with volume resistivity of about $5 \times 10^8 \Omega\text{cm}$ operates well in avalanche mode with wide efficiency plateau without suffering from sparks. Avalanches are well localized on the chamber's area. Significant changes of the detector performance related either to ageing or to the polarization of the electrodes were not observed during 10 days of tests in the GIF.

The results presented in this Section confirmed the right direction of the research on RPCs with high counting rate capability chosen by the Warsaw CMS Group. Moreover, it convinced the CMS collaboration that RPC technique can be implemented in the endcap regions of the CMS detector [28].

4.3 Results on ME 1/1 full scale prototype

In this Section results on the full scale ME 1/1 prototype are presented. The detector was made out of low resistivity bakelite plates of about $4 \times 10^{10} \Omega\text{cm}$ volume resistivity, higher than in the case of RPC 2 prototype discussed in two previous Sections. During tests of the ME 1/1 prototype in the GIF the $1.5\%\text{-SF}_6$ gas mixture was used (see Tab. 3.7). It was demonstrated by others that addition of small quantities of electronegative SF_6 gas suppress formation of streamer discharges at high gas gains, thus, enlarging working voltage plateau [83]. The detector was located at the same distance from the source plane as RPC 2 prototype, namely 105 cm from the irradiation source plane. The muon beam was centered on the area close to one of detector's edges as it is indicated in Fig. 3.18. The same high voltage was applied to both gaps during the tests. The data presented in this Section corresponds to 80 fC threshold.

Detection efficiency for minimum ionizing particles was measured with respect to the beam counter trigger covering area of $6 \times 6 \text{ cm}^2$ with additional requirement of having reconstructed hit in the MWPC closest to the detector under tests. The event was accepted if there was a signal in any of the readout strips covered by triggering scintillators (see Fig. 3.18) within the window of 40 ns width. The efficiency was defined as the ratio of accepted events to the number of triggers recorded.

In Fig. 4.20 the efficiency for muons as a function of the applied voltage is depicted for several intensities of gamma rays. The "source intensities" shown in this, and in all subsequent figures of

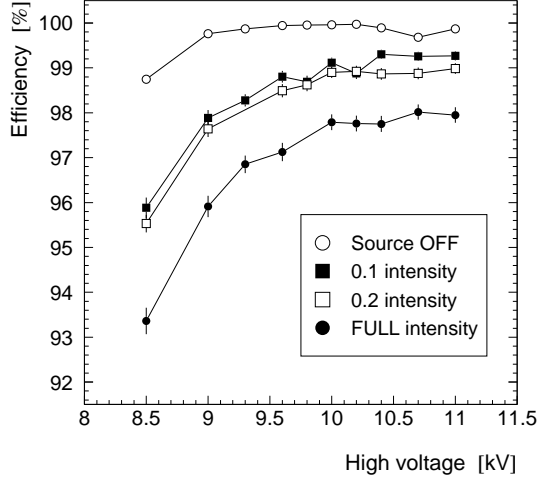


Figure 4.20: Detection efficiency of ME 1/1 prototype as a function of the high voltage for different source intensities. Data for 40 ns time window of acceptance.

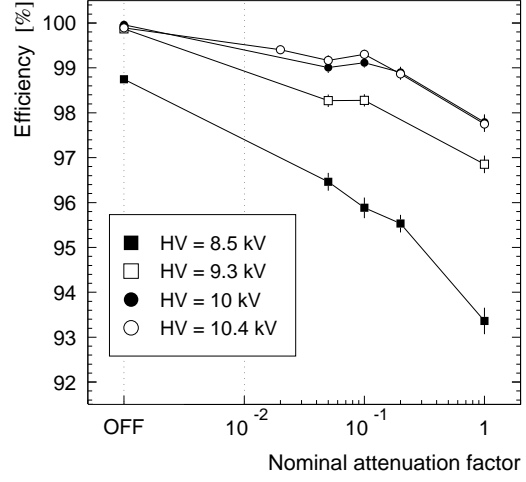


Figure 4.21: Detection efficiency of ME 1/1 prototype as a function of the nominal attenuation factor for several operating voltages. Data for 40 ns time window of acceptance.

this Section, are equal to the nominal attenuation factor (i.e. corresponding to the attenuation of 662 keV photons from ^{137}Cs source alone, without contribution of Compton-scattered photons of lower energies). It can be seen from the figure that even for the highest rate, the efficiency reaches 98% with a 1 kV plateau. From Fig. 4.21 the efficiency variation with increasing source intensity for high voltage values around the knee of the efficiency plateau can be observed. The data without source was taken by gradual increasing of the operating voltage with about 2×10^4 events taken in each voltage point. With the source on, the data for several intensities of gamma rays was taken, while the applied voltage was kept constant. The duration of data taking in single voltage and intensity point varied from tens of minutes to almost 2 hours depending on the occupancy of the data acquisition system.

The dependence of the efficiency on the width of the time window is depicted in Fig. 4.22 for maximum source intensity and for intensity reduced by a factor of 20. For each point the position of time window was individually adjusted to match slight variations of the average signal arrival time with rate for a given applied voltage. The high voltage of 9.3 kV corresponds to the knee of the efficiency plateau (i.e. $> 96\%$ at full source intensity). Even at rates as high as $5 \text{ kHz/cm}^2/\text{gap}$ and 15 ns time window of acceptance the efficiency exceeds 95% at this voltage. It satisfies well the requirements imposed on RPCs for the CMS experiment [28].

The distribution of the arrival time of the fastest signal is shown in Fig. 4.23 for the source intensity of about $1 \text{ kHz/cm}^2/\text{gap}$ and the applied high voltage corresponding to the knee of the

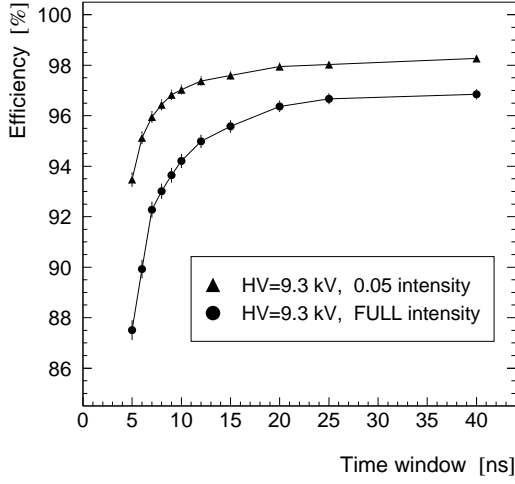


Figure 4.22: The efficiency of ME 1/1 prototype as a function of the width of the acceptance time window for two source intensities.

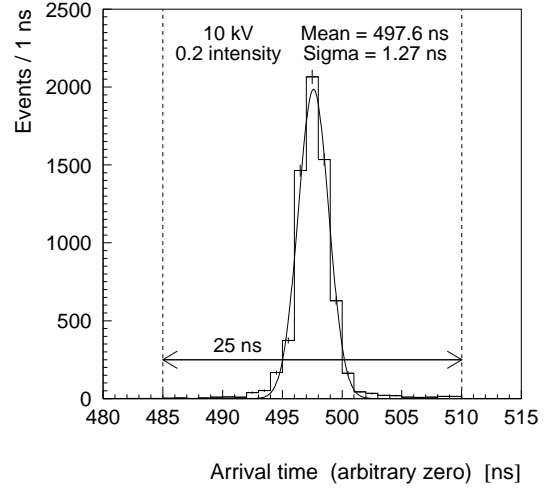


Figure 4.23: The arrival time distribution of the first signal with the source intensity of about $1 \text{ kHz/cm}^2/\text{gap}$ at the applied voltage corresponding to the knee of the efficiency plateau. The fit of Gaussian distribution to the experimental data is also superimposed.

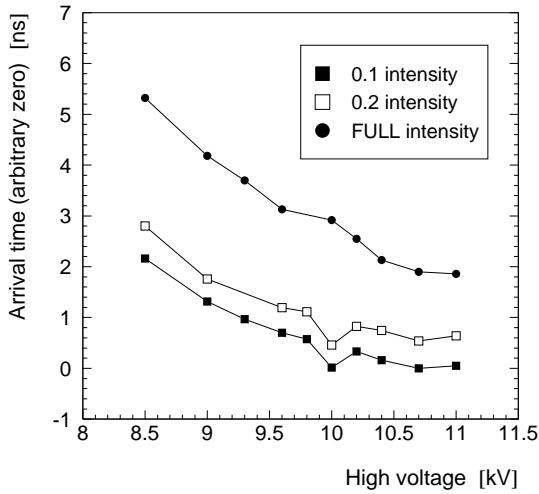


Figure 4.24: The average signal arrival time as a function of the high voltage. Statistical error bars are within marker size.

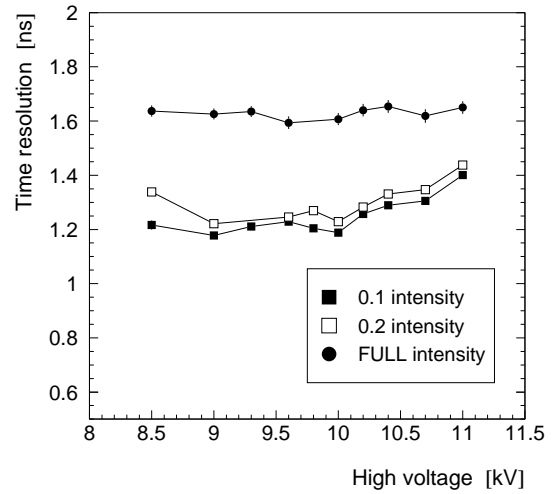


Figure 4.25: The signal arrival time spread of ME 1/1 prototype as a function of the high voltage for several source intensities.

efficiency plateau at maximum intensity. Its shape can be approximated with a Gauss function with $\sigma = 1.3 \text{ ns}$. The full width at the base, defined as the window containing 98% of events, is equal to 12 ns. The width of the time window corresponding to the LHC frequency is also shown in the figure.

The average arrival time of signals as a function of the applied voltage is shown in Fig. 4.24. The time walk related to the variation of the particle flux does not exceed 3.5 ns for voltages in the range of the full efficiency. The shift due to increasing radiation rate decreases with the high voltage to about 2 ns in the middle of the plateau. The feature of small time walk due to rate variation is very important for RPCs operated in the highest background of the CMS experiment.

The time resolution as a function of the high voltage, obtained from a Gaussian fit to the arrival time distribution, is shown in Fig. 4.25. In the studied region where the efficiency exceeds 90% and at constant particle flux the time resolution is nearly constant and only slightly worsens at the highest voltages. A variation of the particle flux affects the time spread of the signal by about 0.5 ns and even at the highest rate the time resolution is better than 1.7 ns. The intrinsic time resolution of the detector should be better since the measured time spread of the signals was biased by: FEB electronics speed, LVDS to ECL converters and limited resolution of TDC modules.

The full scale ME 1/1 prototype shows very good performance when operated in the continuous high radiation rate environment. At the highest rate studied, the efficiency reaches 98% with time resolution better than 1.7 ns. The time walk related to the rate variation is smaller than 2.5 ns in the whole range of source intensities. It was shown that operation characteristics of an IDG version of ME 1/1 RPC prototype are adequate for the muon trigger requirement of the CMS experiment with good safety margin. The “practical efficiency” of 95% for 15 ns time window with plateau exceeding 1 kV was achieved at background rates as high as 5 kHz/cm²/gap. The width of the efficiency plateau was larger than the one obtained for RPC2 prototype of lower resistivity RPC due to use of new gas mixture characterized by: better streamer suppression capabilities and more sustained avalanche development.

4.4 Stability of operation at high rates

It was pointed out in Section 1.2.4 that the Resistive Plate Chambers for the CMS experiment should not only exhibit full efficiency for muons at high counting rates, but also their major characteristics, such as: efficiency, timing, strip multiplicity, and intrinsic noise rate, must be stable over 10 LHC years. In this Section some aspects on the stability of RPC operation at avalanche rates of ~ 1 kHz/cm² are discussed. Two parts of this Section address the short-term (i.e. of the order of hours) and the medium-term (i.e. of the order of days) stability issues studied during, respectively, tests of model RPC detectors in the GIF and laboratory measurements using dedicated PPAC detector with resistive anode.

4.4.1 Short-term stability

An important feature of the RPC behaviour is its dependence on ambient conditions such as temperature and pressure. Apart from air pressure changes, there will be always a pressure gradient between single gap RPC modules if they are chained to the gas distribution system, as will be the case in the CMS [119]. The observed characteristics of irradiated RPCs depend not only on gas transport parameters at given values of E/p and temperature, but on the bakelite resistivity as well, which is temperature-dependent. Moreover, the power dissipation in a RPC detector working at high rates can alter temperature changes providing that air cooling of the detector is not sufficient.

Correlations of major parameters characterizing RPC operation with ambient air temperature and pressure have been studied during tests of RPC2 module in the GIF. Namely, in Figs. 4.26, 4.27, 4.28 and 4.29 the dependencies of: efficiency, arrival time, time spread and strip multiplicity on the ambient air temperature are shown, respectively. The pressure was found to be stable throughout duration of the beam test (i.e. 965 hPa ÷ 970 hPa). It may be deduced from those figures, that when the temperature increases, chamber behaves as if the operating high voltage was raised; the efficiency and strip multiplicity increase and signal arrival time and its spread decrease. There are two important factors explaining experimental observations at least qualitatively. Firstly, at fixed electric field strength and pressure the effective Townsend coefficient α_{eff} and the drift velocity v_d increase with the gas temperature in the range of electric fields of interest: 45 kV/cm ÷ 60 kV/cm (i.e. 9 kV ÷ 12 kV for 2 mm gas gap). For instance, the gas properties simulated using PCMONTE program [131] for gas mixture denoted as *90%-TFE* in Tab. 3.7 exhibit growth of v_d and α_{eff} by 0.8% and 8%, respectively, between 15°C and 20°C at 760 Torr for operating voltage of 10 kV. Such small increase of drift velocity does not change the timing properties of the detector significantly. On the contrary, variations of α_{eff} of the order of few percent may change the gas gain by a factor of several. Secondly, at high rates the bakelite resistivity affects effective electric field inside the gas, thus, it affects the gas transport parameters described above. The conductivity of electrodes increases almost exponentially with temperature and for typical temperature coefficient $a \approx 0.1 \text{ } ^\circ\text{C}^{-1}$ from Tab. 3.2 one can estimate resistivity drop by 30% for temperature rise by 3°C, the effect which is non-negligible and leads to the increase of the amplification field in the gas.

In 2001 a rectangular IDG prototype was exposed to high particle fluxes in the GIF for a longer time period than that during beam tests of RPC2 and ME1/1 prototypes. The aim of such measurements was to demonstrate the significance of factors influencing stability of the gas gain and the detection efficiency, such as: gas composition and temperature of the electrodes, in an environment of LHC experiments — constant flux of radiation corresponding, for example in

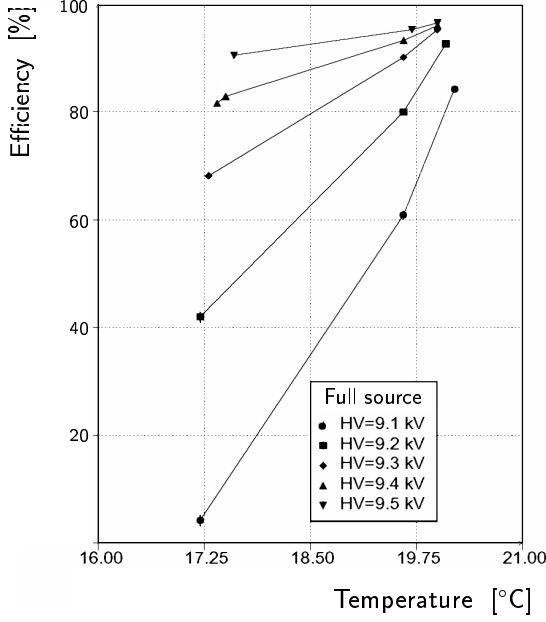


Figure 4.26: Efficiency of RPC 2 as a function of the ambient air temperature.

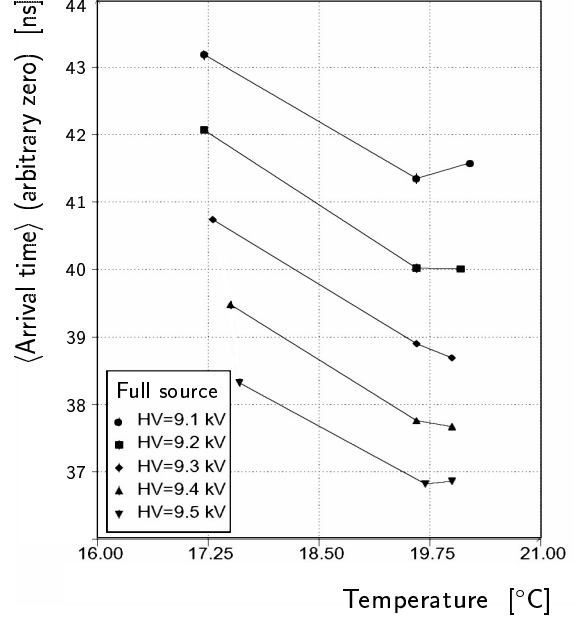


Figure 4.27: The signal arrival time of RPC 2 as a function of the ambient air temperature.

the CMS endcaps, to the ionization rate up to $1 \text{ kHz/cm}^2/\text{gap}$ in RPCs [28].

The distance from the source has been chosen to get ionization rate at maximum source intensity of about $1.1 \text{ kHz/cm}^2/\text{gap}$ according to previous measurements with RPC 2 prototype. The chamber was filled with $97\%-TFE$ gas mixture during first period of data taking, when the muon beam was available, and with $0.5\%-SF_6$ gas mixture afterwards, when the muon beam was switched off (see Tab. 3.7 for description of gas mixtures).

Atmospheric pressure and ambient temperature have been monitored during the experiment by a set of sensors installed in the experimental area [132]. A dedicated temperature sensor was located in contact with one of sub-modules referred as *gap no.1* on the external bakelite surface of RPC which allows the detector temperature monitoring (see Fig. 3.19).

In Fig. 4.30 the detection efficiency and the average number of fired strips in a single event (cluster size) are shown for the $97\%-TFE$ gas mixture as a function of the high voltage for several radiation background fluxes corresponding to: full source intensity (ABS=1), half intensity (ABS=2) and the natural background with the source closed. Even for the highest background rate efficiency plateau of 95 % is reached and it remains constant in the voltage range of at least 1 kV. The cluster size decreases when the radiation is increased at each voltage. For the efficiency measurement presented in the figure only signals inside fixed 50 ns time window with respect to the trigger pulse were accepted for the analysis and electronics threshold was set to 100 fC.

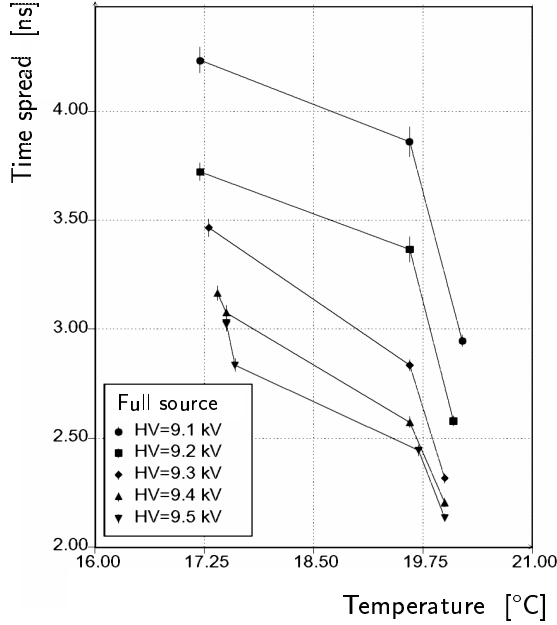


Figure 4.28: The signal arrival spread of RPC 2 as a function of the ambient air temperature.

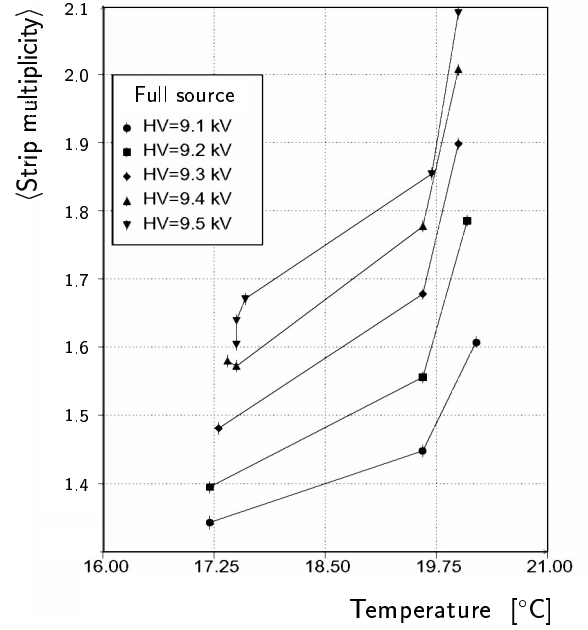


Figure 4.29: The average strip multiplicity of RPC 2 as a function of the ambient air temperature 10 ns time window of acceptance after the earliest signal.

It can be seen in Fig. 4.31 that the cluster rate increases monotonically with the applied voltages. The cluster rate dependence on the applied voltage is similar for the highest and the lowest radiation fluxes with the shift corresponding to the expected ionization rate difference. The spontaneous avalanche noise rate reaches 2 kHz/cm^2 at the highest voltage applied. The dashed line in Fig. 4.31, result of a simple subtraction of the two curves measured, approximates the primary ionization rate due to the flux from the source. Flatness of the dependence in the voltage range of the efficiency plateau for muons indicates the efficiency of gamma rays detection. In the plateau region the rate increases by a factor of about 2.4 what indicates the significant noise component even at high radiation flux.

Adding 0.5% of SF_6 to the basic TFE/Isobutane gas mixture changes the chamber characteristics significantly regarding the avalanche counting rate as can be seen from Fig. 4.32. Due to lack of the muon beam the efficiency curve could not be measured during this period.

The average length of a group of hits constituted one cluster, defined as an average time difference between leading edges of the last and the first hit of a cluster, is shown in Fig. 4.33. It can be seen from figure that the hits assigned to an avalanche induced by single gamma photon are contained within 25 ns window for operating voltages up to 11.2 kV and 11.6 kV for RPC operated in double- and in single gap mode, respectively.

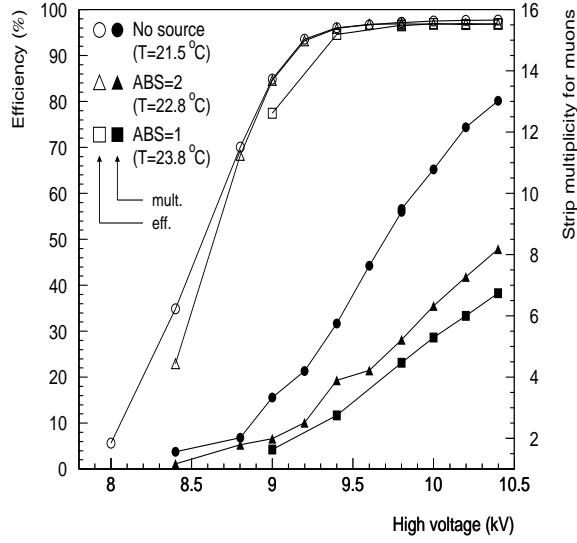


Figure 4.30: Detection efficiency (open markers) and avalanche cluster size (filled markers) as a function of the applied voltage in double gap mode (97%-TFE gas mixture, 100 fC threshold).

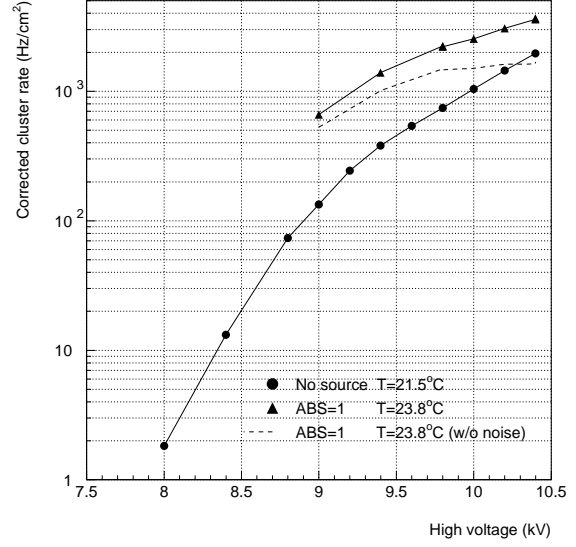


Figure 4.31: Corrected cluster rate as a function of the applied voltage in double gap mode. Average bakelite temperature for each curve measured is indicated (97%-TFE gas mixture, 100 fC threshold).

In order to estimate voltage shift of the efficiency curve for 0.5%-SF₆ gas mixture, which was not measured during the tests, with respect to 97%-TFE one the effective Townsend coefficient α_{eff} was calculated using PCMONTE program [131]. From simulations shown in Fig. 4.34 it can be deduced by inspection of curves marked with open circles (o) and black triangles (▲) that in the region of interest of operating voltages 9 kV ÷ 11 kV the knee of the efficiency plateau should be shifted by 200 V ÷ 350 V toward higher voltages. Since for full source intensity a plateau of the cluster rate of about 1 kHz/cm²/gap is clearly visible for 0.5%-SF₆ gas mixture starting from 9.8 kV, it hints that a single RPC gap of 2 mm width filled with adequate gas mixture may allow the full detection efficiency of ionizing particles with the constant flux as high as 1 kHz/cm².

The ionization rate due to gamma rays measured in each single gap RPC module is half of the rate for double gap operation. The noise rate measured for 0.5%-SF₆ gas mixture is 5 to 10 times smaller than the one for 97%-TFE one in similar working conditions. The avalanche rate measured for the high radiation flux increases by the factor smaller than 1.5 in the voltage range of 1 kV where the efficiency plateau region is expected. The sensitivity of the detector operation to temperature variations is reflected in the noise rate difference for measurements at two values of the ambient temperature. The increase of the detector temperature by 2.5°C only results in increase of the noise rate by a factor of 2 or, alternatively, it shifts the operating voltage by

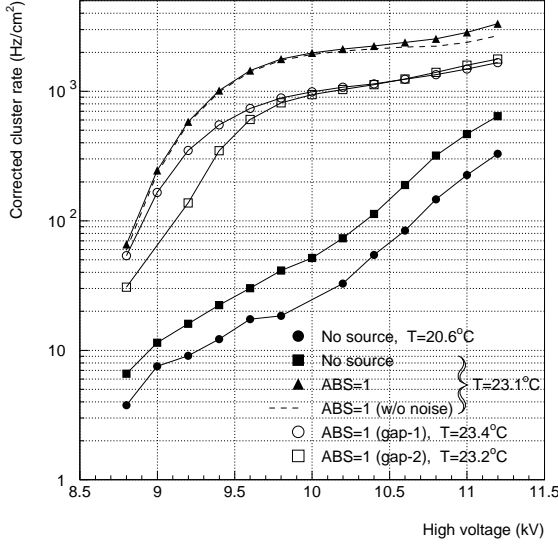


Figure 4.32: Cluster rate as a function of the applied voltage in double gap mode (filled markers) and in single gap mode (open markers) for two gaps independently. Average bakelite temperature for each curve is indicated (0.5% - SF_6 gas mixture, 100 fC threshold, slope method).

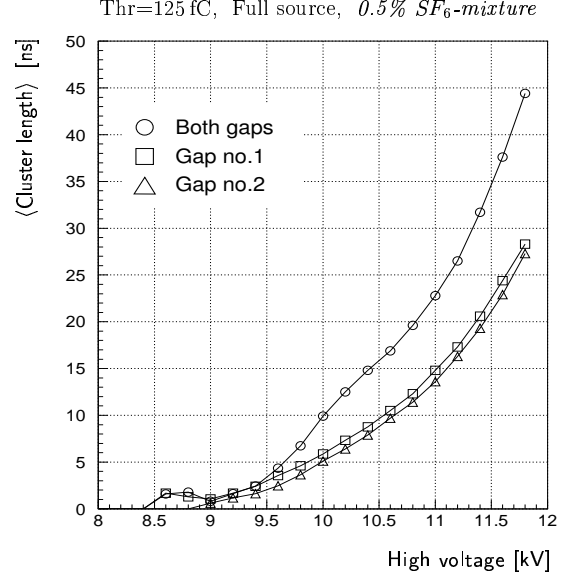


Figure 4.33: Cluster length in time as a function of nominal operating voltage for RPC operated in double- (circles) and in single gap mode (squares and triangles) working at: full source intensity, 125 fC electronics threshold and filled with 0.5% - SF_6 gas mixture.

about 300 V to the lower values. The observed shift exceeds standard correction for temperature and pressure used by others [133, 134], and given by expression:

$$\Delta V = V(p, T) \times \left(1 - \frac{p_o}{p} \times \frac{T}{T_o}\right) \quad (4.1)$$

where $V(p, T)$ is the operating voltage corresponding to pressure p and temperature T , while p_o and T_o denote reference pressure and temperature, respectively. From equation 4.1 one gets 100 V correction for $\Delta T = T - T_o = 2.5^\circ\text{C}$ at most. An additional voltage drop can be attributed to the bakelite conductivity changes by about 23% according to Tab. 3.2.

The current drawn by each sub-module is shown in Fig. 4.35 for fully opened source and for the source closed. The dark current due to the ohmic component (dashed curves) is set by the current flow through the frame and spacers² at a given temperature. It was extrapolated from measurements at low amplification fields at which the current flowing through the gas is negligible.

From the data presented in Figs. 4.32 and 4.35 one can deduce the single avalanche charge as a function of the applied voltage corresponding to the counting rate plateau. The single

²Frame and spacers were made of high resistivity bakelite of $\sim 10^{12} \Omega\text{cm}$.

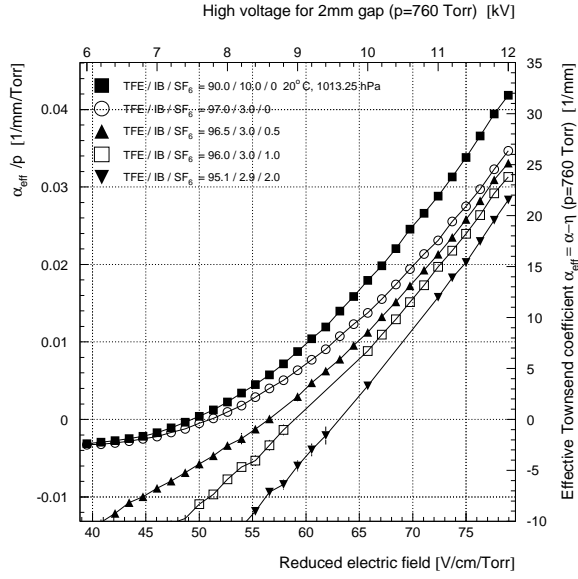


Figure 4.34: PCMONTE simulation of the effective Townsend coefficient α_{eff} for several TFE/Isobutane/SF₆ gas mixtures at normal conditions (statistical errors are within 1%).

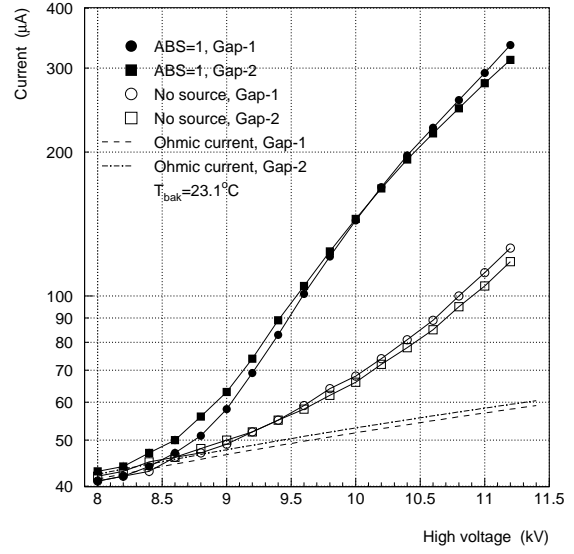


Figure 4.35: The charge current in single RPC gaps as a function of applied voltage. Dashed lines show an estimated ohmic component of the current for the bakelite temperature of 23.1 °C (0.5%-SF₆ gas mixture).

avalanche total charge is about 20 pC at 9.8 kV and at the highest voltage applied it reaches 50 pC due to the charge gain of about 10^7 . Hence, one can estimate the total power dissipated in a single gap detector with negligible ohmic current operated at full efficiency to be of 2.0 W/m² and 7.4 W/m² for 9.8 kV and 11.0 kV, respectively, for the radiation flux of about 1.1 kHz/cm². Without an efficient heat exchange with the detector surrounding the temperature of the chamber could increase due to the avalanche current in the long-term operation.

The effect of the chamber self-heating was observed, indeed, when the high voltage was gradually increased between subsequent runs as it is shown in Fig. 4.36. In each of three periods the applied voltage was increased from 8.8 kV to 11.8 kV in 200 V steps. The open and full circles denote, respectively, the rate of single hits and the rate of clusters obtained by direct counting method. Each experimental point shown in the figure (open and full circles) corresponds to an individual run at fixed high voltage, which duration is depicted by a horizontal error bar. It can be seen that, while an ambient air temperature (open triangles) remained almost unchanged the temperature of the anode of gap no.1 equipped with temperature sensor (full triangles) rose by 1.5 °C during the first period (both gaps active) and then only slightly decreased during next two periods (only one gap active at the time) when high voltage was lowered by few kV. The dotted and dashed curves represent, respectively, the single hit rate and the cluster rate

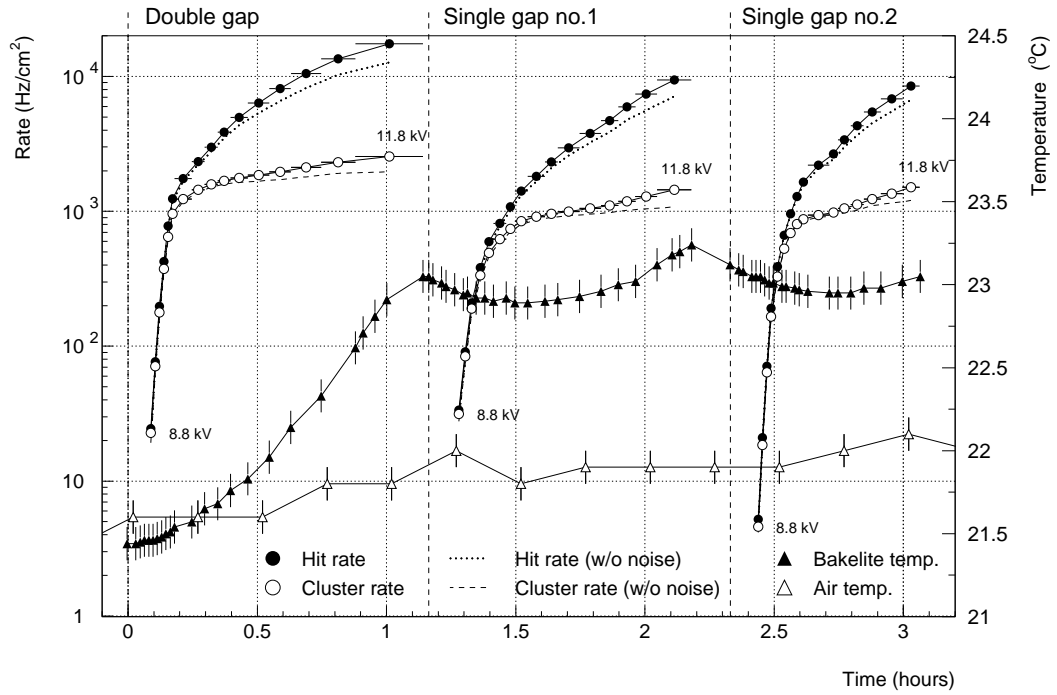


Figure 4.36: Rate of single hits and rate of clusters (direct counting method) for fully opened source. In each of three periods the applied voltage was increased from 8.8 to 11.8 kV in 200 V steps. Changes of bakelite- and air temperatures are shown ($0.5\%-SF_6$ gas mixture, 125 fC threshold).

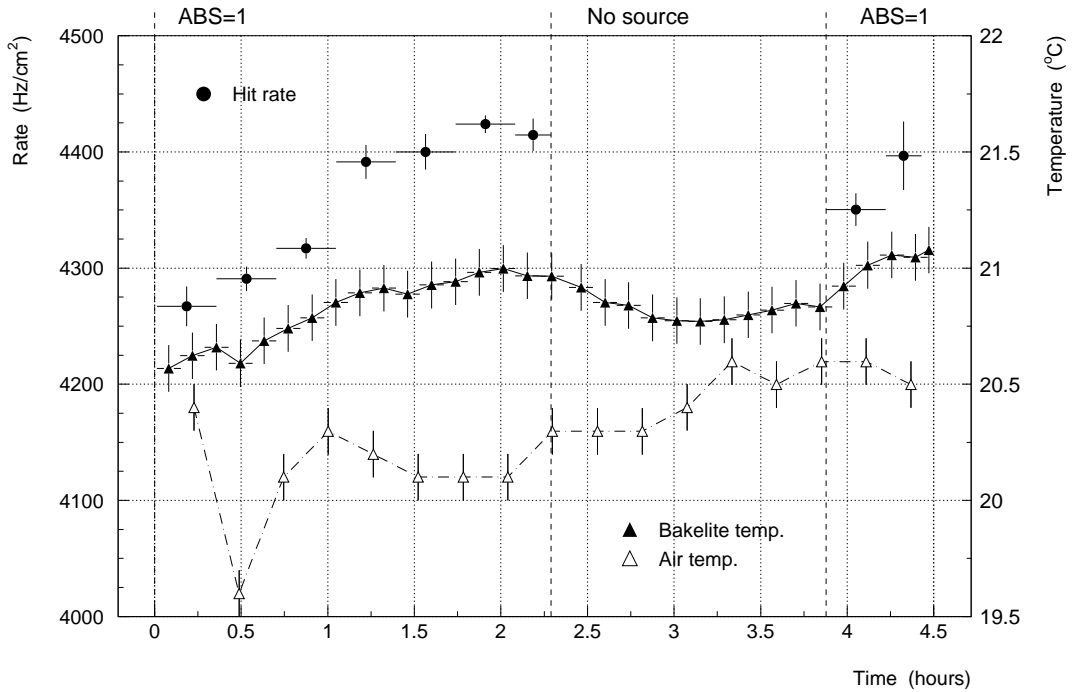


Figure 4.37: Rate of single hits for constant applied voltage of 10.4 kV measured during the three runs: full intensity, no source, full intensity. Changes of bakelite- and air temperatures are shown ($0.5\%-SF_6$ gas mixture, 125 fC threshold).

after subtraction of corresponding counting rates without irradiation source (noise rate). Since pulse-heights of analog signals were not measured during the tests, one can treat the number of responding strips for gamma rays as a measure of the gas gain at given working conditions (i.e. radiation environment, applied electric field). Moreover, from Fig. 4.33 it can be seen that on average the length of clusters from avalanches induced by gamma rays does not exceed 50 ns even for the highest voltages studied. Because the duration of the logical pulses generated by front-end electronics was 100 ns, the number of hits assigned to a single cluster is equal to the number of responded strips. Therefore, the strip multiplicity for gamma rays can be calculated directly from Fig. 4.36 as a ratio of the single hit counting rate (full circles) to the cluster rate (open circles). It remains smaller than 2 up to 10.6 kV and increases to about 6 for the highest voltage studied.

The short-term stability of a RPC operation at the constant applied voltage of 10.4 kV was measured with- and without irradiation. As can be seen from Fig. 4.37, during first two hours of operation at full source intensity the rate of single hits grew by 4%, while the electrode temperature rose by 0.5 °C. During the time period without irradiation the bakelite temperature approaches the level of the ambient one. Re-opening of the source has initiated the heating again. However, the cluster rate due to gamma rays has remained almost unchanged during the experiment. Further studies are needed to observe possible saturation of the gas gain with time, when detector temperature eventually stabilizes due to heat exchange with the ambient air.

The quality of the detector operation depends strongly on the gas mixture used. A small addition of SF₆ to the basic TFE/Isobutane gas mixture stabilizes the operation by substantial reduction of the intrinsic RPC noise. The temperature of the detector influences its characteristics significantly. This effect should be carefully studied for long-term experiments applications. The data would seem to suggest that a single RPC layer having 2 mm gas gap and filled with adequate gas mixture allows one for full detection efficiency of ionizing particles fluxes of about 1 kHz/cm².

4.4.2 Medium-term stability

In RPCs monitoring of the gas gain stability with time raises some difficulties since primary electrons are distributed along the incoming particle's track and, moreover, their number is subjected to statistical fluctuations. Therefore the advantages of using a PPAC detector with separated drift- and amplification regions are numerous: well defined number of primary electrons starting the avalanche at the cathode (e.g. from mono-energetic X-rays); narrow, peaked amplitude pulse-height spectra for gas mixtures based on noble gases (e.g. Argon); easy monitoring of the gas gain by inspection of the main peak position of the pulse-height distribution.

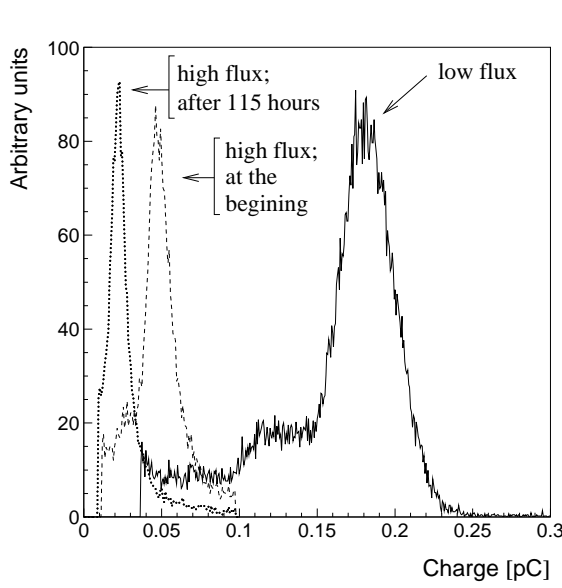


Figure 4.38: Induced charge distributions at nominal working voltage of 4900 V for two intensities of 8 keV X-rays: 120 Hz/cm² (low flux) and 3700 Hz/cm² (high flux). The effect of the pulse-height decrease after 115 hours at high flux is displayed.

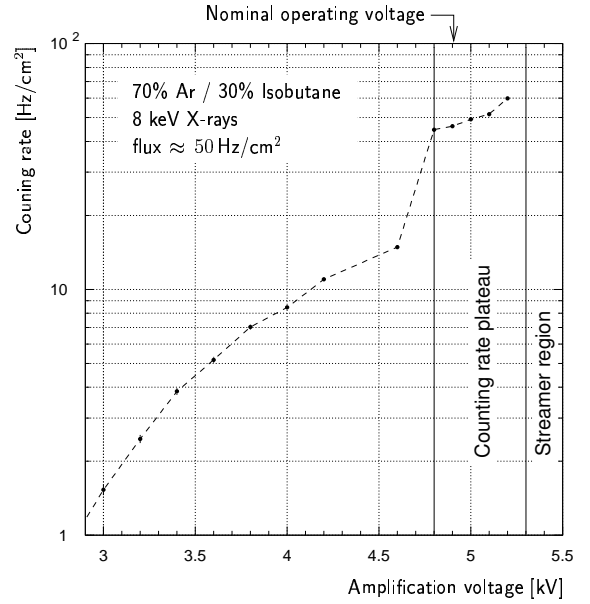


Figure 4.39: Counting rate as a function of voltage applied to the bakelite electrode for low intensity beam of 8 keV photons. The drift voltage was set to -500 V in all measurements.

It is well understood that the dynamic voltage drop across the gas gap due to the avalanche current becomes significant even at moderate avalanche rates when a RPC is made out of high resistivity bakelite [89,96]. From the results shown in previous Sections one can conclude that good stability of the electrical characteristics of the electrodes' material is one of the critical parameters for proper RPC operation at high rates. Several bakelite laminates, provided by different manufacturers, exhibit strong dependence of the specific resistivity on the ambient temperature and the water content. The effect of the resistivity growth with time was observed when a constant polarizing voltage was applied for a long time period. It was demonstrated in previous Sections that low resistivity bakelite plates ($10^8 \div 10^{10} \Omega\text{cm}$) are suitable for stable and fully efficient operation of RPCs at high counting rates, however the data concerns the short-term stability of the detector only.

Similar measurements using PPAC detector were reported before by Fonte et al. [95]. The authors covered wide range of rates up to 10^7 Hz/cm^2 and electrodes' material resistivities from $4 \times 10^7 \Omega\text{cm}$ to $4 \times 10^{11} \Omega\text{cm}$, but their results address short-term effects only. Quantitative investigation of the gas gain as a function of avalanche rate during long-time exposures is crucial for good understanding of the detector operation since it provides a measurement of the electrodes'

resistivity fluctuation in the working conditions of the detector.

In this Section measurements performed with Argon/Isobutane (70/30) gas mixture are reported using experimental set-up presented in Section 3.3.3. Preliminary results have been already reported in Refs. [118, 126]. For each intensity of X-ray beam pulse-height spectra and counting rates of three detectors: a model PPAC with resistive anode and two reference proportional counters, were measured every hour. An example of the charge distribution from PPAC for low intensity of X-ray flux is shown in Fig. 4.38 (solid line). The main peak corresponding to the 8 keV copper fluorescence line can be seen.

The dependence of the measured counting rate at fixed electronics gain and threshold is shown in Fig. 4.39 for low intensity X-ray beam. The counting rate plateau extends from 4800 V up to 5200 V. At higher amplification fields streamer discharges appear. A sharp transition to the counting rate plateau results from characteristic peak-shaped pulse-height distribution when the charge corresponding to the main peak exceeds fixed threshold. In measurements presented in this Section the PPAC was operated at drift voltage of -500 V and nominal amplification voltage of 4900 V, at which the main peak of the pulse-height spectrum corresponds to the gas gain of about $4 \cdot 10^4$ at lower rates assuming that: absorption of a single photon results in liberating of about 250 electrons in the drift region for a given gas mixture [43] and induced charge of the fast electron component constituted only 10% of the total avalanche charge. Hence, on average the avalanche consists of about 10^7 electrons.

At counting rates well above cosmic ray fluxes the effective amplification field is reduced due to dynamic voltage drop in the irradiated part of the detector. The pulse-height spectra for continuous high X-ray flux, corresponding to the rate of avalanches of about 3.7 kHz/cm^2 , are superimposed in Fig. 4.38 at the beginning (dashed histogram) and at the end of test (dotted histogram). Besides an immediate effect of the amplitude decrease with increased rate, a further reduction of the signal during 115 hours of exposure to high flux can be observed. During this particular measurement temperature and pressure were stable within 1°C and 1 hPa, respectively, and the flux monitored by a sealed single wire counter was stable within 3%.

The results of the measurements with different fluxes of X-rays, numbered from I to VII, are plotted in Fig. 4.40 A in chronological order. The average intensity corresponding to each series of data taking is marked at the top of the figure. For data sets I and II the X-ray flux was adjusted by setting the current of an X-ray tube. For remaining ones the flux was controlled by changing the thickness of the absorber in a bottom collimator shown in Fig. 3.25.

In general, the pulse-heights from the PPAC detector exhibited stronger variations of the relative gain with respect to that of a single-wire reference counter arranged in series on the gas flow with PPAC. At low counting rates and at fixed drift and amplification fields in both

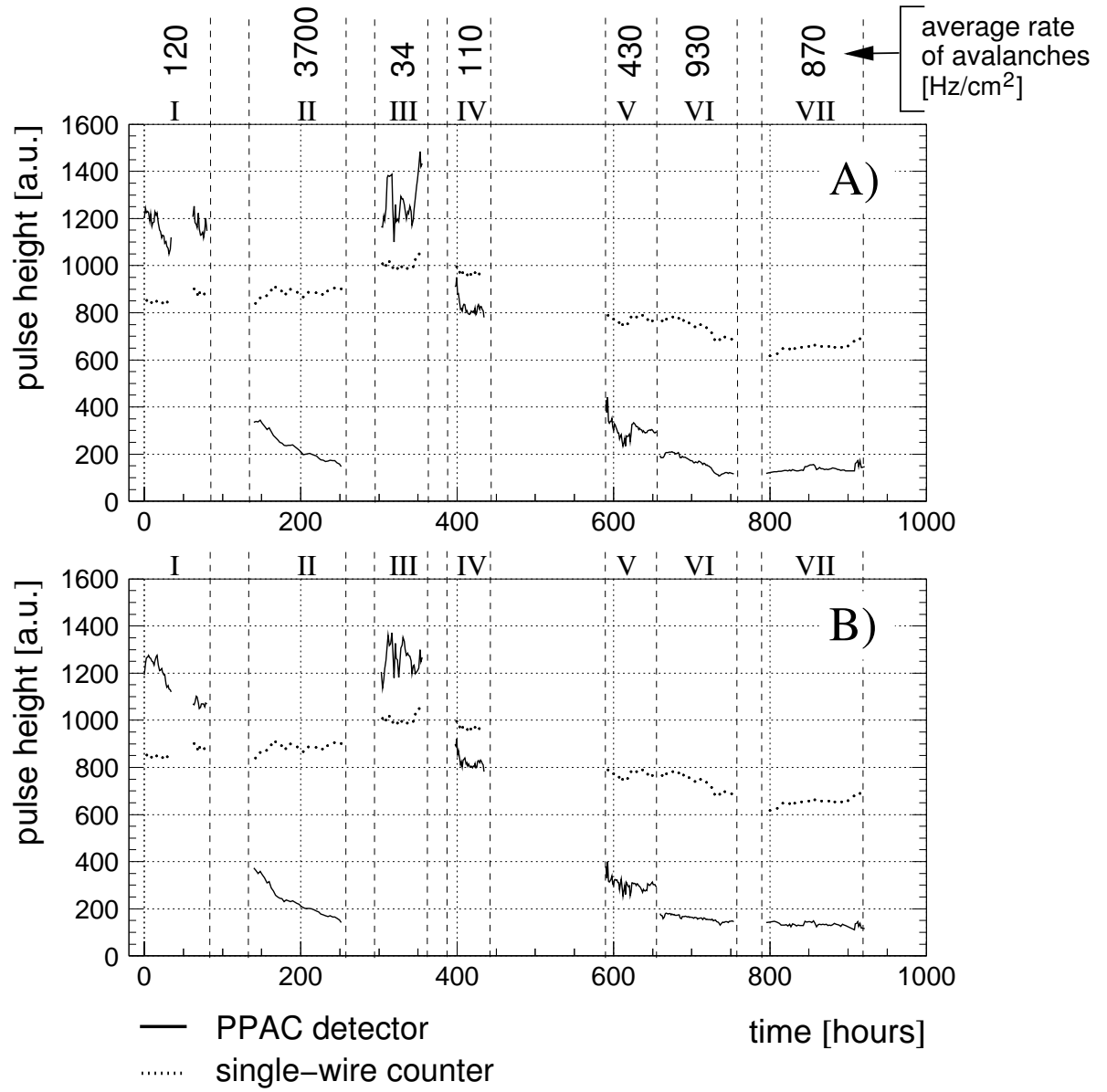


Figure 4.40: Measurements of the gas amplification stability in the PPAC detector for several intensities of X-ray beam. Average induced rates of avalanches are shown at the top of the figure. Pulse-heights not corrected (A) and corrected (B) for p, T changes are shown (solid line). Pulse-heights from the reference single-wire proportional counter are also superimposed (dotted lines).

Table 4.1: Calculated correlation factors h , measured counting rates and initial ambient temperature and pressure for each data set from Fig. 4.40.

Data set number	Correlation factor h	Counting rate in flux monitoring detector [Hz]	Rate of avalanches in PPAC [Hz/cm ²]	Initial ambient conditions	
				p [hPa]	T [°C]
I	3.11 ± 0.01	4.4 ± 0.3	119 ± 7	1005	30.2
II	1.63 ± 0.01	22.7 ± 0.6	3690 ± 92	1009	28.8
III	3.14 ± 0.01	32.1 ± 0.8	34 ± 2	1004	29.8
IV	1.15 ± 0.01	35.5 ± 0.7	114 ± 7	1005	30.4
V	3.61 ± 0.01	44.7 ± 2.8	430 ± 37	997	28.8
VI	3.01 ± 0.01	32.4 ± 0.7	934 ± 58	1003	26.6
VII	3.41 ± 0.01	30.0 ± 2.8	865 ± 95	1016	26.8

detectors an average gas gain should only depend on: temperature, pressure and composition of the gas mixture. To correct for fluctuations of the above parameters a method described in Ref. [135] has been applied. Namely, it was assumed that at any time instant t_i the average gas gain of the PPAC, G_i , and that of a reference detector, M_i , are correlated in the following way:

$$G_i = c \cdot (M_i)^h \quad (4.2)$$

where c and h are constant. For a given set of experimental data $\{t_i, G_i, M_i\}$ a corrected pulse-heights were computed as:

$$G_{corr,i} = G_i \cdot \left(\frac{\langle M \rangle}{M_i} \right)^h \quad (4.3)$$

where $\langle M \rangle$ is the mean value of M_i for a given set of data, while h is chosen to minimize a standard deviation of $G_{corr,i}$ from a smoothed curve³ going through corrected data points calculated for each value of h . Calculated correlation factors h , counting rates measured in the PPAC and in the flux monitoring detector, as well as initial ambient conditions are listed in Tab. 4.1 for each period of irradiation. The pulse-heights corrected for p , T variations in each data set are plotted in Fig. 4.40 B (solid lines). At rates above 100 Hz/cm² clear effect of the avalanche current becomes visible - immediate reduction of the pulse-height followed by further slow decrease of the gas amplification during the exposure (curves II and VI). Comparison of measurements II and III indicates that the detector recovers after heavy irradiation applied during extended time period. Between those two measurements the PPAC detector was active and only the radiation flux was stopped. However, a discrepancy by about 32% was observed between measurements I and IV performed at very similar counting rates and ambient conditions. An explanation of this phenomenon will be discussed later in this Section.

³A method of the least squares spline approximation to a data set was used: B-spline representation with degree $k = 3$ over set of $m = 2k + 2$ knots [136].

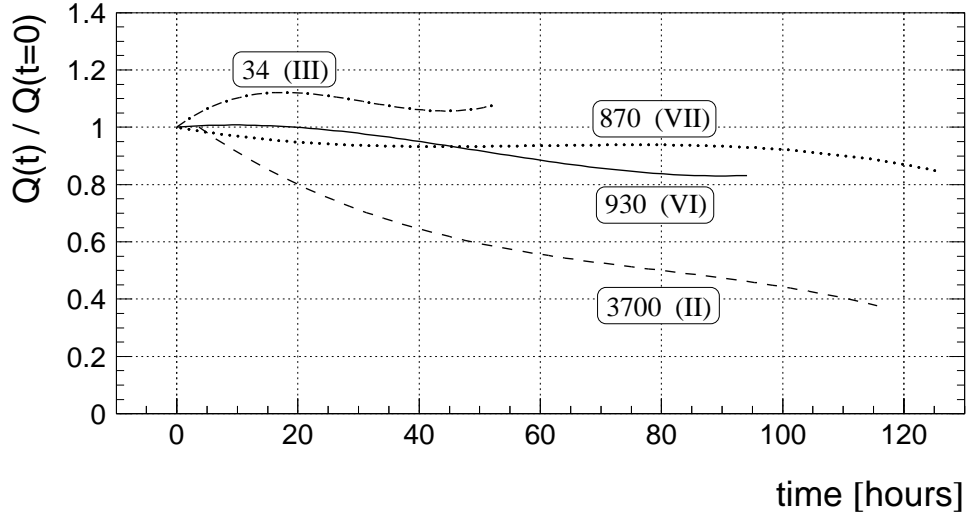


Figure 4.41: Dependence of the normalized gas gain (with respect to the beginning of irradiation for each data set) on time for several counting rates. Smoothed curves through the data corrected for p , T variations are shown. An average counting rate in Hz/cm^2 and an index corresponding to a data set from Fig. 4.40 are indicated for each curve.

In Fig. 4.41 the evolution of normalized pulse-height is shown as a function of the irradiation time for selected radiation rates. The smoothed curves correspond to best correlation factors, h , from Tab. 4.1. At the highest rate the pulse-height is reduced by a factor of 2 after 80 hours of exposure (curve II). Also by inspection of curves VI and VII, one can observe a systematic reduction of the gas gain with time, but with longer time constant. In this case, however, due to limited duration of the irradiation time the observed pulse-height drop can be related to pressure and temperature fluctuations, which were not fully eliminated by correction method used.

The pulse-height measured at the beginning of an irradiation as a function of the avalanche rate per unit area is shown in

Fig. 4.42. The effect of the dynamic reduction of the gas amplification due to avalanche rate can be seen. Filled points connected by a solid line correspond to data taking period after heavy

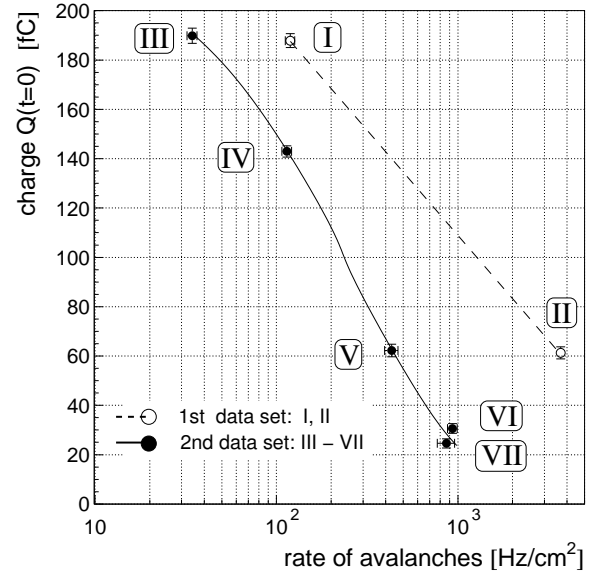


Figure 4.42: Initial values of corrected pulse-heights from a PPAC detector for each data set as a function of the average rate of avalanches per unit area. The lines are guide to an eye.

long-term irradiation during run II. A hysteresis-like behaviour shown in Fig. 4.42 indicates that some avalanche-induced changes influence rate capability of the detector. The difference between initial values of pulse-heights measured during exposures I and IV, as well as II and VI, can be attributed to local changes of the electrical properties of the bakelite electrode during PPAC operation under 3.7 kHz/cm^2 counting rate.

The systematic decrease of the gas gain in the PPAC with time of irradiation observed for the highest flux of X-rays tested could be attributed to the effects like: removing of the water residuals from the bakelite due to dry gas flow, polarization of the bakelite electrodes due to long-term passage of the volume current, deposit of a thin insulating layer on the anode plane and local charging up of the bakelite surface due to the avalanche current what reduces effective amplification field. In order to estimate which resistivity change, $\Delta\varrho$, can explain discrepancy between gas gain observed in measurements I and IV, corresponding to a rate of $R \approx 120 \text{ Hz/cm}^2$, the following model was assumed:

- The effective amplification voltages U_I^{eff} and U_{IV}^{eff} at the beginning of measurements I and IV, respectively, are given by:

$$U_I^{\text{eff}} = U_o - R Q_i d_{\text{bak}} \varrho \quad (4.4)$$

$$U_{IV}^{\text{eff}} = U_o - R Q_{IV} d_{\text{bak}} (\varrho + \Delta\varrho) \quad (4.5)$$

where: $U_o = 4900 \text{ V}$ – is the nominal amplification voltage,

Q_i – is the average total avalanche charge,

$d_{\text{bak}} = 2 \text{ mm}$ – is the thickness of the bakelite electrode,

$\varrho = 2 \times 10^{10} \Omega\text{cm}$ – is the resistivity of PL-#15A bakelite normalized to 30°C .

- Dependence of the observed charge Q on the effective operating voltage $U = U_o + \Delta U$ in the $\pm 100 \text{ V}$ vicinity of the nominal amplification voltage U_o can be parametrized as:

$$Q(U) = Q_o \exp(a \cdot \Delta U) \quad (4.6)$$

where coefficient $a = (8.33 \pm 0.30) \times 10^{-3} \text{ V}^{-1}$ was fitted from the dependence of the main pulse-height peak position on the amplification voltages corresponding to the counting rate plateau shown in Fig. 4.39 (i.e. $4800 \text{ V} \div 5100 \text{ V}$).

Hence, an additional voltage drop, $\Delta U_\varrho = U_I^{\text{eff}} - U_{IV}^{\text{eff}} \approx 33 \text{ V}$, corresponding to resistivity change by $\Delta\varrho$ between measurements I and IV, must occur in order to explain observed reduction of the pulse-height by 32%. Equivalently, the resistivity of the electrode had to increase by a factor of

$$k = \frac{\varrho + \Delta\varrho}{\varrho} = \frac{Q_{\text{IV}}}{Q_{\text{I}}} \left\{ \frac{\Delta U_{\varrho}}{R d \varrho Q_{\text{I}}} + 1 \right\}. \quad (4.7)$$

Under assumption that the measured fast electron component constitutes from 1% to 10% of the total avalanche current, one gets reduction of the bakelite conductivity by the factor k ranging from 4 to 28 during nearly 5 days of operation under heavy flux of X-rays. Such fast changes can be hardly explained by bakelite drying and local flow of the volume current through the electrode on the basis of results presented in Section 3.1.1. Also rate induced polymerization due to use of the organic gas (Isobutane) is very unlikely. The collected charge per unit area corresponding to measurement II is less than 0.1 mC/mm^2 . On the other hand, in planar wireless detectors, where multiplication is obtained over extended regions, no gain variations have been observed after about 10 mC/mm^2 [137]. Therefore, a possible explanation of the observed shift between dashed- and solid curves shown in Fig. 4.42 could be a local charging up of the anode surface leading to local reduction of the effective electric field in the irradiated part of the amplification gap.

The results obtained with the PPAC detector indicate some disadvantageous effects occurring at counting rates above 1 kHz/cm^2 . Namely, the dependence of the charge gain on the induced avalanche rate exhibits hysteresis behaviour. The origin of this effect should be clarified in order to find a remedy. For example, according to the ionic conductivity model presented in Section 3.1.1, water vapours added to the working gas mixture make all internal surfaces of the detector more conductive. Thus, local insulation spots on the bakelite anode are masked and accumulation of ions in thin layers, reducing external amplification field, is prevented. Similar role could be played by a thin layer of linseed oil deposited on the inner anode surface, as well.

Currently a new experimental set-up with more stable X-ray generator suitable for long-term non-interrupted measurements is under construction at the Detector Laboratory of IEP. The tests will be continued using the PPAC detector made out of recently developed low resistivity bakelite of good surface quality (e.g. IT-2002) and filled with a Tetrafluoroethane-based gas mixture.

4.5 Single gap solution

Results from beam tests performed by the Warsaw CMS Group during period of 1997-2001 in the GIF at photon-induced avalanche rates of $\sim 1 \text{ kHz/cm}^2/\text{gap}$ revealed two major issues:

- Very good rate capability in terms of: efficiency plateau, time resolution, rate induced time walk due to utilizing new low resistive developmental composite materials for the electrodes.
- Limitation of operation due to the roughness of the internal surface of electrodes what causes high intrinsic noise at the operating voltage.

Only recently a technology of commercial low resistivity bakelite of small roughness has become available allowing one for significant reduction of spontaneous discharges due to local surface imperfections. Beam test results of year 2001 indicate that single gap module, if carefully assembled and if operated in avalanche mode with adequate gas mixture, might be fully efficient even at rates foreseen for RPCs in the CMS forward region. In other words, a double gap structure in large rapidity regions can be superfluous since it was adopted for the CMS when the rate capability was still a concern for experimental groups [28].

To answer this question two identical rectangular prototypes were constructed, which have dimensions and strip segmentation almost identical to that of previously tested IDG module, as described in Section 3.2.4, and tested in the GIF in 2002. Also experimental set-up was very similar to the one from 2001 year, except that two RPCs have been located closer to the source, namely at 135 cm and 141 cm from the source plane for not-oiled and oiled module, respectively. For the fully opened source (i.e. no lead filters in front of the source; nominal attenuation factor is 1), on the basis of previous results and half-life of the ^{137}Cs radioactive source, one expects rate of avalanches due to gammas of about 1.5 kHz/cm^2 and 1.4 kHz/cm^2 for not-oiled and oiled single gap prototypes, respectively. The muon beam has been centered on one of the spacers of the middle section having 10 mm-wide strips of 12 mm pitch (see Fig. 3.20 A).

The results presented in this Section refer to two gas mixtures tested, denoted as *97%-TFE* and *0.7%-SF₆* in Tab. 3.7, and two intensities of gamma rays, namely fully opened- and fully closed source. The electronic threshold has been set to 100 fC. For correct efficiency evaluation, apart from coincidence provided by a scintillator hodoscope, a reconstructed muon track was required in the MWPC closest to RPCs under test in order to accept an event in off-line analysis. It is worth to mention that one expects 1% inefficiency purely due to dimensions of the spacer in the central part of $10 \times 10 \text{ cm}^2$ tested area. In all figures presented in this Section high voltage values have been normalized to $T_o = 25^\circ\text{C}$ and $p_o = 965 \text{ hPa}$ using formula 4.1. This normalization does not, however, correct for eventual changes of the electrode plate resistivity

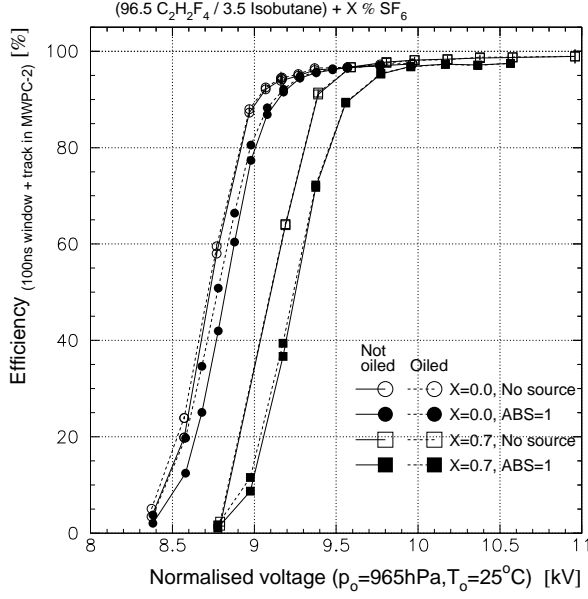


Figure 4.43: Efficiency of single gap RPC modules as a function of normalized H.V. for two gas mixtures: 97%-TFE (circles) and 0.7%- SF_6 (squares) and for two intensities of gamma rays: fully opened source (filled markers) and closed source (open markers). Solid and dashed lines correspond to non-oiled and oiled module, respectively.

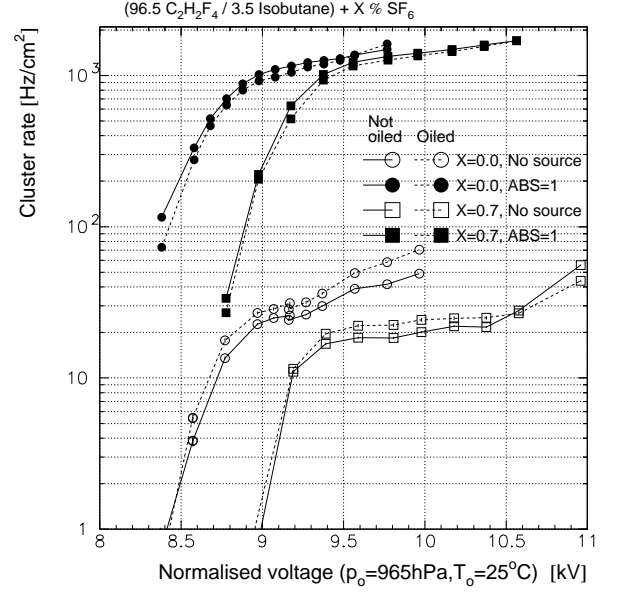


Figure 4.44: Rate of clusters of single RPC modules as a function of normalized H.V. for two gas mixtures: 97%-TFE (circles) and 0.7%- SF_6 (squares) and for two intensities of gamma rays: fully opened source (filled markers) and closed source (open markers). Solid and dashed lines correspond to non-oiled and oiled module, respectively.

(e.g. due to temperature).

The efficiency, cluster rate and current density as a function of corrected high voltage are depicted in Figs. 4.43, 4.44 and 4.45, respectively. Open markers correspond to the irradiation source switched off, while full markers to the source fully opened. Correlations between the efficiency for muons and the current density at full intensity of gamma rays are plotted in Fig. 4.46 for two gas mixtures studied.

The efficiency was calculated for a fixed 100 ns-wide time window of acceptance, while the cluster rate was obtained for hit clusters in 20 μs -wide time window opened before the window for the efficiency measurements. The efficiency dependence on the width of the acceptance window (*gate*) and on electronic threshold is discussed later in this Section. The rates with irradiation source opened at full intensity were calculated using *slope method*, which is more accurate at high rates. For the source switched off the *direct counting* method was implemented, because of too low statistics to perform an exponential fit to the cluster-to-cluster delay distribution.

The following direct observations can be made after inspection of the figures:

- The not-oiled and oiled RPC modules have very similar characteristics. The only difference concerns the dark current (due to ohmic leakage and spontaneous noise) which is consistent with zero within experimental errors for the oiled module, and reaches 2 nA/cm² (dashed

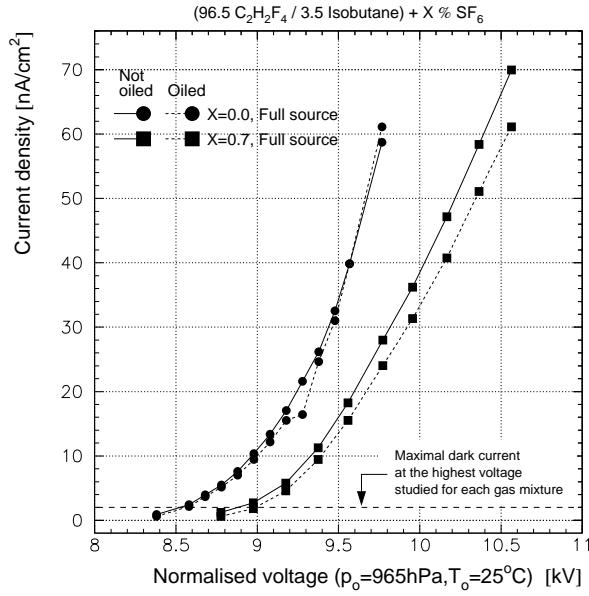


Figure 4.45: Current density in single gap RPC modules as a function of normalized H.V. for two gas mixtures: 97%-TFE (circles) and 0.7%-SF₆ (squares) and at full intensity of gamma rays. Solid and dashed lines correspond to non-oiled and oiled module, respectively.

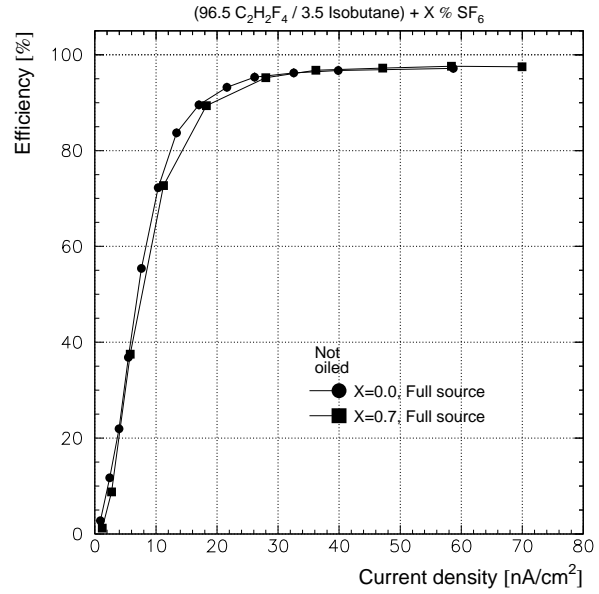


Figure 4.46: Correlation between efficiency and current density measured for not-oiled RPC at full intensity of gamma rays for two gas mixtures: 97%-TFE (circles) and 0.7%-SF₆ (squares).

horizontal line in Fig. 4.45) for not-oiled one at the highest voltages studied for each gas mixture.

- It can be seen from dependence of the current density on the high voltage that dependence of the gas gain on the electric field for 0.7%-SF₆ gas mixture exhibits departure from the Townsend's law, since a linear behaviour is observed at the highest voltages studied. For this reason 0.7%-SF₆ gas mixture provides more sustainable growth of the avalanche size with electric field than 97%-TFE gas mixture.
- As the result of 0.7% addition of SF₆ to the basic gas mixture of TFE/Isobutane (96.5/3.5) the working voltage has to be increased by about 400 V in order to get the same efficiency and cluster rate.
- The efficiency of single gap modules exceeds 95% even at full source intensity. For closed irradiation source the efficiency plateau for muons ($\geq 95\%$) starts at around 9.2 kV and 9.5 kV for 97%-TFE and 0.7%-SF₆ gas mixture, respectively. Corresponding width of the efficiency plateau is 800 V and 1.5 kV for 97%-TFE and 0.7%-SF₆ gas mixture, respectively. At full intensity of gamma rays shorter voltage ranges have been studied for two gas mixtures and the observed width of the efficiency plateau is 450 V and 850 V for, respectively, 97%-TFE and 0.7%-SF₆ gas mixture.
- The efficiency curves corresponding to the same gas mixture and to full intensity of gamma

rays are shifted toward higher voltages with respect to the irradiation source switched off. The shift amounts to 150 V and $200 \div 250$ V for *97%-TFE* and *0.7%-SF₆* gas mixture, respectively. However, the efficiency for muons at full source intensity (local, measured for $10 \times 10 \text{ cm}^2$ area) scales with the current density (global, current divided by detector's active area) and the observed correlation is similar for two gas mixtures tested.

- The counting rate plateau for gamma rays starts at about 9.0 kV and 9.4 kV for *97%-TFE* and *0.7%-SF₆* gas mixtures, respectively. In both cases, the knee of the counting rate plateau corresponds to the measured rate of 1 kHz/cm^2 and the current density of 10 nA/cm^2 . Measured rates increase with high voltage, though even at 800 V above the knee the rise factor is about 1.5 only.
- The counting rate for closed source is about $15 \text{ Hz/cm}^2 \div 20 \text{ Hz/cm}^2$ and $30 \text{ Hz/cm}^2 \div 40 \text{ Hz/cm}^2$ at voltages corresponding the beginning of the efficiency plateau for *97%-TFE* and *0.7%-SF₆* gas mixture, respectively. A kind of counting rate plateau can be seen for both gases, though, in case of *0.7%-SF₆* gas mixture the 20 Hz/cm^2 plateau extends up to 1 kV above the efficiency knee. Such characteristic shape of the cluster rate curves suggests that one deals not only with the intrinsic RPC noise, but also with minimum ionizing particles coming before time window corresponding to the trigger signal from scintillators hodoscope, as it is explained later in this Section.
- The power consumption of each module corresponding to avalanche rate of about 1 kHz/cm^2 ranges between 3 W/m^2 and 5 W/m^2 for the first 400 V of the efficiency plateau for both gases.

The cluster rate without source has been also studied for *97%-TFE* gas mixture when the muon beam from the SPS accelerator has been completely switched off. The data acquisition system has been triggered by a clock pulse (*random trigger*) for experiment without muon beam instead of scintillator hodoscope (*muon trigger*) with muon beam present. These two cases are compared in Fig. 4.47. Empty markers and full markers correspond to the noise measurement with- and without the muon beam, respectively. The higher rate observed with closed irradiation source for muon trigger (open markers) than for random trigger (full markers) data results from the fact, that in $20 \mu\text{s}$ -wide time window, used for background rate measurements and correlated with triggering muon, there is non-negligible contribution due to real muons from the accelerator beam. Such muons either did not trigger the scintillators hodoscope or come during dead time at the DAQ system. One can estimate probability P of detecting at least two muons in the

same event⁴ (i.e. the first muon fell into 100 ns-wide efficiency window, while the second one arrived earlier within 20 μ s-wide window used for cluster rate measurements) providing that the time delay between subsequent muons is exponentially distributed, as follows:

$$P = \int_{t_0}^{t_0 + \Delta t} R \cdot S \cdot \exp[-R \cdot S \cdot t] dt \quad (4.8)$$

where: R denotes intensity of the muon beam per unit area, $S = 10 \times 10 \text{ cm}^2$ is the area covered by triggering scintillators and $t_0 = 150 \text{ ns}$ is the separation in time between beginning of the efficiency window and the end of the window for cluster rate measurements of $\Delta t = 20 \mu\text{s}$ width used in the off-line analysis (see Fig. 3.26). Since the beam profile and variations of the muon flux during the accelerator's spill have not been measured, one has to rely on counting rates provided by scintillators hodoscope located in front of the RPCs. Assumption of constancy and uniformity of the muon flux over area S yields the beam intensity of $R \sim 10 \text{ Hz/cm}^2$. The parameter R can be, however, underestimated because the efficiency of the triggering hodoscope, requiring coincidence of signals from three scintillator counters, has not been determined during the tests. Ranging rate R between 10 Hz/cm^2 and 100 Hz/cm^2 (i.e. the maximum muon rate available in the GIF [117]) results in probability of detecting at least two muons in the same event between $P = 2\%$ and $P = 18\%$.

In Fig. 4.48 a correlation between hits in the MWPC closest to tested detectors and the not-oiled RPC is depicted for range of the arrival times excluding muons which triggered scintillators hodoscope (i.e. hits from last 1.5 μs before the COMMON STOP signal have been rejected). The observed excess of hit pairs on the diagonal line of the figure correspond to ionizing particles crossing MWPC and RPC detectors at a time. In the voltage range studied of 8.6 kV ÷ 10 kV similar correlations have been observed between hits in RPCs and MWPC detectors and between hits in two RPCs. An example of time-correlated hits in two tested RPCs are depicted in Fig. 4.49 showing time difference calculated for each pair of hits, which fall into 20 μs time window for cluster rate measurement, and which originate from two different RPC detectors. If all hits were

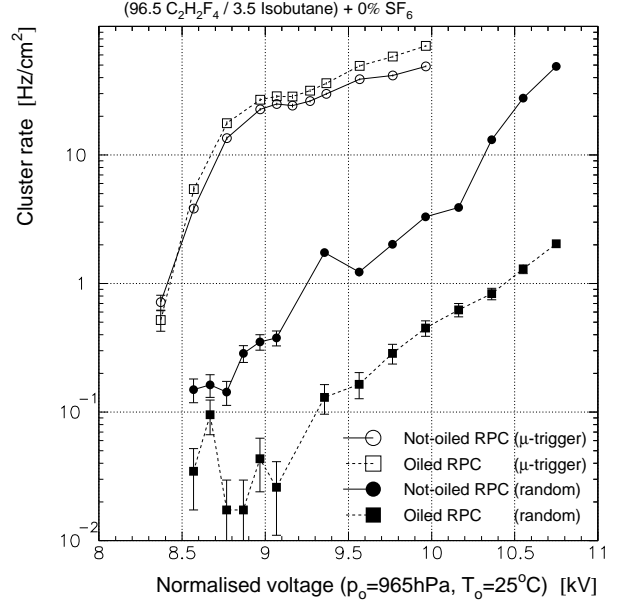


Figure 4.47: Rate of clusters without irradiation source as a function of the normalized H.V. measured with the muon beam (open markers, same as in Fig. 4.44) and when the muon beam was completely shut down (full markers). Solid and dashed lines correspond to non-oiled and oiled module, respectively (direct counting method, 97%-TFE gas mixture).

⁴This is just to remind that an *event* denotes set of last ≤ 16 hits from each readout channel recorded during 32 μs before the COMMON STOP signal.

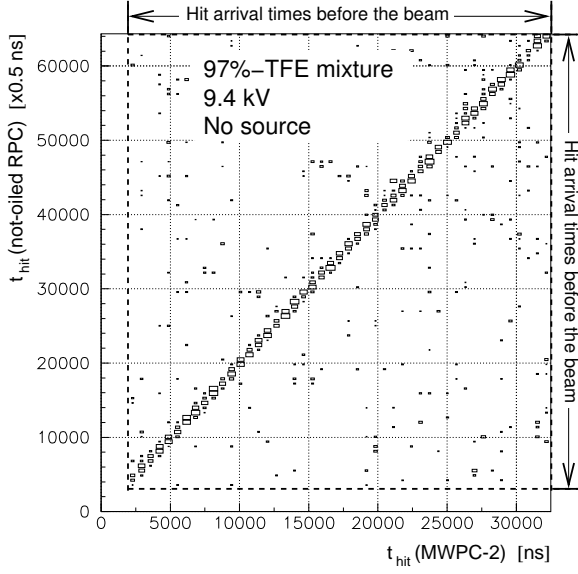


Figure 4.48: Correlation between hit arrival times in one of MWPCs and not-oiled RPC operated at 9.4 kV without irradiation source and filled with 97%-TFE gas mixture. Only hits coming before the main acceptance window used for efficiency and timing measurements are shown.

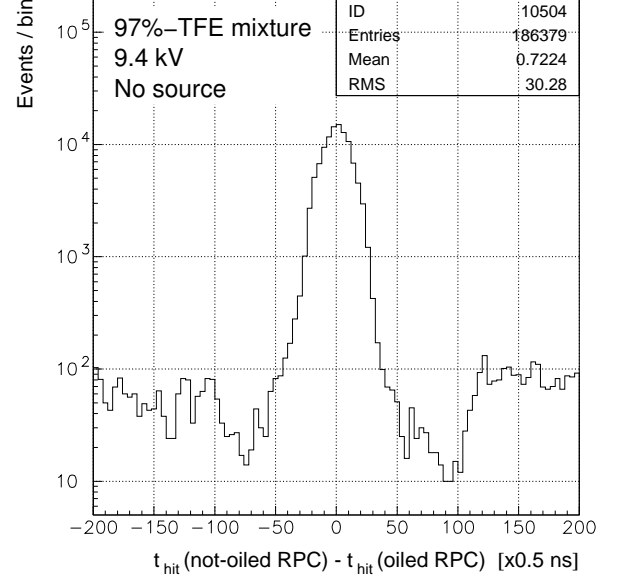


Figure 4.49: Distribution of the arrival time difference calculated for each pair of hits in two RPCs. Only hits coming before the main acceptance window used for efficiency and timing measurements are considered (97%-TFE gas mixture, nominal operating voltage of 9.4 kV in each RPC gap, no source).

uncorrelated (e.g. from gamma rays or spontaneous noise) flat distribution should be observed. An evident peak indicates existence of particles penetrating two gaps at a time.

Different counting rates without irradiation for two tested gas mixtures at voltages corresponding to the efficiency plateau (open markers in Fig. 4.44), measured when the muon beam was present, can be attributed to changes of the beam intensity between two data sets. Namely, the average muon flux measured by scintillators hodoscope over $10 \times 10 \text{ cm}^2$ area was 3 times higher for data set corresponding to 97%-TFE gas mixture.

One can conclude from Figs. 4.47-4.49 that true intrinsic noise should be measured without the muon beam only. Results with random trigger have shown that the spontaneous noise rate is smaller by a factor of 10 in the oiled module. Nevertheless, even for the not-oiled detector it ranges between 1 Hz/cm^2 and 10 Hz/cm^2 over almost 1 kV-wide voltage range starting from 9.4 kV (beginning of the efficiency plateau at the highest gamma rate). From the above results it is possible to infer that both, not-oiled and oiled modules, satisfy well CMS requirements imposed on the intrinsic RPC noise discussed in Section 1.2.4.

From Fig. 4.45 one can expect even better performance on the intrinsic noise rate for 0.7%-SF₆ gas mixture, which exhibits less steeper dependence of the current and the gas gain on the applied voltage (full squares) than SF₆-free gas mixture (full circles). Hence, also dependence of the intrinsic noise rate on the high voltage with SF₆ gas should be less steeper than that depicted

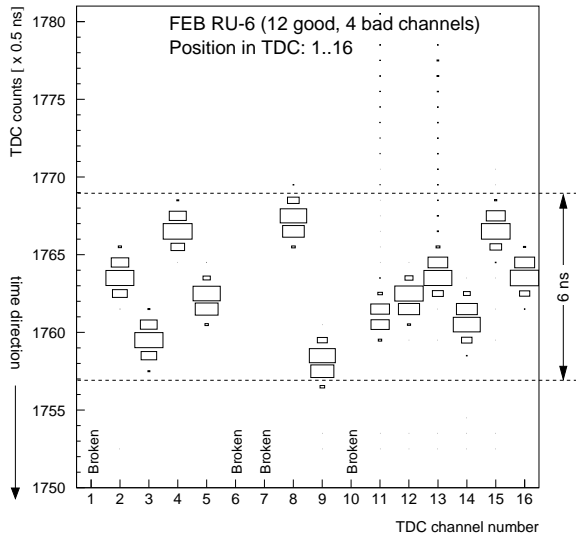


Figure 4.50: Test pulse time distributions for one of front-end boards showing offsets between individual channels due to: front-end chip and LVDS-to-ECL converter. Identical test pulses were injected into all RPC strips simultaneously.

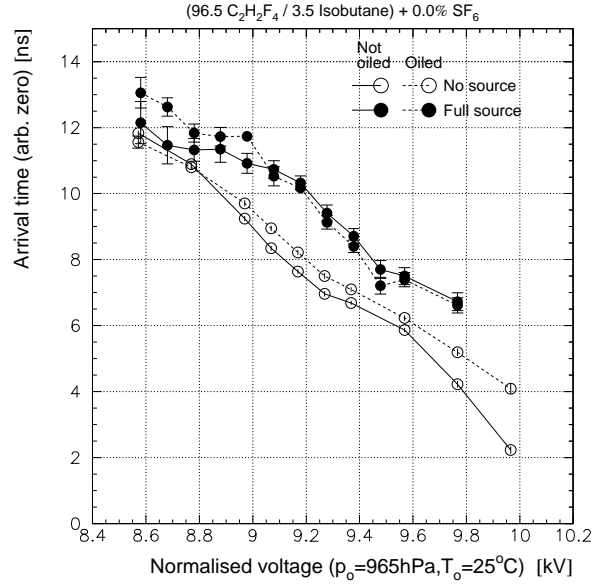


Figure 4.51: Signal arrival time of single gap RPC modules, with respect to the trigger counters, as a function of normalized H.V. for 97%-TFE gas mixture and for two intensities of gamma rays: fully opened source (filled markers) and closed source (open markers). Solid and dashed lines correspond to non-oiled and oiled module, respectively.

in Fig. 4.47.

The timing characteristics of single gap RPCs have been studied. The results presented in this work refer to the same 100 ns time window used for efficiency measurement. The precise calibration of individual electronic channels is mandatory. From a calibration data relative delays and different time spreads have been observed for electronic channels. An example of the response of one of the front-end boards to a test pulse injected simultaneously into all channels⁵ is shown in Fig. 4.50. It can be seen that relative delay between channels reaches 6 ns and that some channels exhibit larger time spreads and have long tails of the time distribution. The following reasons have contributed to the observed non-uniform response of the front-end electronics: the developmental amplifiers used in the front-end boards have not been carefully selected after their production to maintain uniform timing characteristics of all channels, and the LVDS-to-ECL converters placed after FEBs have increased the time spread of the output signals. It should be stressed however, that these drawbacks are specific only to the particular experimental set-up and developmental readout boards used in the tests. In the final front-end boards, to be installed in the CMS detector, only pairs of front-end chips of the same gain and timing characteristics

⁵The calibration run has been performed by injecting a rectangular voltage pulse to the high voltage plane of each RPC module. The amplitude of the pulse was large enough to induce signal above electronic threshold on each strip.

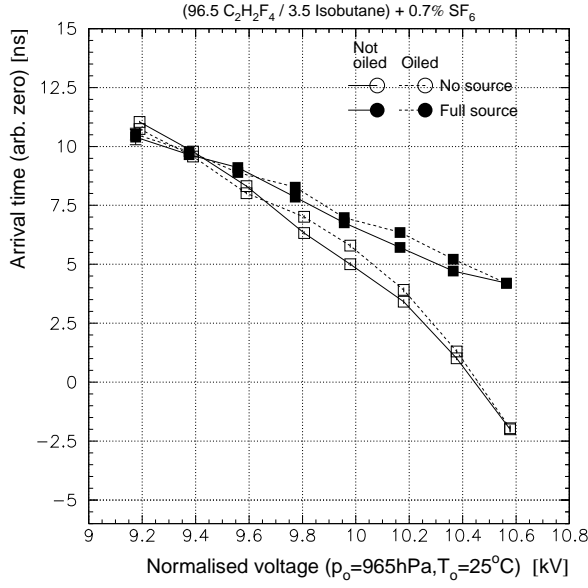


Figure 4.52: Signal arrival time of single gap RPC modules, with respect to the trigger counters, as a function of normalized H.V. for 0.7%-SF₆ gas mixture and for two intensities of gamma rays: fully opened source (filled markers) and closed source (open markers). Solid and dashed lines correspond to non-oiled and oiled module, respectively.

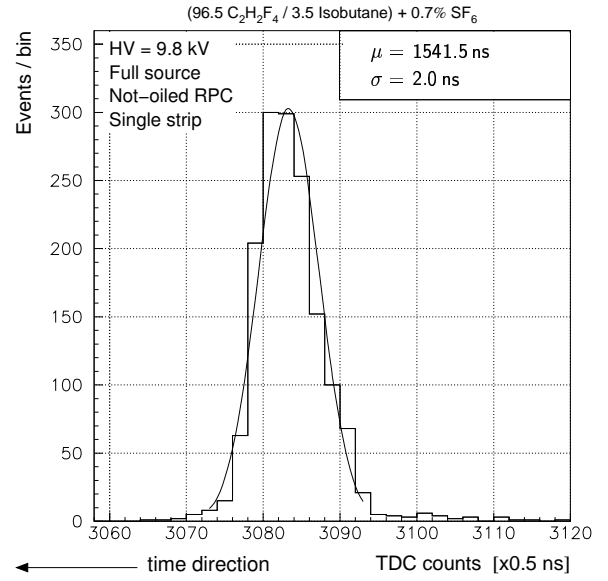


Figure 4.53: Signal arrival time distribution, with respect to the trigger counters, from one of the readout strips of not-oiled RPC module filled with 0.7%-SF₆ gas mixture and operated at 9.8 kV and at full source intensity. A fitted normal distribution is also superimposed.

will be used. Moreover, in the CMS there will be no LVDS-to-ECL converter after the FEB, since the FEB is connected directly to the Link Board⁶ accepting signals in LVDS standard [27].

The calibration run has been done only once during test beam period, therefore the spread of the timing variations between channels could vary from one data taking to another. Nevertheless, for the off-line analysis of the beam test data all hit arrival times have been corrected for individual channel delays according to results from the calibration run.

The mean arrival times, with respect to the scintillators hodoscope, as a function of the operating voltage for 97%-TFE gas mixture are depicted in Fig. 4.51. Data points correspond to the first signal detected during fixed 100 ns-wide time window, the same as in efficiency measurements, from 16 and 12 consecutive strips of not-oiled and oiled RPC, respectively. The hits arrive faster at higher voltages due to increase of the drift velocity and the signal pulse-height. Time walk due to radiation ranges from 1.5 ns to 2.5 ns for 9.4 kV (beginning of the efficiency plateau) and 9.8 kV (400 V above the efficiency knee). In Fig. 4.52 results on mean arrival time for 0.7%-SF₆ gas mixture are shown. It can be seen that in the voltage range between 9.8 kV and 10.2 kV, corresponding to the first 400 V of the efficiency plateau, the time walk due to rate

⁶The Link Board collects LVDS signals from up to 3 FEBs (16-channel each), synchronizes these signals with the LHC clock, performs zero-compression and sends the data by optical link transmitter to the CMS counting room.

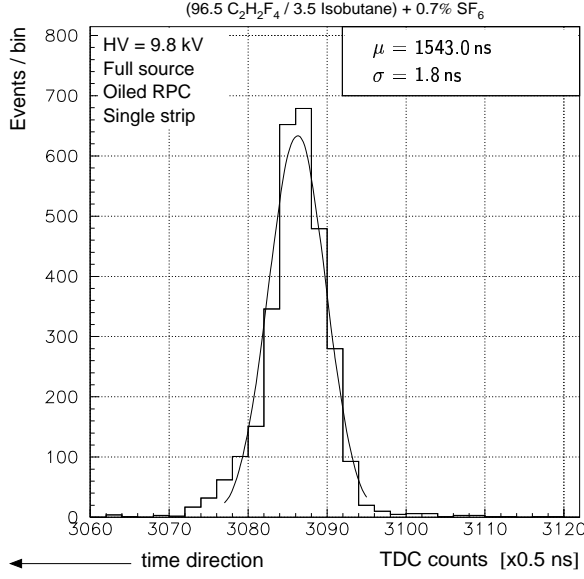


Figure 4.54: Signal arrival time distribution, with respect to the trigger counters, from one of the readout strips of oiled RPC module filled with $0.7\%-SF_6$ gas mixture and operated at 9.8 kV and at full source intensity. A fitted normal distribution is also superimposed.

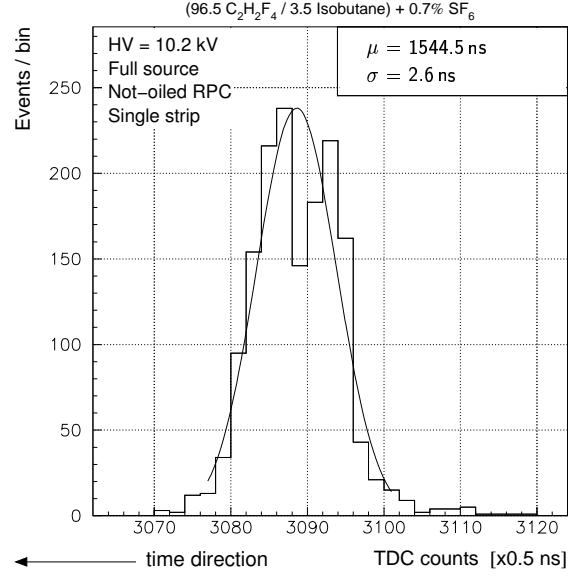


Figure 4.55: Signal arrival time distribution, with respect to the trigger counters, from one of the readout strips of not-oiled RPC module filled with $0.7\%-SF_6$ gas mixture and operated at 10.2 kV and at full source intensity. A fitted normal distribution is also superimposed.

increases from 1.5 ns to 2.5 ns.

The intrinsic RPC time resolution can be approximated from the arrival time distribution from a single strip. However, even such distribution can be affected by eventual non-uniformity of the gas gap thickness over area the signal is read out from. The arrival time distributions⁷ for voltage corresponding to the beginning of the efficiency plateau at full intensity of gamma rays and for $0.7\%-SF_6$ gas mixture are depicted in Figs. 4.53 and 4.54 for not-oiled and oiled RPC, respectively. Their shape can be well characterized by a normal distribution fitted to the data shown in each figure. Arrival time distributions corresponding to 400 V above the efficiency knee for not-oiled and oiled module are presented in Figs. 4.55 and 4.56, respectively. Broader time spectra can be observed than for 9.8 kV data. At voltages higher than 10.2 kV the time distributions exhibit deviation from the Gaussian shape, namely tails occur after the main peak and excess of events in front of the main peak can be observed. The events responsible for increasing of the time spread are characterized by large strip multiplicity (e.g. > 10 for 100 ns gate width), what can be explained as formation of streamers at the highest electric fields studied.

The signal time spread from single strip, resulted from Gaussian function fit to the measured arrival time distribution, as a function of the high voltage is shown in Fig. 4.57 for not-oiled (solid line) and oiled (dashed lines) prototype and for two gas mixtures tested. From the above

⁷Note reversed horizontal time scale in Figs. 4.53-4.56.

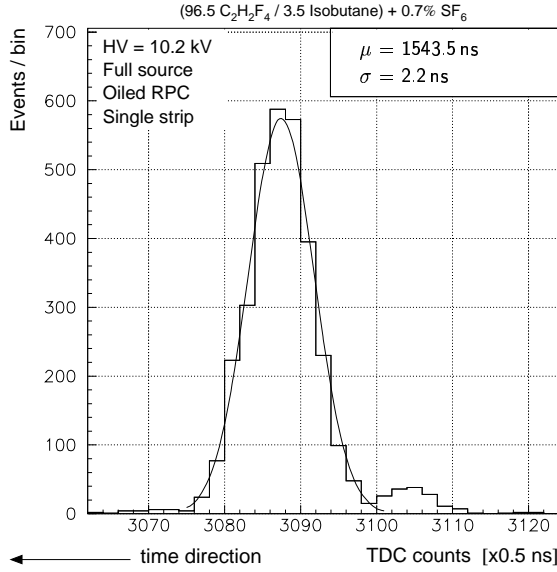


Figure 4.56: Signal arrival time distribution, with respect to the trigger counters, from one of the readout strips of oiled RPC module filled with $0.7\%-SF_6$ gas mixture and operated at 10.2 kV and at full source intensity. A fitted normal distribution is also superimposed.

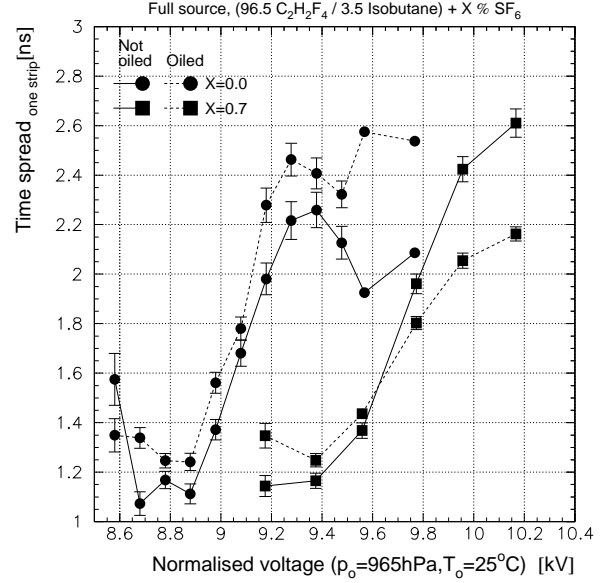


Figure 4.57: Signal arrival time spread of single gap RPC modules, with respect to the trigger counters, as a function of normalized H.V. for $97\%-TFE$ gas mixture and for full intensity of gamma rays. Each point correspond to fitted normal distribution to the main peak of the arrival time distribution from single strip. Solid and dashed lines correspond to non-oiled and oiled module, respectively.

figure it can be concluded that practical time resolution is better than 2.6 ns for the first 400 V of the efficiency plateau for both gases at the highest intensity of gamma rays studied. However, the intrinsic time spread should be even better.

Since the CMS Muon Trigger system has to efficiently assign muons to individual bunch crossings occurring every 25 ns, it is necessary to test performance of RPC detectors as a function of the width of the acceptance window synchronized with the accelerator's clock. During test beams discussed in this Section the acceptance window has been synchronized with the signal from scintillators hodoscope. The dependence of the efficiency on the gate width has been measured in the following way: for each working voltage the time window of acceptance having fixed width was opened symmetrically around mean value of the arrival time distributions shown Figs. 4.51 and 4.52. Four gate widths have been considered, namely: 10 ns, 15 ns, 20 ns and 100 ns.

In Figs. 4.58 and 4.59 the efficiency (open circles) as a function of the high voltage is shown at full intensity of gamma rays for not-oiled RPC filled with $97\%-TFE$ and $0.7\%-SF_6$ gas mixture, respectively. Corresponding gate widths in nanoseconds are indicated for each curve. Obviously 100 ns gate width cannot be used in RPCs working at the LHC because of bunch crossing

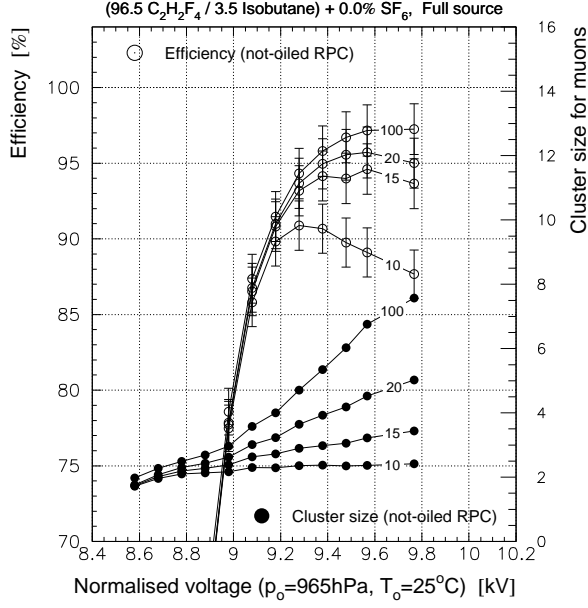


Figure 4.58: Efficiency (open circles) and cluster size in strips (filled circles) for not-oiled RPC module as a function of normalized high voltage for 97%-TFE gas mixture and for full intensity of gamma rays. For each curve the width of the acceptance window in nanoseconds is shown.

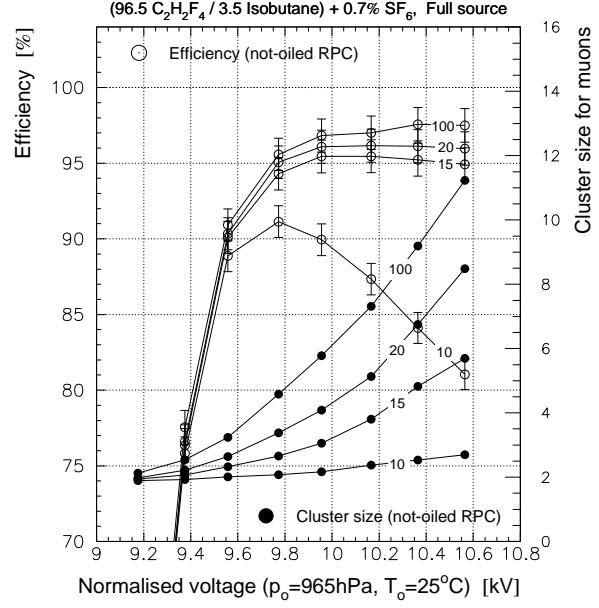


Figure 4.59: Efficiency (open circles) and cluster size in strips (filled circles) for not-oiled RPC module as a function of normalized high voltage for 0.7%- SF_6 gas mixture and for full intensity of gamma rays. For each curve the width of the acceptance window in nanoseconds is shown.

identification requirement. By inspection of the two figures one can conclude that 10 ns gate is too short to achieve the required muon detection efficiency of 95% at avalanche rates of 1 kHz/cm^2 . For 97%-TFE gas mixture the gate width of 20 ns allows one to reach 95% efficiency level. For 0.7%- SF_6 gas mixture even shorter gate of 15 ns is sufficient enough to achieve 95% efficiency over 800 V-wide voltage range. The results on the oiled RPC gap module are very similar and, therefore, are not shown.

The charge induced on a given readout strip consists of two components: direct current due to avalanche development and pick-up from surrounding strips. The first component depends on the distance between avalanche axis and the edge of the strip. There is a characteristic maximum distance from strip at which average-size avalanche can induce on that strip the signal above fixed electronic threshold. The doubled characteristic distance will be referred as *geometric cluster width*. The second component of the induced signal depends on capacitance matrix of the strip under consideration to all other strips. It will be denoted as *cross-talk*. For typical strip geometries used in RPCs, however, the strip width is $\sim 1\text{ cm}$ and only capacitive coupling between pairs of adjacent strips is important. On the first approximation this coupling is reciprocal to the gap between strips and is proportional to the length of their common edge.

The geometric cluster width has been measured during beam tests of the IDG prototype in 2000, when the muon beam partially illuminated two adjacent groups of strips equipped with readout electronics (denoted as Section 1 and 2 in Fig. 3.19 A). Results correspond to the following working conditions: gas mixture denoted as $1.5\%-SF_6$ in Tab. 3.7, operating voltage of 11.2 kV on each RPC gap, irradiation source switched off and 100 fC electronic threshold. The rectangular prototype tested has almost identical strip geometry as two single gap prototypes, namely $10\text{ mm} \times 200\text{ mm}$ strips separated by 2 mm gap from each side. Therefore coupling between a pair of neighbouring strips belonging to different sections is negligible in comparison with coupling between adjacent strips of the same section. The fraction of events having hits in both sections as a function of the muon position along strip direction is depicted in Fig. 4.60 (full circles). A Gaussian function fitted to the data points corresponds to the muon tracks in the vicinity of the border between two sections (open circles). The dispersion $\sigma \approx 6\text{ mm}$ has been found constant for voltages corresponding to the first 1 kV of the efficiency plateau. Hence, one can estimate the observed geometric avalanche width as $4\sigma \approx 24\text{ mm}$ which corresponds to the minimal cluster size of 2 strips having 12 mm pitch providing that cross-talks between strips are neglected. For gas mixtures denoted as $97\%-TFE$ and $0.7\%-SF_6$ one can expect similar geometric cluster width at full efficiency as for $1.5\%-SF_6$ gas mixture, since the efficiency scales with current density for small percentage of SF_6 in the basic TFE/Isobutane gas mixture as can be seen from Fig. 4.46.

The dependence of the strip multiplicity on the high voltage for not-oiled RPC at full source intensity is depicted in Figs. 4.58 and 4.59 (full circles) for $97\%-TFE$ and $0.7\%-SF_6$ gas mixture, respectively. The curves are labeled with corresponding gate widths in nanoseconds. It can be seen from Fig. 4.59 that for 15 ns gate, the narrowest gate providing acceptable efficiency for $0.7\%-SF_6$ gas mixture, for the first 400 V of the efficiency plateau, between 9.8 kV and 10.2 kV, the strip multiplicity increases from 2.8 to nearly 4. Therefore measured cluster size of single gap model detectors having 12 mm strip pitch is higher than 2, which is the upper limit imposed on

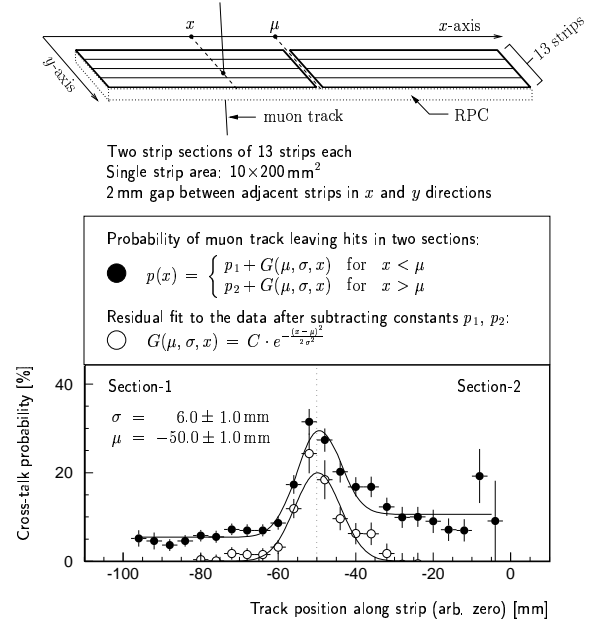


Figure 4.60: Probability of inducing signals on two strip groups at a time as a function of position of the muon track along strip measured for IDG module tested in the GIF in 2000 ($1.5\%-SF_6$ gas mixture, 11.2 kV, no irradiation source, 100 fC threshold).

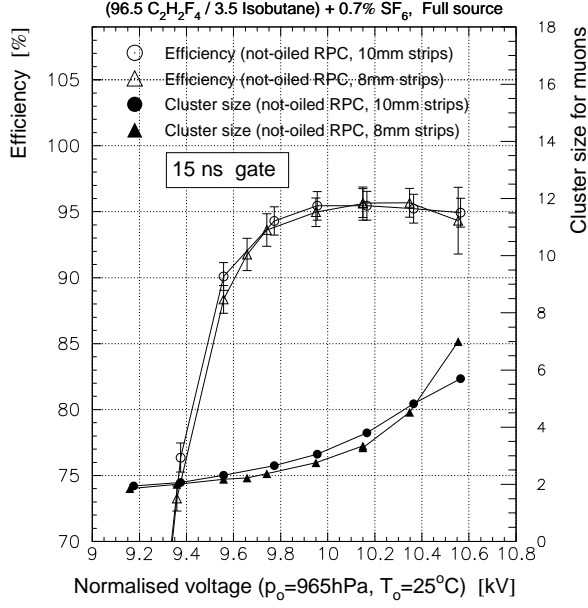


Figure 4.61: Efficiency (open markers) and cluster size in strips (filled markers) for not-oiled RPC module as a function of normalized high voltage for: $0.7\% \text{-SF}_6$ gas mixture, full intensity of gamma rays and two strip sections having: 8 mm (triangles) and 10 mm (circles) strip width. Data for 15 ns acceptance window is shown.

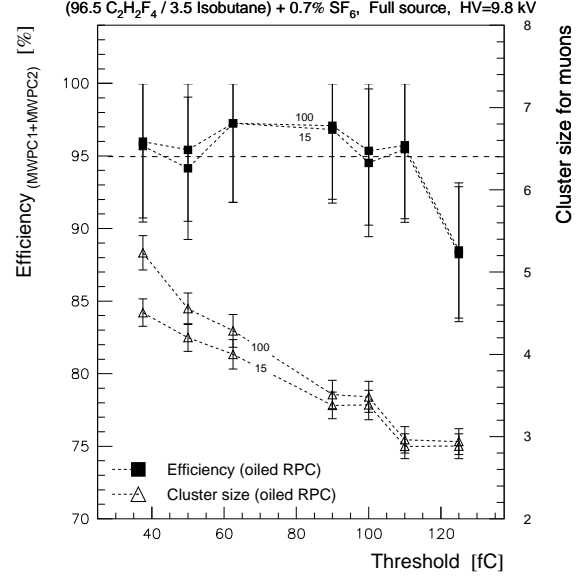


Figure 4.62: Efficiency (squares) and cluster size in strips (triangles) as a function of electronic threshold for oiled RPC module for: nominal voltage of 9.8 kV, $0.7\% \text{-SF}_6$ gas mixture and full intensity of gamma rays. For each curve the width of the acceptance window in nanoseconds is shown.

RPCs for the CMS Muon Trigger. Moreover, the strip multiplicity exceeding geometric cluster width, previously discussed, infers significance of the cross-talk effect for adjacent strips.

The results presented so far in this Section corresponded to the electronic threshold of 100 fC and RPC sections having 10 mm-wide strips of 12 mm pitch (see Fig. 3.20 A). In order to check whether cross-talks can be significantly reduced if one separates readout strips by 4 mm instead of 2 mm providing that the strip pitch is the same, the two tested RPCs have been moved horizontally by 20 cm in such a way that the spot of the muon beam illuminated central area of the section equipped with 8 mm-wide strips (i.e. second section from the right in Fig. 3.20 A). As in the case of previous position the muon beam has been centered on one of the spacers. The results on efficiency and strip multiplicity for not-oiled RPC filled with $0.7\% \text{-SF}_6$ gas mixture and working at full source intensity are depicted in Fig. 4.61. The curves correspond to 15 ns gate width. One can observe that neither significant improvement of the cluster size nor significant degradation of the efficiency can be observed for 8 mm-wide strips. Eventual differences can be attributed, for example, to a slightly different gas gap thickness of the two regions studied.

One can reduce strip-to-strip capacitive coupling and decrease signal cross-talks by increasing gap width between neighbouring readout electrodes beyond 4 mm. However, due to fine strip pitch ($\sim 1 \text{ cm}$) in φ direction of RPC detectors foreseen in the large rapidity regions of the CMS

experiment the gap between strips cannot be increased at will. Further decrease of the strip width can result in unacceptably large regions of reduced efficiency. Nevertheless even for 2 mm gap it is possible to reduce cross-talks by introducing so called *guard strips* in between signal strips. In work by Riegler and Burgarth [138] a reduction by $\approx 30\%$ of the cross capacitance between neighbouring signal strips has been calculated due to use of the guard strips. The authors simulated geometry of single gap RPC equipped with readout plane having: 25 mm wide signal strips, 27 mm pitch and 0.5 mm wide guard strips. They have shown that in order to minimize reflections and cross-talks all strips should be interconnected at one side (i.e. opposite to the location of the amplifiers). Furthermore, it is important that the guard strips are not directly grounded but also included in the termination network. Practically, satisfactory results can be obtained if only each strip is interconnected to its first- and second neighbour via properly matched resistors.

Such fine tuning of the strip segmentation and the termination network is not foreseen in the baseline RPC design for the CMS experiment [28]. Moreover, it is even considered not to terminate readout strips in the endcap chambers at all [139, 140]. One of the reasons is the fact that only single gap chamber or Inverted Double Gap one could provide space necessary to place matching resistors at strip ends.

The dependence of detector characteristics on the electronic threshold has been investigated only for the oiled RPC module filled with $0.7\%-SF_6$ gas mixture. The data has been taken at different position of the chamber, namely when the muon beam partially illuminated RPC frame. For correct evaluation of the efficiency only muons leaving tracks in two MWPCs and crossing area of $8 \times 3 \text{ cm}^2$ over RPC plane were accepted for the analysis, what reduced the number of useful events of each run and, thus, increased statistical errors. The resulting dependence of the efficiency and cluster size on electronic threshold is presented in Fig. 4.62 for two gate widths and for the operating voltage of 9.8 kV corresponding to the beginning of the efficiency plateau. It can be seen from the figure that only at 125 fC, the highest threshold studied, the inefficiency becomes significant. Moreover, a weak dependence of the efficiency on threshold is a characteristic feature of RPCs operated in a saturated avalanche mode. For 15 ns gate the effect of increasing the threshold from 40 fC to 125 fC manifests in reduction of the average strip multiplicity by about 40%. The strip cluster size of 2.8 is a practical limit for full efficiency.

One can conclude on the results presented in this Section that two medium-size single gap modules assembled using novel RPC technique behave very well at radiation environment inducing avalanche rates of about $1 \text{ kHz/cm}^2/\text{gap}$. Performances of the not-oiled and the oiled chamber are very similar at high particle fluxes. The efficiency is $\geq 95\%$ with plateau width exceeding 400 V even for gate width as low as 15 ns. The intrinsic time resolution is better than

2.6 ns. The not-oiled module features very low noise rate, which is well below the required limit of 20 Hz/cm² for RPCs in the CMS detector.

Adding 0.7% of SF₆ to the basic Tetrafluoroethane/Isobutane gas mixture broadens the efficiency plateau, saturates the gas gain and reduces the spontaneous RPC noise. A serious drawback, however, is the mean strip multiplicity greater than 2.8 for the fine readout strip segmentation of 12 mm pitch, which is similar the geometry implemented in the ME1/1 RPC station.

In order to minimize strip multiplicity in RPCs for large rapidity regions of the CMS detector the following issues need to be solved:

- The amount of SF₆ freon in the gas mixture still needs optimization. The value of 0.7% seems to be too small for providing streamer-free efficiency plateau larger than 400 V and, therefore, the gas mixture characterized by more sustained avalanche growth with the electric field should be worked out.
- It is advisable that the geometry of the readout strips in RPC stations having strip pitch ≈ 10 mm in φ direction is revised. The reduction of cross-talks and, thus, of the strip multiplicity could be possible by means of: increase of the gap between strips beyond 4 mm (for the cost of decreasing the strip area) and/or insertion of special guard strips with a network of termination resistors.
- The electronic threshold of 100 fC has been chosen in a conservative way on the basis of results from previous beam tests, when rather high thresholds were crucial to reduce large intrinsic noise rate. It is likely that last two single gap prototypes exhibiting extremely low noise rate can effectively detect muons even at lower voltages providing that an electronic threshold is decreased. If this will be the case the streamer-free efficiency plateau can be naturally enlarged, but it has to be verified experimentally whether working with lower gas gains and at lower thresholds can simultaneously provide reduction of the strip multiplicity to acceptable level, from the PACT system point of view, for the first few hundred volts of the efficiency plateau.

Chapter 5

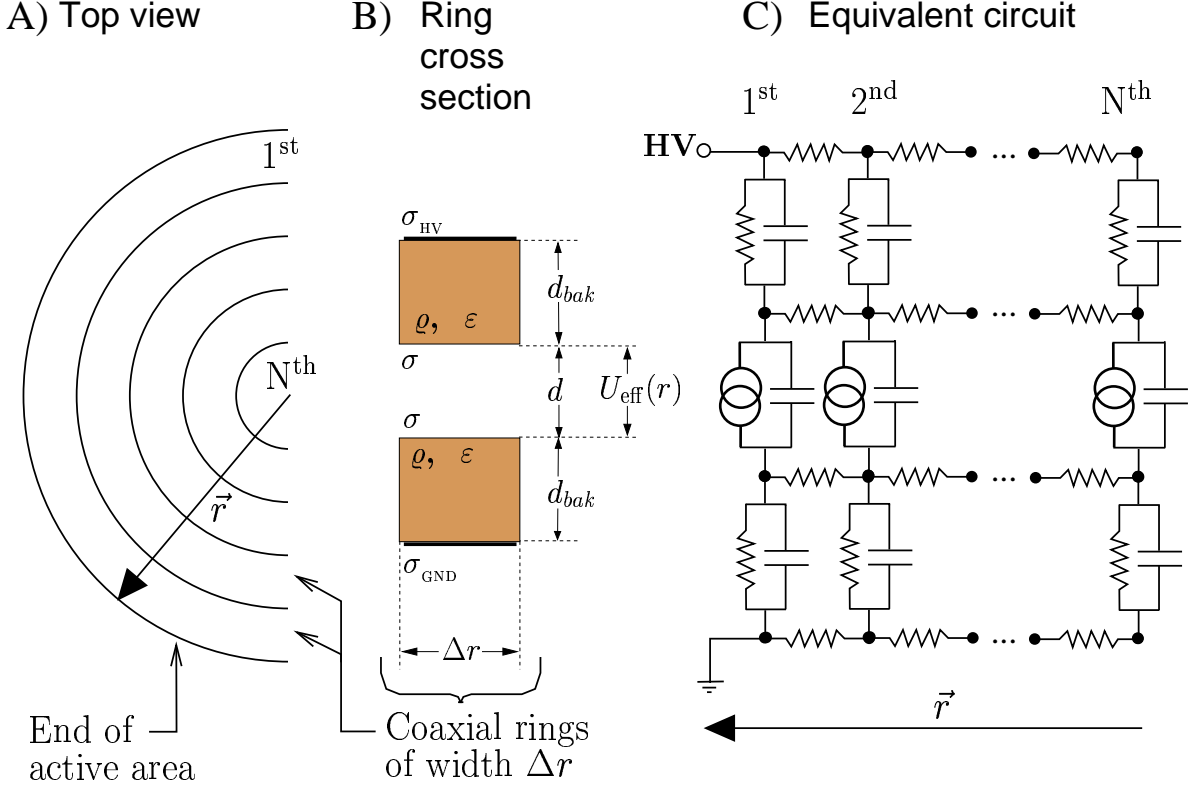
Equivalent circuit simulations

A detailed simulation of a RPC of a given geometry and working at high rates is a complicated matter. Many parameters have to be taken into account, such as: dependence of the total avalanche charge distribution on the electric field, avalanche rate, surface- and volume specific resistances and permittivities of materials constituting the detector.

A significant progress has been done during recent few years in simulation of signals delivered by RPC based on first principles, starting from gas properties calculations [45, 131] and ending on strip-to-strip cross talk [138]. Yet, there is no single computer program which takes into account all known issues concerning RPC operation.

For example, a general purpose program for gaseous detector simulation named GARFIELD- [141], available at CERN program library, has been interfaced with HEED [45], IMONTE [131] and MAXWELL [142] programs and allows one to study almost arbitrary detector geometry and gas mixture. However, at present, it is not suitable for simulation of the whole RPC detector working at high particle fluxes. Firstly, the electric field reaches equilibrium state only after certain time from starting the irradiation, as it has been already demonstrated with pulsed accelerator beams in Section 4.1. The field obtained with MAXWELL electrostatic field solver does not take into account local “resistivity” of the gas, which is in turn dependent of the electric field. Moreover, the surface resistivity is not taken into account, what results in overestimation of the electric field strength near spacers and frames. Secondly, the GARFIELD program itself has not got a space charge mechanism built in, which is of great importance if one operates with electronegative gases in saturated proportional mode.

On the other hand, a dedicated computer code for calculation of the electric field inside a RPC presented in Ref. [65] assumes uniform “resistivity” of the entire gas volume, independent on the electric field. Hence, the results are meaningful for low particle rates only.



SPICE model parameters:

$N, r, d_{bak}, d, \rho, \epsilon, \sigma, \sigma_{HV}, \sigma_{GND}, Q_{tot}(U_{eff})$ **parametrization, avalanche rate**

Figure 5.1: Proposed working model for SPICE simulation: (A) Division of the active area into coaxial rings, (B) Cross section of a single ring, (C) Equivalent electric circuit.

5.1 Proposed model

In this work an equivalent RPC model is proposed to predict effective potential difference across the gas gap, which is a major parameter governing local efficiency and timing. The results can be a good starting point for detailed signal simulations.

The idea is to divide a RPC into cells which can be described in terms of known capacitances, resistances and current sources. To reduce computing time the problem was referred to two dimensions by a simple assumption that the chamber has axial symmetry as depicted in Fig. 5.1 A. For simplicity spacers and frames were not included in the model since they introduce non-zero transverse components of the electric field strength. Therefore, the chamber of radius R has been divided into N rings of width Δr each, which cross section is shown in Fig. 5.1 B. The thickness of the gas gap and of the bakelite plates are $d = 2\text{mm}$ and $d_{bak} = 2\text{mm}$, respectively. The volume- and surface resistivity of the electrodes are given by ρ and σ parameters, respectively.

A relative dielectric permittivity of $\epsilon_r = 10$ was assumed for the bakelite [138]. For a given geometry the voltage potential is distributed over the active area by means of a thin, resistive carbon layer (graphite paint) which is in electrical contact with two ring-shaped outer electrodes connected directly to a high voltage power supply. Surface specific resistances of the graphite are denoted as σ_{GND} and σ_{HV} for the strip- and the high voltage side, respectively. An equivalent electrical circuit is shown in Fig. 5.1 C. Each j -th ring is located at the distance $r_j = r \cdot j/N$ from the centre and has a constant current source dependent on the potential difference $U_{\text{eff}}(r_j)$ given by:

$$I_j = R_{\text{aval}} \cdot S_j \cdot Q_{\text{tot}} \left(\frac{U_{\text{eff}}(r_j)}{d} \right) \quad (5.1)$$

where R_{aval} , S_j and Q_{tot} are: rate of induced avalanches, area of the j -th ring and the average total avalanche charge per single event, respectively. The parametrization of Q_{tot} as a function of the electric field for a given gas mixture can be taken from test beam data.

In simulations presented in this Chapter the dependence of Q_{tot} on the electric field has been extracted from the test beam data discussed in Section 4.4.1 for gas mixture TFE/Isobutane/SF₆ (96.3/3.2/0.5). A tested prototype was exposed to a photon flux inducing rate of avalanches $R_{\text{aval}} \simeq 1.1 \text{ Hz/cm}^2/\text{gap}$. The corresponding current density $\frac{dI}{dS}$ as a function of the effective gas gap voltage defined by equation 2.30 is plotted in Fig. 5.2 for fully opened- (filled circles) and fully closed (open circles) source. Resistivity of the bakelite plates was taken from Tab. 3.2 (i.e. PL-#20 at 23°C). For this particular prototype currents due to spontaneous avalanches (“noise” curve) and leakage through spacers and frames (“ohmic” curve) were

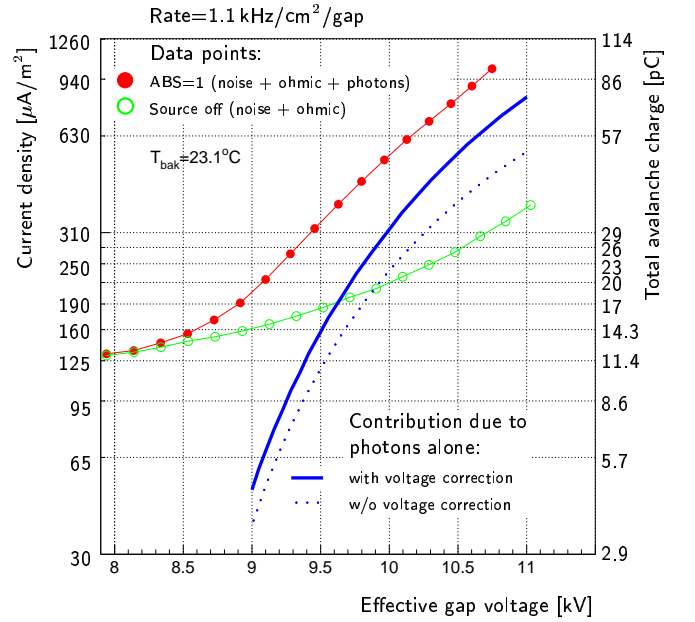


Figure 5.2: Dependence of the measured current density with- and without irradiation (full and open circles, respectively) on the effective gas gap voltage used to extract parametrization of the gas gain (thick, solid curve). Data for prototype tested at the GIF with TFE/Isobutane/SF₆ (96.3/3.2/0.5) gas mixture in 2001.

non-negligible. Contribution due to avalanches induced by photons was derived as follows: two fifth degree polynomial fits were performed to data points corresponding to full source intensity and source switched off, respectively. The resulting curves were subtracted to obtain an analytic parametrization of the average charge induced by gamma photons $Q_{\text{tot}}(E)$ (thick solid curve). A significance of the voltage correction procedure can be seen by comparison of the dotted curve (without correction, i.e. *effective gap voltage* \equiv *nominal voltage*) and the solid curve (with correction) in Fig. 5.2.

5.2 Results of calculation

The simulations were performed using SPICE program [143]. A model having radius $R = 20$ cm consisted of $N = 100$ cells. Length R corresponds to a characteristic distance from the symmetry axis of a trapezoidal ME 1/1 module to the nearest graphite edge, where the voltage potential is supplied. As it was already pointed out in Section 1.2.4, the ME 1/1 station is the most demanding one concerning neutron induced background rates. Therefore the current density inside the gas in simulated model corresponds to the maximal expected hit rate of $1 \text{ kHz/cm}^2/\text{gap}$.

Two volume specific resistances were considered, namely, $10^{10} \text{ } \Omega\text{cm}$ and $10^{11} \text{ } \Omega\text{cm}$, denoted as low- and high resistivity chamber, respectively. For each of them four graphite painting scenarios were calculated as listed in Tab. 5.1. Results of SPICE transient analysis are shown in Figs. 5.3 and 5.4 for low- and high resistivity chamber, respectively. Dotted curves correspond to the edge of the active gas volume, while dashed ones to the middle of the chamber, where additional voltage losses due to graphite surface resistivity may occur. The calculated voltage deviation from the nominal applied voltage due to: avalanche current, graphite coating- and bakelite resistivity are listed together in Tab. 5.1. From present simulation an effect of the carbon layer resistivity is only visible for low resistivity chamber having at least one of two sides coating with graphite layer of $10^6 \text{ } \Omega/\square$ surface resistivity. The results agree with the work by Battistoni et al. [62] showing that full signal transparency is achieved at graphite surface resistivity above $10^5 \div 10^6 \text{ } \Omega/\square$. Hence, one can conclude that a standard graphite coating procedure (last column in Tab. 5.1) does not influence uniformity of the potential distribution over the active area at given rate. Another conclusion from SPICE simulations is a potential danger of increasing resistivity of electrodes due to dry gas flow and/or accumulated charge. Taking into account the gas gain dependence depicted by thick solid curve in Fig. 5.2 and the calculated voltage deviations from the nominal applied voltage one can conclude that an increase of bakelite resistivity by one order of magnitude from $10^{10} \text{ } \Omega\text{cm}$ infers loss of the gas gain by a factor of 2.

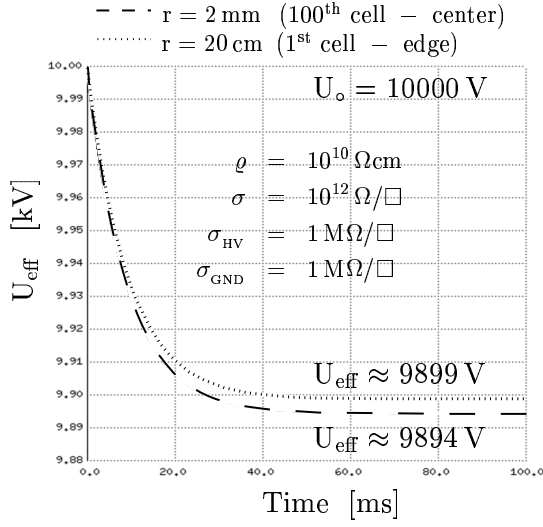


Figure 5.3: Simulated potential difference in the gas gap after starting the irradiation for low resistivity RPC with a highly resistive graphite paint. Gas gain parametrization from Fig. 5.2.

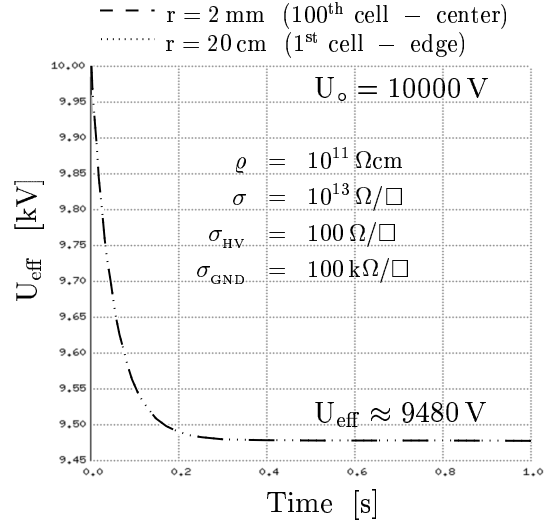


Figure 5.4: Simulated potential difference in the gas gap after starting the irradiation for high resistivity RPC with a standard graphite coating. Gas gain parametrization from Fig. 5.2. The two curves overlay.

Table 5.1: Calculated deviation from the nominal applied voltage of 10 kV at 1 kHz/cm²/gap for several sets of SPICE model parameters. Gas gain parametrization from Fig. 5.2.

Resistivity of the electrodes	Distance from the centre in [mm]	Voltage shift in [V]			
		$\sigma_{HV} = 1 \text{ M}\Omega/\square$ $\sigma_{GND} = 1 \text{ M}\Omega/\square$	$\sigma_{HV} = 100 \text{ k}\Omega/\square$ $\sigma_{GND} = 100 \text{ k}\Omega/\square$	$\sigma_{HV} = 100 \Omega/\square$ $\sigma_{GND} = 1 \text{ M}\Omega/\square$	$\sigma_{HV} = 100 \Omega/\square$ $\sigma_{GND} = 100 \text{ k}\Omega/\square$ *)
$\rho = 10^{10} \Omega\text{cm}$	2	-101	-101	-101	-101
	200	-106	-101	-103	-101
$\rho = 10^{11} \Omega\text{cm}$	2	-520			
	200				

*) A typical graphite coating in RPCs for the CMS experiment.

For simulated chamber geometry with integrated metallic foils on the outer bakelite electrodes ($\sigma_{\text{HV}}, \sigma_{\text{GND}} \ll 10^5 \Omega/\square$) the potential is almost uniformly distributed over the entire outer bakelite surfaces and the results are identical to that plotted in Figs. 5.3 and 5.4 with dotted curves and are independent on radius r . In such chambers all strips must be grounded through load resistors R_o , because readout electrodes are, at the same time, field shaping ones. The constant voltage drop on R_o should be, however, as small as possible. For example, the upper limit on R_o would be about $6 \text{ k}\Omega$ in order to keep strip potential at 100 mV level due to $1 \text{ kHz/cm}^2/\text{gap}$ rate at typical voltage working point corresponding to the total avalanche charge of 30 pC and for strips of of $4 \times 130 \text{ cm}^2$ area, i.e. the longest ones foreseen in the CMS RPC system. However, values of termination resistors foreseen in RPC detectors for the CMS are far below this limit since the characteristic strip impedance is of the order of 10Ω . In the cases of prototypes tested in the GIF, having $R_o = 1 \text{ k}\Omega$ and strips of $1 \times 20 \text{ cm}^2$ area, the voltage drop on load resistors was comparable with electronics noise. It should be stressed that in RPCs having outer metallic anode segmented into strips, the DC component of the current collected from the readout electrodes does not affect fast signals providing that the front-end amplifiers are AC-coupled to strips (e.g. such design is adopted for the CMS detector).

The SPICE model presented in this Chapter shows importance of the stability of the bakelite conductivity with time for RPCs operated under uniform high particle flux. The influence of the graphite paint resistivity on uniformity of the high voltage distribution is marginal up to $1 \text{ M}\Omega/\square$ for medium-size detector operated in avalanche mode under 1 kHz/cm^2 rate of avalanches in a single gas layer.

Similar model can be used to study gas gain behaviour around spacer or frame, though, the results would be biased by neglecting non-zero transverse component of the electric field (e.g. real electron drift lines would be longer what influences avalanche growth). There are recent experimental indications from the BABAR experiment, having RPCs operated in a streamer mode, that conductivity of the linseed oil used to smooth internal bakelite surfaces can exhibit changes by orders of magnitude under certain circumstances, such as: insufficient curing during RPC production, existence of a strong electric field and high bakelite temperature [93]. Since the necessity of linseed oil treatment of RPC modules for the CMS endcaps is still an open issue, the work on SPICE simulation will be continued to study the influence of linseed oil resistivity changes on the performance of RPC detectors working in avalanche mode in large rapidity regions of the CMS detector.

Summary

The subject of this thesis has concerned important component of the CMS muon detection system — the Resistive Plate Chamber detectors. The emphasis has been put on the RPC performance under high particle fluxes which induce rate of avalanches in the sensitive volume of the detector of the order of 1 kHz/cm^2 in a single gas layer.

Firstly electrical and mechanical characteristics of several developmental materials for RPC electrodes have been studied. It was found that a detector operating under high particle flux it will be difficult to maintain constant resistivity level of the electrodes over 10 years of the LHC activity unless the working dry gas mixture contains controlled amount of water vapour.

Afterward novel RPC techniques have been proposed, such as: reinforced gap spacers, elimination of the graphite coating procedure, inverted double gap configuration. This techniques have been implemented in five prototypes made out of low resistivity bakelite plates ($10^9 \div 10^{10} \Omega\text{cm}$). All detectors have been tested in the Gamma Irradiation facility at CERN during period of 1997-2002 under presence of the background radiation similar to that expected at large rapidity regions (up to $|\eta| = 2.1$) of the CMS muon system.

The main aim of the first beam test was to demonstrate the rate capability of a double gap RPC detector operated under constant and uniform high background rate. Results on small-size prototype have confirmed that the electrodes' resistivity does affect chamber characteristics significantly and that RPC having electrodes of conductivity $\sim 10^9 \Omega\text{cm}$ still acts as a set of independent cells with localized discharge. For this level of resistivity the upper limits on the rate of avalanches at which efficient detection of muons is still possible (i.e. $\geq 95\%$) are $7 \text{ kHz/cm}^2/\text{gap}$ and $5 \text{ kHz/cm}^2/\text{gap}$ for pulsed accelerator beams of 2.5 s duration and for continuous and uniform irradiation with gamma rays, respectively. These results have shown usefulness of the RPC technique for the CMS endcap region and significantly contributed to the detector definition in *The Muon Project Technical Design Report* of year 1997 [28].

The next goal was to verify experimentally for the first time whether a full scale prototype of the ME 1/1 RPC station can operate in the environment foreseen in the CMS detector (with required safety factors). The prototype tested has shown very good performance when operated in the continuous high radiation rate environment in the whole range of source intensities studied. It has been demonstrated that operation characteristics of an Inverted Double Gap version of the

ME 1/1 RPC station are adequate for the muon trigger requirement of the CMS experiment with good safety margin. Namely, the efficiency of 95% for 15 ns time window with plateau exceeding 1 kV, the time resolution ≤ 1.7 ns and the time walk related to the rate variation < 2.5 ns at background rates as high as 5 kHz/cm²/gap have been measured. Using the gas mixture containing 1.5% of SF₆ gas in the base gas mixture of Tetrafluoroethane/Isobutane (97/3) resulted in achieving better performances in comparison with previously tested prototype, mainly due to better streamer suppression capabilities and a more sustained avalanche development.

Another beam tests of a medium-size rectangular Inverted Double Gap model detector have been devoted to demonstration of the significance of factors influencing long-term stability of the gas gain and of the detection efficiency, such as gas composition and temperature of the electrodes, under constant flux of radiation corresponding to the ionization rate up to 1 kHz/cm²/gap. It was found that the quality of the detector operation depends strongly on the gas mixture used, namely addition of SF₆ freon as small as 0.5% to the base Tetrafluoroethane/Isobutane gas mixture stabilizes RPC operation by substantial reduction of the intrinsic noise rate. Among the results, a self-heating of the detector has been observed at high rates and significant influence of the detector's temperature on the spontaneous noise rate has been found. The measurements seem to suggest that in the CMS detector the heat dissipated in RPC detectors working at high rates should be efficiently drained off in order to achieve stable RPC operation.

Finally, the aim of the latest beam tests in the GIF was to demonstrate that a single RPC layer of 2 mm gas gap, when filled with adequate gas mixture and made of properly selected electrode material, allows one for full detection efficiency of ionizing particle fluxes of about 1 kHz/cm²/gap. Two single gap prototypes were built using same materials and technology, and later one of them has been coated with linseed oil. Despite different treatment of the internal surfaces their performance was very similar at high rates. The practical efficiency $\geq 95\%$ for 15 ns gate window, the time resolution ≤ 2.6 ns and the rate related time walk ≤ 2.5 ns have been measured for the first 400 V of the efficiency plateau for the gas mixture Tetrafluoroethane/Isobutane/SF₆ (95.8/3.5/0.7). It has been also shown that the problem with too high intrinsic RPC noise can be solved without treatment of the internal bakelite surfaces with the linseed oil mixture. A key role in the success is played not only by utilizing materials characterized by small mechanical roughness ($\sim 0.15 \mu\text{m}$), but also by careful handling of the electrode plates during all phases of RPC construction: starting from the bakelite manufacturing, through its transportation, and ending on assembling technique in a clean environment. Both chambers exhibited very low intrinsic noise rate and dark current in comparison with all previously tested prototypes. Namely, for Tetrafluoroethane/Isobutane (97/3) gas mixture it is < 5 Hz/cm² and < 0.5 Hz/cm² for, respectively, not-oiled and oiled RPC over 400 V of the efficiency plateau. Moreover, from dependence

of the gas gain on the operating voltage for Tetrafluoroethane/Isobutane/SF₆ (95.8/3.5/0.7) gas mixture it is possible to predict even wider low-noise voltage range corresponding to the full efficiency plateau. The data on the strip multiplicity measured for rectangular prototypes of 12 mm strip pitch indicates that keeping the average number of responding strips for single ionizing particle below 2 might be problematic in RPCs for the large rapidity region of the CMS detector.

The possible ageing phenomena have been also studied using dedicated Parallel Plate Avalanche Chamber with resistive bakelite anode operated under intense photon flux from the X-ray generator. The advantages of using a PPAC detector for long-term gas monitoring are numerous, e.g. well defined number of primary electrons starting the avalanche at the cathode and peaked amplitude pulse-height spectra. The results have shown some disadvantageous effects occurring at avalanche rates exceeding 1 kHz/cm², like hysteresis of the charge gain dependence on the counting rate, however, more studies are needed to understand the nature of these processes and to find a remedy. A construction of the new experimental set-up suitable for longer continuous exposures of PPAC detectors to X-ray beams is currently under way at the Detector Laboratory of IEP.

Last, but not least, parametrization of the experimental data on the gas gain dependence on the electric field has been used to predict departure from the nominal applied voltage at avalanche rates of 1 kHz/cm². The model developed by the Author has been based on the numerical code for transient analysis of electric circuits (SPICE). The proposed working electric circuit allows one, for example, to study influence of resistivity changes on the RPC performance.

The Author himself has been responsible for: performing conductivity measurements, selection of the candidate materials and establishing links with bakelite manufacturers. It was his responsibility to prepare the experimental set-up and the data acquisition system for X-ray irradiation tests of the PPAC detector. The measurements and data analysis have been performed by the Author with partial help of two undergraduate students. He has been also responsible for the design of all RPC prototypes and has participated in a team work of assembling the chambers in the Detector Laboratory of IEP. The Author participated in almost all test beams performed by the Warsaw CMS Group at CERN¹ from which the results are discussed in this thesis. He has been partially responsible for developing the data acquisition software and led the work of setting up the detectors and readout electronics during test beams. Most of the results from off-line data analyses presented in this thesis have been obtained by the Author himself.

¹Except one beam test in the GIF in 1997.

Acknowledgments

I am very grateful to my supervisors, Prof. Wojciech Dominik and Prof. Jan Królikowski for their continuous interest, encouragement and support during all these years of preparing this doctorate thesis.

I wish to thank warmly all my colleagues from the Warsaw CMS Group, as well as members of the HEP community of the Warsaw University and the Soltan's Institute for Nuclear Studies for a very pleasant cooperation. In particular, many thanks are addressed to Maciej Górski and Paweł Majewski for their help during laboratory measurements and beam tests, as well as for many fruitful discussions. My special thanks go to engineers from the IEP Detector Laboratory: H. Czyrkowski, R. Dąbrowski, W. Kuśmierz, Z. Lewicki, Z. Sałapa and K. Sułowski for creating a wonderful work atmosphere and for their excellent technical support.

I also would like to thank the INFN groups from Bari and Pavia, and the KODEL group from Korea for very pleasant cooperation during all test beams at CERN. In particular, I am indebted to Prof. Giuseppe Iaselli for kindly providing readout electronics. The successful beam tests would not be possible without help of the following people: Gy. Bencze, F. Szoncsó, I. Crotty, L. Gorn, H. Reithler and M. Wegner. I want express my gratitude to the research departments of two commercial companies: IZO-ERG S.A. Gliwice, Poland, and Pan-Pla Laminates, Frati Group, Pavia, Italy for providing developmental bakelite samples and for a very nice cooperation.

This work was supported in part by the Polish Committee for Scientific Research under grants: KBN 115/E-343/SPUB/P03/119/96, KBN 115/E-343/SPUB/P03/004/97, KBN 2/P03B/054/16 and KBN 5/P03B/024/20.

Finally, the warmest thanks go to my family, and especially to my Parents, who constantly supported and encouraged me during my research.

Appendix A

Conductivity measurement technique

The electric conductivity of tested composite materials has been examined according to standards given in Ref. [102] using a direct DC current measurement.

Firstly, tested bakelite plates have been cut to form $10 \times 10 \text{ cm}^2$ square samples with four mounting holes in the corners, as it is depicted in Fig. A.1. Each of them has three coaxial circular electrodes. One electrode is placed on the bottom side and the other ones on the top of the specimen. Their inner, mid and outer diameters are: $D_1 = 25 \text{ mm}$, $D_2 = 30 \text{ mm}$ and $D_3 = 60 \text{ mm}$, respectively. Depending on the electric circuit configuration the same set of electrodes allows one to measure volume resistivity (Fig. A.2) or surface resistivity (Fig. A.3).

The electric charge is collected from the inner *readout electrode*, while two remaining electrodes are interchangeably used for electric shielding (*guarding electrode*) and for distribution of the applied voltage (*voltage electrode*) depending on chosen configuration. A grounded guarding electrode is necessary to prevent mixing of the volume- and the surface components of the current during the test.

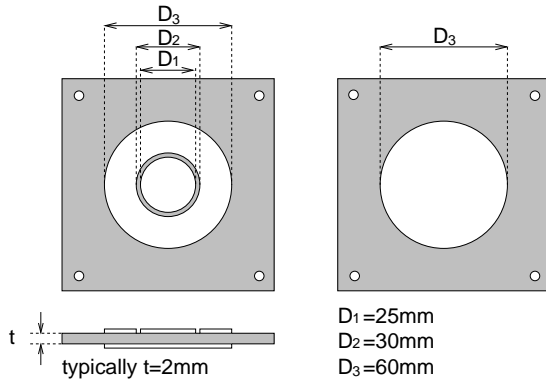


Figure A.1: Coaxial circular electrodes for electric conductivity tests of flat composite materials.

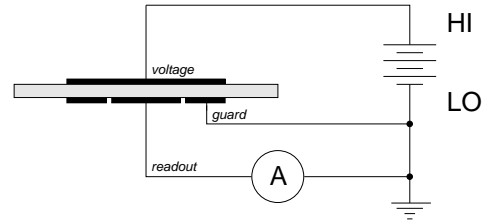


Figure A.2: Electric circuit for volume resistivity measurements.

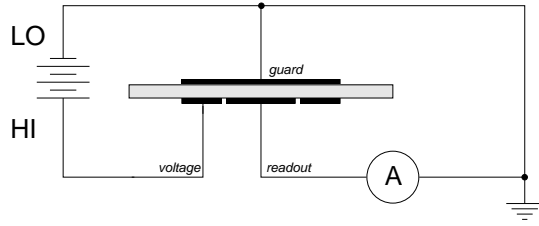


Figure A.3: Electric circuit for surface resistivity measurements.

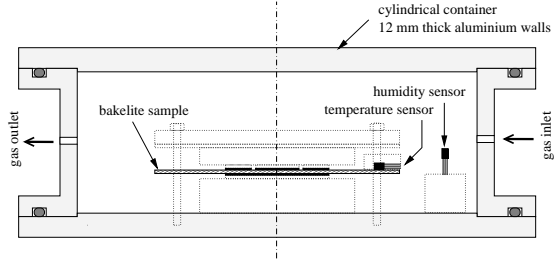


Figure A.4: Cross section of the aluminium container for conductivity tests which provides necessary electric shielding and gas-tightness. A configuration for conductive rubber technique was shown.

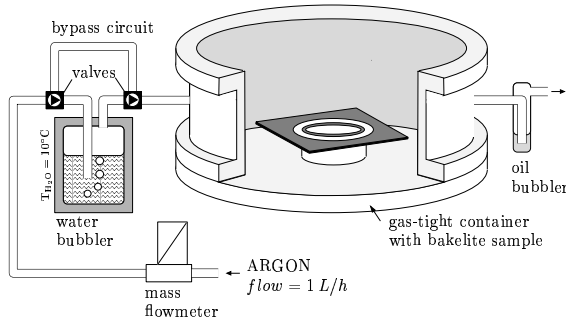


Figure A.5: Experimental set-up for conductivity measurements in dry- and wet gas environments.

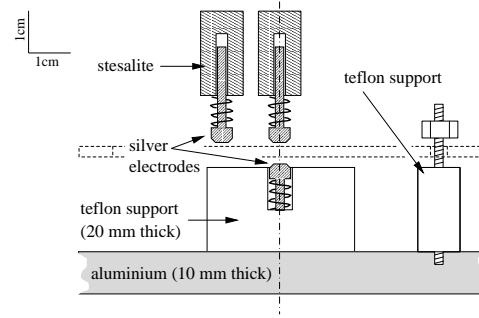


Figure A.6: Special probe for conductivity measurements of specimens with permanent electrodes (i.e. integrated aluminium foil, conductive silver paint).

The volume resistivity, ρ , and the surface resistivity, σ , have been calculated using formulas from Ref. [102]:

$$\rho = \frac{\pi}{4} (D_1 + g)^2 \frac{1}{t} \frac{U}{I - I_o}, \quad (\text{A.1})$$

$$\sigma = \frac{\pi}{2} (D_1 + D_2) \frac{1}{g} \frac{U}{I - I_o}, \quad (\text{A.2})$$

where : $D_1 = 25 \text{ mm}$, $D_2 = 30 \text{ mm}$ = diameters of electrodes used,

$$g = \frac{1}{2}(D_2 - D_1),$$

t = thickness of the sample,

I_o = residual current measured for $U_o = 0$,

I = current measured for test voltage U .

The size of electrodes, the thickness- and the resistivity range of tested specimens imply using precise ammeter with stable voltage source. A KEITHLEY picoammeter Mod. 487¹ fulfills all requirements given above. It has a built-in precise D-C source up to 500 V with selectable polarity. The unit is capable to measure currents from 10 fA to 2 mA. It is fully controlled through IEEE-488 GPIB bus line from a PC machine. More detailed specifications concerning precision and stability of the unit are listed in Tab. A.1.

Depending on the resistivity of the sample and the ambient temperature variations the accuracy of the measured current ranges from $\frac{\delta I}{I} = 1 \times 10^{-3}$ (i.e. the best case: $U = 500$ V, $\rho = 10^8 \Omega\text{cm}$ and $T = 18^\circ \div 28^\circ\text{C}$) to $\frac{\delta I}{I} = 6 \times 10^{-3}$ (i.e. the worst case: $U = 10$ V, $\rho = 10^{12} \Omega\text{cm}$ and $T = 35^\circ\text{C}$). The relative uncertainty of the applied voltage, assuming ambient temperature

Table A.1: Accuracy specifications of KEITHLEY 487 unit.

Current measurement (I)		
Range	Resolution	Accuracy (over 1 year) $T = 18^\circ \div 28^\circ\text{C}$
2 nA	10 fA	$0.3\% I + 500 \text{ fA}$
20 nA	100 fA	$0.2\% I + 3 \text{ pA}$
200 nA	1 nA	$0.15\% I + 20 \text{ pA}$
$2 \mu\text{A}$	10 nA	$0.15\% I + 200 \text{ pA}$
$20 \mu\text{A}$	100 nA	$0.1\% I + 2 \text{ nA}$
$200 \mu\text{A}$	$1 \mu\text{A}$	$0.1\% I + 20 \text{ nA}$
2 mA	$10 \mu\text{A}$	$0.1\% I + 200 \text{ nA}$
Temperature coefficient $T = 0^\circ \div 18^\circ\text{C}$ or $T = 28^\circ \div 50^\circ\text{C}$		$0.15 \times (\text{applicable accuracy}) / ^\circ\text{C}$
Constant voltage source (U)		
Range		$\pm 505 \text{ V}$ in 10 mV steps
Accuracy (over 1 year) $T = 18^\circ \div 28^\circ\text{C}$		$0.15\% U + 40 \text{ mV}$
Temperature coefficient $T = 0^\circ \div 18^\circ\text{C}$ or $T = 28^\circ \div 50^\circ\text{C}$		$0.008\% U + 2 \text{ mV}/^\circ\text{C}$
Peak-to-peak noise $0.1 \text{ Hz} \div 20 \text{ MHz}$		$< 30 \text{ mV}$

¹Kindly provided by the Faculty of Physics, Warsaw University of Technology, Warsaw, Poland. This essential contribution is here acknowledged.

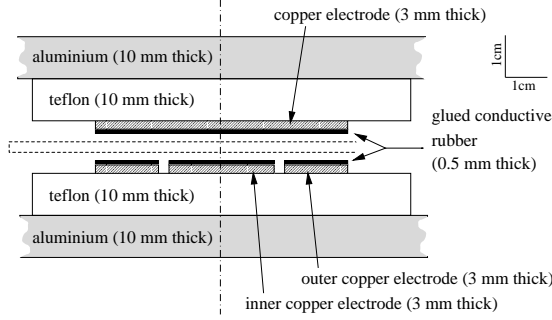


Figure A.7: Special probe for resistivity measurements using conductive rubber technique.

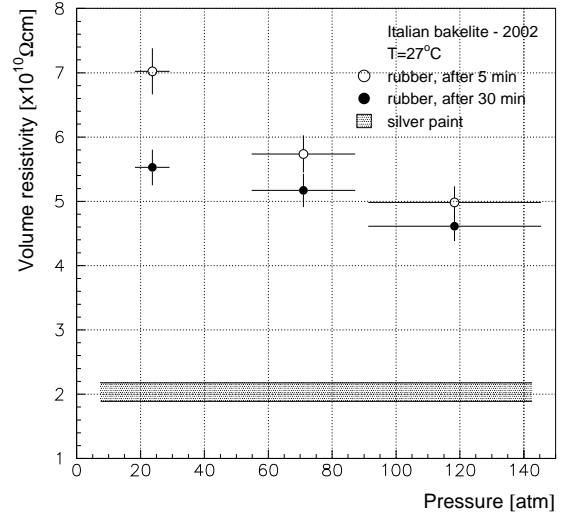


Figure A.8: Comparison of conductive rubber technique and silver paint method for IT-2002 sample at test voltage of 500 V.

changes between 15°C and 35°C, is equal to: $\frac{\delta U}{U} = 6 \times 10^{-3}$ and $\frac{\delta U}{U} = 2 \times 10^{-3}$ for $U = 10$ V and $U = 500$ V, respectively.

The diameters of electrodes: $D_1 = 25$ mm, $D_2 = 30$ mm and $D_3 = 60$ mm are known with accuracy $\delta D = 0.5$ mm, what yields $g \pm \delta g = 2.5 \pm 0.4$ mm. The thickness of each sample has been measured with micro-meter in four test points. The accuracy of the thickness t has been taken as $\delta t = 30 \mu\text{m}$ (typical std. dev.) $\oplus 10 \mu\text{m}$ (micro-meter precision) $\approx 32 \mu\text{m}$. Thus, estimated relative errors on the volume- and surface resistivity are:

$$\frac{\delta \rho}{\rho} = \frac{\delta D}{D_1 + g} \oplus \frac{\delta g}{D_1 + g} \oplus \frac{\delta t}{t} \oplus \frac{\delta U}{U} \oplus \sqrt{2} \frac{\delta I}{I - I_o} \approx 3 \div 4 \%, \quad (\text{A.3})$$

$$\frac{\delta \sigma}{\sigma} = \sqrt{2} \frac{\delta D}{D_1 + D_2} \oplus \frac{\delta g}{g} \oplus \frac{\delta U}{U} \oplus \sqrt{2} \frac{\delta I}{I - I_o} \approx 16 \% \quad (\text{A.4})$$

for typical tested materials of $\rho = 10^8 \div 10^{12} \Omega\text{cm}$ (or $\sigma = 10^8 \div 10^{12} \Omega/\square$) and for test voltage range $U = 10 \div 500$ V. A dominant contribution to these errors is due to uncertainty of: electrodes' dimensions and the thickness of the specimen under test.

Each tested sample has been mounted inside a special aluminium gas-tight container which cross section is shown in Fig. A.4. Its walls provide necessary electric shielding. The box can be connected to a gas line allowing one to monitor long-term changes of conductivity in controlled and arbitrary chosen gas environment. A configuration for dry- and wet Argon tests can be seen in Fig. A.5.

Table A.2: Types of electrodes used in conductivity tests.

	Name	Description	Class
1	<i>Conductive silver paint</i>	Electrodes painted directly on a cleaned specimen's surface using silver conductive paint of few Ω/\square (Electon 15SL or 40AC by Amepox Ltd, Łódź, Poland)	permanent
2	<i>Integrated aluminium foil</i>	Specially developed samples with 50 μm thick aluminium foil integrated with one or both outer bakelite surfaces during the production process; later the foil can be etched to form electrodes	permanent
3	<i>Conductive rubber technique</i>	0.5 mm thick conductive rubber electrodes firmly pressed to the specimen's surface	removable
4	<i>Metal depositing technique</i>	Thin layer of silver deposited on the specimen's surface in a vacuum chamber (main drawback: resistivity changes due to drying in vacuum)	permanent
5	<i>Self-adhesive copper tape</i>	Commercially available copper tape with self-adhesive conductive glue attached to the specimen's surface (main drawback: adhesion and conductivity of glue changes with time)	permanent

In general, two classes of electrodes can be distinguished:

- *permanent* - a conductive layer is permanently attached to the specimen's surface,
- *removable* - a conductor is in electrical contact with the sample only for duration of the test.

A brief summary of all tested types of electrodes is given in Tab. A.2. In this work, however, only results obtained using first three methods are reported.

For the first two methods listed in Tab. A.2 the sample under test is mounted in the bottom of the aluminium container by means of four Teflon screws. A sufficient electric contact is provided by three silver tips gently pressed to the permanent electrodes. A schematic cross section is depicted in Fig. A.6. However, for some bakelite types a combination of silver painted electrodes on one side and aluminium foil ones on the opposite side has been used.

A special probe for conductive rubber technique, shown in Fig. A.7, is constituted of 0.5 mm thick conductive rubber electrodes glued, using conductive silver epoxy, onto the rigid 3 mm thick copper electrodes, which have identical shape as the rubber ones. The copper electrodes are mounted on 1 cm thick insulating Teflon cylinders of 80 mm diameter. Since a reasonable pressure must be applied to the rubber in order to make it conductive, the flat 10 mm thick aluminium

plate is put on the top of the structure, which is firmly pressed to the bottom aluminium lid by four M5 steel screws, as it is schematically shown in Fig. A.4. The applied pressure has been calculated from moment of force measured with a dial torque wrench for each of four nuts. A large uncertainty for pressure is due to unknown friction coefficient for steel nuts used (e.g. typical range is $0.1 \div 0.2$). For some bakelite types a combination of aluminium foil electrodes on one side and conductive rubber ones on the opposite side has been used, as well.

The conductive rubber technique is used as an alternative method because it is not sensitive to eventual change of adhesion of the aluminium foil to the bakelite skin or to ageing of the conductive paint. However, in most cases resistivity measured using the rubber technique was systematically overestimated by a factor of about 2-3 in comparison with other methods. A typical dependence of the measured resistivity on the pressure applied to the rubber electrodes is shown Fig. A.8. A gray area corresponds to results obtained with silver painted electrodes. The observed discrepancy between methods can be attributed to a smaller effective area of charge collection (i.e. worse electric contact) than the one resulting from geometry of the readout electrode. A workaround is possible by wetting the rubber with tap water prior to measurements, although such method is not adequate for long-term tests. Moreover, if the resistivity of tested samples is below $10^9 \Omega\text{cm}$ all three methods lead to comparable results, as can be seen from Fig. 3.6 for PL-#19 type laminate in its “fresh” state — i.e. shortly after removal of the aluminium foil from the readout side.

A single resistivity test (*run*) is performed in 4 steps listed below:

1. Cleaning the specimen’s surface with a soft paper-tissue soaked in iso-propanol² and exposing it to a dry, clean stream of air before placement inside a shielded container.
2. Performing picoammeter zero check for 1 min to determine a constant offset of the measured current.
3. Applying a constant voltage of $U_o = 0$ for at least 5 minutes to discharge the electrodes and to measure the residual current $I_o(t)$.
4. Applying a constant test voltage of U for at least 5 minutes while measuring the current $I(t)$.

In the case of subsequent and long-term conductivity tests of the same sample steps 2-4 are cyclically repeated.

The probe for resistivity measurements is also equipped with commercially available electronic humidity- and temperature sensors located inside the gas box, as it is shown in Fig. A.4. The humidity sensor (Honeywell IH-3610-2 type) measures relative humidity of the gas medium with 2% accuracy. The temperature sensor (National Semiconductor LM-35 type) is in touch with the specimen’s surface and its accuracy is 0.5°C .

²Not applicable to the silver painted electrodes.

Bibliography

- [1] S. GLASHOW, *Partial-symmetries of weak interactions*, Nucl. Phys. **22** (1961) 579.
- [2] S. WEINBERG, *A model of leptons*, Phys. Rev. Lett. **19** (1967) 1264.
- [3] A. SALAM, *Weak and electromagnetic interactions*, In *Elementary Particle Theory*, page 367, ed. by N. Svartholm, Aspenäsgråden, 1968.
- [4] P. HIGGS, *Broken symmetries, massless particles and gauge fields*, Phys. Lett. **12** (1964) 132.
- [5] P. HIGGS, *Broken symmetries and the masses of gauge bosons*, Phys. Rev. Lett. **113** (1964) 508.
- [6] P. HIGGS, *Spontaneous symmetry breakdown without massless bosons*, Phys. Rev. **145** (1966) 1156.
- [7] F. ENGLERT and R. BROUT, *Broken symmetry and the mass of gauge vector mesons*, Phys. Rev. Lett. **13** (1964) 321.
- [8] G.S. GURALNIK, C.R. HAGEN, and T.W. KIBBLE, *Global conservation laws and massless particles*, Phys. Rev. Lett. **13** (1964) 585.
- [9] R. SANTONICO and R. CARDARELLI, *Development of Resistive Plate Counters*, Nucl. Instr. and Methods **187** (1981) 377.
- [10] R. SANTONICO, *Fast muon tracking with Resistive Plate Chambers*, In *Proceedings of the Large Hadron Collider Workshop*, volume 3, page 838, ed. by G. Jarlskog and D. Rein, CERN 90-10, ECFA 90-133, Aachen, Germany, 4-9 October 1990.
- [11] Eds. P. LEFEVRE and T. PETTERSSON, *The Large Hadron Collider - Conceptual Design*, CERN/AC 95-05, 1995.
- [12] LHWG COLLAB., *Search for the Standard Model Higgs Boson at LEP*, CERN LHWG Note/2002-01, 19 July 2002.
- [13] K. HAGIWARA ET AL., *Review of Particle Physics*, Phys. Rev. **D 66** (2002), <http://pdg.lbl.gov>.

- [14] S. VILLA, *The Global Electroweak Fit*, arXiv:hep-ph/0209359 v1, 30 Sept. 2002, <http://www.arxiv.org>.
- [15] ATLAS COLLAB., *ATLAS Detector and Physics Performance Technical Design Report*, CERN/LHCC 99-15, 1999.
- [16] CMS COLLAB., *CMS Technical Proposal*, CERN/LHCC 94-38, 1994.
- [17] G. WROCHNA, *Physics at LHC*, CERN CMS CR-2002/015.
- [18] K. LASSILA-PERINI, *Higgs Physics at the LHC*, CERN CMS CR-2001/018.
- [19] R.N. CAHN, Rep. Prog. Phys. **52** (1989) 389.
- [20] G. SEGNERI, *Squarks and Gluino searches with CMS at LHC*, CERN CMS CR-2002/007.
- [21] S. BANERJEE, *Prospects of B-Physics with CMS*, CERN CMS CR-2001/004.
- [22] LHCb COLLAB., *LHCb Technical Proposal*, CERN/LHCC 98-4, 1998.
- [23] G. WROCHNA, *Heavy Ion Physics with CMS Detector*, CERN CMS CR-2002/012.
- [24] ALICE COLLAB., *ALICE Technical Proposal*, CERN/LHCC 95-71, 1995.
- [25] ATLAS COLLAB., *ATLAS Technical Proposal*, CERN/LHCC 94-43, 1995.
- [26] TOTEM COLLAB., *TOTEM Technical Proposal*, CERN/LHCC 99-7, 1999.
- [27] CMS COLLAB., *The Trigger and Data Acquisition Project Technical Design Report - The Trigger Systems*, volume 1, CERN/LHCC 2000-38, 2000.
- [28] CMS COLLAB., *The Muon Project Technical Design Report*, CERN/LHCC 97-32, 1997.
- [29] G. BRUNO, *The RPC detectors and the muon system for the CMS experiment at the LHC*, PhD thesis, University of Pavia, Pavia, 2001 (unpublished).
- [30] K. BANZUZI ET AL., *Layout of the Link System for the RPC Pattern Comparator Trigger*, CERN CMS IN-2000/043.
- [31] G. IASELLI ET AL., *Study of Detailed Geometry of Barrel RPC Strips*, CERN CMS IN-2000/044.
- [32] G. BRUNO ET AL., *RPC System Geometry Simulated in CMSIM 118-120 and ORCA 4.2*, CERN CMS IN-2000/054.
- [33] A. KALINOWSKI ET AL., *Muon Trigger Algorithms Based on 6 RPC Planes*, CERN CMS NOTE-2001/045.

-
- [34] R. CARDARELLI ET AL., *Progress in resistive plate chambers*, Nucl. Instr. and Methods **A 263** (1988) 20.
- [35] J.W. KEUFFEL, *Parallel-Plate Counters and the Measurement of Very Small Time Intervals*, Phys. Rev. **73** (1948) 531.
- [36] J.W. KEUFFEL, *Parallel Plate Counters*, Rev. Sci. Instr. **20** (1949) 202.
- [37] G. CHARPAK and F. SAULI, *The multistep avalanche chamber*, Phys. Lett. **78 B** (1978) 523.
- [38] A. PEISERT, *The parallel plate avalanche chamber as an endcap detector for time projection chamber*, Nucl. Instr. and Methods **217** (1983) 229.
- [39] V.V. PARAKHOMCHUK ET AL., *A spark counter with large area*, Nucl. Instr. and Methods **93** (1971) 269.
- [40] YU.N. PESTOV, *Status and future developments of sparks counters with a localized discharge*, Nucl. Instr. and Methods **196** (1982) 45.
- [41] H.A. BETHE ET AL., *Bremsformel für Elektronen relativistischer Geschwindigkeit*, Z. Phys. **76** (1932) 293.
- [42] D. GROOM, *Energy loss in matter by heavy particles*, Particle Data Group Notes PDG-93-06, 1993.
- [43] F. SAULI, *Principles of operation of multiwire proportional and drift chambers*, CERN Yellow Report 77-09, 1977.
- [44] G. MALAMUD ET AL., *Specific primary ionization induced by minimum ionizing electrons in CH₄, C₂H₆, C₃H₈, i-C₄H₁₀, argon, dimethylether, triethylamine and tetrakis(dimethylamino)ethylene*, J. Appl. Phys. **74**(6) (1993) 3645.
- [45] I. SMIRNOV, HEED - a program to compute energy loss of fast particles in gases, ver. 1.01, CERN Program Library, <http://consult.cern.ch/writeup/heed>.
- [46] H. FISCHLE ET AL., *Experimental determination of ionizing cluster size distributions in counting gases*, Nucl. Instr. and Methods **A 301** (1991) 202.
- [47] F.F. RIEKE and W. PREPEJCHAL, *Ionization Cross Sections of Gaseous Atoms and Molecules for High-Energy Electrons and Positrons*, Phys. Rev. **A 6**(4) (1972) 1507.
- [48] C.D. BROYLES ET AL., *The Measurement and Interpretation of the K Auger Intensities of Sn¹¹³, Cs¹³⁷, and Au¹⁹⁸*, Phys. Rev. **89** (1953) 715.

-
- [49] S. ALTIERI ET AL., *RPC γ sensitivity simulation*, Nucl. Instr. and Methods **A 456** (2000) 99.
 - [50] S. ALTIERI ET AL., *Simulation of Resistive Plate Chamber sensitivity to neutrons*, Nucl. Instr. and Methods **A 461** (2001) 57.
 - [51] H. RAETHER, *Electron Avalanches and Breakdown in Gases*, Butterworths, London, 1964.
 - [52] W. LEGLER, *Die Statistik der Elektronenlawinen in elektronegativen Gasen, bei hohen Felddärken und bei großer Gasverstärkung*, Z. Naturforschg. **16 a** (1961) 253.
 - [53] P. FONTE ET AL., *Streamers in MSGC's and other detectors*, SLAC-JOURNAL-ICFA-15-1.
 - [54] S. RAMO, *Currents induced in electron motion*, Proc. IRE **27** (1939) 584.
 - [55] E. GATTI ET AL., *Signal evaluation in multielectrode radiation detectors by means of a time dependent weighting vector*, Nucl. Instr. and Methods **193** (1982) 651.
 - [56] S. ALTIERI ET AL., *The bakelite for the RPCs of the experiment CMS*, Nucl. Instr. and Methods **A 456** (2000) 132.
 - [57] H. SCHÖPF and B. SCHNIZER, *Theory describing cathode signals from charges moving in counters with poorly conductive cathode*, Nucl. Instr. and Methods **A 323** (1992) 338.
 - [58] T. HEUBRANDTNER ET AL., *A simple theory for signals induced by a point charge moving in a resistive plate chamber*, Nucl. Instr. and Methods **A 419** (1998) 721.
 - [59] T. HEUBRANDTNER and B. SCHNIZER, *The quasi-static electromagnetic approximation for weakly conducting media*, Nucl. Instr. and Methods **A 478** (2002) 444.
 - [60] T. HEUBRANDTNER ET AL., *Static Electric Fields in an Infinite Plane Condensor with One or Three Homogeneous Layers*, CERN OPEN/2001-074.
 - [61] W. RIEGLER, *Induced signals in resistive plate chambers*, Nucl. Instr. and Methods **A 491** (2002) 258.
 - [62] G. BATTISTONI ET AL., *Resistive cathode transparency*, Nucl. Instr. and Methods **202** (1982) 459.
 - [63] G. AIELLI ET AL., *Logistic Saturated Avalanche Model*, talk given at *VI-th Workshop on RPCs and Related Detectors*, LIP, Coimbra, Portugal, 26-27 November, 2001 (article will be published in the Proceedings in Nucl. Instr. and Methods A).

-
- [64] C. LIPPMANN and W. RIEGLER, *Detailed Models for Timing and Efficiency in Resistive Plate Chambers*, In *Proceedings of the VI-th Workshop on RPCs and Related Detectors*, LIP, Coimbra, Portugal, 26-27 November 2001 (to be published in Nucl. Instr. and Methods A).
- [65] V. AMMOSOV ET AL., *Electric field and currents in resistive plate chambers*, Nucl. Instr. and Methods **A 401** (1997) 217.
- [66] M. ABBRESCIA ET AL., *Effect of linseed oil treatment on the performance of Resistive Plate Chambers*, Nucl. Instr. and Methods **A 394** (1997) 13.
- [67] M. ADLINGER ET AL., *Study of Resistive Plate Chambers for muon detection at hadron colliders*, Nucl. Instr. and Methods **A 340** (1994) 370.
- [68] M. BERTINO ET AL., *Performance of resistive plate counters at beam flux up to 140 Hz/cm^2* , Nucl. Instr. and Methods **A 283** (1989) 654.
- [69] C. BACCI ET AL., *Study of resistive plate chambers for muon detection at hadron colliders*, Nucl. Instr. and Methods **A 340** (1994) 466.
- [70] C. BACCI ET AL., *Measurement of the efficiency and time resolution of double-gap resistive plate chambers*, Nucl. Instr. and Methods **A 345** (1994) 474.
- [71] I. CROTTY ET AL., *Investigation of resistive parallel plate chambers*, Nucl. Instr. and Methods **A 329** (1993) 133.
- [72] I. CROTTY ET AL., *The nonspark mode and high rate operation of resistive parallel plate chambers*, Nucl. Instr. and Methods **A 337** (1994) 370.
- [73] M. IORI and F. MASSA, *Performances of a RPC at high ionization rates*, Nucl. Instr. and Methods **A 306** (1991) 159.
- [74] R. CARDARELLI ET AL., *Performance of a resistive plate chamber operating with pure CF_3Br* , Nucl. Instr. and Methods **A 333** (1993) 399.
- [75] C. BACCI ET AL., *Test of a resistive plate chamber operating with low gas amplification at high intensity beams*, Nucl. Instr. and Methods **A 352** (1995) 552.
- [76] R. CARDARELLI, *Operation of Resistive Plate Chambers with Pure CF_3Br* , Sci. Acta University of Pavia **8(3)** (1993) 159.
- [77] I. CROTTY ET AL., *Further studies of avalanche mode operation of resistive parallel plate chambers*, Nucl. Instr. and Methods **346** (1994) 107.
- [78] L. ACITELLI ET AL., *Study of the efficiency and time resolution of an RPC irradiated with photons and neutrons*, Nucl. Instr. and Methods **A 360** (1995) 42.

-
- [79] ATLAS COLLAB., *ATLAS Technical Design Report, Muon Spectrometer*, CERN/LHCC 97-22, 1997.
 - [80] LHCb COLLAB., *LHCb Muon System Design Report*, CERN/LHCC 2001-010, 2001.
 - [81] A. DI CIACCIO, *Resistive Plate Chambers in ATLAS*, Nucl. Instr. and Methods **A 384** (1996) 222.
 - [82] A. BALDIT ET AL., *RPC tests for the ALICE dimuon trigger*, CERN ALICE internal note / DIM / 98-16.
 - [83] P. CAMARRI ET AL., *Streamer suppression with SF₆ in RPCs operated in avalanche mode*, Nucl. Instr. and Methods **A 414** (1998) 317.
 - [84] I. CROTTY ET AL., *The wide gap resistive plate chamber*, Nucl. Instr. and Methods **A 360** (1995) 512.
 - [85] E. CERRON ZEBALLOS ET AL., *High rate resistive plate chambers*, Nucl. Instr. and Methods **A 367** (1995) 388.
 - [86] E. CERRON ZEBALLOS ET AL., *A new type of resistive plate chamber: The multigap RPC*, Nucl. Instr. and Methods **A 374** (1996) 132.
 - [87] E. CERRON ZEBALLOS ET AL., *Latest results from the multigap resistive plate chamber*, Nucl. Instr. and Methods **A 392** (1997) 145.
 - [88] M.C.S. WILLIAMS ET AL., *The development of the multigap resistive plate chamber*, Nucl. Phys. **B 61** (1998) 250.
 - [89] H. CZYRKOWSKI ET AL., *Tests of RPC prototypes in RD5 during 1994 runs*, Sci. Acta University of Pavia **11**(1) (1996) 197.
 - [90] M. ABBRESCIA ET AL., *Progresses in the simulation of Resistive Plate Chambers in avalanche mode*, Nucl. Physics **B 78** (1999) 459.
 - [91] C. LIPPMANN ET AL., *Space Charge Effects and Induced Signals in Resistive Plate Chambers*, In *Proceedings of the VI-th Workshop on RPCs and Related Detectors*, LIP, Coimbra, Portugal, 26-27 November 2001 (to be published in Nucl. Instr. and Methods A).
 - [92] M. ADLINGER ET AL., *Measurements of the efficiency and time resolution of double gap Resistive Plate Chamber*, Nucl. Instr. and Methods **345** (1994) 474.
 - [93] F. ANULLI ET AL., *Mechanism affecting performance of the BaBar RPC chambers and searches for remediation*, In *Proceedings of the VI-th Workshop on RPCs and Related Detectors*, LIP, Coimbra, Portugal, 26-27 November 2001 (to be published in Nucl. Instr. and Methods A).

-
- [94] P. VITULO, *Update on the bakelite gluing*, talk given at CERN's CMS Week, June 2002 (unpublished).
- [95] P. FONTE ET AL., *New materials for extremely high counting rate proportional-mode RPCs*, Sci. Acta University of Pavia **13**(2) (1998) 11.
- [96] L. PONTECORVO ET AL., *Study of the characteristics of Resistive Plate Chambers in the RD5 experiment*, Sci. Acta University of Pavia **8**(3) (1993) 145.
- [97] G. BENCIVENNI ET AL., *Glass Electrode Spark Counter*, Sci. Acta University of Pavia **8**(3) (1993) 181.
- [98] E. ABLES ET AL., *ABS plastic RPCs*, Sci. Acta University of Pavia **11**(1) (1996) 373.
- [99] M. ĆWIOK ET AL., *Bakelite chambers for time-of-flight measurements*, Nucl. Instr. and Methods **A 433** (1999) 523.
- [100] H. CZYRKOWSKI ET AL., *Materiały o wysokiej oporności w fizyce cząstek*, Proceedings of the workshop *Materiały i układy elektroizolacyjne w przemyśle*, Ustroń-Jaszowiec, Poland, 7-9 October 1998; internal IEP report IFD-2/98 (in Polish) .
- [101] M. ĆWIOK, *Warsaw RPC R&D overview*, talk given at *RPC Under High Radiation Environment Workshop*, Korea University, Seoul, Korea, 21-22 February 2000 (unpublished).
- [102] Ed. AMERICAN SOCIETY FOR TESTING AND MATERIALS, *Annual Book of ASTM Standards: Test Methods for D-C Resistance or Conductance of Insulating Materials*, volume 10.01 (D 257-90), West Conshohocken, PA., 1990.
- [103] G.H. GRAYER, *Resistivity measurements on RPC materials*, Sci. Acta University of Pavia **11**(1) (1996) 285.
- [104] J. VA'VRA, *Physics and Chemistry of Aging - Early Developments*, In *Proceedings of the International Workshop on Aging Phenomena in Gaseous Detectors*, DESY, Hamburg, Germany, 2-5 October 2001 (to be published in Nucl. Instr. and Methods A).
- [105] L. MALTER, *Thin Film Field Emission*, Phys. Rev. **50** (1936) 48.
- [106] M. ADOLFINI ET AL., *Proposal for the RPC muon detector*, CERN LHCb NOTE 2000-053.
- [107] R. ARNALDI ET AL., *Influence of temperature and humidity on bakelite resistivity*, Nucl. Instr. and Methods **A 456** (2000) 140.
- [108] W. DOMINIK, *Resistivity of commercially available materials for RPC electrodes*, CERN CMS NOTE-1997/023.

-
- [109] S.H. AHN ET AL., *Temperature and humidity dependence of bulk resistivity of bakelite for resistive plate chambers in CMS*, Nucl. Instr. and Methods **A 451** (2000) 582.
- [110] G. PUGLIESE ET AL., *Aging study for Resistive Plate Chambers of the CMS Muon Trigger Detector*, In *Proceedings of the International Workshop on Aging Phenomena in Gaseous Detectors*, DESY, Hamburg, Germany, 2-5 October 2001 (to be published in Nucl. Instr. and Methods A).
- [111] G. AIELLI ET AL., *Further Advances in Aging Studies for RPCs*, In *Proceedings of the International Workshop on Aging Phenomena in Gaseous Detectors*, DESY, Hamburg, Germany, 2-5 October 2001 (to be published in Nucl. Instr. and Methods A).
- [112] M. ĆWIOK, *Status of the research on RPCs in Warsaw*, talk given at CERN's CMS Week, March 2002 (unpublished).
- [113] G. PASSALEVA ET AL., *First Results from an Aging Test of a Prototype RPC for the LHCb Muon System*, In *Proceedings of the International Workshop on Aging Phenomena in Gaseous Detectors*, DESY, Hamburg, Germany, 2-5 October 2001 (to be published in Nucl. Instr. and Methods A).
- [114] R. GUIDA, *Report on some preliminary analysis result concerning the gas*, talk given at CERN's joint meeting of RPC groups from ALICE, ATLAS and CMS - *RPCs @ GIF* coordinated by A. Sharma (CERN, EP-TA1), 27 August 2002 (unpublished).
- [115] D. MARLOW ET AL., *Recent Experiences with Aging in RPC Systems*, In *Proceedings of the International Workshop on Aging Phenomena in Gaseous Detectors*, DESY, Hamburg, Germany, 2-5 October 2001 (to be published in Nucl. Instr. and Methods A).
- [116] M. ABBRESCIA ET AL., *Beam Test Results on Resistive Plate Chambers for the CMS Experiment*, CERN CMS NOTE-1997/062.
- [117] S. AGOSTEO ET AL., *A facility for the test of large area muon chambers at high rates*, Nucl. Instr. and Methods **A 452** (2000) 94.
- [118] J. ŁAGODA, *Detektory gazowe typu RPC w układzie bieżącej detekcji mionów w eksperymencie CMS*, Master's thesis, Warsaw University, 1999 (in Polish, unpublished).
- [119] I. CROTTY ET AL., *RPC Gas Distribution Layout*, CERN CMS IN-2001/019.
- [120] F. LODDO ET AL., *Front end electronics for RPC detector of CMS*, Sci. Acta University of Pavia **8**(2) (1998) 113.
- [121] A. COLALEO ET AL., *First results on RB2 muon barrel RPC detector for CMS*, In *Proceedings of the VI-th Workshop on RPCs and Related Detectors*, LIP, Coimbra, Portugal,

- 26-27 November 2001 (to be published in Nucl. Instr. and Methods A), CERN CMS CR-2002/009.
- [122] H. CZYRKOWSKI ET AL., *Beam test results of Inverted Double Gap RPCs with high counting rate capability for the CMS experiment*, Sci. Acta University of Pavia **8**(2) (1998) 161.
- [123] H. CZYRKOWSKI ET AL., *New developments on resistive plate chambers for high rate operation*, Nucl. Instr. and Methods **A 419** (1998) 490.
- [124] H. CZYRKOWSKI ET AL., *Results of tests of Inverted Double Gap RPC at the CERN GIF facility*, CERN CMS NOTE-1998/065.
- [125] H. CZYRKOWSKI ET AL., *Highly efficient resistive plate chambers for high rate environment*, Nuclear Physics **B 78** (1999) 438.
- [126] M. ĆWIOK ET AL., *Medium-term stability of a Parallel Plate Avalanche Chamber with a bakelite electrode operated in high radiation flux*, Nucl. Instr. and Methods **A 456** (2000) 91.
- [127] M. ĆWIOK ET AL., *The performance of RPCs with bakelite electrodes of various resistivity under high radiation fluxes*, Nucl. Instr. and Methods **A 456** (2000) 87.
- [128] M. ĆWIOK ET AL., *Effect of temperature variation and gas composition on the stability of the RPC operation*, In *Proceedings of the VI-th Workshop on RPCs and Related Detectors*, LIP, Coimbra, Portugal, 26-27 November 2001 (to be published in Nucl. Instr. and Methods A), CERN CMS CR-2002/002.
- [129] M. ĆWIOK, *GIF '2000 beam test results*, talk given at *CMS Forward RPC Workshop*, Korea University, Seoul, Korea, 20-22 November 2000 (unpublished).
- [130] S. ALTIERI ET AL., *Preliminary results on double gap RPC in a high background environment*, Sci. Acta University of Pavia **13**(2) (1998) 139.
- [131] S. BIAGI, PCMONTE - a program to compute gas transport parameters (previous versions are known as IMONTE and MAGBOLTZ2), ver. 5.1, July 2002, code kindly provided by the author.
- [132] M.J. CLAYTON (ESS-CERN), private communication;
data from URL address <http://pcessgif04.cern.ch/envdata.html>.
- [133] M. ABBRESCIA ET AL., *Resistive plate chambers performances at cosmic rays fluxes*, Nucl. Instr. and Methods **A 359** (1995) 603.
- [134] M. ABBRESCIA ET AL., *Resistive plate chambers performances at low pressure*, Nucl. Instr. and Methods **A 394** (1997) 341.

-
- [135] R. BOUCLIER ET AL., *Aging of microstrip gas chambers: problems and solutions*, Nucl. Instr. and Methods **381 A** (1996) 289.
 - [136] NORBAS (E210) - portable collection of subprograms for various calculations with polynomial splines in one or two dimensions, MATHLIB, CERN Program Library, 1993.
 - [137] F. SAULI, *Fundamental understanding of aging processes: review of the workshop results*, In *Proceedings of the International Workshop on Aging Phenomena in Gaseous Detectors*, DESY, Hamburg, Germany, 2-5 October 2001 (to be published in Nucl. Instr. and Methods A).
 - [138] W. RIEGLER and D. BURGARTH, *Signal Propagation, Termination, Crosstalk and Losses in Resistive Plate Chambers*, CERN EP/2001-014.
 - [139] S.H. AHN ET AL., *Beam test result of a large real-size RPC for the CMS/LHC experiment*, Nucl. Instr. and Methods **A 456** (2000) 23.
 - [140] S.H. AHN ET AL., *Performance of a large forward resistive plate chamber for the CMS/LHC under high radiation environment*, Nucl. Instr. and Methods **A 469** (2001) 323.
 - [141] R. VEENHOF, GARFIELD - a program simulating gaseous detectors, ver. 7, 2001, CERN Program Library, <http://consult.cern.ch/writeup/garfield>.
 - [142] MAXWELL 2D/3D - a finite-element method solver for electro-magnetic fields, Ansoft Corporation, 1984-1999.
 - [143] SPICE - a general purpose program to calculate the response of networks with discrete components including voltage and current generators, Berkeley, ver. 3f.4, 1993.